Catalytic Hydrodeoxygenation of bio-oil produced from the co-pyrolysis of biomass and plastic waste

Thesis submitted in partial fulfilment of the requirements for the degree of

DOCTOR OF PHILOSOPHY

By

K JANAKI

(196107009)

Department of Chemical Engineering

Indian Institute of Technology Guwahati

Assam- 781039, India

May 2025

Catalytic Hydrodeoxygenation of bio-oil produced from the co-pyrolysis of biomass and plastic waste

K JANAKI

Department of Chemical Engineering

Indian Institute of Technology Guwahati

Assam- 781039, India

CERTIFICATE

This is to certify that the thesis entitled **“Catalytic Hydrodeoxygenation of bio-oil produced from the co-pyrolysis of biomass and plastic waste”** being submitted by **Ms. K Janaki** for the award of the degree of Doctor of Philosophy has been carried out by her at Department of Chemical Engineering, Indian Institute of Technology Guwahati, under my guidance and supervision. This work has not been submitted to any other University or Institute for the award of any degree or diploma.

Prof. Kaustubha Mohanty	**Prof. Vinu Ravikrishnan**
Supervisor	***Co-Supervisor***
Department of Chemical Engineering	Department of Chemical Engineering
Indian Institute of Technology Guwahati	Indian Institute of Technology Madras
Date:	Date:

DEDICATION

This thesis is dedicated to Dr Lakshmana Chary Vuruptoor (my Grand Father)

Acknowledgement

First and foremost, I extend my deepest gratitude to my supervisor, **Prof. Kaustubha Mohanty** and co-supervisor, **Prof. Vinu Ravikrishnan** for their invaluable guidance, unwavering support, and constant encouragement throughout this journey. Their expertise, patience, and dedication has been instrumental in shaping this research and fostering my intellectual growth. I would like to thank the **Department of Science and Technology-Waste Management Technologies, India (S.O. DST/TDT/WMT/Plastic Waste/2021/09)** and **Hindustan Petroleum Corporation Ltd (HPCL) R&D, Bangalore, India** for funding the present research.

I wish to extend my heartfelt appreciation to my doctoral committee members, **Prof. Mahuya De**, **Prof. Partho Sarathi Gooh Pattader**, and **Prof. Selvaraju Narayanasamy**, for their invaluable guidance and constructive feedback provided during my seminars and progress reviews. Their input has been instrumental in the accomplishment of my thesis. I would also like to thank **Prof Saroj S Baral**, my MTech supervisor for enabling my research abilities.

I express my gratitude to **Prof. Kaustubha Mohanty**, the current Head of the Department of Chemical Engineering, and **Prof. Anugrah Singh**, the former Head, for their administrative support. Additionally, I appreciate the continuous encouragement and assistance received from all the staff members of the Chemical Engineering Department. I am thankful to the Department of Chemical Engineering, IIT Guwahati, the Central Instruments Facility at IIT Guwahati, Analytical lab IIT Guwahati, Department of Chemical Engineering IIT Madras, National Centre for Combustion Research and Development, IIT Madras for granting access to instrumental facilities.

I would like to thank several funding agencies namely the Department of Science and Technology-International Travel Scheme (DST-ITS), Hindustan Petroleum Corporation Ltd

(HPCL) R&D, Bangalore, India, Institute Travel Grant for attending various conferences in-person ie., BIORESTEC 2023, Lake Garda, Italy; PyroAsia Symposium 2023, Kuala Lumpur, Malaysia; AIChE 2024 Annual Meeting during October 27-31, 2024 at San Diego California.

I would also like to acknowledge my friend's Dr Sharvari Gadegoankar, Dr Sachin Gautham MB, Dr Dileep Maarishetty, Dr Ankit Agarwalla, Dr Jayaram Krishna JV, Mr Abhishek Kumar, Mr Shree Sharan, Mr Harshavardhan Thodupunoori, Ms Aarti Rajput, Ms Pooja Singh, Ms Suchetna Kushwah, Dr Rammohan Draksharapu, Dr Vallabh Prabhudesai, Dr Subhan Pal, Dr Prabhat Patel, Dr Naveen Yaranal, Mr Anweshan, Ms Priyanka Prajapati for their help and support.

I am indebted to the selfless help and co-operation of my research group members, Dr Vasu Chaudhury, Dr Saurabh Chakraborty, Mr Om Prakash, Ms Anindita Das, Mr Pikesh Kumar, Mr Shanku Borah, Mr Kesavaulu Saalu, Mr Saptaswa Biswas, Dr Satya Sundar Mohanty, Mr Saket Kuchibotla, Mr Shubham Sharma, Mr Pragadesh Babu, Dr Marippan, Dr Balaji Muthuswamy, Ms Sravani, Mr Francis Prashanth, Mr Vishnu, Dr Puja Priyadarshini Nayak.

My Ph.D. endeavour would not have been successful without the love, trust, support and blessings of my parents and family members. I thank my brother Mr Krishna Teja Komandur and my sister in law Ms Vaishnavi Shesham and sisters Ms Madhavi Komanduri, Madhuri Komanduri, and Dr Mrudhula Komanduri for their constant support and love.

I am deeply grateful to God for His unwavering guidance and divine grace throughout the journey of completing this Ph.D. thesis.

Sincerely,

K Janaki

Abstract

Biofuels are essential in advancing sustainable energy solutions and decreasing reliance on fossil fuels. They are derived from renewable resources like biomass and waste. They contribute to energy security while mitigating greenhouse gas emissions and air pollution. Biofuels are crucial for decarbonizing sectors like transportation and aviation, where alternatives to liquid fuels are limited. Additionally, the usage of biofuels boosts rural economies by creating markets for agricultural residues and non-edible feedstocks. Moreover, their use promotes a circular economy by converting waste into valuable products. As a cleaner and renewable energy source, biofuels are pivotal in achieving global climate goals and sustainable development.

This thesis highlights the significance of co-pyrolysis and catalytic hydrodeoxygenation (HDO) techniques for producing upgraded biofuels. Co-pyrolysis is a well-established process that yields bio-oil, but its commercial fuel applications are limited due to a high oxygen content (approximately 25–50 wt.%). To address this limitation, catalytic HDO offers a promising solution by reacting oxygen-containing compounds in bio-oil with hydrogen in the presence of a catalyst to produce upgraded liquid fuels and water. Over the past three decades, substantial progress has been made in developing HDO catalysts, with a prominent surge in research intensity over the last ten years. Various catalytic systems have been explored, including silica-, alumina-, and zeolite-supported noble and non-noble metal catalysts. However, challenges such as high costs, limited availability, poor stability, and water-induced deactivation have shifted research focus toward cost-effective and readily available catalysts. Due to their affordability, environmental benefits, and energy efficiency, recent attention has turned to waste-derived catalysts, such as red mud, biochar, and eggshells. These waste-derived materials can be effectively utilized as feedstock for pyrolysis and as catalysts for the subsequent

upgrading processes. This dual utilization provides economic advantages and promotes environmental sustainability by repurposing waste materials.

This study investigates the feasibility of co-pyrolyzing *Mesua ferrea* L. oilseed, groundnut de-oiled cake (GDC), and wheat straw (WS) with polyethylene terephthalate (PET) plastic. The thermal decomposition behavior and kinetic parameter estimation are conducted using thermogravimetric analysis (TGA) under non-isothermal conditions in a nitrogen atmosphere at heating rates of 10, 20, and 30 °C min^{-1}. The thermal degradation behavior of biomass-PET mixtures (*Mesua ferrea* L.: PET, GDC: PET, and WS: PET) is compared with the degradation behavior of the individual components. Chemical kinetics is a critical aspect of the study as it provides insight into the reaction mechanisms, serving as the foundation for creating reliable kinetic models. These models are essential for designing large-scale industrial reactors optimized for this feedstock combination. Among the methods used, the Distributed Activation Energy Model (DAEM) yielded the lowest activation energy values: 127.9 kJ mol^{-1} for the oilseed, 201.5 kJ mol^{-1} for PET, and 156.2 kJ mol^{-1} for co-pyrolysis. The results demonstrate that blending *Mesua ferrea* L. oilseed with PET plastic substantially reduces activation energy, highlighting the synergistic effects of co-pyrolysis. This reduction facilitates more efficient reactor design, making the process more feasible and cost-effective.

Co-pyrolysis of *Mesua ferrea* L. (Nahar) and PET plastic focused on understanding the composition of pyrolysates and the thermal decomposition of complex feedstock mixtures. Feedstocks were analyzed using TGA (at a 15 °C/min heating rate), bomb calorimetry, and proximate/ultimate analyses. Both biomass and PET had low moisture content (3.33% and 0.61%, respectively) and high volatile matter content (88% for biomass and 94.53% for PET). Analytical pyrolysis coupled with GC/MS revealed the production of significant quantities of fatty acids (~79%) from Nahar and benzoic acid (24%) and acetylbenzoic acid (15.5%) from

PET at 590 °C. Feedstock mixtures of biomass and PET in ratios of 1:1, 2:1, and 1:2 w/w produced a mixture dominated by aliphatic and carboxylic acids. Fixed-bed co-pyrolysis experiments conducted at 550–650 °C (with a heating rate of 15 °C/min) identified 600 °C as the optimal temperature for biomass and co-pyrolysis (2:1 feedstock ratio), yielding high pyrolytic liquid outputs (27 wt.% for biomass alone and 35 wt.% for co-pyrolysis). Bio-oil characterization indicated significant proportions of fatty acids and carboxylic acids, including n-hexadecanoic acid, octadecenoic acid, octadecanoic acid, and benzoic acid.

Mechanistic studies revealed that decarboxylation and decarbonylation of fatty acids such as palmitic acid, stearic acid, oleic acid were dominant pathways for the formation of hydrocarbons such as hexadecane, pentadecane, heptadecane, and heptadecene. Research on HDO, particularly for converting fatty acid model compounds like palmitic acid into sustainable aviation fuels, is critical. One study employed red mud, a by-product of bauxite ore processing, as a support material impregnated with nickel (Ni) and cobalt (Co) metals. Catalyst characterization using X-ray diffraction (XRD) and X-ray photoelectron spectroscopy (XPS) confirmed the successful incorporation of Ni and Co into the red mud lattice. Morphological analysis indicated effective immobilization of the metals on the support. Catalyst performance was evaluated for palmitic acid HDO, systematically analyzing the effects of catalyst type, temperature, reaction time, and hydrogen pressure on selectivity and conversion. At optimal conditions (240 °C, 5 MPa hydrogen pressure, and 4 hours), the process achieved high selectivity for hexadecane (87%) and hexadecanol (10%). Catalyst reusability studies revealed stable performance for up to three cycles, with a slight decrease in conversion by the fifth cycle, demonstrating good stability and a synergistic effect of Ni-Co on red mud. Reaction pathways shifted from decarboxylation (DCX) to HDO at higher pressures, with hexadecanol identified as an intermediate at lower temperatures and pressures. FTIR analysis of fresh and spent catalysts indicated coke formation after recycling, which may impact long-term performance.

Catalytic hydrodeoxygenation of bio-oil produced from co-pyrolysis of *Mesua ferrea* L. (commonly known as Nahar, a non-edible oilseed) and PET plastic. The operating parameters, such as temperature and biomass: plastic feedstock ratio, were optimized, and it was found that maximum bio-yield (35 wt%) was obtained at 600 °C, 2:1 (biomass: plastic). The qualitative analysis of the co-pyrolyzed oil revealed that the fatty and carboxylic acids (~55%) dominated the composition. Hence, the bio-oil was upgraded for future applications. In the upgradation process, red mud (RM) was utilized as a support for mono (Ni) and bi-metallic catalysts (Ni-Co, Ni-Mo) at various concentrations of nickel (5 wt.% each). Ni-Co/RM catalyst was found to be having low coke formation (6.04 wt.%) and high hydrocarbon yield (80%). The resultant upgraded oil exhibited an oxygen content of 13% with degree of deoxygenation of 47%. The properties of the HDO oil were obtained using mono and bi-metallic catalysts at a reaction temperature of 300 °C, 4 MPa of initial hydrogen partial pressure, 10 wt.% of bio-oil to catalyst ratio were found to be optimal conditions. The catalyst was recycled for 3 times and the activity of the catalyst reduced gradually. The characterization of spent catalysts revealed the presence of coking and phase transfer of metal on the support. The primary reaction mechanism that followed was hydrodeoxygenation (HDO) and decarboxylation (DCO). Overall, applying Ni (10wt%), Ni-Co, and Ni-Mo supported Red-mud catalysts improved HDO reactions.

CONTENTS

Contents

List of Tables

List of Figures

Chapter 1.

Introduction and Literature

1.1 Global Scenario

World energy demand has increased remarkably due to fast population growth and rapid expansion of industrialization and transportation. Currently, the primary energy demand is fulfilled by the consumption of fossil fuels. Nevertheless, the usage of fossil fuels creates various environmental issues, such as the emission of carbon dioxide (CO_2) and harmful gases. For example, coal combustion releases CO_2 and SOx, which leads to soil acidification. Besides coal, nuclear fission for electricity is also considered a significant source [1]. However, nuclear energy requires sophisticated infrastructure with potential environmental and human health risks [2]. The consumption of natural resources such as coal, petroleum, and natural gas is expected to increase at an annual rate of 1.6% over the next 20 years. Petroleum fuels, although valuable, are depleting at a rate much faster than they can regenerate. Despite environmental concerns related to fossil-based fuels, petroleum-derived liquid hydrocarbons, such as gasoline and jet fuels, remain the most attractive and practical options for transportation. The global effects, including extreme climate change and the rise of diseases linked to environmental pollution, emphasize the urgent necessity to explore alternative energy sources. Acknowledging these adverse ecological effects, society desires sustainable, cleaner energy alternatives to address these challenges [3]. Fig. 1 describes the global scenario for renewable energy.

Global biofuel production is expected to increase five times by 2050, implying an overall contribution of 25% in the transport sector. Hydrogen and its derivatives would offer a solution to transport needs that are hard to meet through direct electrification, mitigating close to 2.2 Gigatons of CO_2 ($GtCO_2$) emissions in the 1.5 °C Scenario compared to the Planned Energy

Scenario in 2050. A combination of energy efficiency measures and low-carbon approaches would reduce transport consumption from 121 Exajoules (EJ) in 2018 to close to 94 EJ by 2050. Adoption of stringent efficiency standards for new cars and trucks can reduce cumulative emissions in road transport by an estimated 15 $GtCO_2$ equivalent until 2050 [4].

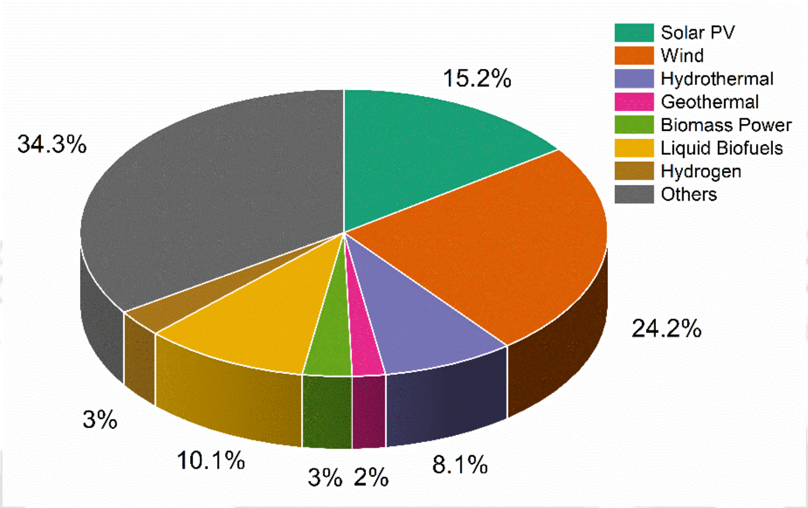

Figure 1. Global scenario for renewable energy [5]

1.2 Indian Scenario

In 2024, the transportation sector in India is projected to consume a substantial amount of petroleum fuels. According to the Petroleum Planning and Analysis Cell (PPAC), India's fossil fuel consumption has steadily increased. For 2024, estimates suggest that the transportation sector will use approximately 800 million barrels of petroleum fuels. In this context, petroleum resources are expected to be depleted worldwide by 2042, even without considering the anticipated increase in fuel consumption [6]. These issues originate from the inherent limitations of petroleum fuels. To control pollutant emissions and mitigate the energy crisis, various efforts are being made to find new eco-friendly sources for future generations. Renewable energy sources can reduce negative environmental impacts and eliminate dependence on petroleum fuels. The National Policy on Biofuels (2018) of the Government of

India aims to promote the production and use of biofuels, set blending targets, and provide financial incentives. It targets a 20% ethanol blend in petrol and a 5% biodiesel blend in diesel by 2030 [7].

The need for renewable biofuels primarily relies on starch-based feedstock, which competes with edible resources. Ideally, second-generation biofuels derived from lignocellulosic biomass (such as wood, grass, energy crops, and agricultural residues) are preferred, as they can integrate well with existing energy infrastructure. Lignocellulosic biomass has been recognized as the most promising feedstock for renewable biofuel production because it is abundant and does not compete with edible resources. The annual production of biofuels in India, considering both ethanol and biodiesel, can substitute approximately 17.8% to 22.2% of gasoline consumption and approximately 1.2% to 1.8% of diesel consumption [8]. Unlike petroleum sources, lignocellulosic biomass is considered a carbon-neutral source, which helps mitigate the effects of global warming. From an economic perspective, using lignocellulosic biomass as feedstock for biofuel production is much cheaper than using edible biomass like corn starch or crude oil. Therefore, successfully adopting lignocellulosic biomass requires suitable technologies to produce significant amounts of biofuels [9]. Fig. 2 represents the Indian scenario for renewable energy.

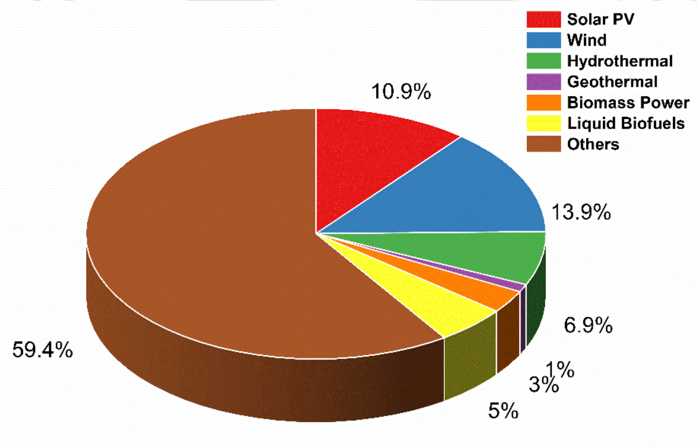

Figure 2. Indian scenario for renewable energy [10]

1.3 Biomass as a potential source for alternate energy

Biomass is a mixture of organic and inorganic components in appropriate proportions. The elemental composition (CHNSO) of the biomass typically varies with different geographic locations. The C, H, N, and O content generally varies as 30-60%, 5-10%, 1-7%, and 64-23% respectively. The presence of Sulfur and inorganic elements is usually less than 1%. The heating value of the biomass depends upon its carbon content. A reaction between the carbon compounds and the phenolic polymers with hydrogen results in dehydration reactions, forming the aqueous phase in the bio-oil. The nitrogen-containing compounds are present in the biomass due to fertilizers in the soil [11]. Fig. 3 shows the different types of biomass that are used for production of bioenergy.

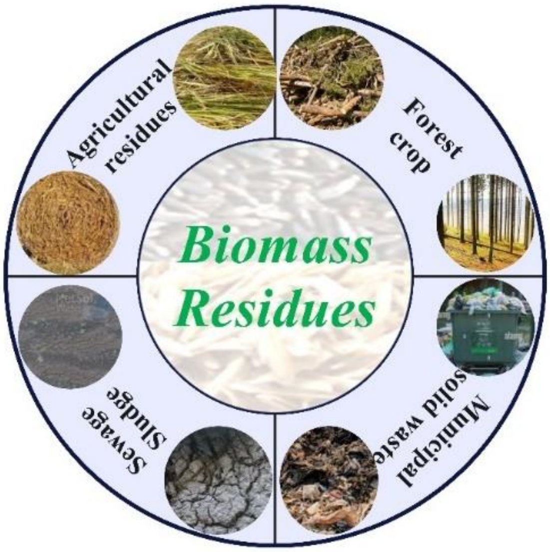

Figure 3. Types of biomass residues

The conversion of biomass to biofuels plays a vital role in transportation. The biofuels produced from starch and vegetable oil are categorized into first-generation. Owing to the various disadvantages of first-generation biofuels, producing second- and third-generation biofuels from agricultural residues, forest residues, and microalgal biomass was considered feasible [12]. The non-edible oilseeds (e.g., Japtropha) and algal species are considered second and third-generation feedstocks used for biodiesel production. As mentioned earlier, biomass composition differs with each crop; hence, the classification depends on the scope and purpose of the study. The primary characterization, such as the physicochemical properties of the biomass, is a critical step in deciding the potential of the biomass for the production of biofuels [13]. A comprehensive comparison of different types of biomasses is presented in Table 1.

Table 1. An overview of types of biomasses classified under different categories

Biomass Feedstock	Proximate Analysis (%)				Ultimate Analysis (%)					Biochemical composition (%)			HHV (MJ kg^{-1})	Ref
	Moisture	Volatile matter	Fixed carbon	Ash	C	H	N	O*	S	Hemicellulose	Cellulose	Lignin		
Sunflower stalks	7	76	12	6	49	7	0.9	38	-	25	46	20	19.8	[14]
Potato stalks	7	73	16.5	3.5	46	6	-	50	-	33	59	7	17.6	[15]
Millet stem	8	68	13	12	39	6	0.7	55	0.3	11	31	21	14.8	[16]
Banana leaves	8.4	73.1	11.3	7.2	43	7	1	48	0.3	34.3	43.3	15	17.8	[17]
Azadirachta indica	1	88	9.5	1.8	43	4	2	50	1	NA	NA	NA	18.1	[18]
Phyllanthus emblica	5.3	73	3.32	18	50	7	2	40	0.1	21.4	46.1	10.2	19.2	[19]
Ulva lactuca	9.5	77.8	0.4	21.8	35	7	1	56	1	48	18	3.5	14.4	[20]
Water Hyacinth	8.3	-	-	19	35	5	2.8	39	-	-	-	-	11.5	[21]
Petroleum Sludge	21.4	63.3	11.8	3.8	50	7	1.7	38	3.5	-	-	-	12.4	[22]
Peach stones	6.9	72.4	19.8	0.86	49	7	0.3	43	-	25.1	29.5	39.3	18.4	[23]
Wolffia arrhiza	4.8	72.6	12.2	10.4	36	6	5.3	36	1.16	-	-	-	17.7	[24]

* indicates by difference

1.3.1 Structure and composition of Biomass

Lignocellulosic biomass is made up of three major components, namely, cellulose, hemicellulose, and lignin. The biomass also contains proteins, oils, and other components that contribute to ash. The composition of these components varies with different types of biomass. These are contained in a cell wall, which is primarily divided into two parts, i.e., primary and secondary walls, each playing a vital role in the structure and functioning of plants. The most abundant part of the plant is cellulose, which is usually present up to 35-50%. The molecular arrangement of β-1,4-glycosidic bonds, which bind D-pyran glucose units, provides structural stiffness to the plants. The D-pyran glucose is a linear polysaccharide in both crystalline and amorphous forms. The crystalline nature of the cellulose exists in the primary cell wall, whereas the amorphous cellulose is mainly present in the secondary cell wall. The amount of cellulose determines the mechanical properties and bio-oil quality obtained from pyrolysis [25]. The second principal component is hemicellulose, which accounts for 20-35% of the biomass. Compared to cellulose, it is more amorphous making it easily degradable and readily accessible for biofuel production. It includes the sugars such as D-xylose, mannose, L-arabinose, galactose, and glucuronic acid. It plays a critical role in forming bonds between cellulose fibres into microfibrils and facilitates the cross-links between lignin and, thereby, the plant's strength. Xylans are predominant in hardwood, whereas glucomannans are primarily present in softwood [26]. The third valuable component of biomass is lignin. It makes up 5-25% of the composition with 3D polymer of phenylpropanoid units. The purpose of lignin is to provide ample strength to the cell walls and protect the plant from pathogens and other environmental stress. Lignin is made up of three major components such as p-coumaryl alcohol, coniferyl alcohol, and sinapyl alcohol, which form p-hydroxyphenyl (H), guaiacyl (G), and syringyl (S) units, respectively. The distribution of such monomeric units determines the reactivity and decomposition of lignin. In summary, understanding the molecular structure and converting the lignocellulosic biomass to valuable compounds depends on biomass composition [27]. Fig. 4 represents the structure of lignocellulosic biomass with the type of compounds that are produced from each component.

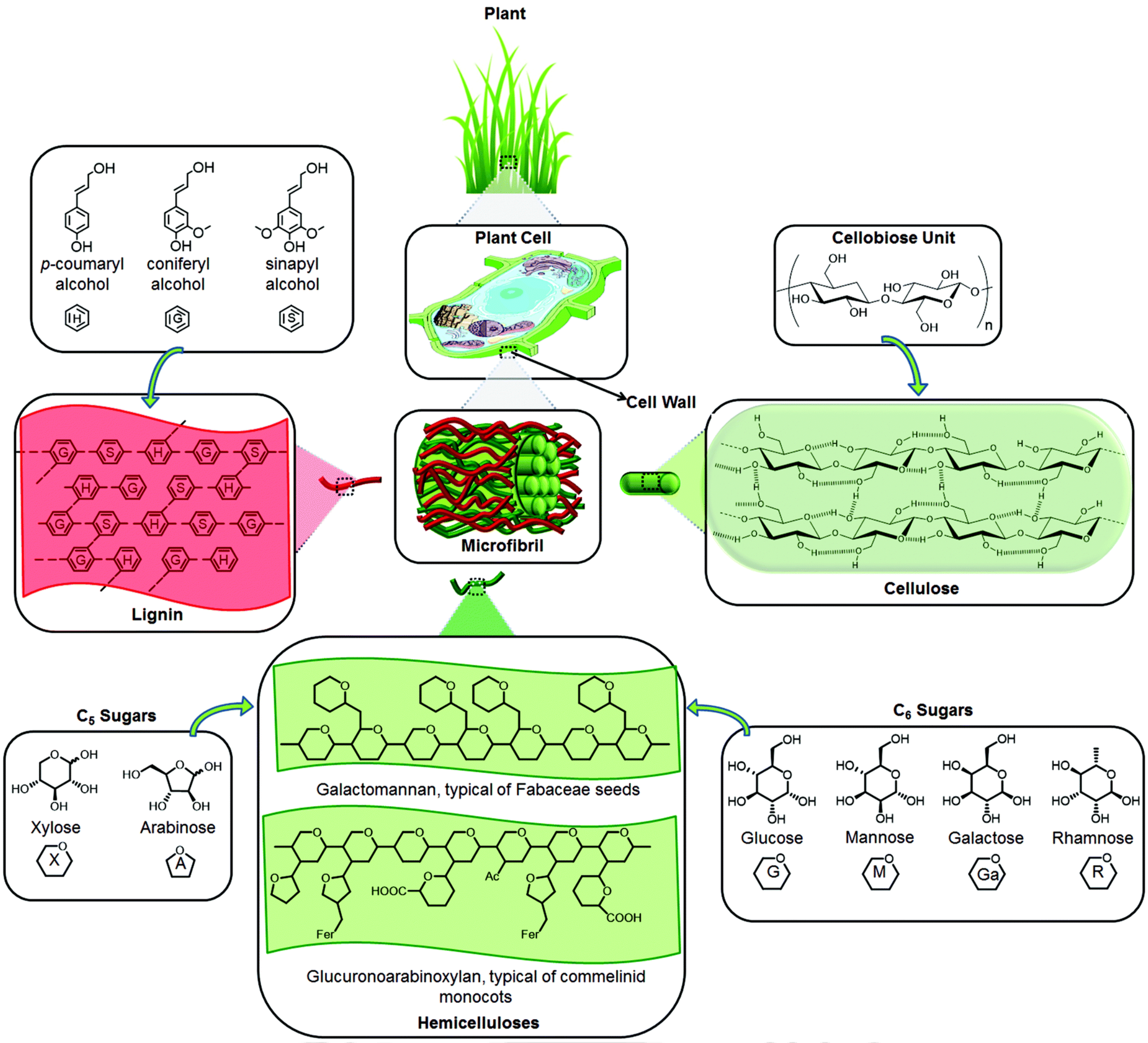

Figure 4. Structure and components of lignocellulose biomass [28]

Different conversion technologies are used to transform biomass into biofuels efficiently. The primary methods are thermochemical and biochemical conversion technologies. The biochemical conversion of the biomass takes place by different processes like anaerobic digestion, alcoholic fermentation, and photo-biological hydrogen production. These techniques utilize an enzyme or yeast in the conversion of biomass to bioethanol. The limitations of biochemical conversion technology include size reduction, crystallinity, cellulase deactivation, and tolerance of ethanol by yeast. However, the thermochemical approach encompasses processes like pyrolysis, gasification, combustion, and liquefaction. Thermochemical conversion technologies offer benefits such as the availability of equipment, lower water usage, and shorter processing times. Thermochemical methods use thermal energy to decompose organic material, whereas biochemical conversion involves three stages: anaerobic digestion, fermentation, and photochemical reactions [29]. The selection of conversion technology is based on the type and characteristics of the biomass feedstock and its environmental impact. Biofuels are becoming a viable alternative to conventional fuels, making it crucial to identify effective conversion methods. Thermochemical methods typically require a lot of energy and often need catalysts or solvents, while biochemical methods take longer. Therefore, advanced methods combining these approaches will likely be the most promising solutions [30]. Additionally, both thermochemical and biochemical conversion of biomass result in lower greenhouse gas emissions [31].

1.4 Plastic Waste Management

A rapid increase in the production of plastics over the last five decades prompted the consumption of a wide range of goods. Physical properties such as easy processing, inexpensive, high corrosion resistance, and durability make them widely used [32]. However, plastic has low degradability, indicating that completely decomposing takes millions of years. According to the US EPA, 33.4 Million tonnes of plastic waste was generated in 2017, of which 75% ended up in landfills. In India, the use of single-use plastics is banned indicating that by 2035, 30% of the landfill pollution caused by plastics will be reduced [33]. According to the current waste management techniques, it is assessed that 12 billion metric tons of plastic waste will be disposed of in landfills. Inappropriate disposal of plastic waste can further create environmental problems such as microplastics, macroplastics, and nanoplastics. These smaller plastics can enter the human health visa food route by posing high risks [34].

Considering the above challenges, certain thermochemical technologies, such as incineration, can decompose high volumes of plastic waste with efficient thermal energy recovery. Many European incineration plants use waste plastics for carbon management in the energy production sector. Regardless, this technique releases many toxic pollutants, namely phosgene, dioxins, PAHs, and heavy metals, which harm the ecosystem and human health. Although, owing to the many advantages and drawbacks of incineration plants, a significant challenge is flue gas cleaning, which increases the cost and reduces the efficiency of the process [35]. Thermochemical technologies such as pyrolysis, gasification, and hydrothermal carbonization produce bio-oil, biochar, and gas. The physicochemical characterization of typical plastic waste is essential to identify the potential of the feedstock. Additionally, it should be noted that antioxidants enhance the quality of the polymers, lubricants, additives, etc. A literature review of different plastics is presented in Table 2.

Table 2. Comparison of different plastic types classified under different categories

Plastic	Proximate Analysis (%)				Ultimate Analysis (%)					Ref
	Moisture	Volatile matter	Fixed carbon	Ash	C	H	N	O*	S	
PET	0.6	88.3	10.1	1.0	65	5	0.07	31	-	[36]
PET	-	84.8	14.5	0.7	61	2.7	-	35.1	-	[37]
HDPE	-	99.7	-	0.06	86	14	-	-	-	[38]
LDPE	-	100	-	-	86	14	-	-	-	[39]
PP	0.06	99.8	0.15	0.03	83	16	0.1	-	-	[36]

1.5 Thermochemical conversion pathway

The thermochemical conversion methods utilize heat to break down the particles at high temperatures with faster reaction rates to produce different biofuels, such as solid char, liquid biofuels, and syngas. Additionally, products like bio-oil, syngas, and others can be directly used in the existing fossil fuel-based industries. The thermochemical conversion comprises of combustion, torrefaction, pyrolysis, liquefaction, gasification, and catalytic transesterification. Fig. 5 provides a comparison of advantages and limitations of different thermochemical conversion processes. When compared, direct combustion is considered ineffective because of the release of harmful particulate matter and fly ash. Hence, developing advanced techniques for converting biomass to biofuels is crucial [40].

Torrefaction is a thermochemical technique generally performed at temperatures between 200 °C - 300 °C in an inert environment and is often referred to as mild pyrolysis. This process can be categorized into dry torrefaction and wet torrefaction. As the names suggest, dry torrefaction occurs under dry and inert conditions, while wet torrefaction, known as hydrothermal carbonization (HTC), occurs in an inert, subcritical water environment. These processes are tailored to different biomass feedstocks based on their moisture content. Dry Torrefaction is suitable for dry biomass with moisture content below 10%, such as crop residues and sawdust. Conversely, HTC is ideal for wet biomass, like sewage sludge and manure, with a moisture content of up to 80% [41]. Conventional dry torrefaction is an endothermic reaction that should be performed in an inert atmosphere. In addition to the vast amount of energy required, an air-tight environment should be maintained to prevent any seepage of air, which would make this process economically inviable. An alternative to this process is oxidative torrefaction, in which oxygen is supplied in limited, which begins the biomass's surface oxidation and produces additional heat. Such a heat generation process reduces the need for external energy and the cost of inert gas supply [42]. Traditional heating sources have multiple challenges, including excessive energy requirements and secondary vapor cracking. These issues can be fixed by using microwave irradiation as the heat source. Microwave torrefaction (MWT) uses electromagnetic energy to directly heat biomass feedstock, leading to faster heating and reaction rates and increased energy efficiency [43]. A comparative investigation on dry and microwave torrefaction of spent coffee grounds found that MWT consumed significantly less energy than DT at shorter torrefaction durations (<30 minutes), reducing about 35%–55% at temperatures of 200 °C – 300 °C [44].

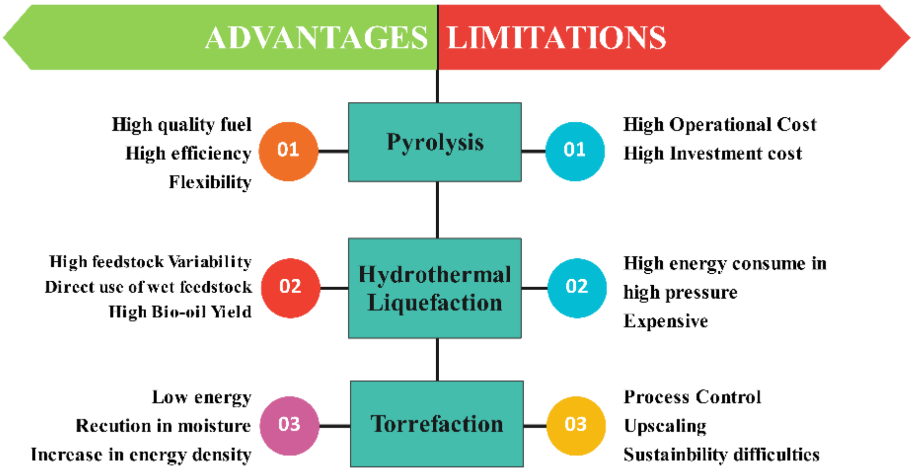

Figure 5. Advantages and Limitations of different thermochemical conversion processes

The hydrothermal treatment is classified into liquefaction and carbonization based on the operating temperature. In hydrothermal carbonization (HTC), also known as wet torrefaction, hydrochar is produced at low temperatures, typically around 180 °C - 250 °C. Hydrothermal liquefaction occurs at higher temperatures (280 °C - 400 °C), producing bio-oil. Hydrothermal gasification is performed at temperatures higher than 400 °C, during which water converts into a gas phase. The HTG process is generally associated with many challenges, such as higher temperatures and corrosion. In particular, HTL is advantageous over HTC and HTG due to the operating temperatures [40]. The HTL process is especially suitable for converting liquid biomass sources into high-quality bio-oil, and it is conducted at temperatures between 280 °C

– 370 °C with typical pressures of 10 MPa to 25 MPa. In the HTL process, water is used as a medium to extract value-added compounds from biomass. At room temperature, the water stays as a polar solvent, but when the temperature reaches a sub-critical point, the polarity of water shifts from high to low or none, indicating a low dielectric constant to produce hydrochar or bio-oil. A significant advantage of this process is the direct usage of wet feedstocks without needing to dry them before the process. Although wet feedstocks can be used, the system has to be pressurized with an inert medium, making it a challenge [41]. Table 3 provides a summary of key studies employing torrefaction and HTL of biomass.

Table 3. Comparison of key studies of thermochemical conversion processes with salient results

Process: Torrefaction					
Feedstock	Type of Process/reactor	Optimal Process Parameters	Yield of Products (%)	Results	Ref
Sugarcane leaves	Dry Torrefaction: Muffle furnace	T: 275 °C t: 30 min	Solid: 67.9	• Reduction in Sulfur: 50% • Energy yield: 70%	[42]
Mustard Stalk	Dry Torrefaction: Tube furnace	T: 300 °C t: 20 min	Solid: 64.5	• HHV: 21.26 MJ kg^{-1} • Energy Yield: 81.3%	[43]
Rice husk	Wet Torrefaction: High-pressure batch reactor	T: 240 °C t: 60 min	Solid: 48	• Reduction in ash: 0.9% • Energy yield: 52%	[44]
Sugarcane leaves	Wet Torrefaction: High-pressure batch reactor	T: 250 °C t: 30 min	Solid: 34.5	• Increase in Carbon: 28.53% • Energy yield: 43%	[42]
Rice husk	Oxidative Torrefaction	T: 300 °C t: 30 min O$_2$:0-15 vol%	Solid: 55–85	• HHV: 18.91 MJ kg^{-1} • Energy yield: 64-89%	[45]
Process: Hydrothermal Liquefaction/Carbonization					

Raw empty fruit bunch	Hydrothermal Liquefaction: Batch reactor	T: 390 °C t: 120 min P_{N2}: 2.5 MPa Solvent: Water Biomass: Water- 1:10	Biocrude: 30.16 ± 0.98	• Lower Impact of retention time increase on biocrude (30 to 240 min): 41%	[46]
Rice straw	Hydrothermal Liquefaction: Batch reactor	T: 280 °C t: 15 min P_{N2}: 0.3 MPa Solvent: Water Biomass: Water- 1:6	Biocrude: 30.16 ± 0.98	• Gas yield: 6 wt% • Hydrochar yield: 22 wt% • Aqueous Phase: 55 wt%	[47]
Rice straw	Hydrothermal Liquefaction: Batch reactor	T: 280 °C t: 15 min P_{N2}: 5.5 MPa Solvent: Methanol Biomass: Water- 1:6	Biocrude: 23 wt%	• Production of Phenol in bio-oil: 18.2%	[48]
Olive tree pruning	Hydrothermal Carbonization: High pressure batch reactor	T: 220 °C t: 3 h P_{He}: 0.2 MPa Solvent: Water Biomass: Water- 1:20	Hydrochar: 47.7 wt%	• HHV: 30 MJ kg^{-1} • Gas yield: 47.7–71.1 wt% • Liquid yield: 8.3–12.3 wt%	[49]
Spent Coffee Grounds	Hydrothermal Carbonization: High pressure batch reactor	T: 180 °C t: 1 h P_{N2}: 1.0 MPa Solvent: Water Biomass: Water- 1:3	Hydrochar: 87.2 wt%	• HHV: 23.64 MJ kg^{-1} • Gas yield: 3.1 wt% • Liquid yield: 9.7 wt%	[50]

1.5.1 Pyrolysis

Pyrolysis is a thermochemical process in which biomass is heated without oxygen to obtain different value-added products such as bio-oil, biochar, and non-condensable gases. The bio-oil obtained is a dark-coloured liquid with high acidity and viscosity. The typical operating temperatures range from 250 °C - 700 °C depending upon the value-added product. At T< 300

°C, the main product obtained is biochar. In contrast, bio-oil is obtained when the temperature is maintained at 400 °C - 600 °C. Non-condensable gases yield increases with increased temperature above 700 °C [51]. The pyrolysis process is categorized into three types based on the heating rate: slow, fast, and flash pyrolysis. The bio-oil obtained from slow pyrolysis (heating rate: 2-50 °C min^{-1}) is more viscous than that obtained from fast pyrolysis (heating rate: 100 °C s^{-1}). The primary product obtained is non-condensable gas in Flash pyrolysis (heating rate: >1000 °C s^{-1}) [52]. Additionally, bio-oil yield also depends on the type of reactor used. Some reactors for pyrolysis are fixed-bed, fluidized-bed, auger, and rotary kiln reactors. Although fluidized-bed reactors are most frequently used, the disadvantages, such as small particle size and high operational cost, make their use complicated. In this concern, Fixed-bed reactors are considered to be widely used owing to several advantages such as uniform heat transfer, ease of scale, and high bio-oil yields [53].

1.5.1.1 Biomass pyrolysis

The biomass components, such as hemicellulose, cellulose, and lignin, simultaneously degrade at different temperatures, complicating the reaction mechanism. Typically, the degradation temperature for hemicellulose is 200 °C - 350 °C, whereas cellulose degradation occurs within a temperature range of 350 °C - 650 °C. The third component, lignin, has thermal stability and degrades over various temperatures, such as 150 °C - 900 °C, with biochar as the main product. Among the components, hemicellulose and cellulose contribute to the production of bio-oil. A high bio-oil yield is usually obtained in the active pyrolysis zone (400 °C - 600 °C) [3]. Additionally, rapid cooling of the vapor is essential to convert the aerosols into liquid products. Moreover, a particle size of less than 3 mm is required to produce higher bio-oil yields due to heat transfer limitations to the biomass. Further, removing condensed solid char is crucial for controlling cracking reactions. Char, primarily carbon, has several uses, including fuel, synthesizing novel carbon materials and adsorbents, and enhancing soil fertility. Non-condensable gases, mainly consisting of H_2, C_1-C_5 hydrocarbons, CO, and CO_2, can be utilized for heating or electricity generation [54]. The gases can also be transformed into valuable chemicals via Fischer-Tropsch synthesis if the H_2 ratio exceeds 1. The energy required for the fast pyrolysis process can be sourced from burning char or gases [55]. Fig. 6 indicates the different by-products produced from the conversion of biomass to value-added products.

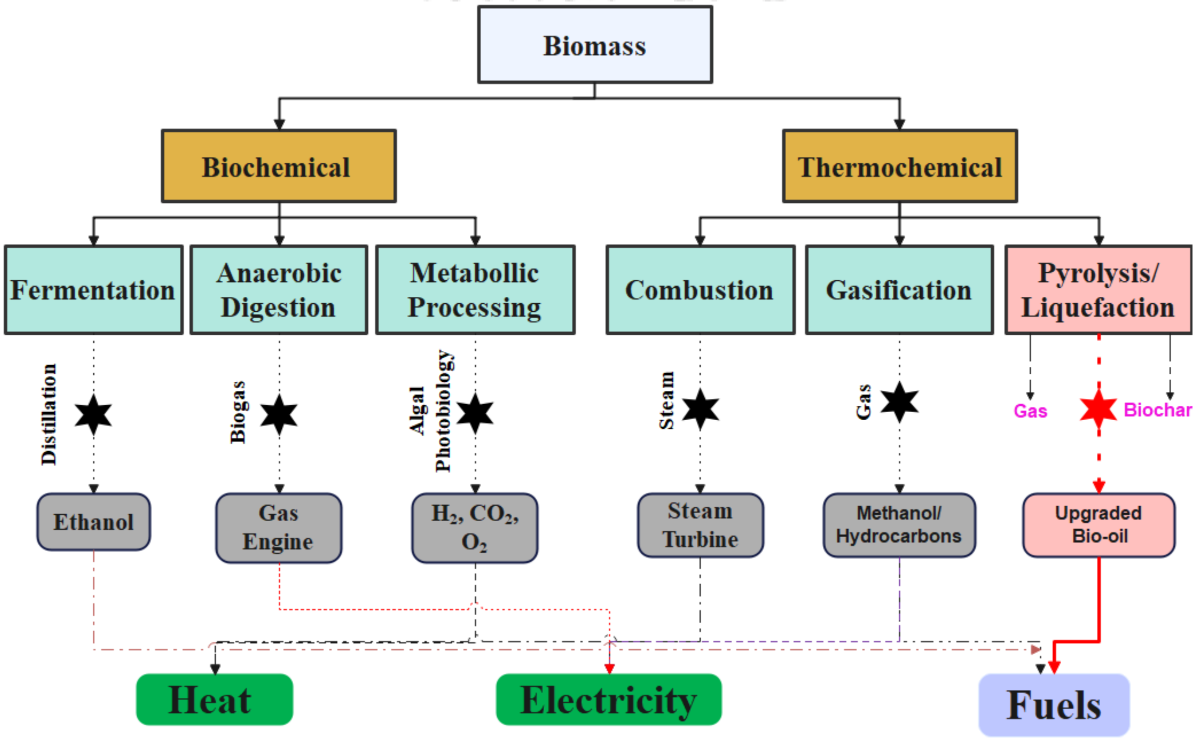

Figure 6. Biomass conversion for production of different value-added products

Bio-oil obtained from fast pyrolysis is highly viscous, dark brown, has a calorific value (20-25 MJ kg^{-1}), and is usually less than fossil-derived fuels due to a mixture of polar and non-polar compounds. The colour of the oil is due to the presence of soot and ash particles. It contains more than 300 oxygenated compounds, most of which are aliphatic and aromatic compounds, which help produce chemicals. The physical properties, such as density and oxygen content of the oil, vary between 950 kg m^{-3} - 1100 kg m^{-3} and 30-35 wt%, respectively. It also has high acidity and poor ignition. A comparison of the physical properties of the bio-oil with the existing fossil fuels is shown in Table 4. It can be seen that the bio-oil has higher moisture content and lower HHV, indicating that the upgradation of oil is necessary to meet the existing criteria of transportation fuels [56].

Table 4. Comparison of physical properties of bio-oil with existing [56].

Physical Property	Bio-oil	Diesel	Heavy Fuel Oil
Water (wt%)	15-30	0-0.001	0.1-7
Ash	0-0.2	0.001	0.03-0.1
Carbon	44-58	86	85-86
Hydrogen	5.5-7.2	13	11-12
Oxygen	35-50	0	0-0.1
Sulfur (wt ppm)	<400	10-500	10000-21000
Stability	Unstable	Stable	Stable
HHV (MJ kg^{-1})	16-21	43	38-41

1.5.1.2 Plastic pyrolysis

The pyrolysis of plastic alone produces oil and syngas with enhanced H/C ratio and calorific value, resulting in lower oxygen content. A significant issue associated with the pyrolysis of only plastics is that the melted and softened particles clog the feedline due to the highly viscous nature of the wax products and the inhibition of fluidization. The categorical separation of the mixed plastics is also considered a significant challenge, viewing the existing infrastructure for segregating the plastics. Due to the above factors, waste plastics are often considered part of municipal solid waste. Therefore, comprehending the nature of the feedstock and their usage in co-pyrolysis with biomass is critical as a large volume of plastics can be processed while the need for segregation of mixed plastic is significantly reduced [57]. The above concerns mentioned while pyrolyzing the plastic alone paved the way for more efficient use of the feedstocks by co-pyrolyzing with biomass or any other suitable raw materials. The production of biofuels by co-pyrolysis is considered easy and safe as it doesn't require high-pressure systems. This process is also advantageous as it recovers the essential chemicals and reduces the dependency on fossil fuels while emitting less carbon than the fossil fuels themselves. The biodiesel produced from this process has physical-chemical properties similar to petro-diesel, such as low viscosity, which improves its application efficiency of combustion. Hence, co-pyrolysis has the potential to derive alternate fuels [23]. Fig. 7 represents the different conversion processes employed in deriving value-added products from plastic.

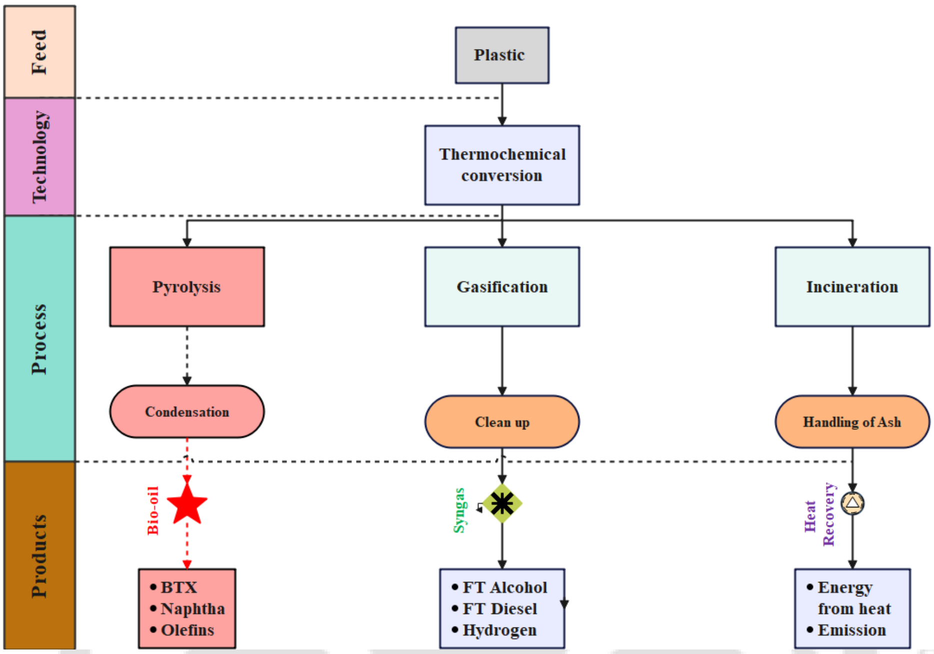

Figure 7. Plastic conversion for production of different value-added products

1.5.1.3 Reactor configuration for pyrolysis

A reactor is considered the heart of the pyrolysis process. Its design is critical to the success of commercial process plants as the products' yield and selectivity depend on it. Notably, research is ongoing to develop novel lab-scale and industry-level reactors. Performing fast pyrolysis conditions is more difficult owing to the heterogeneity of the feedstock, heat and mass transfer limitations, product separation, and operational difficulty [56].

In conventional pyrolysis reactions, fixed beds, fluidized beds, rotating cones, and ablative reactors are among the many reactor configurations available for applied pyrolysis. The reactors are heated electrically to attain the desired temperature at a specific heating rate [58].

Additionally, micropyrolyzer is among the reactors available for analytical pyrolysis. In the micropyrolyzer, a known mass of 2-3 μg or mg is placed in a steel cup and heated by an electric source at a heating rate of > 1000 °C s^{-1}. They are essential analytical instruments for accurately determining the composition of pyrolysis products. By connecting these reactors to devices like gas chromatographs (GC), mass spectrometers (MS), flame ionization detectors (FID), Fourier transform infrared spectrometers (FTIR), or thermal conductivity detectors (TCD), precise data can be collected. However, these reactors are limited by the requirement for finely ground biomass samples of low mass. Microreactors play a vital role in understanding pyrolysis product distribution and kinetics, which are vital for reactor design and scale-up [58].

Improved heat and mass transfer can be attained through appropriate reactor designs at larger scales. Operating pyrolysis in a continuous mode is more cost-effective for commercial or industrial applications. Based on the design, the pyrolysis reactors are classified as follows: fixed beds, fluidized beds, rotating cones, and ablative reactors are among the many reactor configurations available for applied pyrolysis. The reactors are heated electrically to attain the desired temperature at a specific heating rate. Fast pyrolysis can be conducted by fluidizing the feed with sand/or like-wise particles, which ensures uniform heat distribution. In these systems, the circulating sand bed is heated either by electrical coils or indirectly through the combustion of gas and char by-products produced during pyrolysis. The key advantages of these reactors are their low residence time, high efficiency, and simple design. However, construction and operational costs increase as the reactor size scales up [59]. Fluidized bed reactors are categorized into three types: bubbling, entrained, and circulating. In bubbling beds, the gas velocity is 1.5 to 2 times the minimum fluidization velocity, which allows biomass particles to be carried by the gas's drag force. Feedstock particles smaller than 2 mm are typically used to ensure optimal fluidization. Circulating fluidized beds operate at even higher gas velocities compared to bubbling and entrained beds, with biomass decomposition occurring in the riser section. Unconverted particles are recycled back into the system through a down comer. These systems can efficiently process feedstock sizes up to 6 mm. When using particles smaller than 2–3 mm, typical bio-oil yields of 70–75 wt% can be achieved. Entrained char particles are removed through filters to prevent contamination of the oil fraction. In ablative reactors, biomass is pressed against a heated reactor wall, with the rate of devolatilization being significantly influenced by factors such as the velocity of the feedstock, the pressure applied to press the biomass against the hot surface, and the temperature. Although these reactors can process larger biomass particles, thermal erosion, feed size, and feeding parameters are critical considerations. Particles up to 20 mm in size can be fed into the reactor. Enhancing heat transfer rates is crucial for achieving the desired level of conversion, and feedstock recycling is necessary to ensure complete conversion [60].

In rotating cone reactors, feedstock is introduced at the bottom of a rotating cone, where it moves upward in a spiral motion, absorbing heat from the hot walls and heated sand. This design allows for the processing of particles up to 6 mm in size, which can result in high oil yields. The overall operating costs of this reactor are relatively low due to the minimal use of carrier gas. Liquid yields ranging from 60% to 70% on a dry basis are typically achieved. Screw reactors offer improved feedstock mixing and precise residence time control by continuously transporting the feedstock through a tubular section. These reactors can handle feedstock particles as large as 50 mm. Temperature is regulated throughout the reactor to ensure complete conversion. However, a significant limitation of screw reactors is their low heat transfer rate, which restricts their application compared to fluidized bed reactors [61]. Fig. 8 describes the various reactor configurations employed in pyrolysis process.

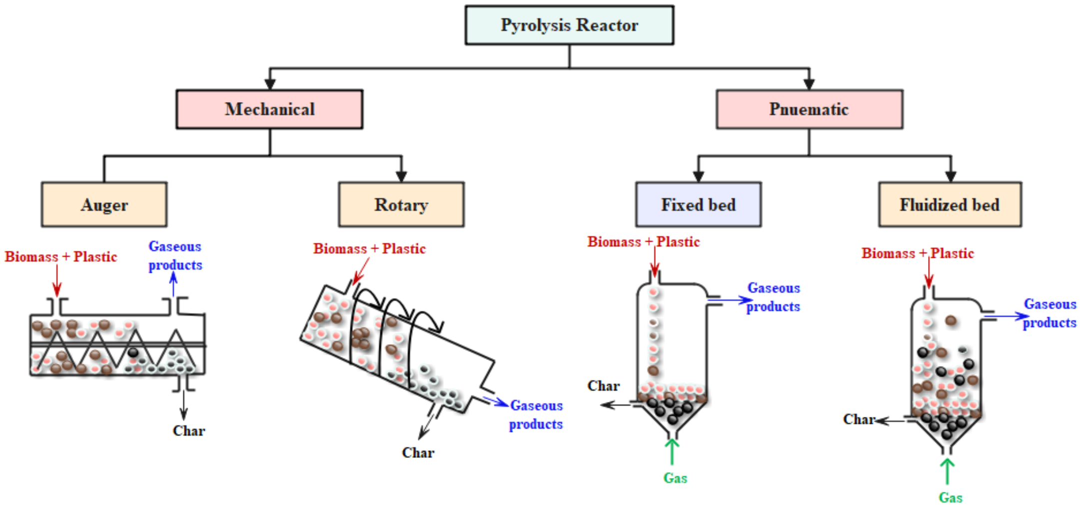

Figure 8. Reactor types for pyrolysis process

1.6 Kinetic Parameters Estimation of Thermal and Co-Pyrolysis using Iso-Conversional Model-Free and Model Fitting Methods

The pyrolysis reactions are often complex, and understanding the mechanism is paramount. Comprehending the mechanism forms a crux in improving the quality of the products. During the process, the feedstock particles undergo numerous reactions; hence, it is very complex to model every reaction. Thus, a thorough study of theoretical techniques and simulation methods for modelling biomass pyrolysis is conducted, spanning from the atomic and molecular level to the reactor level. This approach aims to provide a deeper understanding of both intraparticle and external diffusion rate kinetics [62].

Thermogravimetric analysis (TGA) is a well-established method for conducting kinetic studies. This technique measures the mass change of a material over time or as the temperature changes under controlled conditions. Through this analysis, the material's composition and its components' contribution can be assessed. TGA also helps identify the kinetic triplet, analyze the effects of different heating rates, and determine the reaction rate. The process can be carried out using either isothermal or non-isothermal approaches, with the latter being more advantageous due to its reduced likelihood of errors, shorter investigation time, and the need for less experimental data. Within non-isothermal methods, the model-fitting and model-free approaches are commonly used for kinetic studies, with the model-free method being preferred for its lower margin of error [63].

The primary goal of kinetic analysis is to interpret experimentally determined parameters such as activation energy (E), the pre-exponential factor (k_0), and the reaction mechanism. Each of these parameters is linked to a fundamental theoretical concept: E corresponds to the energy barrier, and k_0 is related to the frequency of vibrations in the activated complex. It is recommended to first select an appropriate rate equation and then fit it to experimental data, as the accuracy and relevance of the kinetic parameters heavily depend on the proper choice of this equation, which should reflect the key aspects of the actual mechanism. Therefore, accurately interpreting the reaction mechanism is more crucial than simply fitting data to a polynomial function [64]. Various factors, such as the heating rate, the source of materials, and the experimental apparatus used, influence the activation energy values. As a result, activation energy values obtained for different feedstocks should be considered specific to the conditions under which they were measured. The non-isothermal kinetic models were developed in the past decades to obtain kinetic parameters by considering the correlation between heating rates and temperatures when a reaction rate reaches the maximum. From the literature, activation energies derived from iso-conversional methods were deduced to be the most reliable. In these methods, the activation energy is calculated by estimating multiple curves at various heating rates, while pre-exponential factors are calculated by assuming the reaction is first-order [64].

Two primary kinetic methods are used to analyze biomass pyrolysis kinetics: model-fitting and isoconversional. The uncertainty in estimating kinetic parameters associated with model-fitting methods can be mitigated using isoconversional methods. Several isoconversional kinetic methods exist, including the Friedman differential, the Ozawa-Flynn-Wall linear integral, the

Kissinger-Akahira-Sunose, Starink and Simplified Distributed activation energy model (DAEM). These methods offer different approaches to determining effective activation energies, each with advantages and disadvantages. The Friedman isoconversional method is the most widely used due to its simplicity and high accuracy. Although the Friedman method is sensitive to data noise, this issue can be minimized by considering data for a specific conversion degree and its surrounding values or by employing advanced smoothing techniques.

The kinetics of the solid-state reactions are usually considered by the following set of equations:

$$\frac{d(x)}{dt} = k\, f(x) \tag{1}$$

where, *x* is the mass of the volatiles released at time (t) and *A* is the rate constant, the correlation between the temperature and rate constant is assumed to follow the Arrhenius law:

$$k = k_0 * e^{-\frac{E}{RT}} \tag{2}$$

where k_0 is the pre-exponential factor, *E* is the apparent activation energy of the reaction. The rate of conversion, x, biomass can be written as follows,

$$\frac{dx}{dt} = k * f(x) \tag{3}$$

The conversion is defined as a follows

$$x = \frac{\alpha_0 - \alpha_t}{\alpha_0 - \alpha_f} \tag{4}$$

α_0 represents initial mass, α_t is mass at certain time (t), α_f is final mass that is left after the reaction.

According to the n^{th} order reaction kinetics, f(x) the reaction model can be described as

$$f(x) = (1-x)^n \tag{5}$$

Solving the equation for reaction model,

$$\frac{dx}{dt} = k_0 * e^{-\frac{E}{RT}} * (1-x)^n \tag{6}$$

$$\frac{dx}{dT} = \frac{k_0}{\beta} * e^{-\frac{E}{RT}} * (1-x)^n \tag{7}$$

Re-arranging of the equation (8) yields the following equation

$$\frac{dx}{(1-x)^n} = \frac{k_0}{\beta} * e^{-\frac{E}{RT}} * dT \tag{8}$$

In the above equation, the conversion of biomass is expressed as a function of temperature. Integration of the equation (9),

$$g(x) = \int_0^x \frac{dx}{f(x)} = \int_0^T \frac{A}{\beta} * e^{\frac{-E}{RT}} * dT \tag{9}$$

$$g(x) = \frac{AE}{\beta R} * \int_0^x u^{-2} * e^{-u} du = \frac{AE}{\beta R} * p(u) \tag{10}$$

Here, the integral conversion is represented by g(x) and $u = \frac{E}{RT}$. Since p(u) has no exact solution, numerical approximations are employed for solving this equation. The different kinetic methods used in the present study to determine the kinetic triplet are presented in Table 5.

Table 5. Kinetic modelling equations used in determination of the kinetic triplet

S.No.	Model	Equation	Plot	Determination of kinetic parameter	Ref
1.	Differential Friedman Method	$\ln = -\frac{E}{RT} + \ln(Af(x))$	$\ln\left(\frac{dx}{dt}\right)$ vs $\frac{1}{T}$	The activation energy is obtained from the slope of the plot. The frequency factor is calculated from the intercept.	[65]
2.	Kissinger–Akahira–Sunose (KAS)	$\ln\left(\frac{\beta}{T^2}\right) = \ln\left(\frac{AE}{Rg(x)}\right) - \frac{E}{RT}$	$\ln\left(\frac{\beta}{T^2}\right)$ vs $\frac{1}{T}$	The activation energy is obtained from the slope of the plot. The frequency factor is calculated from the intercept.	[66]
3.	Ozawa-Flynn-Wall (OFW)	$\ln(\beta) = \ln\left(\frac{AE}{Rg(x)}\right) - 2.315 - 0.457 * \frac{E}{RT}$	$\ln(\beta)$ vs $\frac{1}{T}$	This method uses Doyle's approximation. E can be calculated from the slope The frequency factor can be calculated from the intercept	[67]
4.	Starink Method (STR)	$\ln\left(\frac{\beta_i}{T_{\alpha,i}^{1.92}}\right) = Constant - 1.0008 * \left(\frac{E_\alpha}{RT_{\alpha,i}}\right)$	$\ln\left(\frac{\beta_i}{T_{\alpha,i}^{1.92}}\right)$ vs $\left(\frac{1}{T_{\alpha,i}^{1.92}}\right)$	A temperature approximation integral is used in this model for simplification of the kinetic model. Activation energy is determined from the slope of the plot. The frequency factor is calculated from the intercept	[68]
5.	Simplified Distributed activation energy model (DAEM)	$\ln\left(\frac{\beta}{T^2}\right) = \ln\left(\frac{AR}{E}\right) + 0.6075 - \frac{E}{RT}$	$\ln\left(\frac{\beta}{T^2}\right)$ vs $\frac{1}{T}$	The activation energy is determined from the slope of the plot while the intercept provides the information of the pre-exponential factor.	[69]
6.	Avrami theory	$\ln(\ln(1-\alpha)) = \ln(A_\alpha) - \frac{E_\alpha}{RT_\alpha} - n\ln(\beta)$	$\ln(\ln(1-\alpha))$ vs $\ln(\beta)$	The order of the reaction is calculated from the slope of the plot	[70]

The activation energy (E_α) from different models is calculated plotting conversion factor vs Temperature as described in Table 5.

The TGA decomposition is divided into 3 stages: dehydration (upto 200 °C), devolatilization (200-600 °C), and char formation zone (> 600 °C). The kinetics are calculated in the devolatilization stage, which is considered to be an active pyrolysis zone. In the active pyrolysis zone, cellulose, hemicellulose, additives, extractives, polymers, proteins, and lipids decompose. The devolatization generally doesn't reach zero in this zone due to the simultaneous decomposition of all these compounds. Various recent studies reported the kinetic parameters of individual feed long with co-feed, presented in Table 6. It is observed from the literature that the co-feed shows better results with a significant decrease in activation energy compared to individual feeds.

Table 6. Activation energies for individual and co-feed in several studies

Feedstock Biomass	Plastic	Feedstock ratio (B:P)	Method	Activation energy (kJ mol^{-1})			Ref
				Biomass	Plastic	Co-feed	
Bamboo	PP	4:1	KAS	217.6	188.3	213.8	[71]
Bamboo Sawdust	LLDPE	1:3	OFW	265	165	230	[72]
Dunaliella salina (DS)	PET	1:1	Coats and Redfern	84	280	7	[73]
Corn stalk	LDPE	9:1	OFW	165	296	193	[74]
Corn cob	PET	1:1	Starink	40.39	67.72	44.41	[75]
Azadirachta indica seeds	LDPE	1:1	KAS	-	-	145.67	[76]

*: PP: Polypropylene; LLDPE: linear low-density polyethylene; PET: Polyethylene terephthalate; LDPE: Low-density polyethylene

1.7 Significance of Analytical and Applied co-pyrolysis

1.7.1 Application of Py-GC/MS in thermal and co-pyrolysis

The suitability of pyrolysates derived from biomass and plastic feedstocks for industrial applications largely relies on their quality, which is defined by various factors, including the type of impurities, thermal stability, corrosiveness, reactivity, and the proportion of oxygenated compounds. The presence of highly oxygenated compounds in the bio-oil, such as acids, ketones, and aromatics, tends to decrease the calorific value while producing high molecular weight compounds, ultimately increasing fuel viscosity and clogging issues. Identifying such compounds is necessary before the industry applies these fuels. Hence, analytical pyrolysis plays a crucial role in determining the composition of the pyrolysates and provides valuable insights into determining the reaction pathway. Recently, fast pyrolysis and fast co-pyrolysis have gained noteworthy attention as efficient methods for analyzing the first compounds of the vapor to determine the reaction pathway. Additionally, the high heating rates used in the fast pyrolysis yield liquid fuels up to 70%. A reliable and efficient method for examining the products and intermediates generated during fast pyrolysis is using pyrolysis-gas chromatography-mass spectrometry (Py-GC/MS) [77].

This method integrates micropyrolyzer (Py) with gas chromatography (GC) and mass spectrometry (MS), enabling rapid and effective analysis with minimal sample requirements. Py-GC-MS is advantageous in assessing complex mixtures because it can identify products in a single experiment without the need for prior separation. This feature makes the technique more efficient and time-saving than other separation methods. Additionally, it can analyze both liquid and solid samples, including solid polymers dissolved in suitable solvents. The process is highly automated, which reduces analysis time and increases productivity. Different types of pyrolysis processes, such as co-pyrolysis, catalytic pyrolysis, and catalytic co-pyrolysis, enhance the quality of the pyrolysate to produce value-added products. Synergistic interaction of the different feedstocks can ensure the tuning of properties to produce high-quality products. Hence, Py-GC/MS is a better way to understand the effects of additives and fillers on the products [78].

1.7.1.1 Methodology

The suitability of pyrolysates derived from biomass and plastic feedstocks for industrial applications largely relies on their quality, which is defined by various factors, including the type of impurities, thermal stability, corrosiveness, reactivity, and the proportion of oxygenated compounds.

The presence of highly oxygenated compounds in the bio-oil, such as acids, ketones, and aromatics, decreases the calorific value while producing high molecular weight compounds, ultimately increasing fuel viscosity and clogging issues. Identifying such compounds is necessary before the industry applies these fuels. Hence, analytical pyrolysis plays a crucial role in determining the composition of the pyrolysates and provides valuable insights into determining the reaction pathway. Different types of pyrolysis processes, such as co-pyrolysis, catalytic pyrolysis, and catalytic co-pyrolysis, enhance the quality of the pyrolysate to produce value-added products. Synergistic interaction of the different feedstocks can ensure the tuning of properties to produce high-quality products. Hence, Py-GC/MS is a better way to understand the effects of additives and fillers on the products. The Py-GC/MS systems are generally operated online and offline mode. The above-described procedure represents the online mode. Meanwhile, in the offline Py-GC/MS mode, the pyrolysis of the feedstocks is carried out in a separate unit, and then the samples are analyzed using different analytical instruments. The significant advantage of offline Py-GC/MS is that heterogeneous mixtures are analyzed efficiently [79]. Micro-furnace, curie point, and resistively heated filaments are commonly used among the available pyrolyzers. Fig. 9 shows the schematic representation of Py-GC/MS systems. Initially, the furnace is preheated in the micro-furnace system, and then the sample is injected into the pyrolysis chamber. A significant drawback of this system is the slow heating rate compared to other types of pyrolyzers, along with the versatility concerning the temperature-control program. Another potential challenge is maintaining the system's cooling ability between consecutive runs, which can impact the reproducibility and equilibrium of the system [85].

The curie-point analyzer has an induction-assisted pulse heating process with a ferromagnetic sample holder. The temperature at which the feedstock loses its magnetic properties is known as curie point temperature. Although the system's temperature control is precise, and the heating of the sample takes place within 0.2-0.4 seconds, a significant challenge is that the temperature program has an upper-temperature limit of the metal's curie point [80]. The third type of Py-GC/MS is the resistively heated filament system in which a part of the resistive metal produces heat by passing an electric current through it. Later the, the voltage is reduced at the desired temperature and used to sustain it. These advantages authorize more precise control over the pyrolysis temperature and heating rate compared to other pyrolyzers [81].

The general procedure of Py-GC/MS analysis involves a few steps: preparation of the sample, pyrolysis, GC, MS, and data analysis. Drying is usually performed for solid samples before introducing them into a sample cup. A 50-100 µg sample is loaded into the sample holder and then placed into the pyrolysis chamber. An inert gas continuously passes through the chamber, and the sample is heated to the desired temperature. In the GC column, the temperature program of the samples is optimized so that efficient separation occurs based on the compounds' boiling point and other physical properties. Meanwhile, in the Mass spectrometer, the ion source and transfer line temperatures affect the analysis. The data can be quantified from the MS spectra, which are further analyzed to identify the compounds. Many libraries are available to identify the compounds, and searching through the library locates all the similar spectra in the reference and sorts the compounds as per their similarity. The observed and experimental value evaluation can be determined by duplicating the experiment [82].

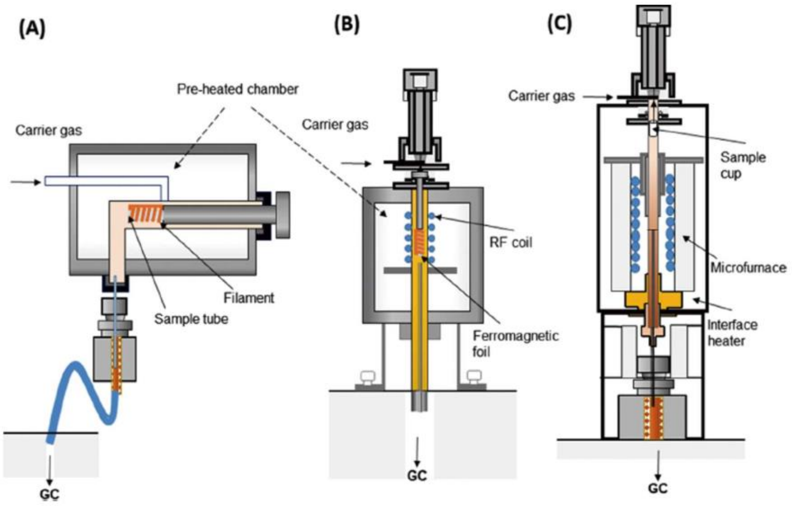

Figure 9. Different Py-GC/MS reactors (A) microfurnace (B) pulse-mode (C) Resistive filmane/Curie-point pyrolyzer [88]

1.7.1.2 Py-GC/MS of Single feedstock

Lignocellulosic and plastic feedstocks have been broadly studied as promising sources of hydrocarbon fuels. The chemical compositions of feedstocks change drastically, indicating different pathways. For example, the pyrolysate composition of herbaceous compounds included acids, esters, ketones, and furans. Meanwhile, the dominant compounds in woody biomass include carbonyls, phenolics, and furans. Besides the feedstock type, temperature also plays a crucial role in analytical pyrolysis in producing desirable properties. A study on raw tea oil camellia shells (TOCS) indicated the presence of acids and phenols comprising of 38% [84]. A study on the effect of temperature on switchgrass revealed that hydrocarbon content increased with an increase in temperature (6.5-11.5%), while a decrease in oxygen content (24-17%) was observed [85]. Table 7 indicates the analytical pyrolysis of different biomass and plastic.

Identifying polymer composition and functional groups is also essential in both polymer manufacturers and consumer industries. The composition of polymers can be acquired by performing spectroscopic analyses such as FTIR and NMR. Meanwhile, Py-GC/MS is a valuable tool for detailed structural analysis. For instance, a study on pyrolysis of facemasks revealed that more than 70% of the liquid fuel was entrapped in the GC column due to heavier hydrocarbons with carbon numbers of C35 to C70 [86]. Compared to fast pyrolysis, slow and intermediate pyrolysis tends to produce heavy and waxy compounds, decreasing liquid fuel production. Additionally, a higher yield of gaseous compounds is observed at high pyrolysis temperatures by enhancing the yield of cyclic aliphatic and aromatic compounds. Some studies also state that the production of alkenes was predominant at high temperatures of 700 °C for shorter residence times (60 s) [87]. Nevertheless, significant energy consumption is needed for the system to be operated at high temperatures. Hence, acquiring reliable fundamental data on pyrolysis characteristics to determine the thermal decomposition kinetics and distribution of products is crucial for developing appropriate thermo-chemical conversion of biomass and plastic feedstocks.

Table 7. Analytical Pyrolysis of different biomass and plastic

Feedstock	Mode of heating	Operating Temperature (°C)	Siginificant Observations	Ref
Switch Grass	Resistive heated filament	450-650	• Hydrocarbons (6.49-13.77%) • Acids (13.24-17.78%)	[88]
Corn cob	Resistive heating filament	400-600	• Furans (30.88-40.97%)	[89]
Poplar Saw dust	Resistive heating filament	600	• Carbonyls (40.09 %), furans (25.95 %), phenols (15.76 %), aromatic derivatives (11.01 %)	[90]
Cellulose	Micro-furnace	650	• Tar yield: 19.9	[91]
JP-10 with HY catalyst	Curie-point	500	• Alkenes (C2-C6): 11.9	[92]
PE plastic	Micro-furnace	600	• Alkanes: 38.4% • Alkadiene: 8.97%	[93]
Wasted fishing net	Micro-furnace	410	• Yield of ε-caprolactam: 60 wt.%	[94]

1.7.1.3 Py-GC/MS of co-feedstocks

Although using single feedstocks is advantageous (reduced contamination, predictable outcomes) in determining the reaction pathway, this process's significant drawbacks are the limited feedstock availability, low product diversity, and economic considerations [95]. Besides analyzing the pyrolysate composition of single feedstocks, the product distribution of co-pyrolysis of two or more feedstocks is also gaining significant importance. Literature also states that during co-pyrolysis, several inorganic elements in ash act as catalysts and promote the production of secondary cracking reactions. Additionally, co-feedstocks result in synergistic interactions between the volatiles or with the char, leading to different reaction mechanisms compared to individual feedstocks [96]. Table 8 indicates the analytical co-pyrolysis of different biomass and plastic. The reaction pathways include decarboxylation, decarbonylation, dehydration, hydrogenation, etc. Operating parameters such as the nature of the feedstock and blending ratio are crucial in deciding the product's quality and quantity. Table 8 lists a detailed literature study determining the pyrolysate composition of co-feedstocks by Py-GC/MS. A study on single, binary, and tertiary waste blends (date pits, coffee waste and cow dung) shows that the yield of amines and aldehydes is less than 2% while increasing the acid and ketone content (32-44%) [97].

The co-pyrolysis of biomass and plastic is gaining interest in applying this technique in waste consumption and sustainable utilization. The addition of plastics to biomass enhances the H/C ratio of the oil, thereby promoting its quality and quantity. The pyrolysate composition of pine wood and Urea-formaldehyde resin revealed a positive synergistic effect with an accelerated decomposition of oxygenated compounds, phenols, and lipids [98]. This resulted in the production of low-molecular-weight compounds such as acids and alcohols. Regardless, the higher acidity and viscosity of the co-pyrolytic oil is a significant challenge for upscaling the technology. Although the synergistic effect of feedstocks can be seen from Py-GC/MS analysis, it isn't easy to quantify the effect of one feed over the other. In summary, this process is practical in obtaining different value-added products while consuming a huge volume of waste. Nonetheless, the co-pyrolysis process has several drawbacks, such as higher logistical and operational challenges, which usually affect the overall economics of the process. Also, handling multiple feedstocks increases the operation cost and requires specialized equipment.

Table 8. Analytical co- pyrolysis of Biomass and Plastic

Feedstock		Ratio (B:P)	Mode of heating	Operating Temperature (°C)	Siginificant Observations	Ref
Biomass	Plastic					
Chestnut	Polystyrene	2:1	Micro-furnace	550	• Yield of Furans: 2.7% • Anhydro sugars: 44.8%	[99]
Stem Wood	Paper Reject	1:1	Resistive heated filament	270	• Yield of Hydrocarbons: 55% • Acids: 5%	[100]
Cellulose	Polystyrene	7:3	Micro-furnace	600	• Yield of Ethylbenzene increases due to hydrogenation of styrene	[101]
Poplar wood	HDPE+ wood plastic mixtures	0.72:0.69:1	Resistive heated filament	625	• Yield of Hydrocarbons: 64.80%	[102]

1.8 Significance of Applied co-pyrolysis for production of bio-oil

Pyrolysis techniques vary based on their heating rates, and they are classified as slow, intermediate, and fast pyrolysis. Research has shown that increasing the rate of heat transfer by reducing the residence time of the vapors and increasing the inert gas flow increases bio-oil production. Also, it aids in limiting secondary reactions such as cracking and polymerization. Suitable optimization of these parameters can lower the formation of undesirable by-products and maximize liquid yield. The liquid yield depends on several factors, including the feedstock, operating temperature, vapor residence time, char separation, and ash content [3].

Additionally, efficient heat, mass transfer, and reaction kinetics play critical roles in pyrolysis. Reducing biomass particle size to below 1-3 mm is one way to improve heat transfer. Feedstocks are typically dried to less than 10% moisture to minimize water content in the pyrolytic liquid. Fast pyrolysis offers the advantage of processing a wide range of feedstocks with proper drying, yielding up to 70-75% pyrolytic liquid on a moisture-free basis. By-products like char and non-condensable gases can be reused for process heat [88].

A reactor is crucial in the pyrolysis process, and significant research has been devoted to developing suitable reactors for fast pyrolysis. A reactor is crucial in pyrolysis, and significant research has been devoted to developing suitable reactors for fast pyrolysis. For thermochemical conversion processes several reactor configurations such as fluidized bed, fixed bed, rotating cone, circulating fluid, autoclave reactor is used depending on the process conditions, scale of operation and feasibility. The fixed bed reactor is one of the most widely used types of pyrolysis. It typically consists of a packed stationary bed within a vertical or horizontal tube, with carrier gas flow directed upwards or downwards. Approximately 75% of commercial pyrolysis use downdraft fixed bed reactors, which are favored for non-aqueous thermochemical processes like pyrolysis due to their simple design [103]. Temperature is a critical factor in thermochemical processes, significantly influencing both the yield and properties of bio-oil. As the temperature increases, the bio-oil yield increases to an optimal point (around 500 °C). Beyond this temperature, the yield starts to decline due to the breakdown of volatile tars into gaseous products [104]. Usually, temperature ranges of biomass components such as hemicellulose, cellulose, and lignin are 180 ºC – 240 ºC, 230 ºC – 310 ºC, and 300 ºC – 500 ºC, depending on the heating rate. Whereas, at low temperatures (<300 °C), degradation occurs at the heteroatom sites in biomass, forming heavy tars. Beyond this temperature, the yield starts to decline due to the breakdown of volatile tars into gaseous products. At such elevated temperatures, both the primary and secondary reactions change the reaction pathway, affecting the composition of products. Fine-tuning the reaction temperature to optimize char formation and secondary decomposition can help improve liquid oil yields. Numerous experimental studies have explored the effect of temperature on liquid oil yields [103,104]. Increasing temperature increases biomass conversion due to the excess energy available to break the chemical bonds. Additionally, an indirect correlation exists between the char mass and the feed's initial mass. Generally, conversion remains low (0-20%) due to the thermal degradation behavior of various feedstocks. The temperature range at which 80-90% of conversion occurs is also known as the active pyrolysis zone at temperatures (300 ºC - 500 °C). Additionally, some denser biomass types decompose slowly, even beyond 500 °C. The solid mass remaining after the initial pyrolysis stage is called semi-coke, and temperatures above 400 °C lead to further degradation of this mass [105]. Table 9 describes the key studies available for pyrolysis of biomass in different reactors.

Table 9. Applied pyrolysis of biomass in different reactor configuration

Feedstock	Type of reactor	Operating Temperature (°C)	Yield of Products	Siginificant Observations	Ref
Camelina meal (CM)	Fixed bed	300-525	• Increase in bio-oil yield: 38-41 wt.% • Decrease in biochar yield: 52-26 wt.%	• Optimal Temperature: 525 °C • Oxygen content of bio-oil: 11.0 wt.%	[106]
Flax straw	Horizontal tube furnace	400-600	• Increase in bio-oil yield: 35-40.3 wt.% • Decrease in biochar yield: 42.8-29.5 wt.%	• Optimal Temperature: 500 °C • Oxygen content of biochar: 19.45 wt.%	[107]
Miscanthus	Fluidized bed reactor	400-500	• Increase in bio-oil yield: 34-46 wt.%	• Optimal Temperature: 500 °C	[108]

			• Decrease in biochar yield: 37-19 wt.%	• Oxygen content of bio-oil: 38 wt.%	
Food waste	Tubular reactor	300-600	• Increase in bio-oil yield:25-44.2 wt.% • Decrease in biochar yield: 44.1-22 wt.%	• Optimal Temperature: 500 °C • Oxygen content of bio-oil: 22.7 wt.%	[109]
Madhuca indica	Fixed-bed	450-600	• Increase in bio-oil yield:33-48.65 wt.% • Decrease in biochar yield: 26-14 wt.%	• Optimal Temperature: 525 °C • HHV: 41.8 MJ kg^{-1}	[110]

Numerous varieties of biomass and plastic feedstocks show synergistic interactions during co-pyrolysis. Examples include wood-plastic composites, sugarcane bagasse with plastic waste [111], biomass mixtures such as bamboo, empty fruit bunch, and sawdust with plastics like HDPE and PS [112], paper rejects combined with cable plastics [113]. The yield of biofuel depends on both the chemical composition and the physical structure and stability of the biomass. Chen et al. (2017) demonstrated the synergistic interaction between woody biomass and plastic composites during fast pyrolysis at 600°C, resulting in more stable pyrolysis products than biomass-only pyrolysis [119]. In another study, the aliphatic hydrocarbons derived from polyethylene (PE) were seen to improve the thermal decomposition of sugarcane bagasse, improving biofuel yield. This occurs due to hydrogen transfer from the PE to the bagasse, which reduces polymerization and char formation during co-pyrolysis [114]. Table 10 indicates the literature of applied co-pyrolysis of biomass and plastic.

Table 10. Applied co-pyrolysis of biomass and plastic

Feedstock		T (°C) and Ratio (B:P)	Reactor Type	Operating T (°C)	Siginificant Observations	Ref
Biomass	Plastic					
Poplar wood	Poly Vinyl Chloride	1:1	Fixed-bed	750	Oil yield: 30.3 wt.% HCl gas yield: decreased by 53 wt.%	[115]
Rice Bran Wax	Polypropylene	1:3	Fixed-bed	550	Oil yield: 81 wt.% HHV: 43.76 MJ kg^{-1}	[116]
Rubber Seed Cake	Polystyrene	1:1	Semi-batch reactor	500	Oil yield: 48.7 wt.% HHV: 37.48 MJ kg^{-1}	[117]
Date seeds	PET plastic	3:7	Fixed-bed	500	Oil yield: 59.16 wt.% HHV: 43.28 MJ kg^{-1}	[118]

1.9 Need for Bio-oil Upgradation

The crude bio-oil produced from pyrolysis has several undesirable characteristics, such as a high Total Acid Number (TAN), elevated oxygen content, and aging potential. Therefore, upgrading the bio-oil is necessary to make it suitable for use as a transportation fuel. The available upgrading methods include physical, chemical, and catalytic techniques [119].

Due to its unfavourable properties, crude bio-oil cannot be directly blended with fossil fuels. Some critical physical upgrading methods are:

(i) Filtration: Hot vapor filtration is crucial to reduce the ash content of bio-oil to below 0.01%, which also helps lower alkali content to less than ten ppm. Char particles in bio-oil can catalyze secondary reactions, reducing the oil yield by up to 20% and decreasing the average molecular weight. However, achieving fine particle filtration is challenging due to the liquid's physicochemical properties [120].

(ii) Solvent Addition: Polar solvents homogenize bio-oil and reduce its viscosity. Methanol, in particular, has shown a significant impact on oil stability. When bio-oil is mixed with 10 wt% methanol, its aging rate is reduced by 20 compared to oil without additives [120].

The second method, chemical upgrading techniques for bio-oil include: gasification, hydrothermal treatment, hydrodeoxygenation, and steam reforming. Gasification, which converts bio-oil into syngas, has garnered significant attention recently. However, there is a minor energy penalty due to the lower energy efficiency of the pyrolysis process, the need to transport bio-oil to centralized plants, and the energy demands of the gasification step [121].

1.9.1 Hydrodeoxygenation of bio-oil

Hydrodeoxygenation is a process that removes oxygen from bio-oil in the presence of hydrogen, often referred to as hydrogenolysis, hydrogenation, or hydrotreatment. This technique is similar to hydrodesulfurization and hydrodenitrogenation, used in petroleum refineries to treat crude oil. When a catalyst is employed, the process is known as catalytic hydrodeoxygenation (HDO). However, the catalysts used in HDO differ from those in conventional refinery processes. Several studies have focused on catalytic HDO using model compounds, which have provided valuable insights into reaction mechanisms. However, these findings are not comprehensive enough to generalize for the HDO of bio-oil [122].

The reaction mechanisms involved in HDO include hydrogenation, hydrodeoxygenation, decarboxylation, hydrogenolysis, and dehydration. Since different reactions take place at various sites on the catalyst, understanding the overall process becomes more complex. Numerous heterogeneous catalysts are available for HDO, but selecting the appropriate active site remains a challenge due to the complexity of the reactions involved [123]. The fundamental chemistry of the process can be represented as:

Oxygenated biomass + Hydrogen → Deoxygenated compound + Water

$$CH_{1.33}O_{0.43} + 0.77\ H_2 \rightarrow CH_2 + 0.43\ H_2O \tag{1}$$

However, undesirable reactions may occur at different catalyst sites, complicating the selection of an efficient catalyst. Catalyst stability is another issue, as products tend to cause metal sintering and leaching. While precious metal catalysts offer better stability, they are often economically unfeasible.

HDO is categorized into two types [124]:

(i) Partial or Mild HDO: This process occurs at low temperatures (150 °C - 250 °C) and high hydrogen pressure (>100 bar) in the presence of a catalyst. It is primarily used to stabilize acidic oxygen compounds.

(ii) Complete HDO: This process occurs at higher temperatures (350 °C – 400 °C) and pressures (~200 bar of hydrogen) and is used to thoroughly remove oxygen from high molecular weight alkanes and aromatic hydrocarbons.

Common oxygenated compounds in bio-oil include phenols, carboxylic acids, aldehydes, and carbohydrates. Selecting an appropriate catalyst and process conditions is critical for achieving high efficiency and avoiding undesirable side reactions.

1.9.2 Catalyst for the HDO Process

Catalytic hydrodeoxygenation (HDO) utilizes a range of catalysts to promote various reactions within the process [125]. The performance of different catalysts is outlined below:

(i) Metal Catalysts: HDO reactions primarily take place at metal sites, where cleavage of C-C bonds occurs. The choice of metal catalyst often depends on the desired product, with decarboxylation and decarbonylation being the key reactions. These reactions help remove functional groups like carboxyl (-COOH) and aldehyde (-CHO) from the bio-oil. Examples of metal-based catalysts include sulfided metals, Pd-Fe bimetallic catalysts, and Nb-phosphate-supported Pd catalysts. Ruthenium (Ru)-based catalysts are particularly effective for deoxygenation reactions. Palladium (Pd)-based catalysts are more suited for hydrogenation reactions. For instance, Pd catalysts have been shown to favour hydrogenation in the hydrodeoxygenation of compounds like eugenol [125].

(ii) Solid Acid Support: These are essential in promoting dehydration, hydration, and hydrolysis during hydrodeoxygenation (HDO). The selectivity and catalytic activity for C-O bond cleavage, specifically the removal of water molecules, depend heavily on the presence of Brønsted and Lewis acid sites. These sites also play a crucial role in isomerization reactions. For example, Brønsted acid sites produce fructose from isomerized glucose, with a lower fraction of these sites favoring the process. In contrast, Lewis acid sites positively influence the formation of fructose from glucose during isomerization reactions [125].

(iii) Bifunctional Metal-Acid Sites: Bifunctional metal-acid catalysts are commonly used in the HDO process, where metal particles are dispersed over solid acid supports. A notable class of catalysts includes bimetallic systems, which combine a reducing metal with an oxophilic metal. These catalysts facilitate the hydrogenolysis of C-O-C bonds, mainly through ring-opening reactions that involve the removal of water molecules. The proximity between the reducing and oxophilic metals on the support material is critical for higher catalytic activity, as it ensures effective interaction between the metals during the reaction. However, understanding the complex interactions between the metal and acid sites in bifunctional catalysts is more challenging than monofunctional catalysts used in HDO reactions [125].

(iv) Common Types of Catalysts for HDO: Several types of catalysts are employed in hydrodeoxygenation reactions, including: Oxides (Provide stability and are used to support metal catalysts), Noble Metals (These catalysts, such as those based on palladium and ruthenium, offer high activity and stability but are often more expensive).

Each of these catalyst types brings unique features that impact the overall performance of the HDO process.

(a) Metal Oxides:

Metal oxides like molybdenum trioxide (MoO_3) have been employed for catalytic hydrodeoxygenation due to their ability to oxidize olefins into ketones and aldehydes through the Mars-van Krevelen mechanism [126]. In HDO, these catalysts work in reverse Mars-van Krevelen mode, which involves:

Adsorption Step: The oxygenated compound adsorbs onto a vacant catalyst site.

Desorption Step: The deoxygenated compound is released, and oxygen adsorbs onto the catalyst.

Regeneration Step: Hydrogen reacts with the adsorbed oxygen, forming water and regenerating the oxygen vacancies.

Several metal oxides, including MoO_3, V_2O_5, Fe_2O_3, and CuO, are active for HDO of compounds such as acetone, with MoO_3 showing the highest activity. MoO_3 selectively cleaves C-O bonds over C-C bonds, making it valuable for bio-oil upgrading. The performance of these oxides is governed by the availability and strength of their acid sites. Lewis acid sites facilitate oxygen chemisorption, while Brønsted acid sites contribute to hydrogen availability at the catalyst surface [127].

(b) Reduced Transition Metals:

Transition metals such as Nickel (Ni), Platinum (Pt), Palladium (Pd), Ruthenium (Ru), and Rhodium (Rh) are highly active in HDO, enabling both hydrogenation and deoxygenation reactions. Unlike metal sulfides, these metals do not require external sulfur sources to maintain their catalytic activity. However, sulfided catalysts like Ni-MoS_2/ZrO_2 require continuous sulfur addition to prevent deactivation, which can lead to increased sulfur content in the product [128].

Noble metals offer advantages in operating at lower temperatures, reducing primary cracking reactions, and preventing coking and catalyst deactivation. However, they are costly and require higher hydrogen consumption for effective hydrogenation. Noble metals perform best when used as bifunctional catalysts, where the metal sites facilitate hydrogen donation, and metal-support interfaces enable the activation of oxygen-containing compounds [129].

(c) Non-Noble Metals

Non-noble metals, particularly Ni-based catalysts, offer a cost-effective alternative to noble metals. Bimetallic catalysts, such as Ni-Fe systems, exhibit higher activity in C-O bond hydrogenolysis compared to their monometallic counterparts. Carbon-supported Ni catalysts, such as mesoporous or activated carbon supports, provide benefits like reduced coke formation and enhanced stability. Studies have demonstrated that different catalysts follow distinct pathways during HDO. For instance: Ni/HBeta facilitates the conversion of phenolics to cycloalkanes and aromatic hydrocarbons. This versatility of catalysts, ranging from noble to non-noble metals and metal oxides, offers multiple pathways for optimizing HDO reactions based on the desired products and reaction conditions [130].

1.9.3 Role of Support in the HDO Process

Support materials play a crucial role in influencing the performance of catalysts in hydrodeoxygenation (HDO). The nature of the support affects various properties such as acidity, coke formation, interaction with oxygenates, and water resistance, which are essential for catalyst activity, selectivity, and stability.

(i) Effect of Support Material on Catalyst Activity

The support material can impact the catalytic activity by influencing the interaction between the active metal sites and the oxygenated compounds subjected to HDO. Different supports may favor different pathways, depending on their acidity and interaction with the catalyst.

γ-Al_2O_3: While γ-Al_2O_3 is commonly used in hydrotreating processes, its use in HDO is limited due to its tendency to react with water in bio-oil, forming Boehmite, which reduces the catalyst's activity. The potential trapping of catalytic active sites within the support lattice causes this. Additionally, γ-Al_2O_3 has higher acidity, which can lead to increased coke formation, further reducing catalytic performance [126]

Carbon-based Supports: Carbon-supported catalysts have gained popularity due to their lower acidity, which reduces coke formation during HDO. Carbon-based supports exhibit more excellent stability, making them a favorable option for HDO processes [131].

Silica (SiO_2): Silica has been identified as a promising support material due to its lower acidity and better performance in reducing deoxygenation. Studies show that Ni/SiO_2 has a higher deoxygenation efficiency compared to Ni/Al_2O_3 and Ni/activated carbon (AC) in the HDO of anisole, likely due to the interaction between the support and the model compound [132].

1.9.4 Key roles of support in catalyst performance

There are three main aspects in which the support material plays a crucial role.

(i) Coke Formation: The tendency of the catalyst to form coke is related to the acidity of the support. Higher acidity tends to promote coke formation, leading to catalyst deactivation. Therefore, supports with lower acidity (e.g., carbon or silica) are preferable to minimize coke formation and extend catalyst life [133].

(ii) Interaction with Oxygenated Compounds: The interaction between the support and the oxygenates plays a significant role in determining the overall activity and selectivity of the HDO process. Supports with favorable interactions can improve active metal site dispersion and facilitate oxygenated compounds' deoxygenation without excessive side reactions [134].

(iii) Resistance to Water and Regeneration Potential: Water produced during the HDO process can interact with the support, potentially deactivating the catalyst. Supports that resist reaction with water, such as carbon-based materials, tend to perform better in bio-oil upgrading. Additionally, the support should have a high probability of regeneration to allow for prolonged catalyst use over multiple cycles [135].

(iv) Influence on Selectivity: The support material significantly influences the selectivity of the desired products. For example, supports that allow stronger interactions between the metal catalyst and oxygenated compounds tend to facilitate selective C-O bond cleavage over C-C bond cleavage, which is crucial for optimizing bio-oil upgrading. This makes selecting support materials a critical factor in designing effective catalysts for HDO reactions [136].

1.9.5 Waste-derived catalysts

Considering the above conditions, it is vital to choose an appropriate catalyst. The two features of the catalyst material are a low coke tendency, which is associated with acidity. Secondly, the support should have sites that can activate oxygenated compounds to provide sufficient activity. Therefore, catalyst support should be economically viable, leading to low coke formation.

Waste-derived catalysts as a support material or direct use in the upgradation of pyrolytic vapor have gained much attention recently. Some of the catalysts derived from waste are biochar, oil palm ash, oyster shell, blast-furnace slag, etc. The advantage includes abundant availability and is economically viable. The feedstock source of these catalysts generally ended up in landfills which is a threat to the environment. These naturally available sources can be utilized effectively to produce various products such as bio-oil, char, and ash. Approximately 4 MT of oil palm ash is produced annually, and inappropriate disposal of such waste leads to numerous problems. Additionally, the catalyst derived from furnace slag has a high concentration of silicates, aluminium ferrites of calcium, and different oxide compounds. Therefore, the catalyst derived from waste has potential in the pyrolysis process [137].

Red mud is another valuable waste resource that can be used as a catalyst and its properties are presented in Fig. 10. It is a sludge that is produced during the processing of bauxite ore. The ore is washed, ground, and dissolved in sodium hydroxide under heat and pressure. While the liquid product is further processed, and the solid product (red mud) is dumped in a landfill. Depending upon the type/grade of the aluminium ore used, the amount of waste red mud generated is approximately 0.3-2.5 tonnes. Red mud contains many metal oxides such as Fe_2O_3, Al_2O_3, SiO_2, CaO, Na_2O, TiO, K_2O, and MgO, and several minor components like Cr, V, S, Ni, Cu, Mn, Zn, etc [138]. Some of the applications of red mud include biomass pyrolysis [139], hydrodeoxygenation [140], hydrogenation, and liquefaction [141].

Figure 10. Properties of Applications of red-mud as waste derived catalysts

1.9.5.1 Application of waste-derived catalysts in catalytic hydrodeoxygenation of model compounds and bio-oil

Bio-oil contains many different compounds, making the composition complicated. Hence, it is challenging to interpret the HDO of raw bio-oil. Much research is also focused on the oxygen group removal of ROOH and R-O-R, which are significant bio-oil compounds derived from non-edible oilseeds [142]. Conventional biofuels are produced from second-generation feedstocks. The second-generation feedstocks include soybean oil, rapeseed oil, and non-edible oilseeds, which usually contain high amount of oil. Further processing these seeds produces value-added products and paves the way for waste valorisation. Non-edible oilseeds usually contain triglycerides, which represent a significant composition. The decomposition of triglycerides into free fatty acids is crucial to producing biofuels with carbon content comparable to fossil fuels. These free fatty acids can be directly used as biodiesel but not in aviation fuels due to their poor characteristics, such as low cold flow properties and storage stability [143]. Standard practices for converting triglycerides to free-fatty acids include saponification, transesterification, and one-pot hydrodeoxygenation [144].

The carboxyl and alkenyl compounds in the fatty acids tend to increase the corrosivity while decreasing the stability. Therefore, HDO is one such pathway to convert these compounds into stable alkanes and ensure that the fuel properties are compatible with existing commercial ones [145]. Additionally, these reactions are accompanied by decarboxylation (DCX) or decarbonylation (DCN) reactions by decreasing the chain length of the compounds and emitting CO_2. Esterification reactions also take place; however, it increases further yield of alcohols. HDO, through esterification, is a common pathway that proceeds over a catalyst with weak acidity and mild conditions. Finally, while the direct hydrodeoxygenation (HDO) of triglycerides to alkenes has been demonstrated, most studies in the literature focus on employing fatty acids as model compounds. This is mainly due to their higher reaction rates compared to triglycerides. Fatty acids, being simpler molecules with fewer functional groups, allow for a more straightforward investigation of reaction mechanisms, catalyst performance, and optimization of HDO conditions [146].

Noble metals like Pd and Pt are highly effective and durable catalysts for this purpose, but their high cost and limited availability large-scale implementation. As a result, there is a pressing need to develop cost-effective and widely available catalysts with solid performance in HDO [147]. Ni is considered a viable catalyst among non-noble metals due to its ability to facilitate hydrogenation and deoxygenation reactions at lower temperatures. Literature suggests that the catalytic activity of Ni-based catalysts is influenced by both the dispersion of Ni particles and the properties of the support material. A recent investigation on the HDO of stearic acid using Ni-doped hierarchical ZSM-5 showed a 100% conversion, producing C8-C17 hydrocarbons [148]. However, a fundamental limitation of monometallic Ni catalysts is the tendency for Ni particles to agglomerate on the support surface due to high surface energy. This issue is commonly addressed using high surface area supports or incorporating additional metals into the catalyst. In this regard, combining Co with Ni-based catalysts has attracted attention for its improved stability and reduced coke formation [149]. Recent studies have demonstrated the versatility of red mud (RM) based catalysts in various applications, including catalytic fast pyrolysis, hydrodeoxygenation of bio-oil [150], and ammonia decomposition [151], underscoring RM's potential as a catalyst or support material. Table 11 shows the comparison of various catalysts employed in the catalytic HDO of palmitic acid.

Additionally, research has explored the HDO of palmitic acid using Ni/RM and Ni-MoOx/RM catalysts. With 7 wt% Ni loading on RM at 260 °C, the reduced Ni/RM catalyst achieved 100% conversion of palmitic acid with a strong selectivity for pentadecane formation, indicating a decarboxylation/decarbonylation reaction pathway [151]. When MoOx was added at 7 wt% loading to Ni/RM and the reaction was conducted at 250 °C, the maximum yields were 40% hexadecane and 20% pentadecane [152]. While studies have explored catalytic HDO of palmitic acid using reduced red mud catalysts, there is limited literature focusing on the role of Ni and Co oxides (in pre-reduced or calcined form) in promoting the hydrodeoxygenation pathway to produce hexadecane at lower temperatures, around 240 °C.

Table 11. Catalytic hydrodeoxygenation of palmitic acid

Model Compound	Catalyst	Calcined/ Reduced	Reaction Condition	Major Product	Selectivity (S), Conversion (C), and observations	Ref
Palmitic acid	Ni/TS-1	Reduced	T: 260 °C t: 2-10 h H_2 P: 1-5 MPa	Pentadecane	• S: 91.6% • C: 100% • Reaction: DCX, Carbon loss from chain	[153]
Palmitic acid	Ni-Mo/ZSM-5	Reduced	T: 300 °C t: 4 h H_2 P: 3.5 MPa	Branched and normal >C12 compounds	• S: 65% • C: 99% • Reaction: DCX, Carbon loss from chain	[154]
Palmitic acid	Ni/MoO_2@Mo_2CT_x	Reduced	T: 280 °C t: 4 h H_2 P: 4 MPa	Hexadecane	• S: 97% • C: 100% • Reaction: HDO C16/C15: 1.39	[155]
Palmitic acid	NiMo/RM	Reduced	T: 250 °C t: 4 h H_2 P: 4 MPa	Hexadecane	• S: 61.8% • C: 100% • Reaction: HDO Alcohol/Alkane: 2.25	[152]

As mentioned in section 1.8, the co-pyrolysis of biomass and plastic contains oxygenated compounds, increasing the acidity and decreasing the heating value. Additionally, the acidic compounds present in the bio-oil make it difficult for transportation and handling purposes. The instability in the composition is observed due to compounds causing repolymerization. All these properties limit the direct use of co-pyrolysis oil as drop-in transportation fuels. One significant goal of upgrading bio-oil is to produce value-added hydrocarbons. Aliphatic and aromatic hydrocarbons are produced via catalytic HDO, indicating that the deoxygenation of oil is efficient with less hydrogenation, indicating less hydrogen consumption [156]. A study on bio-oil hydrodeoxygenation showed that two stages are required to remove the oxygen altogether [157].

The interaction of catalysts with different compounds in the bio-oil varies with the operating parameters, such as temperature, catalyst-to-feed ratio, and initial hydrogen pressure. The reactivity of the compounds is usually as follows: alcohols> ketones > alkyl ethers > carboxylic acids ≈ m- and p-phenols ≈ naphthol > phenol > diaryl ethers ≈ o-phenols ≈ alkyl furans > benzofurans > dibenzofurans. The products of HDO are liquid (having aqueous rich fraction and oil rich fraction), gases, and coke. The bio-oil fraction obtained after HDO is usually referred to as upgraded oil. Although the aqueous phase constitutes a significant water portion, some organic compounds are responsible for the HHV of this fraction [158]. A study on the HDO of bio-oil over Pd/C catalyst indicated that the HHV of the aqueous phase (yield: 62%) formed was 7.2 MJ kg^{-1} [134]. One investigation on Ni/RM for hydrodeoxygenation of the aqueous phase of pinyon-juniper oil reported a significantly improved hydrocarbon yield of 47.8% [140]. Gas is typically considered an undesirable by-product. Methane, one of the gases produced during the hydrodeoxygenation of bio-oil, poses challenges for handling and storage due to its low density. Due to the complexity of bio-oil, researchers have proposed various strategies to optimize operational parameters and catalyst designs for the HDO process

[159]. Table 12 discusses some of the catalysts and operating conditions used in the catalytic hydrodeoxygenation of bio-oil.

Table 12. Catalytic hydrodeoxygenation of raw bio-oil

Feed	Reactor Type	Catalyst	Operating condition	Product yield (%)	Major compounds	Ref
Cotton Straw Bio-oil	Stainless autoclave	Pt/TiO_2	T: 280 °C t: 4 h H_2 P: 4 MPa	--	• Hydrocarbons: 33.80% • Alkylphenols: 51.38% • Oxygenated compounds: 13.28%	[160]
Lignin-derived bio-oil	Stainless autoclave	Ru3%/Hβ-25	T: 180 °C t: 2 h H_2 P: 3 MPa	80.5	• Cycloalkanes: 42.99% • Arenes: 50.74% • Aromatic ketones: 0.65% • Alkyl ketones: 5.30% • Alkyl alcohols: 0.32%	[161]
Lignin-derived bio-oil	Batch	GaNi/MCM-41-HBeta	T: 380 °C t: 50 min H_2 P: atm	93.31	• Hydrocarbon: 35.39% • Benzene: 30.03%	[162]
Pine sawdust bio-oil	Stainless autoclave	Mo_2C/CNF	T: 350 °C t: 1 h H_2 P: 5 MPa	--	• Phenols: 56-78% • Cyclic ketones: 7-30% • Carboxylic acids: 2-8% • Esters: 0-9% • Aromatic: 0-2%	[163]
Pine sawdust bio-oil	Batch	Fe-Co/SiO_2	T: 300 °C t: 1 h H_2 P: 3.45 MPa	23.85-26.94	• Hydrocarbon: 22.44% • Esters: 61.47% • Phenols: 8.72% • Alcohols: 3.38% • Aldehydes: 2.42% • Ketones: 0.88%	[164]

1.10 Thesis motivation and objectives

The literature on bio-oil upgrading reveals significant advancements in chemical processes such as co-pyrolysis and catalytic hydrodeoxygenation. Recent studies highlight the potential of catalytic hydrodeoxygenation to utilize biomass and plastic economically and sustainably. Despite the growing interest in co-pyrolysis, further research is required to overcome challenges such as reducing bio-oil's oxygen content and acidity. Much of the current research on catalytic hydrodeoxygenation focuses on deoxygenating bio-oil in the presence of a solvent using a single catalyst with varied reaction conditions. However, to better understand how different catalysts affect the properties of bio-oil and its deoxygenation, it is essential to evaluate multiple catalysts under various reaction conditions.

While the primary goal of co-pyrolysis is to effectively convert waste streams into valuable products such as bio-oil and reduce the negative impact of waste accumulation, equal attention must be paid to the quality of the bio-oil produced. Literature suggests that optimizing process parameters increases bio-oil yield and improves its properties. This motivates the search for an appropriate combination of biomass and plastic for biofuel production. Research indicates that the interaction between biomass and plastic enhances the H/C ratio and reduces the O/C ratio. Co-pyrolysis has been reported to significantly improve bio-oil yield, making it a promising thermochemical conversion process for waste valorization. Bio-oil from biomass-plastic co-pyrolysis requires upgrading to be suitable for use as a fuel. Hydrodeoxygenation (HDO) is an effective catalytic process to remove oxygen from bio-oil, thereby improving its energy content, stability, and compatibility with existing fuel infrastructure. The catalytic HDO process mimics refinery techniques for fossil fuels, making it an essential step in refining bio-oil into higher-quality liquid fuels.

Extensive research has been conducted on the hydrodeoxygenation of model oxygenates, with a few studies focusing on the HDO of bio-oil derived from biomass pyrolysis using various catalysts. To design an effective HDO reactor and catalyst, it is crucial to understand the rate-limiting steps and kinetics of the competing reactions involved. However, due to the complex composition of bio-oil, identifying the reaction rate, rate-limiting steps, and reaction mechanisms becomes challenging. While the reaction kinetics and mechanisms of HDO for model oxygenates are relatively straightforward, they do not account for the interactions between different oxygenates in real bio-oil, which is inevitable. For example, many studies have investigated the HDO of palmitic acid, a common component of bio-oil. However, in the HDO of actual bio-oil, the conversion of fatty acids can be affected by the presence of other functional groups, such as aromatic acids, ketones, aldehydes, and alcohols, which are primarily derived from cellulose and hemicellulose. Therefore, the data derived from HDO studies on single model oxygenates may not be directly applicable to designing catalysts and processes for real bio-oil HDO. Moreover, catalyst performance can vary significantly when transitioning from model oxygenates to complex bio-oils. Based on these gaps in the literature, the objectives of this thesis are as follows:

1. Identification and characterization of potential feedstock for thermochemical conversion of different regional biomass and plastics.
2. Thermal and co-pyrolysis of biomass and plastic for the production of different products such as bio-oil and biochar.
3. Low cost-catalyst development using red-mud for catalytic hydrodeoxygenation of model compound.
4. Catalytic hydrodeoxygenation of the produced co-pyrolytic oil in the presence of the red-mud catalysts and characterization of catalytically hydrodexoygenated oil using different techniques.

Chapter 2.

Experimental Methodology and Characterization Techniques

This chapter describes the experimental methodologies used in different processes such as thermal pyrolysis, co-pyrolysis and catalytic hydrodeoxygenation of bio-oil. The fundamental characterization techniques used for feedstock are also briefly summarized in this chapter. Similarly, the catalyst synthesis procedure and characterization techniques employed for the physicochemical characterization of catalysts and the feedstocks (biomass and bio-oils) are listed and described.

2.1 Materials

2.1.1 Feedstock collection and pretreatment

The *Mesua ferrea* L. oilseed was collected from Harmuti region of Assam, a part of Northeastern region of India (27.1393° N, 93.9292° E). Whereas, wheat straw, groundnut deoiled cake, were collected from Rajasthan, India. The feedstocks were cleaned with distilled water to remove the contaminants, and subsequently sun-dried for 48–72 h to reduce the bound moisture content. The feedstocks were ground into particles of average size 1 mm.

The PET plastic waste was obtained from Central Institute of Petrochemicals Engineering and Technology (CIPET), Guwahati, India. The plastic particles had a flaky nature. The average particle size of the particles were ~ 300 µm.

2.1.2 Model compound for hydrodeoxygenation and raw- material for catalyst synthesis

Fresh red mud was obtained from the National Aluminum Company (NALCO), Damonjodi, Odisha, India. Various metal salts were taken for impregnation on the surface of RM, e.g., nickel nitrate hexahydrate ($Ni(NO_3)_2 \cdot 6H_2O$), and cobalt nitrate hexahydrate ($Co(NO_3)_2 \cdot 6H_2O$). Palmitic acid was purchased from Sigma-Aldrich, whereas n-Decane was procured from TCI chemicals. The hydrogen gas used in hydrodeoxygenation process (99.9% pure) was procured from Assam Air Products, Guwahati.

2.2 Methodology

2.2.1 Identification of potential feedstock for bio-oil production

2.2.1.1 Physico-chemical characterization of feedstocks

Proximate analysis of the feedstocks was conducted in TGA-2000A, Navas Instruments (an automatic multiple samples TGA). In this process, 0.5 g of feed were taken in a crucible. Initially, the moisture content physically adsorbed on feed was determined by heating sample at 110 °C in the presence of nitrogen gas, which was at a flow rate of 100 mL min^{-1}. Further, the volatile matter of the samples were evaluated by increasing temperature to 900 °C at 80 °C min^{-1}. Finally, the fixed carbon content of the samples were estimated by changing nitrogen gas flow to air. The rate of flow of air is maintained at 100 mL min^{-1} and holding the sample at a temperature of 900 °C for 45 min. Ash content of the sample was recorded by noting the mass of the residue.

The elemental composition (CHNS) of feedstocks were investigated using an Elementar Vario Micro CHNS analyzer. Around 2.5 to 3 mg was considered for analysis. The oxygen content of the samples was found out by means of difference. The calorific value of the samples were obtained using an IKA 2000 Bomb Calorimeter. Typically 0.5 g of samples was used in this process. The lignocellulosic component analysis and extractive content were obtained following the NREL method [165]. The determination of structural components of biomass facilitates the thermal decomposition range of different components of biomass. A method described by Obernberger et al [166] was used to measure the bulk density of the biomass. This crucial property provides information required for the storage and transportation of biomass. Each analysis mentioned above was performed in triplicate to minimize the error.

2.2.1.2 FTIR analysis of the feedstocks

Functional groups present in biomass, plastic samples were investigated using an FTIR spectrometer (PerkinElmer, Spectrum Two). The scanning range was chosen to be 400 cm^{-1} - 4000 cm^{-1}.

2.2.1.3 Thermal decomposition behavior of feedstocks

Thermal decomposition of the individual feedstocks and co-feedstocks were performed using PerkinElmer TGA 4000 instrument under a Nitrogen atmosphere. A sample of 5-8 mg was taken in a crucible and heated 30 °C to 900 °C, where Nitrogen gas flow rate was maintained constantly at 20 mL min^{-1}. The heating rate of the sample was 10, 20, and 30 °C min^{-1} respectively. Additionally, the co-feedstocks were prepared in the feedstock ratio of 1:1, 2:1 and 1:2. The results obtained from the thermal decomposition of biomass aided the study of the kinetics of thermal pyrolysis.

2.2.1.4 Kinetic modelling studies of thermal and co-pyrolysis of biomass and plastic

Thermochemical conversion of biomass and plastic via the pyrolysis process is complicated owing to various compounds present in the feedstocks. It is difficult to determine the reaction mechanism of thermal and co-pyrolysis due to the simultaneous decomposition of different biochemical and polymeric compounds. Nevertheless, the overall reaction mechanism can be proposed as explained in section 1.6.

The different kinetic methods used in the present study to determine the kinetic triplet are presented in Table 13.

Table 13. Kinetic modelling equations for the iso-conversional model-free methods

S.No.	Model	Equation	Plot	Determination of kinetic parameter	Ref
7.	Differential Friedman Method	$\ln\left(\frac{dx}{dt}\right) = -\frac{E}{RT} + \ln(Af(x))$	$\ln\left(\frac{dx}{dt}\right)$ vs $\frac{1}{T}$	The activation energy is obtained from the slope of the plot. The frequency factor is calculated from the intercept.	[65]
8.	Kissinger–Akahira–Sunose (KAS)	$\ln\left(\frac{\beta}{T^2}\right) = \ln\left(\frac{AE}{Rg(x)}\right) - \frac{E}{RT}$	$\ln\left(\frac{\beta}{T^2}\right)$ vs $\frac{1}{T}$	The activation energy is obtained from the slope of the plot. The frequency factor is calculated from the intercept.	[66]
9.	Ozawa-Flynn-Wall (OFW)	$\ln(\beta) = \ln\left(\frac{AE}{Rg(x)}\right) - 2.315 - 0.457 * \frac{E}{RT}$	$\ln(\beta)$ vs $\frac{1}{T}$	This method uses Doyle’s approximation. E can be calculated from the slope The frequency factor can be calculated from the intercept	[67]
10.	Starink Method (STR)	$\ln\left(\frac{\beta_i}{T_{\alpha,i}^{1.92}}\right) = Constant - 1.0008 * \left(\frac{E_\alpha}{RT_{\alpha,i}}\right)$	$\ln\left(\frac{\beta_i}{T_{\alpha,i}^{1.92}}\right)$ vs $\left(\frac{1}{T_{\alpha,i}^{1.92}}\right)$	A temperature approximation integral is used in this model for simplification of the kinetic model. Activation energy is determined from the slope of the plot. The frequency factor is calculated from the intercept	[68]
11.	Simplified Distributed activation energy model (DAEM)	$\ln\left(\frac{\beta}{T^2}\right) = \ln\left(\frac{AR}{E}\right) + 0.6075 - \frac{E}{RT}$	$\ln\left(\frac{\beta}{T^2}\right)$ vs $\frac{1}{T}$	The activation energy is determined from the slope of the plot while the intercept provides the information of the pre-exponential factor.	[69]

2.2.2 Analytical and applied thermal and co-pyrolysis of biomass and plastic

2.2.2.1 Curie point analysis of biomass and plastic for pyrolysate composition

Analytical fast pyrolysis experiments were done using a JHI-07 hybrid pyrolyzer (Japan Analytical Industry Co. Ltd.) in Curie point pyrolysis mode. In this method, a known mass of sample is placed in a pyrofoil, which is made of a special alloy. This pyro-foil is kept in the coil of a high-frequency oscillator, which creates a magnetic field and causes eddy currents to flow through the device. This process consequently heats the pyrofoil to attain its Curie point temperature. Due to the close contact of the sample with the pyro-foil,the sample reaches the desired pyrolysis temperature, which is apparently the curie point temperature of the pyro-foil. This process requires about 0.2–0.4 s to reach the appropriate temperature as compared to a typical furnace-type analytical pyrolysis device. As a result, this analytical Py-GC/MS makes it possible to conduct rapid pyrolysis at heating rates above 1000 °C s^{-1}, while simultaneously reducing the likelihood of secondary cracking reactions. This study involves fast pyrolyzing the individual biomass, plastic and their mixtures (1:2, 1:1, 2:1 w/w) at 590 °C.

In a typical experiment, the sample (800 ± 20 µg) was packed inside a pyrofoil and sealed using flat-nose pliers. Further details about the sample preparation methodology and operation of the curie point pyrolyser is available elsewhere[167]. The duration of pyrolysis was set at 30 s. An extremely sensitive microbalance (Sartorius CUBIS Series, accuracy of 1 µg) was used to measure the mass of the empty pyrofoil, the pyrofoil with the sample, and the pyrofoil after the experiment. All the fast pyrolysis experiments were repeated twice.

The pyrolysates were swept to the Gas Chromatograph attached with Mass Spectrometer system (Shimadzu GC-2010 and QP 2020 plus, Japan) using ultra-high pure helium gas (5.5 grade). The GC/MS had a DB-5MS (30 m × 0.25 mm i.d. × 0.25 µm film thickness) for separating the different compounds in the pyrolytic vapors. The carrier gas flow rate through the column was kept constant at 1.6 mL min^{-1}, and the split ratio was set to 1:90. The temperature of the injection port was maintained at 300 °C. The oven temperature of the GC column program was as follows: hold at 40 °C for 2 min, ramped up to 300 °C at a rate of 5 °C min^{-1}, and then held at 300 °C for 5 min. With the ion source and interface temperatures set at 250 °C and 300 °C, respectively, the electron ionization voltage was 70 eV. The mass-to-charge (m/z) scan range was 12–500 Da. To identify the compounds, NIST14 and Wiley08 libraries were used. The pyrolysates were semi-quantitatively analyzed using GC/MS peak area % of the individual compounds and based on the various functional group categories.

2.2.2.2 Fixed-bed thermal and co-pyrolysis for bio-oil production

The individual feedstocks (biomass and PET plastic) and co-feedstocks (Biomass: PET (B:P) of 1:1, 2:1, 1:2 w/w) were pyrolyzed (40 g) in a fixed bed reactor of Inconel 800 with an outer diameter of 73 mm, inner diameter of 62.62 mm, and a length of 438 mm, and was operated in semi-batch mode. A split tubular furnace with a single heating zone was used to uniformly supply heat to reactor wall. The furnace was equipped with a PID controller to accurately control the heating rate and maintain the temperature. Nitrogen gas, which generally serves as a fluidizing and carrier gas, was pre-heated to a temperature of 250 °C, and passed through the bottom of reactor with a flow rate of 500 mL min^{-1}. The hot vapors were passed through a well-insulated transfer line to a straight single-pass condenser made of SS316. The condensed vapours were collected in a storage vessel and labelled as bio-oil. The present research is aimed to analyze the effect of temperature and feedstock ratio on the pyrolytic product yield. The slow pyrolysis of biomass was conducted at heating rate of 15 °C min^{-1}. The final temperatures were 550, 600 and 650 °C. The amount of liquid product formed was calculated by considering the mass of the condensable vapors. The mass of the char (including wax) was determined by collecting the residue left in the reactor. The yield of non-condensable gas was determined using the overall mass balance as described in equation 12. This temperature (650 °C) was chosen as an optimum to further study the effect of plastic addition on the quantity and quality of the bio-oil. All the studies were repeated thrice. The schematic representation of experimental setup employed in this study is shown in Fig. 11.

$$\text{Yield of gas} = 100 - \text{Yield of Liquid} + \text{yield of Char (including wax)} \quad (12)$$

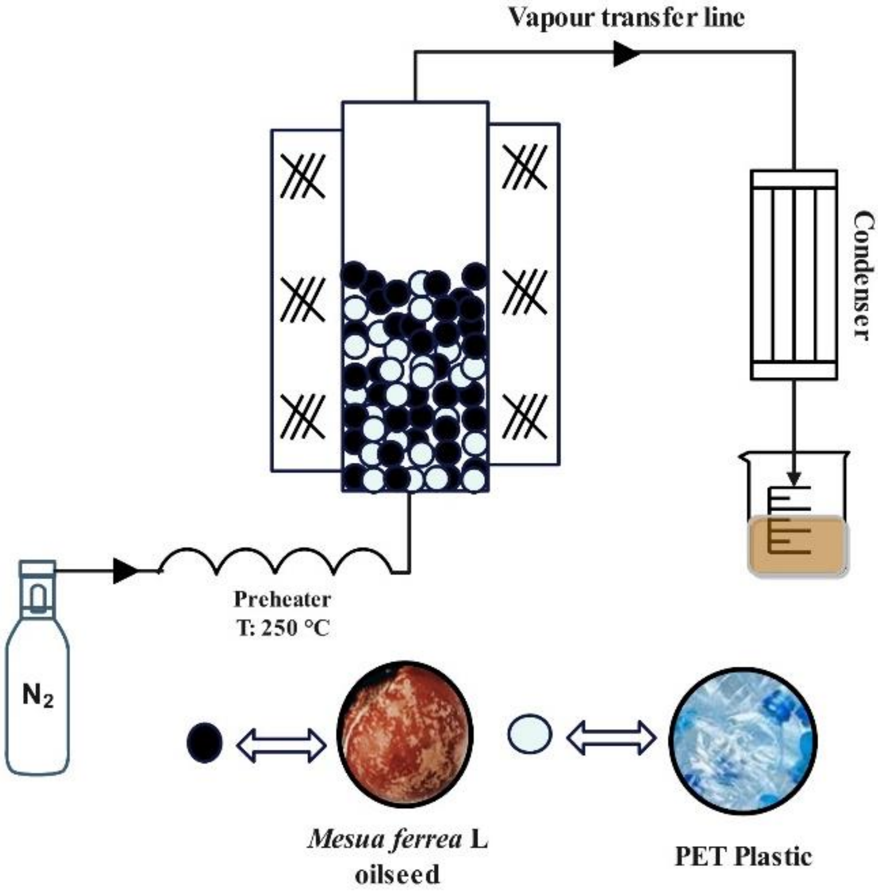

Figure 11. Experimental setup for applied pyrolysis of biomass and plastic to produce bio-oil

2.2.3 Low-cost catalyst development using waste-material as support for catalytic hydrodeoxygenation of model-compound

2.2.3.1 Catalyst(s) synthesis

Conventional wet-impregnation method was employed for the synthesis of RM-supported Ni, and Co metal catalysts. Initially, the red mud was oven-dried 100 °C to ensure the removal of moisture and ground to get uniform particle size. Further calcining the dried RM at 550 °C in a muffle furnace for 4 h to removes impurities. To produce impregnated metal catalysts, 5 g calcined RM was mixed and stirred in the presence of DI water at room temperature. For Ni/RM, 10 wt% of nickel precursors were mixed for 1 h with the above RM solution at room temperature and then raised to 80 °C. This ensures the evaporation of water which indeed forms a slurry of the catalyst solution. The prepared catalysts were thereafter dried at 110 °C and calcined at 550 °C for 4 h to obtain catalyst in powder form. Ni-Co/RM were synthesized by the same procedure. During the synthesis of bimetallic catalysts 5 wt% of nickel precursor and 5 wt% of cobalt precursor (in the case of Ni-Co/RM) were added to the mixture of RM following the above-mentioned procedure.

2.2.3.2 Hydrodeoxygenation of Palmitic acid

Catalytic hydrodeoxygenation of palmitic acid was performed in a 250 mL high-pressure batch reactor. Typically, in an experiment. 0.1152 g of calcined catalyst, 30 mL of n-Decane and 5 wt% palmitic acid were added to the reactor. Tightly closing the reactor and flushing with hydrogen ensures the removal of any trace of air. Further, hydrogen gas added up to a partial pressure of 4 MPa at 25 °C. The initial experiments were performed at 240 °C, 4 MPa for 4 h at a stirring speed of 450 rpm with different catalysts (RM, Ni/RM, Ni-Co/RM) with continuously stirring the reactor at 450 rpm to determine the selectivity of fatty alcohols and long-chain alkanes. The catalyst that is better suited in terms of promising product selectivity was chosen for further experiments. The effect of temperature (210, 240, 270 °C), time (3, 4, 5 h) and hydrogen pressure (3, 4, 5 MPa) were studied by varying these operating conditions. After the reaction is over, the solid and liquid phases of the reaction products were separated using a 0.25 μm filter paper. The qualitative analysis of the obtained liquid was performed by directly injecting it into a gas chromatograph/mass spectrometer, GC/MS (Make: Shimadzu GC-2010 Plus and Model: QP2020,). A capillary column (RTx-5MS, Length: 30 m, ID: 0.25 mm, Thickness: 0.25 μm) with helium (99.9995%) as the carrier gas at a flow rate of 1.49 mL min^{-1}. The column temperature was held at 45 °C for 1 min, then ramped up to 250 °C at 10 °C min^{-1}, and held for 10 min. The temperatures of injector and interface were set to 280 °C, while ion source temperature of the MS was set to 250 °C. Compounds were detected within a mass range of 50 to 500 Da. The GC/MS system was calibrated using known quantities of pure compound standards. Analyte peak area ratios were plotted against their relative amounts, and yields were calculated using response factor values. The catalysts were separated using a filter paper and the filtered catalysts were dried at 105 °C. The dried catalysts were used in the subsequent recycle experiments. The coking of the spent catalyst was observed using FTIR.

2.2.4 Catalytic hydrodeoxygenation of raw bio-oil produced from co-pyrolysis of biomass and plastic

Catalytic hydrodeoxygenation of raw co-pyrolytic oil was performed in a 100 mL high-pressure batch reactor. Typically, 25 g of bio-oil, with an appropriate catalyst, were added to the reactor in an experiment. Tightly closing the reactor and flushing with hydrogen ensures the removal of any trace of air. Further, hydrogen gas added up to a partial pressure of 4 MPa at 25 °C. The initial experiments were performed at 240 °C, 4 MPa for 2 h at a stirring speed of 315 rpm with different catalysts (RM, Ni/RM, Ni-Co/RM) while continuously stirring the reactor to determine the conversion of bio-oil and selectivity to different classes of compounds. The catalyst that is better suited in terms of promising product selectivity was chosen for further experiments. The effect of temperature (180, 240, 300 °C), time (2, 4, 6 h), and catalyst loading (10, 15, 20 MPa) were studied by varying these operating conditions. After the reaction, the solid and liquid phases of the products were separated using 0.25 μm filter paper. The liquid was qualitatively analyzed by injecting into a gas chromatograph/mass spectrometer (GC/MS), NMR, CHNS, and bomb calorimeter. The solid catalysts were collected using filter paper, dried at 105 °C, and reused in subsequent recycling experiments. The recycled catalysts underwent characterization using XRD, FTIR, FESEM, FETEM-EDX, and XPS.

2.2.5 Characterization of liquid product and catalyst(s)

2.2.5.1 Characterization of fresh and spent catalyst(s)

The physical, chemical, and textural aspects of the catalysts (both fresh and spent) were studied by various characterization methods. The surface area of samples was measured by nitrogen absorption-desorption isotherms (Quantacrome, Autosorb-IQ MP). The catalysts were degassed at 150 °C under vacuum for 4 h before adsorption studies. Brunauer-Emmett-Teller (BET) isotherm method was used to estimate the surface area of the catalyst. Inductively Coupled Plasma-Atom Emission Spectroscopy (ICP-AES) on an ICP spectrometer (ICAP 6000 SERIES; Thermo Fisher Scientific) was used for the determination of metals (Si, Al, Na, Ca, Ti, Fe, Ni and Co). In a typical analysis, 100-150 mg of sample was dissolved into HNO_3 (10 mL) for digestion and then diluted up to 50 mL by distilled water prior to analysing in an ICP spectrometer.

Morphological and elemental analysis of the support and catalysts were obtained using a Zeiss Sigma Scanning Electron Microscopy (FESEM) instrument, Field Emission Transmission Electron Microscopy (FETEM) attached with an energy dispersive X-ray analyser (EDX) were used to analyse the impregnation of metals and elemental composition of the samples. The crystallographic analysis was performed using X-ray diffraction (XRD) patterns by using a Rigaku Smart Lab diffractometer with Cu Kα radiation (wavelength: 0.154 nm) at 45 kV and 112 mA. The diffraction angle was considered over range of 2Θ of 10° to 80°. The functional groups of the fresh and spent catalyst was performed using Fourier transform infrared spectroscopy (FTIR) in the range of 450-4000 cm^{-1}. The PHI 5000 Versa Probe-II (K alpha from Thermo Fischer Scientific instruments, UK was used for X-ray photoelectron spectroscopy analysis. The samples were dispersed in ethanol and deposited onto a silicon wafer, which was secured onto a sample plate with conductive carbon tape. This plate was placed in the load lock chamber until the vacuum level reached 10^{-7} mbar. Subsequently, the sample plate was moved to the analyzer chamber (2 x 10^{-9} mbar) for further examination. A flood gun and an X-ray source (Al K alpha, 1486.6 eV) were utilized for the analysis.

2.2.5.2 Characterization of liquid products

The bio-oil produced from both co-pyrolysis and catalytic hydrodeoxygenation under the optimal conditions was subjected to GC/MS and ^{1}H-nuclear magnetic resonance (NMR) spectroscopy for qualitative and semi-quantitative analysis of the products. The acetone-bio-oil mixture obtained after washing the condenser was separated using a rotary evaporator, and the recovered solvent was used for subsequent experiments. The HHV was estimated using a bomb calorimeter, and the CHNS content of the sample was determined using a CHNS/O analyzer (Elementar Vario Micro CHNS analyzer). The classification of the compounds according to organic functional groups was done using GC/MS analysis. GC system is equipped with RTx-5MS column (15 m length x 0.25 mm i.d. x 0.25 µm film thickness) (Shimadzu TQ8040). Typically, 1 mL of the sample was introduced via the injection port, which was maintained at 250 °C. The column conditions were set as follows: 80 °C for 5 min, ramp to 300 °C at 5 °C min^{-1}, finally kept at 300 °C for 5 min. Mass spectrum was analyzed in the range of 45 to 700 m/z, executed in electron ionization (EI) mode at 70 eV. The NIST library was utilized for identifying the compounds. To determine the different classes of organic compounds of bio-oil, ^{1}H-NMR (Bruker ASCEND 600) was used. A sample of 200 µL was mixed with DMSO-d6 solvent in 1:1 ratio and then subjected ^{1}H NMR analysis. FTIR analysis was done to analyze the different functional groups (PerkinElmer, Spectrum Two).

CHAPTER 3.

Identification and characterization of potential feedstock for thermochemical conversion of different regional biomass and types of plastics

3.1 Background

Rapid depletion of fossil-based resources leads to constant energy demands and a continuous environmental threat. This dire need has paved the way for developing renewable and sustainable energy that is also environmental-friendly. There are different types of renewable energy resources of which biomass energy is the most prevalent form owing to various advantages. Some benefits include producing valuable end products such as bio-oil, syngas, and bioethanol, which are compatible with current fossil fuels. However, biomass has some undesirable properties, such as poor bulk and energy density, significant moisture content (typically around 10 wt%), and a highly complex structure. All these unwanted properties make it difficult to transfer the technology to a commercial scale [168]. The heterogeneous nature of biomass is because of variation in geographic area and climatic conditions. Lignocellulosic biomass is inexpensive and available throughout the year. India is regarded as the world's third-largest source of biomass energy. It is estimated that the global availability of biomass is approximately 200 billion tons per year [169].

Alternative fuels like those made from waste materials, known as biofuels, are attracting a lot of interest because of their many benefits and the abundance of feedstocks such as organic solid waste. Non-edible oil seeds, wheat husk, sawdust, wheat straw, bagasse, algal biomass, de-oiled cake, oil seed outer shells, etc., are some of the raw materials utilized in the generation of biofuels. Numerous experiments have been done using agricultural waste, including non-edible oil crops, to generate biofuels. In addition, during biodiesel production from non-edible oil seeds, pyrolysis and co-pyrolysis technologies can be employed to create value-added chemicals from the shell waste and de-oiled cake of the seeds. High levels of protein can be found in groundnut seed. Around 30-35 kg of oil and 50 kg of meal can be extracted from a quintal of groundnuts on average [170]. The cake, which is full of protein, was traditionally fed to cattle or used as manure. Due to the excess availability of deoiled cakes as a by-product from the oil extraction process, this can be a potential feedstock for production of biofuel and value-added chemicals [171]. *Mesua ferrea* L., also known as cobra saffron, is abundantly available in the North-East part of India and is considered the state tree of Mizoram, India. It is also abundantly available in state of Uttar Pradesh and the Western Ghats. The oil obtained from *Mesua ferrea* L. non-edible oilseed is used for daily lighting purposes. Bio-oil extracted from this seed after suitable upgradation can be used as a transportation fuel by blending 20-30 wt% with the existing fossil fuels. A few studies are available in the literature that discusses the applications of oil derived from *Mesua ferrea* L. non-edible oilseeds. The use of oil generally includes the production of polymers, polyols, medicines [172]. Extensive use of this non-edible oilseed for production of bio-oil is yet to be explored. Additionally, wheat straw (WS), a significant by-product of wheat farming, is generated in large quantities and necessitates efficient disposal methods. According to the Global Agricultural Information Network (GAIN) report for 2023-24, India's wheat production totaled 112.5 million metric tons (MMT), resulting in approximately 191 MMT of WS as agricultural residue [6].

Polystyrene (WPS), polyethylene terephthalate (PET), low density polyethylene (LDPE), and polyvinyl chloride (PVC) types of wastes are only a few examples of the common plastics whose volume is rising. The Global scenario says that about 150 million tonnes of plastic are discarded and end up in landfills. Additionally, despite recycling garbage equivalent to almost 100 million barrels of oil, an estimate of 8 million tonnes of landfill space still exists, according to research by European nations [174]. One such technology that can be employed in bio-oil production is pyrolysis. This chapter emphasizes the importance of understanding the kinetic behavior and product distribution from the analytical fast pyrolysis of this non-edible oilseed.

Investigating the kinetic parameters of the pyrolysis of biomass process provides valuable information on its thermal degradation behavior. It also aids in a fundamental understanding of the reaction mechanism. Furthermore, determination of the kinetic parameters assists in the techno-economic estimation of the pyrolysis process. Standard methods used to assess kinetic parameters are model-fitting and model-free methods [105]. Some of the iso-conversional methods include Friedman (FM), Ozawa-Flynn-Wall (OFW), Kissinger-Akahira-Sunose (KAS), Starink, simplified Distributed Activation Energy Model (DAEM), and Miura-Maki-Integral. An advantage of employing model-free isoconversional methods for kinetic analysis is that there is no possibility of selecting incorrect models and obtaining inaccurate kinetic triplets. The information obtained from estimating kinetic parameters are used in the pyrolysis reactor design [175].

Literature on the estimation of apparent activation energy of the *Putranjiva roxburghii (putranjiva) (PR)* and *Cassia fistula (amaltas) (CF)* non-edible oilseeds using KAS, OFW, and STR models provided to be in the range of 150.44-240.69 kJ mol^{-1}, 151.36-239.94 kJ mol^{-1}, and 150.77-240.97 kJ mol^{-1} for PR biomass and 73.83-287.37 kJ mol^{-1}, 77.65-283.94 kJ mol^{-1}, and 74.34-287.44 kJ mol^{-1} for CF biomass [105]. Although many studies are available on pyrolysis kinetics using iso-conversional either model-free methods or model-fitting methods of different types of biomass, there is limited research on applying both model-free and model fitting methods for determining the kinetics of biomass. Chutia et al. [176] conducted the kinetic analysis on the *Mesua ferrea* L. deoiled cake and reported that apparent activation energy in two zones, namely S_{II} and S_{III}, was 94.04 kJ mol^{-1} and 146.98 kJ mol^{-1}, respectively. This study primarily focused on analyzing the thermal decomposition behavior of biomass and estimation of kinetic triplet (E_a, A, and n) using FM, OFW, KAS, STR, simplified DAEM, and Avrami models. Additionally, a recent study on the determination of the kinetics of co-pyrolysis of pinewood with a variety polymer wastes such as PP, PET, and PC yielded the highest synergistic effect of biomass with PET plastic. DAEM kinetic model was employed to estimate the average activation energy, which was found to be 250-290 kJ mol^{-1} [177].

The aim and scope of this study is to analyze feasibility of the co-pyrolysis of *Mesua ferrea* L. oilseed, groundnut de-oiled cake (GDC), wheat straw (WS) with Polyethylene Terephthalate (PET) plastic at a ratio of 1:1. Additionally, the thermal decomposition behavior and the kinetic parameters estimation is carried out using TGA equipment under non-isothermal conditions in nitrogen atmosphere at three different heating rates of 10, 20, 30 °C min^{-1}. Furthermore, the *Mesua ferrea* L.: PET, GDC: PET and WS: PET mixture thermal degradation behavior is compared with that of the biomass and PET components individually. The study of chemical kinetics is extremely important since it is predicated on the rate of reaction, which gives crucial background information regarding the working mechanisms of the chemical processes that are being considered. So, it's important to get accurate experimental data in order to make reliable and useful kinetic models that can be used to make a full-size industrial reactor for this process that uses this feedstock.

3.2 Experimental Methodology

The physicochemical characterization of the feedstocks was performed through proximate (moisture, volatile matter, ash, and fixed carbon), ultimate (carbon, hydrogen, nitrogen, sulphur, and oxygen), and compositional (hemicellulose, cellulose, and lignin) analysis. The methodology employed in determining these parameters is provided in section 2.1.1.1.

Thermal pyrolysis and co-pyrolysis experiments were conducted using a TGA. Around 10 mg of each sample was pyrolyzed under a nitrogen flow rate of 19.8 mL min^{-1}, with the temperature increasing from 30 °C to 900 °C. The tests were conducted at three different heating rates (10, 20, and 30 °C min^{-1}) to evaluate the pyrolysis kinetics under both slow and intermediate heating conditions. Slow heating rates are preferred for accurate kinetics analysis, while higher rates are beneficial for industrial applications, as they improve biofuel quality and economic efficiency. However, very high heating rates can cause thermal lag, leading to abrupt changes in thermal degradation, as observed in TGA. Each pyrolysis test was repeated in duplicate to ensure consistency. The average TGA data were then used to calculate the pyrolysis kinetic parameters. The methodology for kinetic parameters estimation is provided in section 2.2.1.4.

3.3 Results and Discussions

3.3.1. Physico-chemical characterization of the feedstock

The physicochemical characterization of the *Mesua ferrea* L. oilseed (also known as Nahar seed), wheat straw, and groundnut deoiled cake along with the PET is represented in Table 14, which shows that all of the biomasses and plastic contain no more than 10% moisture. The biomass, along with the plastic having low amount of moisture is considered to be a suitable feedstock for the thermochemical conversion to liquid fuels. The literature on the pyrolysis processes indicates that the faster heat transmission to the particles occurs when the feedstock has a lower moisture content (<10%) [178]. Furthermore, it is observed that the biomasses and the PET had a higher content of volatile matter (> 70% in case of all the types of biomass) and (94.3% for PET), respectively, and a low ash content (1.9% for Nahar) and (0.058% for PET), respectively. Furthermore, compared to the biomass with the low volatile matter, the biomass and plastic with a higher volatile content contained more reactive chemicals that quickly degraded to produce more gaseous compounds (both condensable and non-condensable). Moreover, lower ash content is an essential pyrolysis property that a feedstock must possess. Higher combustion rates and less slag formation at higher temperatures are the advantages of less ash content. This dramatically improves the thermochemical conversion and decreases the operational costs. The feedstock having a high volatile matter and less ash content signifies the instant ignition of fuel [179]. The fixed carbon is used as a heat generator during the combustion due to its high energy value. An inadequate sample combustion and difficulties with waste disposal are additional issues associated with a high ash level. The energy value of feedstock is significantly influenced by its fixed carbon content [180]. As compared to wheat straw, and groundnut deoiled cake, the oilseed contained less amount of moisture, high volatile matter, low ash and fixed carbon content, indicating that *Mesua ferrea* L. oilseed is a suitable feedstock for bio-oil production through thermochemical technologies. The elemental analysis of the *Mesua ferrea* L. oilseed and PET confirm a higher percentage of carbon ie., 77.42% and 62.88%, respectively, and a low nitrogen and sulphur content which lowers the SO_x and NO_x emissions during the co-pyrolysis [104]. The high calorific value of the co-feedstock of the *Mesua ferrea* L and PET confirms the ease of the biofuel production.

Table 14. Physicochemical characterization of biomass and plastic feedstocks

Properties	*Mesua ferrea* L.	Wheat Straw	Ground Nut Deoiled Cake	PET Plastic
Moisture	3.2 ± 0.30	5.0± 0.90	5.6± 0.40	0.6± 0.8
Volatile Matter	88.6 ± 0.20	74.5± 0.57	83± 0.30	94.3± 0.15
Ash Content	1.9 ± 0.03	11.6± 0.04	4.8± 0.08	0.1± 0.02
Fixed Carbon	6.3 ± 0.1	8.7± 0.28	6.6± 0.35	5.0± 0.2
C	77.4	40.7	44.8	62.9
H	9.2	5.8	11.2	4.7
N	0.7	1.3	7.2	0.4
S	0	--	0.31	0.0
O	12.7	52.2	36.4	32.0
Bulk Density (kg m^{-3})	425.4 ± 09	160.2± 07	--	
Extractive Content	46.4± 0.2	7.4± 0.3	7.1± 0.5	--
Hemicellulose	18.6	21.8	21.5	--
Cellulose	11.1	34.8	33.2	--
Lignin	23.9	36.0	38.2	--
Gross Value (MJ kg^{-1})	34.7± 2.1	16.4± 1.8	15.5± 3.7	23.0± 2.5

3.3.2 FTIR of feedstocks

The FTIR analysis is used to identify functional groups present in biomass and plastic feedstocks as shown in Fig. 12. The peak at 1031 cm^{-1} was associated with the C-O bond of alcoholic compounds. The presence of the C-O-C bond was confirmed by the peak at 1160 cm^{-1}. This peak is mainly seen in cellulose and hemicellulose components of biomass. The stretching at 1368 cm^{-1} was due to the C–H bending of the methyl group present in cellulose, hemicellulose, and lignin. The peak at 1458 cm^{-1} was due to the C–H deformation occurring in methyl and methylene functional groups. The stretching of ketonic groups was found at 1613 cm^{-1} [181]. The peaks at 1706 cm^{-1} and 1739 cm^{-1} were associated with the unconjugated carbonyl/carboxyl group of hemicellulose and lignin respectively. The peak at 2859 cm^{-1} was mainly attributed to the C–H bond in the methylene group present in aliphatic compounds [182]. The origin of these aliphatic methylene groups can be attributed to being present in the fatty acids that are present in biomass. In the case of the PET, the FTIR peak at 871 cm^{-1} is of the H vibration to the phenyl rings. The stretching at 1248 cm^{-1} is due to the C-O stretch present in terephthalate group. The peak at 1343, 1411, and 1452 cm^{-1} was observed, due to the C-O vibration of ethylene glycol. The peak at 1721 cm^{-1} is mainly attributed to the C = O bond in the carboxylic acid group present in the compounds. The peak at 2962 cm^{-1} is mainly attributed to the C-H symmetrical stretching present in the alkyl and alkene compounds [183]. From the above FTIR results, different functional groups imply a high probability of production of gases such as carbon dioxide, hydrogen, carbon monoxide, and a wide variety of hydrocarbons.

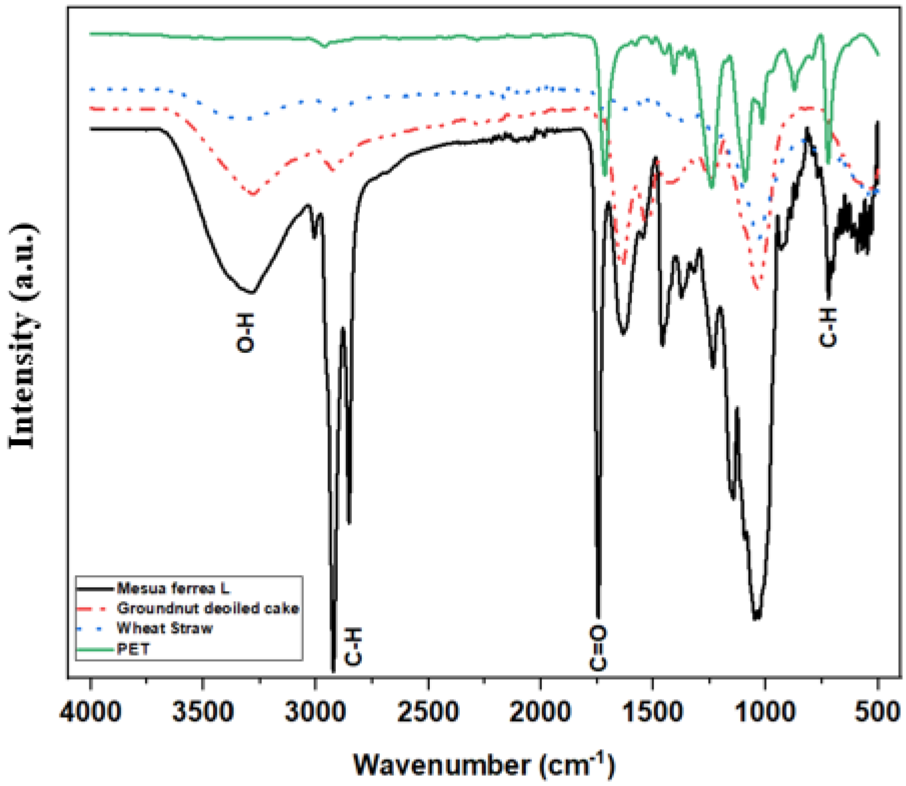

Figure 12. FTIR peaks of feedstocks

3.3.3 Thermal decomposition behaviour of feedstocks

3.3.3.1 Individual feedstocks

Biomass decomposition for different types was characterized by three distinct zones: dehydration zone (up to 150 °C), devolatilization zone (150-650 °C), and char formation zone (650-900 °C). A similar thermal decomposition pattern was observed for all types of biomasses [104]. Initially, moisture and low molecular weight volatile compounds are evaporated in the dehydration zone. In the oilseed ie., *Mesua ferrea* L., a minimal weight loss (1-1.66 wt.%) for all heating rates was observed in this zone. Whereas, the groundnut deoiled cake (GDC) and wheat straw (WS) was noted to be 2.5-4 wt.% and (1.2-2.4 wt.%) respectively. In the second stage, thermal decomposition of hemicellulose (200 °C - 350 °C) and cellulose (230 °C - 500 °C) occurred. This stage is considered as an active pyrolysis region that attributes to a maximum mass loss of the samples (*Mesua ferrea* L.: 88.66-90.57 wt.%, GDC: 47-57.5 wt.%, WS: 60.8-67.09 wt.%). As the temperature increased in the active pyrolysis zone, higher molecular weight fractions were fragmented to form low molecular weight compounds [179]. Further in this zone, the decomposition of all three biochemical constituents (hemicellulose, cellulose, and lignin) occurred via an endothermic cracking reaction. In the char formation zone, the rate of degradation of lignin was relatively slow. This can be attributed to hydroxyl groups associated with phenolic compounds. The stability of these compounds is usually high [184]. Heating rate of the sample was increased from 10 - 30 °C min^{-1}. It was observed from Fig. 13 that thermal decomposition behaviour of biomass samples remained similar. There was a slight shift in the temperature range at which biomass compounds degraded. A recent study on pyrolysis of Palm Fronds (PF), Olive leaves (OL), and wheat straw (WS), indicates that active pyrolysis occurs at 123–568 °C for PF, 121–560 °C for OL, and 114–525 °Cfor WS [185].

From the DTG graph, it was evident that biomass degradation occurred in three stages corresponding to degradation of hemicellulose (200 °C - 350 °C), cellulose (350 °C - 550 °C), and lignin (>550 °C). A negative sloped peak with shoulders at different temperatures indicated degradation of these compounds via depolymerization reaction [171]. According to literature, cellulose degradation usually follows two mechanisms. The first one is the depolymerization reaction in which carbon dioxide and carbon monoxide are released in lesser fractions. The second mechanism occurs when lighter fractions combine to form higher molecular fractions at relatively higher temperatures. Also, bio-oil formed at this temperature has many organic compounds [186]. After 500 °C, the DTG graph was almost linear, suggesting that lignin degradation was slow. Nevertheless, as seen from Fig. 14, when the heating rate of biomass varied from 10-30 °C min^{-1}, there was an increase in maximum degradation rate and a slight shift in the DTG peaks. Such change is mainly associated with an influence of heat and mass transfer at different heating rates [171]. Conversely, higher heating rates led to slower reactions and shifted the DTG profiles to higher temperatures, as the internal temperature failed to reach the necessary decomposition threshold[187]. After pyrolysis, the amount of residual char also exhibited slight variation depending on the heating rate. Notably, during the final heating stage (devolatilization), intense heat flux reduced the viscosity of the biomass and accelerated the generation of volatile products, a behaviour observed in various biofuels [22].

In the reactive stage, two peaks correspond to the decomposition of hemicellulose and cellulose, while lignin decomposition did not produce a distinct peak, as El-Sayed SA et al. (2024) . The first peak resulted from removing the moisture and light volatile compounds during the initial stage. Comparing the peaks of hemicellulose and cellulose across all samples revealed distinct shapes and positions, suggesting that the thermal degradation rate is influenced by the biomass's distribution of organic and inorganic compounds [185].

In contrast, plastic has shown a higher initial stability and the three zones occurred in the temperature ranges of 30–375 °C; 375–600 °C; 600–900 °C. The plastic degradation occurs due to additive fillers, diethylene glycol, and terephthalate monomers [174]. The weight loss for PET plastic was infinitesimal ie., 0.2-0.8 wt% in temperature range of 30-375 °C. However, active pyrolysis zone of PET plastic occurred at 375-600 °C with a significant degradation of 78.8, 71.6, 83.8 wt% for the above specified heating rates.

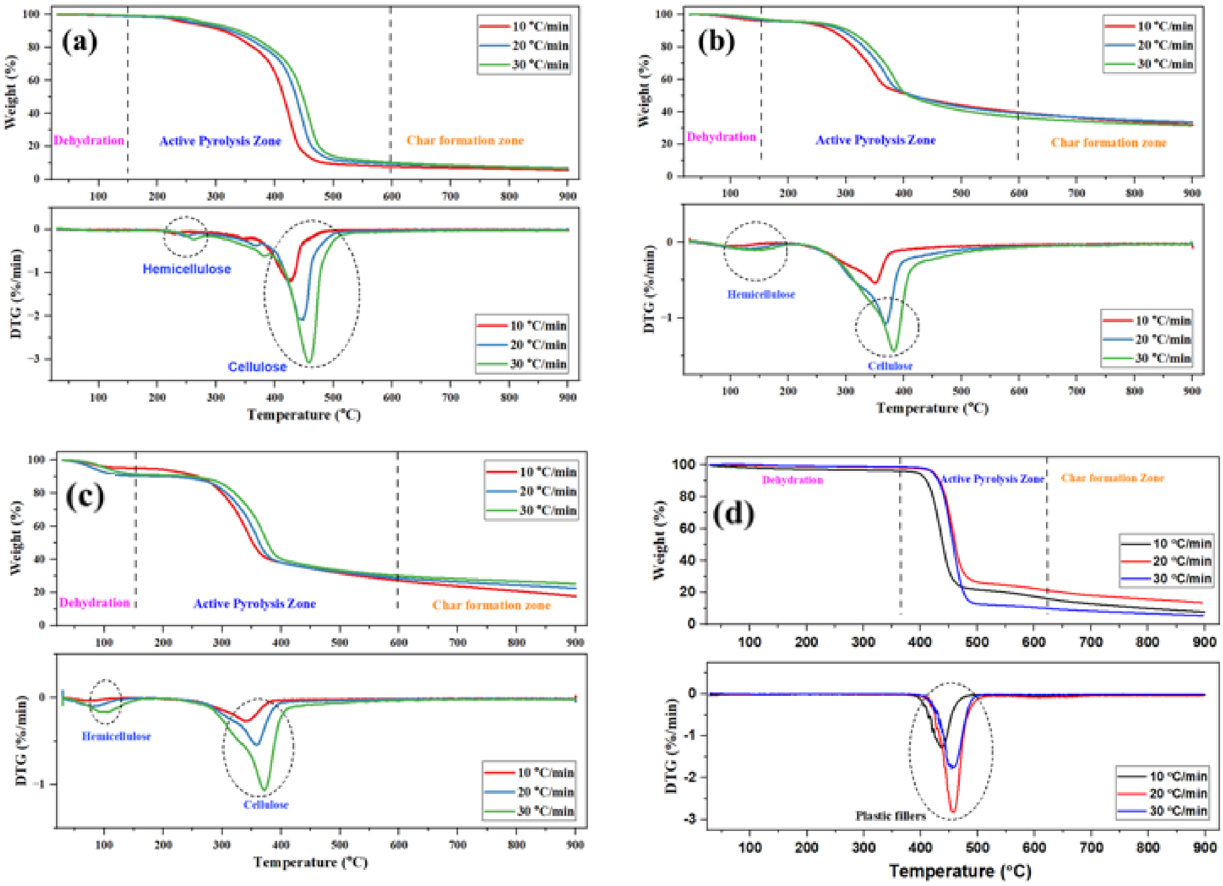

Figure 13. TG-DTG of (a) Nahar seed (b)GDC (c) Wheat straw (d) PET plastic

3.3.3.2 Co-feedstocks

However, the addition of the PET to the biomass feedstock facilitated an increase of degradation of the mixture in the active pyrolysis zone (150–600 °C) as observed in Fig. 14. For an instance, the maximum weight loss of GDC: PET mixtures in the active pyrolysis zone was noted to be 60-62 wt%. The primary constituents of the co-pyrolysis mixture of the biomass and PET, hemicellulose, cellulose, lignin, diethylene glycol, and terephthalate, undergo decomposition in the presence of heat to evolve numerous volatile species. In the presence of a continual source of heat energy, heavier molecular weight compounds fragment into smaller molecular weight components in the second zone [184]. Further, the DTG shift for the co-pyrolysis mixture (GDC: PET) was found to be 420, 435, and 440 °C. A similar trend was observed for *Mesua ferrea* L.: PET (409.08–433.51 °C) and wheat straw: PET (437.67–465.64 °C).

A likewise trend was observed in a recent study on *Samanea saman* seeds and PET plastic, where the DTG peak shifted from 165–195 °C as the heating rate varied from 10–50 °C min^{-1} [186]. Similar observations in the DTG curves were found in [16,182]. The behavior was accompanied by faster heating rates and a less efficient mass transfer among the particles. As the heating rate increases, the peak temperatures rise, indicating that the feedstock has reached the required degradation temperature in lesser time [188]. According to Mohanty et al. (2020), such a trend demonstrated that the overall reaction pathway was unaltered by the rate of heating [189]. The degradation of biomass happens in numerous stages at lower heating rates and temperatures. Insufficient heat transport to biomass particles slows decomposition. At reduced heating rates, there is a considerable transfer of heat through the biomass [190].

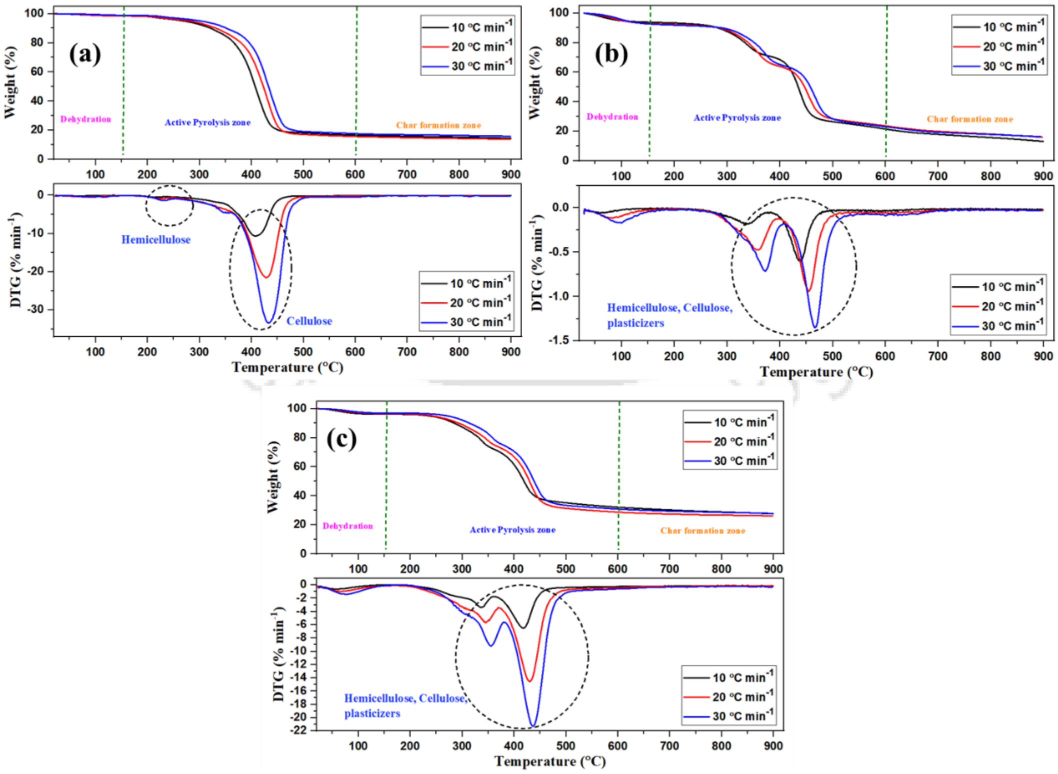

Figure 14. TGA-DTG behaviour of co-feedstocks (a) *Mesua ferrea L.*-PET (1:1) (b) WS-PET (1:1) (c) GDC-PET (1:1)

3.4 Estimation of kinetic parameters using different models

The activation energy and the pre-exponential factor, also known as the kinetic variables, were estimated using five model-free iso-conversional methods: DFM, KAS, OFW, STR, and DAEM. The kinetic parameters were calculated for the active pyrolysis zone mentioned in Section 2.2.1.4 for the different feedstocks. The kinetic analysis showed that the data fitted well in the conversion range of 0.1–0.9 for the oilseed, 0.1-0.8 for GDC, 0.1-0.8 WS and 0.2–0.9 for both the PET and the co-feedstock, respectively. Fig. 15 represents the variation of the activation energy with conversion (α). The reason for such a trend can probably be attributed to the simultaneous degradation of various components present in the feedstock [191]. The experimental data in Table 15, Table 16, Table 17, Table 18 are consistent with all of the models, as shown by a high coefficient of determination values (R^2). The R^2 values of all of the models for the different feedstocks were greater than 0.9, indicating a good fit of the data with the models.

The apparent activation energy of the *Mesua ferrea* L. oilseed, groundnut de-oiled cake (GDC) and wheat straw for the DFM was 148.55, 141.39 and 152.99 kJ mol^{-1} respectively. At the same time, the integral methods, such as KAS, OFW, STR, and DAEM were found to be 137.06, 141.24, 137.41 and 137.06 kJ mol^{-1}, respectively for oilseed. Whereas, GDC and WS resulted in E values of 127.49-131.02 kJ mol^{-1} and 175.94-178.13 kJ mol^{-1} respectively. The variation in the E values for each model is due to the simultaneous decomposition of the biomass components, paving the way for a multi-step reaction [188]. It was also observed that the activation energy increases as the reaction nears completion, i.e., an increase in the conversion value of up to 0.9. It is evident that when the conversion values increase, the apparent activation energy correspondingly increased. The emission of lighter volatiles at low temperatures (200 °C) resulted in a low activation energy value at a lower conversion ($\alpha = 0.1$). Low to high molecular weight compounds were released as the process' temperature increased, requiring more energy (often provided by an external source), which raised the activation energy. This suggested that the process was predominantly endothermic [17].

A study on the *Phoenix dactylifera* oilseeds revealed that the activation energy obtained from DFM method was 161.43 kJ mol^{-1} [192]. An analysis revealed that the average activation energies obtained from the OFW method of the *Mesua ferrea* L. de-oiled cake in two zones, of T = 130–260 °C and T = 260–380 °C, were 94 kJ mol^{-1} and 147 kJ mol^{-1}, respectively [176]. In the present investigation, however, the average activation energy determined by the same kinetic analysis in the pyrolysis zone of 150–550 °C was 131.02 kJ mol^{-1}. Consequently, the reported activation energy suggests that the thermochemical conversion of the GDC could be more energy efficient than the *Mesua ferrea* L. de-oiled cake. Another study on the determination of the kinetic parameters by the KAS and OFW methods for the Karanja seed cake agreed with the present study. The *E* values were obtained to be 110–127 kJ mol^{-1} [193].

The kinetics variable estimation for the PET plastic performed by the different methods found that the KAS method yielded the lowest activation energy with a good R^2 correlation for all of the conversion values. The detailed values are provided in Table details. The average apparent activation energy for the methods, such as the DFM, KAS, OFW, STR and DAEM are 240.83, 201.45, 202.95, 201.77 and 201.45 kJ mol^{-1}. A study on the kinetic parameter's estimation of PVC plastic waste by the OFW model provided that the plastic decomposition is a two-stage process with average activation energy values of 141 kJ mol^{-1} and 266 kJ mol^{-1} [174]. The literature also reported that the pyrolysis kinetics of the fire-retardant polyolefins cables have an activation energy of 155 and 239 kJ mol^{-1} in two distinct conversion ranges [194].

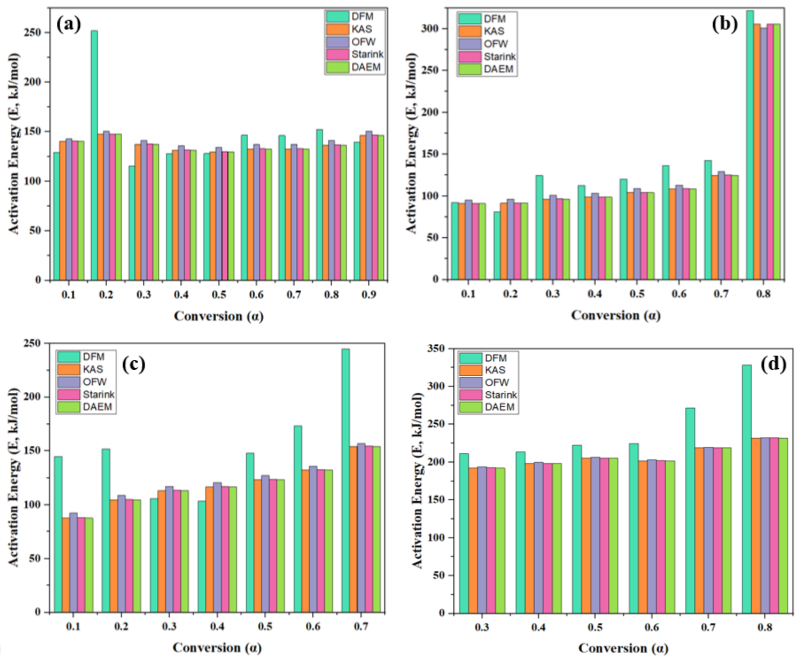

Figure 15. Kinetic parameter estimation of (a) *Mesua ferrea* L. oilseed (b) GDC (c) Wheat straw (d) PET plastic

Table 15. Activation Energy and the pre-exponential factors for *Mesua ferrea* L. oilseed

Conversion	**DFM**			**KAS**			**OFW**			**STR**			**DAEM**		
α	E kJ mol^{-1}	A min^{-1}	R^2	E kJ mol^{-1}	A min^{-1}	R^2	E kJ mol^{-1}	A min^{-1}	R^2	E kJ mol^{-1}	A min^{-1}	R^2	E kJ mol^{-1}	A min^{-1}	R^2
0.1	129.2	5.4×10^{9}	0.81	140.3	1.3×10^{11}	0.99	142.9	1.2×10^{9}	0.99	140.6	1.0×10^{11}	0.99	140.3	1.2×10^{12}	0.99
0.2	251.9	8.2×10^{8}	0.95	147.4	1.2×10^{11}	1.00	150.4	1.2×10^{9}	1.00	147.7	1.0×10^{11}	1.00	147.4	5.5×10^{11}	1.00
0.3	115.5	1.0×10^{8}	1.00	137.3	8.4×10^{9}	0.99	141.2	1.0×10^{8}	0.99	137.6	7.1×10^{9}	0.99	137.3	2.4×10^{10}	0.99
0.4	127.7	1.1×10^{8}	1.00	131.4	2.4×10^{9}	1.00	135.9	3.3×10^{7}	1.00	131.8	2.0×10^{9}	1.00	131.4	4.7×10^{9}	1.00
0.5	128.1	1.5×10^{9}	1.00	129.6	1.7×10^{9}	1.00	134.4	2.4×10^{7}	1.00	130.0	1.4×10^{9}	1.00	129.6	2.5×10^{9}	1.00
0.6	146.6	3.8×10^{10}	0.99	132.5	2.9×10^{9}	1.00	137.2	4.1×10^{7}	1.00	132.9	2.4×10^{9}	1.00	132.5	3.1×10^{9}	1.00
0.7	146.2	3.9×10^{10}	1.00	132.5	2.9×10^{9}	1.00	137.3	4.2×10^{7}	1.00	132.9	2.5×10^{9}	1.00	132.5	2.4×10^{9}	1.00
0.8	152.3	1.0×10^{11}	1.00	136.3	5.9×10^{9}	1.00	141.0	8.3×10^{7}	1.00	136.7	5.1×10^{9}	1.00	136.3	3.7×10^{9}	1.00
0.9	139.5	4.9×10^{9}	0.99	146.2	2.9×10^{10}	1.00	150.7	3.7×10^{8}	1.00	146.6	2.5×10^{9}	1.00	146.2	1.3×10^{10}	1.00
Average	**148.6**	$\mathbf{9.1 \times 10^{17}}$		**137.1**	$\mathbf{3.4 \times 10^{10}}$		**141.2**	$\mathbf{3.7 \times 10^{8}}$		**137.4**	$\mathbf{2.5 \times 10^{10}}$		**137.1**	$\mathbf{1.9 \times 10^{11}}$	

Table 16. Activation Energy and the pre-exponential factors for Groundnut deoiled cake

Conversion	**DFM**			**KAS**			**OFW**			**Starink**			**DAEM**		
α	E kJ mol^{-1}	A min^{-1}	R^2	E kJ mol^{-1}	A min^{-1}	R^2	E kJ mol^{-1}	A min^{-1}	R^2	E kJ mol^{-1}	A min^{-1}	R^2	E kJ mol^{-1}	A min^{-1}	R^2
0.1	92.3	2.2 x 10^{7}	0.99	90.9	1.7 x 10^{7}	0.99	95.3	3.1 x 10^{5}	0.99	91.2	1.4 x 10^{7}	0.99	90.9	1.6 x 10^{8}	0.99
0.2	80.9	1.7 x 10^{6}	0.97	91.5	1.7 x 10^{7}	0.99	96.2	3.3 x 10^{5}	0.99	91.7	1. x 10^{7}	0.99	91.5	7.4 x 10^{7}	0.99
0.3	124.5	8.6 x 10^{9}	0.99	96.2	4.0 x 10^{7}	0.99	101.0	7.8 x 10^{5}	0.99	96.5	3.4 x 10^{7}	0.99	96.2	1.1 x 10^{8}	0.99
0.4	112.4	6.7 x 10^{8}	0.99	98.5	5.6 x 10^{7}	0.99	103.4	1.1 x 10^{6}	0.99	98.8	4.8 x 10^{7}	0.99	98.5	1.0 x 10^{8}	0.99
0.5	120.1	2.9 x 10^{9}	0.99	104.1	1.6 x 10^{8}	0.99	109.1	2.8 x 10^{6}	0.99	104.5	1.4 x 10^{8}	0.99	104.2	2.3 x 10^{8}	0.99
0.6	136.5	5.6 x 10^{10}	0.99	108.3	3.4 x 10^{8}	0.99	113.1	5.7 x 10^{6}	0.99	108.7	2.9 x 10^{6}	0.99	108.4	3.7 x 10^{8}	0.99
0.7	142.5	1.0 x 10^{11}	0.99	124.8	7.2 x 10^{9}	0.99	129.0	9.7 x 10^{7}	0.99	125.1	6.0 x 10^{9}	0.99	124.8	5.9 x 10^{9}	0.99
0.8	321.9	6.8 x10^{23}	0.98	305.4	4.2 x 10^{23}	0.99	301.1	1.0 x 10^{21}	0.99	305.7	3.3 x 10^{23}	0.99	305.5	2.6 x 10^{23}	0.99
Average	**141.4**	**8.5 x 10^{22}**		**127.5**	**5.2 x 10^{23}**		**131.0**	**1.3 x 10^{20}**		**127.8**	**4.1 x 10^{22}**		**127.5**	**3.2 x 10^{22}**	

Table 17. Activation Energy and the pre-exponential factors for wheat straw

Conversion	**DFM**			**KAS**			**OFW**			**Starink**			**DAEM**		
α	E kJ mol^{-1}	A min^{-1}	R^2	E kJ mol^{-1}	A min^{-1}	R^2	E kJ mol^{-1}	A min^{-1}	R^2	E kJ mol^{-1}	A min^{-1}		E kJ mol^{-1}	A min^{-1}	R^2
0.1	144.6	1.8 x 10^{12}	0.98	87.6	8.5 x 10^{6}	0.99	92.2	1.6 x 10^{5}	0.99	87.9	7.3 x 10^{6}	0.99	87.6	8.0 x 10^{7}	0.99
0.2	151.7	3.7 x 10^{12}	0.95	104.6	3.2 x 10^{9}	0.99	108.7	4.9 x 10^{6}	0.99	104.9	2.7 x 10^{8}	0.99	104.6	1.4 x 10^{9}	0.99
0.3	105.5	3.2 x 10^{9}	0.90	113.0	1.6 x 10^{10}	0.99	116.9	2.2 x 10^{8}	0.99	113.3	1.3 x 10^{9}	0.99	113.0	4.5 x 10^{9}	0.99
0.4	103.3	1.6 x 10^{8}	0.93	116.6	2.9 x 10^{10}	0.99	120.6	3.9 x 10^{7}	0.99	116.9	2.4 x 10^{9}	0.99	116.6	5.7 x 10^{9}	0.99
0.5	147.9	1.0 x 10^{12}	0.95	123.4	1.0 x 10^{10}	0.98	127.2	1.3 x 10^{9}	0.99	123.6	8.8 x 10^{9}	0.98	123.3	1.5 x 10^{10}	0.98
0.6	173.2	1.1 x 10^{14}	0.99	132.3	5.7 x 10^{11}	0.98	135.8	6.4 x 10^{8}	0.98	132.6	4.7 x 10^{10}	0.98	132.3	6.2 x 10^{11}	0.98
0.7	244.8	5.3 x 10^{19}	0.90	154.3	3.7 x 10^{12}	0.96	156.8	3.2 x 10^{10}	0.96	154.6	3.1 x 10^{12}	0.96	154.3	3.1 x 10^{12}	0.96
Average	**152.9**	**7.5 x 10^{18}**		**118.8**	**5.4 x 10^{11}**		**122.6**	**4.7 x 10^{9}**		**119.1**	**4.5 x 10^{11}**		**118.8**	**4.5 x 10^{11}**	

Table 18. Activation Energy and the pre-exponential factors for PET plastic

Conversion	**DFM**			**KAS**			**OFW**			**Starink**			**DAEM**		
α	E kJ mol^{-1}	A min^{-1}	R^2	E kJ mol^{-1}	A min^{-1}	R^2	E kJ mol^{-1}	A min^{-1}	R^2	E kJ mol^{-1}	A min^{-1}		E kJ mol^{-1}	A min^{-1}	R^2
0.3	211.1	1.3×10^{15}	0.96	192.2	3.1×10^{13}	0.93	194.0	2.2×10^{11}	0.94	192.5	2.6×10^{13}	0.93	192.2	8.4×10^{13}	0.93
0.4	213.4	2.0×10^{15}	0.97	198.1	1.0×10^{14}	0.91	199.8	6.7×10^{11}	0.92	198.4	8.2×10^{13}	0.91	198.1	1.9×10^{14}	0.91
0.5	222.5	9.1×10^{15}	0.97	205.1	3.6×10^{14}	0.94	206.4	2.3×10^{12}	0.95	205.4	2.9×10^{14}	0.94	205.1	4.9×10^{14}	0.94
0.6	224.5	1.1×10^{18}	0.93	201.5	2.1×10^{14}	0.92	203.2	1.4×10^{13}	0.93	201.9	1.7×10^{14}	0.92	201.5	2.2×10^{14}	0.92
0.7	271.7	2.5×10^{19}	0.94	218.9	4.1×10^{15}	0.96	219.7	2.3×10^{13}	0.96	219.2	3.3×10^{15}	0.96	218.9	3.3×10^{15}	0.96
0.8	328.2	1.5×10^{23}	0.76	231.6	3.2×10^{16}	0.92	231.9	1.7×10^{14}	0.93	231.9	2.6×10^{16}	0.92	231.6	3.0×10^{15}	0.93
Average	**240.8**	**1.2×10^{21}**		**201.5**	**8.0×10^{14}**		**202.9**	**4.7×10^{12}**		**201.8**	**6.5×10^{14}**		**201.5**	**7.3×10^{14}**	

Lastly, the kinetic parameters estimation of the co-pyrolysis of oilseed and PET plastic provided the activation energy and the pre-exponential factor, the values obtained for DFM method was around 185.29 kJ mol^{-1}. While the values ranged from156.24–159.30 kJ mol^{-1} for the KAS, OFW, STR and DAEM methods. The detailed values are provided in Table 19,20, and 21. As presented in Fig. 16, the obtained *E* and *A* values of co-feedstocks were higher than those of the biomass alone and lower than the PET plastic itself. The addition of the biomass waste to the plastic significantly reduced the activation energy of the plastic waste. The activation energy increased with the increase in the conversion stating a possible interaction of both feedstocks. The obtained results are well in agreement with some of the literature available [179].

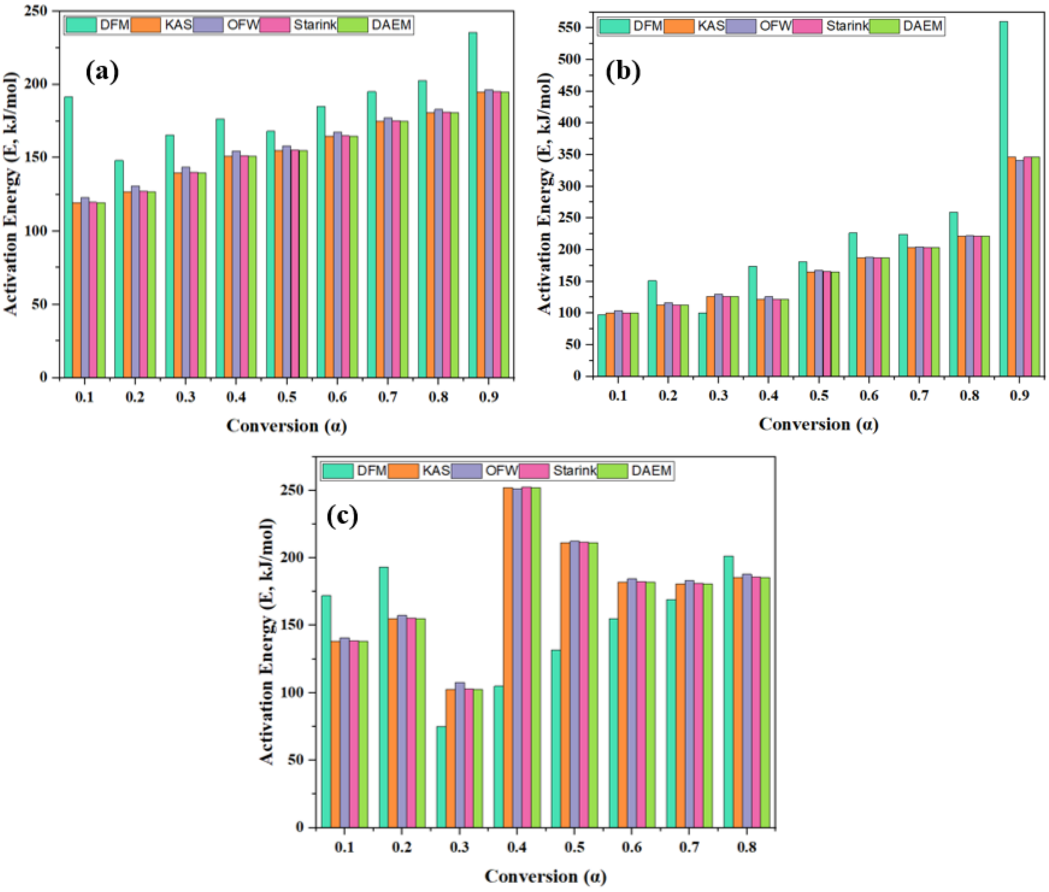

Figure 16. Kinetic parameter estimation of (a) Nahar-PET (1:1) (b) GDC-PET (1:1) (c) wheat straw-PET (1:1)

The iso-conversional methods such as Friedman, the KAS, the OFW, Starink, and the simplified DAEM are used to calculate the pre-exponential factors. The average values of *A* obtained for the DAEM method, were 1.99×10^{11}, 5.29×10^{24}, 1.53×10^{13}, for the biomass, co-feed and plastic, respectively. The pre-exponential factor is thought to be a temperature-dependent variable, in accordance with the hypothesis of the molecular collision of the reactants. According to the findings shown in Table 14-21, the *A* values ranged from 10^7 to 10^{25}. This suggested that the different feedstocks have a complex composition that includes a number of different molecules ranging from a lower to a higher mass [70]. It is believed that the majority of the surface reactions occur at lower exponential values ($A > 10^9$). Hemicellulose, cellulose, and diethylene glycol typically decompose at high *A* values (about 10^9 to 10^{12}) and at a lesser conversion ($\alpha < 0.5$), while lignin and terephthalate decay at greater *A* values ($\alpha > 10^{14}$) and at a higher conversion ($\alpha > 0.5$). The increased pre-exponential factor indicated more frequent molecular collisions, while the simultaneously higher apparent activation energy suggested a more complex reaction pathway, consistent with the kinetic compensation effect [182].

Table 19. Activation Energy and the pre-exponential factors for *Mesua ferrea* L.: PET plastic (1:1)

Conversion	**DFM**			**KAS**			**OFW**			**Starink**			**DAEM**		
α	E kJ mol^{-1}	A min^{-1}	R^2	E kJ mol^{-1}	A min^{-1}	R^2	E kJ mol^{-1}	A min^{-1}	R^2	E kJ mol^{-1}	A min^{-1}	R^2	E kJ mol^{-1}	A min^{-1}	R^2
0.1	191.5	1.2 x 10^{15}	0.99	119.2	1.3 x 10^{9}	0.96	123.0	1.7 x 10^{7}	0.96	119.5	1.1 x 10^{9}	0.96	119.2	1.2 x 10^{10}	0.96
0.2	148.0	7.5 x 10^{10}	1.00	126.8	2.4 x 10^{9}	0.98	130.8	3.2 x 10^{7}	0.98	127.1	2.1 x 10^{9}	0.98	126.8	1.1 x 10^{10}	0.98
0.3	165.5	1.7 x 10^{12}	1.00	139.7	2.2 x 10^{10}	1.00	143.4	2.4 x 10^{8}	1.00	140.1	1.8 x 10^{10}	1.00	139.7	5.7 x 10^{10}	1.00
0.4	176.5	1.3 x 10^{13}	1.00	151.2	1.6 x 10^{11}	1.00	154.5	1.6 x 10^{9}	1.00	151.5	1.3 x 10^{11}	1.00	151.2	3.0 x 10^{11}	1.00
0.5	168.1	2.9 x 10^{12}	0.99	154.9	3.0 x 10^{11}	1.00	158.1	2.9 x 10^{9}	1.00	155.2	2.5 x 10^{11}	1.00	154.9	4.3 x 10^{11}	1.00
0.6	185.1	5.2 x 10^{13}	1.00	164.6	1.7 x 10^{12}	1.00	167.4	1.5 x 10^{10}	1.00	164.9	1.4 x 10^{12}	1.00	164.6	1.7 x 10^{12}	1.00
0.7	195.0	2.7 x 10^{14}	1.00	174.7	9.6 x 10^{12}	1.00	177.2	7.7 x 10^{10}	1.00	175.0	7.9 x 10^{12}	1.00	174.7	7.7 x 10^{12}	1.00
0.8	202.7	9.5 x 10^{14}	0.99	180.5	2.5 x 10^{13}	1.00	182.8	1.9 x 10^{11}	1.00	180.8	2.1 x 10^{13}	1.00	180.5	1.5 x 10^{13}	1.00
0.9	235.2	1.7 x 10^{17}	0.99	194.6	2.7 x 10^{14}	1.00	196.4	1.8 x 10^{12}	1.00	195.0	2.2 x 10^{14}	1.00	194.6	1.1 x 10^{14}	1.00
Average	**185.3**	**2.0 x 10^{16}**		**156.2**	**3.4 x 10^{13}**		**159.3**	**2.4 x 10^{11}**		**156.6**	**2.8 x 10^{13}**		**156.2**	**1.5 x 10^{13}**	

Table 20. Activation Energy and the pre-exponential factors for GDC: PET plastic (1:1)

Conversion	**DFM**			**KAS**			**OFW**			**Starink**			**DAEM**		
α	E kJ mol^{-1}	A min^{-1}	R^2	E kJ mol^{-1}	A min^{-1}	R^2	E kJ mol^{-1}	A min^{-1}	R^2	E kJ mol^{-1}	A min^{-1}	R^2	E kJ mol^{-1}	A min^{-1}	R^2
0.1	97.9	4.1×10^{7}	0.98	100.3	9.8×10^{7}	0.91	104.1	1.5×10^{6}	0.93	100.2	7.9×10^{7}	0.91	100.3	9.3×10^{8}	0.91
0.2	151.1	8.5×10^{11}	1.00	112.3	6.8×10^{8}	0.97	116.4	9.8×10^{6}	0.97	112.6	5.8×10^{8}	0.97	112.3	2.9×10^{9}	0.97
0.3	100.0	2.0×10^{7}	1.00	125.9	7.5×10^{9}	1.00	129.7	9.2×10^{7}	1.00	126.2	6.3×10^{9}	1.00	125.9	2.0×10^{10}	1.00
0.4	174.1	6.6×10^{12}	1.00	121.5	1.2×10^{9}	1.00	125.9	1.8×10^{7}	1.00	121.8	1.1×10^{9}	1.00	121.5	2.4×10^{9}	0.99
0.5	181.0	2.2×10^{13}	0.99	165.0	2.5×10^{12}	1.00	167.7	2.1×10^{10}	1.00	165.4	2.1×10^{12}	1.00	165.0	3.6×10^{12}	0.99
0.6	226.7	5.7×10^{16}	1.00	187.0	9.9×10^{13}	0.99	188.7	6.8×10^{11}	0.99	187.3	8.1×10^{13}	0.99	187.0	1.1×10^{14}	0.99
0.7	224.2	3.3×10^{16}	1.00	203.3	1.5×10^{15}	1.00	204.4	8.8×10^{12}	1.00	203.6	1.2×10^{15}	1.00	203.3	1.2×10^{15}	0.99
0.8	259.6	9.9×10^{18}	1.00	221.5	2.9×10^{16}	1.00	221.9	1.5×10^{14}	1.00	221.8	2.3×10^{16}	1.00	221.5	1.8×10^{16}	1.00
0.9	560.5	9.6×10^{39}	0.99	346.0	2.2×10^{25}	1.00	340.5	5.1×10^{22}	1.00	346.2	1.8×10^{25}	1.00	346.0	9.6×10^{24}	1.00
Average	**219.4**	**1.1×10^{39}**		**175.9**	**2.5×10^{24}**		**177.7**	**5.7×10^{21}**		**176.1**	**1.9×10^{24}**		**175.8**	**1.1×10^{24}**	

Table 21. Activation Energy and the pre-exponential factors for wheat straw: PET plastic (1:1)

Conversion	**DFM**			**KAS**			**OFW**			**Starink**			**DAEM**		
α	E kJ mol^{-1}	A min^{-1}	R^2	E kJ mol^{-1}	A min^{-1}	R^2	E kJ mol^{-1}	A min^{-1}	R^2	E kJ mol^{-1}	A min^{-1}	R^2	E kJ mol^{-1}	A min^{-1}	R^2
0.1	171.9	7.8×10^{13}	0.93	138.2	1.4×10^{11}	0.98	140.8	1.2×10^{9}	0.99	138.5	1.1×10^{11}	0.98	138.2	1.3×10^{12}	0.91
0.2	193.2	1.9×10^{15}	0.86	155.1	2.2×10^{12}	0.89	157.4	1.8×10^{10}	0.90	155.4	1.9×10^{12}	0.89	155.1	9.9×10^{12}	0.97
0.3	74.8	1.1×10^{5}	1.00	102.3	4.4×10^{7}	1.00	107.6	8.8×10^{5}	1.00	102.7	3.8×10^{7}	1.00	102.3	1.0×10^{8}	1.00
0.4	104.8	1.4×10^{8}	0.89	252.2	3.2×10^{13}	0.90	251.1	1.3×10^{16}	0.91	252.5	2.5×10^{18}	0.90	252.2	4.8×10^{18}	0.99
0.5	131.8	1.5×10^{9}	0.97	211.4	2.3×10^{15}	0.92	212.3	$1..3 \times 10^{13}$	0.93	211.7	1.9×10^{15}	0.92	211.4	3.3×10^{15}	0.99
0.6	154.9	8.7×10^{10}	1.00	182.1	1.1×10^{13}	0.96	184.5	8.7×10^{10}	0.97	182.4	9.1×10^{12}	0.96	182.1	1.2×10^{13}	0.99
0.7	168.9	8.9×10^{11}	1.00	180.8	8.0×10^{12}	0.98	183.4	6.6×10^{10}	0.98	181.1	6.6×10^{12}	0.98	180.8	6.7×10^{12}	0.99
0.8	201.2	1.1×10^{14}	0.97	185.3	1.5×10^{13}	0.98	187.9	1.2×10^{11}	0.98	185.7	1.2×10^{13}	0.98	185.3	9.2×10^{12}	1.00
Average	**150.2**	**2.6×10^{14}**		**175.9**	**4.0×10^{17}**		**178.1**	**1.6×10^{15}**		**176.3**	**3.2×10^{17}**		**175.9**	**6.0×10^{17}**	

3.4 Conclusion

The physicochemical characterization and thermal analysis of the *Mesua ferrea* L. oilseed, groundnut de-oiled cake, wheat straw and PET plastic confirms the bioenergy potential of feedstocks to produce biofuel. The apparent activation energy and pre-exponential factor was determined by different iso-conversional methods which include the DFM, KAS, OFW, STR and DAEM methods. The useful functional groups present in the material were confirmed by the FTIR analysis. Among all of the methods, the DAEM method provided the lowest activation energy (for the oilseed, E= 127.9 kJ mol^{-1}; PET, E = 201.5 kJ mol^{-1}; and co-pyrolysis, E = 156. 2 kJ mol^{-1}). From the analysis, it is can be seen that blending of *Mesua ferrea* L. oilseed with plastic can significantly reduce the activation energy to design the pyrolysis reactor in a effective way.

Chapter 4.

Thermal and co-pyrolysis of Biomass and Plastic for the production of different products such as bio-oil

4.1 Background

Biomass, a renewable resource, is generally processed using different chemical and biological processes, creating other products based on the operating parameters of the process. The pyrolysis process typically involves the conversion of biomass to high-value products. The pyrolytic oil comprises substantial amounts of oxygenated compounds and water, making it unsuitable for immediate use as a biofuel. Moreover, the inherent instability of bio-oil and the potential for changes in its characteristics during prolonged storage emphasize the need for upgrading. Upgrading aims to enhance stability, increase calorific value, and improve fuel properties [195].

Mesua ferrea L., commonly referred to as Nahar, is widely distributed over the Uttar Pradesh, and Northeastern India. Moreover, it is found in Sri Lanka, Thailand, Myanmar, the Philippines, and Malaysia [182]. The oil extracted from these seeds has the potential for blending at around 20-30 wt.% with existing fossil-derived fuels. While there are a few existing studies that delve into the applications of such non-edible oilseeds, the oil obtained from it is primarily utilized in producing polymers, polyols, and medicines [196]. However, bio-oil production from this non-edible oilseed has great potential through pyrolysis. The current study emphasizes the need to understand the pyrolysate composition from fast pyrolysis of this seed and the typical reactions involved in the production of oil components.

The pyrolytic liquid obtained from biomass generally has a high calorific value indicating a significant energy potential to replace fossil-based fuels. Nevertheless, undesirable properties such as high viscosity and high oxygen content limit the application of these oils in the transportation sector. The pyrolysis liquid derived from biomass usually contains compounds such as hydrocarbons, long-chain fatty acids, esters, amides/nitriles, alcohols, ketones and many others at varying elemental composition [196]. For example, a recent study on the pyrolysis of municipal sludge digestate produced bio-oil at 32.30 wt.% yield with 6.15% nitrogen and higher heating value (HHV) of 29.53 MJ kg^{-1} [197]. Moreover, a recent review on the pyrolysis of protein-rich feedstock concluded that nitrogen compounds in the bio-oil are due to proteins present in the sample [198].

Investigations on employing plastic as a co-feedstock to enhance the quality of biomass pyrolysis oil are reported widely. Such research aims to produce bio-oils for direct use as fuels. Co-pyrolysis process is an efficient technique for converting different types of waste into diverse valuable products. Adding plastic feedstock to biomass pyrolysis increases the stability of the bio-oil by reducing the water or aqueous phase. It also aids in the increase of the H/C (mol/mol) of the pyrolytic oil by reducing the oxygenated compounds. Moreover, compared to catalytic pyrolysis, co-pyrolysis is a better technique as it reduces the production cost, as catalysts tend to escalate the overall operational expenses in the pyrolysis process [199]. The synergy between different types of plastics and biomass yields bio-oils of varying quantities and properties. As the precise interaction mechanisms remain unknown, further in-depth studies are required.

In India, the packaging sector generates the largest amount of plastic waste, accounting for approximately 42% of total consumption. Following closely is the consumer products, which utilizes around 24% of plastic on average. Additionally, about 100 million tonnes of waste, including household waste, are discarded annually. Consequently, such feedstock not only acts as a waste but also provides an opportunity to produce as a valuable resource for energy recovery purposes. Among the available plastic materials, polyethylene terephthalate is considered 3rd most used plastic, accounting for 35% of global plastic consumption. PET is typically used for packaging and in garments and food containers [200]. Recycling used plastics mainly aids the environment by decreasing the need for virgin raw materials. This also ensures that the risk of landfills is reduced. Each year, millions of tonnes of PET materials are collected worldwide. These recyclable PET materials can be processed and reintroduced to the market. At the same time, non-recyclable plastics end up in landfills, which can take up to 500 years to degrade and potentially release contaminants into the soil and water [200].

Recently, a surge in the research investigations on co-pyrolysis of mixed feedstocks such as lignocellulosic biomass with waste plastics is observed, indicating the potential for producing aromatics and hydrocarbons. A study on the co-pyrolysis of Thar lignite coal and plastic revealed that the oil yield for 1:1 feedstock ratio (23 wt.%) was lesser than individual plastic pyrolysis (67.0 wt.%) [201]. An increase in aromatic compounds was noted with an increase in plastic in the feedstock ratio. Another study on co-pyrolysis of waste newspaper and HDPE showed that bio-oil contained a significant proportion of alcohols and hydrocarbons (85%) [202]. Similar results were obtained in the co-pyrolysis of Eucalyptus spp. biomass and PET plastic in a fixed bed reactor at lower heating rates (1-5 °C min^{-1}). This study found that an increase in the plastic (0 to 25 wt.%) in the feedstock ratio at higher temperatures decreased the bio-oil yield by 20 wt.% [203]. Another recent study on co-pyrolysis of wheat straw and PET indicated that the increase in blend ratio from 20 to 80 increases the oil yield from 41 to 50 wt.% [204]. Although, many literature studies indicate that addition of plastic increases the bio-oil yield, there are also studies reporting that higher amount of biomass in the mixture can enhance the bio-oil yield. For example, co-pyrolysis of Fiscus with PET plastic showed that the oil yield increased from 41.4 to 56 wt.% with increase in ratio to 4:1 (Biomass: PET) [205]. However, there are many challenges to convert the mixtures into biofuels and added value chemicals. These limitations necessitate further comprehensive studies for successful integration into various industries.

The current study investigates the co-pyrolysis of non-edible oil seed (*Mesua ferrea* L.) and PET plastic at different feedstock ratios. As compared to different species of lignocellulosic biomass, *Mesua ferrea* L. being a unique variety of oilseed, produces different fatty acids that can produce hydrocarbons. Moreover, Pyrolysis of PET plastic can be used as an alternate to recycling process to produce variety of chemicals such as benzoic acid, terephthalic acid, vinyl benzoate and many others. The primary aim is to study the composition of the condensable pyrolytic vapour (which is usually the oil fraction) by analytical curie-point pyrolyzer with a gas chromatograph/mass spectrometer (Py-GC/MS). Further, the effects of temperature on pyrolysis of oil seed, and the mixtures of oil seed with PET (Biomass: PET (B:P) of 1:1, 2:1, and 1:2 w/w) on the yield and quality of the pyrolytic-oil are studied, and the optimal temperature is evaluated. The main reason for comparing the pyrolysis in a Curie point Py-GC/MS versus a fixed bed reactor is to unravel the condensable vapor composition at widely different pyrolysis time scales. Pyrolysis timescale is of the order of milliseconds in a Curie point pyrolyzer, while it is of the order of few minutes in the fixed bed reactor [80]. Therefore, the pyrolysis vapors from the fixed bed reactor are expected to undergo secondary cracking reactions due to the longer residence time. Moreover, the cracking reactions occur in a reaction-controlled regime in a Curie point pyrolysis system, while significant mass and heat transfer limitations might become important in a longer residence time fixed bed reactor. Therefore, it is interesting to compare the product distribution, especially in the oil fraction, from both the type of pyrolysis reactors.

4.2 Experimental methodology

The pyrolysis of individual and co-feed was done in a fixed-bed reactor as described in section 2.2.2.2. The characterization of pyrolytic products (bio-oil, bio-char and non-condensable gases) were analyzed using GC/MS, NMR, CHNS(O), and calorific value as described in 2.2.2.3 and 2.2.5.2. A pictorial representation of the process is provided in Fig. 17. In a typical process as represented in Fig. 17, the biomass and plastic are fed to both curie-point analyser and fixed-bed reactor in a quantity of 800 ± 20 µg and 75 g respectively. The pyrolytic vapours from a curie-point analyzer and the condensed bio-oil from fixed-bed reactor are analyzed using GC/MS.

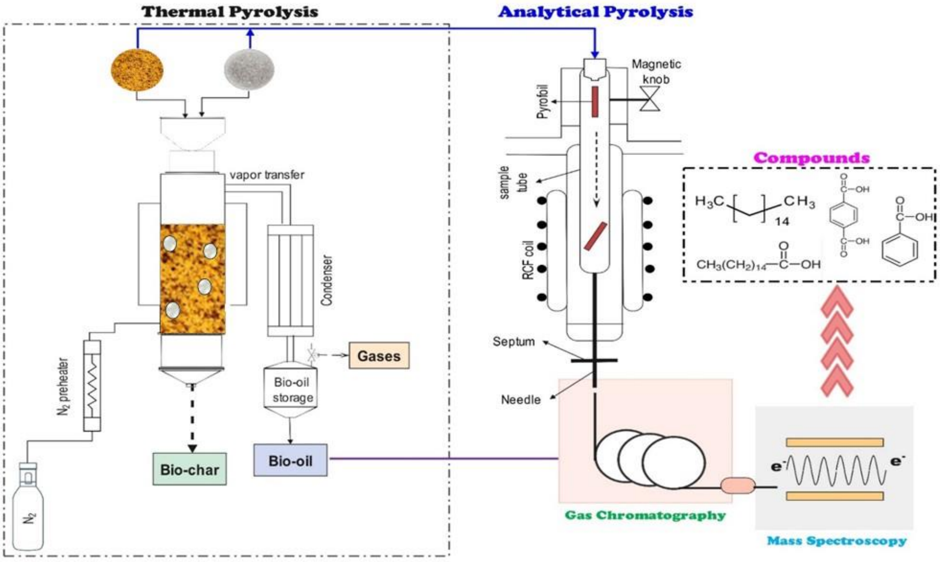

Figure 17. Analytical and applied pyrolysis of *Mesua ferrea* L. oilseed and PET plastic

4.3 Results and Discussions

4.3.1 Analytical Fast Pyrolysis of oilseed, plastic and co-feed

The classification of the compounds obtained from the Py-GC/MS is based on the functional groups present in the pyrolysate vapor. The classification includes aliphatic acids, aromatic acids, esters, alkane, alkene and other oxygenates (ketones, alcohols). The relative peak area% of the various functional groups is given in Fig. 18. The detailed list of compounds is given in

Table 22-26. The vapour composition of biomass revealed that the selectivity to aliphatic acids was higher followed by alkanes and alkenes. The aliphatic acids include octanoic acid ($C_8H_{16}O_2$) (2.4%); nonanoic acid ($C_9H_{18}O_2$) (1.0%); n-hexadecanoic acid ($C_{16}H_{32}O_2$) (28.3%); 9-octadecenoic acid ($C_{18}H_{34}O_2$) (33.4%); octadecanoic acid ($C_{18}H_{36}O_2$) (25.0%). The origin of these compounds can be attributed to their natural occurrence in plant-based materials due to the lipid metabolism or oxidation of alkane or alkene. Following the short-chain fatty acids, hydrocarbons (6.3%) and aldehydes (1.2%) were the other compounds. The thermal degradation behavior of triglycerides is very complex and involves numerous reactions. The conversion of fatty acids to short-chain hydrocarbons occurs by free-radical or carbonium ion pathways [206].

Table 22. Py-GC/MS analysis of *Mesua ferrea* L. oilseed at 590 °C

Compounds	Peak area (%)
3-Buten-1-ol, 2-methyl-	1.95
Nonanal	1.56
Octanoic acid	1.72
Nonanoic acid	1.39
Pentadecane	1.23
8-Heptadecene	1.32
Heptadecane	1.24
n-Hexadecanoic acid	26.99
Octadecanoic acid, 2-propenyl ester	1.83
Oleic Acid	23.07
Oleic Acid	6.79
Octadecanoic acid	17.59
9,12-Octadecadienoic acid (Z,Z)-	2.24
Glycidyl palmitate	3.25
9-Octadecenoic acid (Z)-, oxiranylmethyl ester	3.83
Myristic acid glycidyl ester	2.46
Squalene	1.55

The lipid pyrolysis products are derived from the humin or humic compounds usually present in waxy materials of wood barks [206]. The pyrolysis of triglycerides, commonly referred to as fats, results in fatty acids. Aliphatic acids also known as fatty acids are often made up of hydrophobic molecules, which means they are not readily soluble in water. It is worthwhile to note that the amounts of saturated and unsaturated aliphatic acids in this seed is significant. The production of octadecanoic acid and hexadecanoic acid, which originate from lecithin in phospholipids is significant[207]. A study reported maximum n-hexadecanoic acid (27%) from bark compost via Py-GC/MS analysis[208].

Table 23. Py-GC/MS analysis of PET plastic at 590 °C

Compound	Peak area (%)
Benzene	3.60
1,2-Propanedione, 1-Phenyl-	5.62
Benzoic Acid	26.98
Benzoic Acid, 4-Methyl-	0.65
1-Penten-3-One, 4-Methyl-1-Phenyl-	1.32
Biphenyl	2.33
4-Vinylbenzoic Acid	1.20
1,2-Ethanediol, Monobenzoate	0.79
Diethylene Glycol Dibenzoate	0.26
1,1'-Biphenyl, 4-Methyl-	0.24
2,4-Imidazolidinedione, 5-Ethyl-5-Phenyl-	3.51
Terephthalic Acid, 2-Chlorophenyl Ethyl Ester	0.32
4-Acetylbenzoic Acid	14.21
1,1'-Biphenyl, 4-Ethenyl-	0.34
1,4-Benzenedicarboxylic Acid, Monoethyl Ester	0.82
9h-Fluoren-9-One	0.30
1,4-Benzenedicarboxylic Acid, Bis(2-Hydroxyethyl) Ester	0.68
Fenbufen	1.56
Biphenyl-4-Carboxylic Acid	1.80
N-Hexadecanoic Acid	1.22
9-Octadecenoic Acid, (E)-	1.76
9-Octadecenoic Acid, (E)-	1.13
1,2-Ethanediol, Dibenzoate	10.77
Octadecanoic Acid	3.02
M-Terphenyl	1.57
3-Methylbenzoic Acid, 2,5-Dichlorophenyl Ester	0.79
P-Cyanophenyl 4'-Pentyl-4-Biphenylcarboxylate	0.35
1-Penten-3-One, 4-Methyl-1-Phenyl-, (E)-	1.16
2-Pentafluoropropionyloxy-3-Methoxybenzoic Acid	8.92
Benzamide, N,N-Diethyl-	0.69
1,2,4-Benzenetricarboxylic Acid, 3,5-Dinitro-, Trimethyl Ester	0.46
Terephthalic Acid, Di(4-Trifluoromethoxybenzyl) Ester	0.48

(1,1'-Biphenyl)-2,2'-Dicarboxaldehyde	1.15

The pyrolytic decomposition of PET plastic generally reveals the presence of mono and polyaromatic hydrocarbons. In spite of that, the PET waste in this study shows the presence of aromatic acids, aromatics and ester in higher ratio. Some of those include, benzoic acid (43%), 4-acetyl benzoic acid (16%), benzene (4.88%) and 1,2-ethanediol, dibenzoate (13%). A recent study on the Py-GC/MS of PET plastic demonstrated the presence of benzoic acid (22%) and esterified acids such as ethan-1,2-diylbenzoate (6%)[209].

Table 24. Py-GC/MS analysis of *Mesua ferrea* L. oilseed and PET plastic at B:P -1:1 feedstock ratio, 590 °C

Compound	Peak area (%)
3-Buten-1-Ol, 2-Methyl-	1.10
1-Hexene	0.64
Benzene	0.99
Benzene	2.64
1-Heptene	0.57
Heptane	0.35
1-Octene	0.37
Octane	0.57
Nonanal	0.59
1,2-Propanedione, 1-Phenyl-	3.59
Benzoic Acid, Ethyl Ester	0.44
1-Dodecene	3.40
Benzoic Acid	3.35
Benzoic Acid, 4-Methyl-	0.51
Biphenyl	1.26
1-Tridecene	0.69
1,2-Ethanediol, Monobenzoate	0.96
Cyclohexadecane	0.34
Hexadecane	0.45
2,4-Imidazolidinedione, 5-Ethyl-5-Phenyl-	2.15
1-Hexadecanol	0.42
4-Acetylbenzoic Acid	9.26
1,4-Benzenedicarboxylic Acid, Monoethyl Ester	0.89
Heptadecane	0.42
1,4-Benzenedicarboxylic Acid, Bis(2-Hydroxyethyl) Ester	1.10
4-Phenylbenzhydrazide	0.35
Biphenyl-4-Carboxylic Acid	0.73
N-Hexadecanoic Acid	15.20

Octadecanoic Acid, 2-Propenyl Ester	0.41
9-Octadecenoic Acid, (E)-	12.42
9-Octadecenoic Acid, (E)-	4.69
1,2-Ethanediol, Dibenzoate	7.86
Octadecanoic Acid	12.69
1,1':4',1''-Terphenyl	1.18
9,12-Octadecadienoic Acid (Z,Z)-	0.92
14-Pregnane	0.92
Octadecanoic Acid, 2-Propenyl Ester	0.45
Z-5-Methyl-6-Heneicosen-11-One	1.22
Eicosanoic Acid	0.55
Ethanone, 1-(3,4-Dimethylphenyl)-	0.56
1-Penten-3-One, 4-Methyl-1-Phenyl-, (E)-	0.70
Oleoyl Chloride	0.46
Octadecanoic Acid, 2,3-Dihydroxypropyl Ester	0.72
Benzamide, N,N-Diethyl-	0.92

The pyrolysate composition of co-feed (1:1, 2:1, 1:2 w/w) revealed that the vapor contains a mixture of aliphatic acids and aromatic acids. The major compounds observed in the vapor was n-hexadecanoic acid of 15% for 1:1 w/w; 9-octadecenoic acid of 51% for 2:1 w/w; benzoic acid of 18% for 1:2 w/w. The addition of PET to the biomass decreased the formation of aliphatic acids due to the presence of carboxylic acids. A recent study on rape stalk with PET plastic (1:1) ratio indicated that acids content increased in the pyrolysis of co-feed (32%) compared to rape stalk (20) and PET (21%). This is due to the presence of oxygenated compounds in PET plastic[177]. Formation of shorter-chain hydrocarbons indicates the removal of carbon dioxide of the fatty acid. This is essentially known as decarboxylation reaction and an alkyl radical is formed as one of the products of this reaction. The formed alkyl radical reacts with molecular oxygen to produce a peroxy radical. Further, initiation of free radical chain reaction leads to the formation of short-chain hydrocarbons[210]. The biomass lipids undergo cracking to produce aliphatic hydrocarbons, long-chain aliphatic acids, and esters. In plastic pyrolysis, the dominant reactions include isomerization and aromatization, forming aliphatic and aromatic compounds [177].

Table 25. Py-GC/MS analysis of Bio-oil obtained from co-pyrolysis of *Mesua ferrea* L. oilseed and PET plastic at B:P -2:1 feedstock ratio, 590 °C

Compounds	Peak area (%)
2-Butene, (E)-	0.40
Acetic Acid, Chloro-, Octyl Ester	0.47
1,3-Pentadiene, (Z)-	0.79
Oxetane, 3-(1-Methylethyl)-	0.50
1-Hexene	0.42
1-Heptene	0.61
Heptane	0.27
1-Octene	0.24
2,6-Dimethylhepta-1,5-Diene	0.56
1-Nonene	0.23
Cyclopropane, 1,1-Dimethyl-2-(2-Methyl-1-Propenyl)-	0.34
2,6-Octadiene, 2,7-Dimethyl-	0.60
1-Undecene	0.38
3-Undecene, (E)-	0.37
Z-1,6-Undecadiene	0.42
Octanoic Acid	1.72
Benzoic Acid	1.28
3-Dodecen-1-Ol, Acetate, (E)-	0.46
1-Tridecene	0.23
1-Tetradecene	0.48
1-Pentadecene	0.27
Pentadecane	0.77
Diethyl Phthalate	0.88
1-Hexadecene	0.47
Cis-7-Tetradecen-1-Ol	0.69
3-Heptadecene, (Z)-	2.05
3-Heptadecene, (Z)-	0.47
Heptadecane	0.70
N-Hexadecanoic Acid	8.72
Octadecanoic Acid, 2-Propenyl Ester	1.10
9-Octadecenoic Acid, (E)-	52.09
(E)-9-Octadecenoic Acid Ethyl Ester	1.78
Octadecanoic Acid	9.71
11-Hexadecynal	0.42
Hahnfett	2.98
Z-14-Octadecen-1-Ol Acetate	0.52
9-Octadecenoic Acid, 1,2,3-Propanetriyl Ester, (E,E,E)-	0.33
Octadecanoic Acid, 2-Propenyl Ester	0.67
Glycidyl Palmitate	0.35

9,12-Octadecadienoic Acid (Z,Z)-, 2,3-Dihydroxypropyl Ester	0.52
Oleoyl Chloride	1.66
Octadecanoic Acid, 2,3-Dihydroxypropyl Ester	0.65
Glycidyl Oleate	0.68
13-Docosen-1-Ol, (Z)-	0.45
Squalene	0.30

Table 26. Py-GC/MS analysis of Bio-oil obtained from co-pyrolysis of *Mesua ferrea* L. oilseed and PET plastic at B:P -1:2 feedstock ratio, 590 °C

Compounds	Peak area (%)
2-Butene	0.29
Acetic Acid, Chloro-, Octyl Ester	0.41
Cyclobutane, Methylene-	0.96
1-Hexene	0.27
Benzene	2.75
1-Heptene	0.42
2,6-Dimethylhepta-1,5-Diene	0.42
Benzene, Ethenyl-	0.44
Cyclopropane, 1,1-Dimethyl-2-(2-Methyl-1-Propenyl)-	0.27
2,6-Octadiene, 2,7-Dimethyl-	0.44
1-Cycloundecene	0.25
Vinyl Benzoate	2.95
Benzoic Acid	18.19
3-Dodecen-1-Ol, Acetate, (E)-	0.25
1,1'-Biphenyl	1.69
3-Hexadecene, (Z)-	0.32
Pentadecane	0.35
2,4-Imidazolidinedione, 5-Ethyl-5-Phenyl-	1.43
Diethyl Phthalate	1.45
1-Hexadecanol	0.46
4-Acetylbenzoic Acid	2.41
8-Heptadecene	0.83
Heptadecane	0.33
N-Hexadecanoic Acid	8.28
Decanoic Acid, 2-Propenyl Ester	0.52
Isopropyl Linoleate	2.58
Oleic Acid	26.68
1,2-Ethanediol, Dibenzoate	9.67
Octadecanoic Acid	9.20
P-Terphenyl	0.71
Hahnfett	1.24
Octadecanoic Acid, 2-Propenyl Ester	0.37

Benzoic Acid ,2-[(3-Methylbenzoyl) Hydrazonomethyl]Phenyl Ester	0.48
Ethanone, 1-(2,4-Dimethylphenyl)-	0.30
Oleoyl Chloride	1.13
Octadecanoic Acid, 2,3-Dihydroxypropyl Ester	0.34
Glycidyl Oleate	0.38
2-[(Biphenyl-4-Carbonyl)-Amino]-5-Methyl-Benzoic Acid	0.54

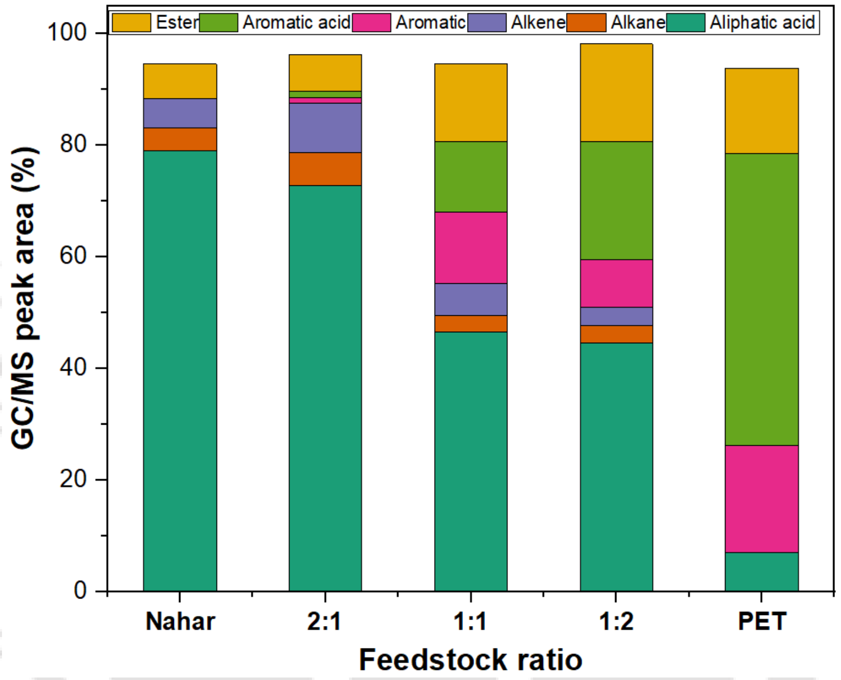

Figure 18. Effect of feedstock ratio on co-pyrolysis in analytical pyrolysis

4.3.2 Effect of operation parameters on biomass pyrolysis and co-pyrolysis

4.3.2.1 Effect of temperature

Slow pyrolysis of the feedstock was performed in the semi-batch fixed bed reactor, and the results are depicted in Fig. 19. The pyrolytic liquid generated during co-pyrolysis due to the rapid breakdown and depolymerization of the biomass and plastic. According to the findings of this investigation, an increase in pyrolysis temperature led to a greater oil yield. At 600 °C, the yield of bio-oil increased to a maximum of 27 wt.% for biomass and 28.5 wt.% for 1:1 co-feed. A further increment in temperature reduced the oil yield (biomass 24.5 wt.%, co-feed (1:1) 26 wt.%). Further increasing the pyrolysis temperature to 600 and 650 °C led to an increase in yield of non-condensable gases. The gas yield increased from 31 wt.% to 42 wt.% as the temperature rises from 550 °C to 650 °C. Fig. 19 depicts the variation in product yields with respect to increase in process temperature. It is evident that the amount of char produced decreases sharply. The char yields were 52 wt.% for biomass and 43.4 wt.% for co-feed at 550 °C. When the temperature was raised to 600 °C, the char yield decreased to 31 wt.%, 26.9 wt.% for biomass, co-feed, respectively. The enhanced conversion of lignin in the biomass is the primary cause of the decreased char yield at higher temperatures [192]. Additionally, more gas is produced with increase in temperature because more feed is converted to fuel. At higher temperatures, the secondary reactions of vapors to gases become more prominent. A study on thermal pyrolysis of *Acacia nilotica* in a fixed-bed reactor at an optimal temperature of 500 °Cand 15 °C min^{-1} heating rate reported a bio-oil yield of 37 wt.% [211]. A similar trend of distribution of pyrolytic products was observed in thermal pyrolysis of *Phoenix Dactylifera* seeds with a maximum yield of 45 wt.% at 600 °C [212].

Fig. 19 illustrates the effect of temperature on the co-pyrolysis of biomass and plastic. Bio-oil yield was maximum (28.5 wt.%) at 600 °C for 1:1 feedstock ratio, indicating a higher synergistic effect. The increase in oil yield, a significant outcome of our research, underscores the importance of co-pyrolysis involving the seed and PET for liquid production. PET pyrolysis alone promotes the char formation due to the presence of high molecular weight waxy compounds and suppresses gas production. This suggests that Oxygen containing aromatic structures found in PET, such as benzoic acid (BA) and terephthalic acid (TPA), could be harnessed in the char fraction rather than subjecting such compounds to cracking and deoxygenation reactions to generate gases. With each incremental rise in temperature, the plastics underwent precise cracking reactions, transitioning into a more gaseous phase [213].

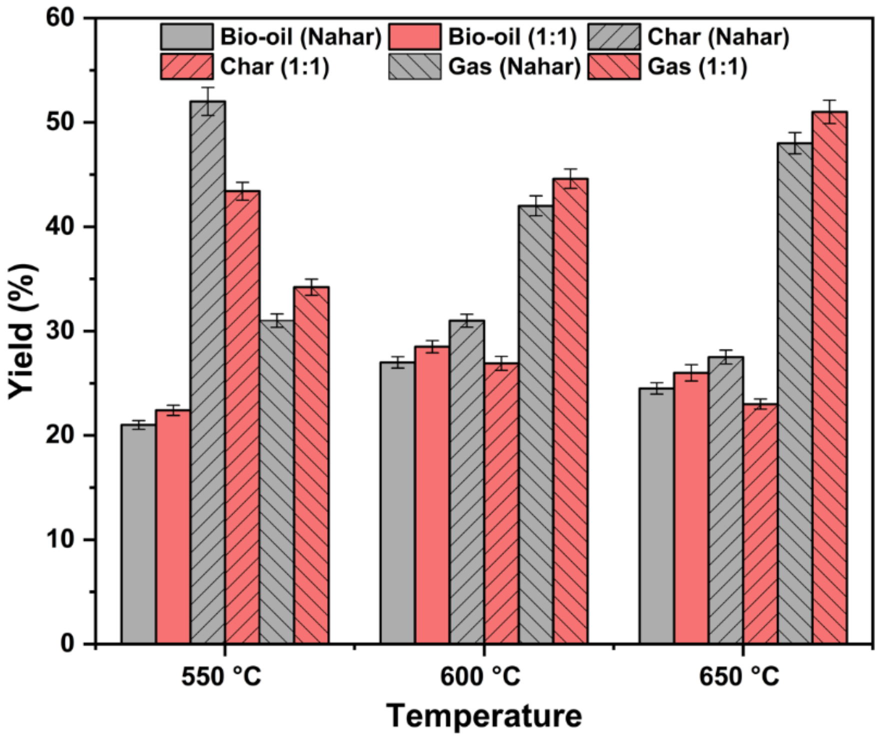

Figure 19. Effect of Temperature on pyrolytic product yield of biomass and 1:1 feedstock ratio

4.3.2.2 Effect of plastic ratio on co-pyrolysis of biomass and plastic

Fig. 20 shows the yield of products from co-pyrolysis at different feedstock ratios. The amount of plastic in the feedstock ratio of 1:1, 1:2, had a negative synergistic effect when compared to 2:1. From the individual pyrolysis and pyrolysis of co-feed with 1:1 biomass: plastic ratio, the operating parameters such as temperature (600 °C), residence time (2 h) were fixed. The bio-oil yield was maximum (35 wt.%) for 2:1 (B: P). Moreover, the gas yield (30 wt.%) and char yield (35 wt.%) were optimal, signifying the synergistic effect observed with equal composition mixture. The addition of plastic enhanced the production of non-condensable gases. This signifies that the gas-phase interaction primarily occurs between PET and oilseed, specifically between the hydrocarbon oxygenates of PET and the primary pyrolysis products of oil seed [214].

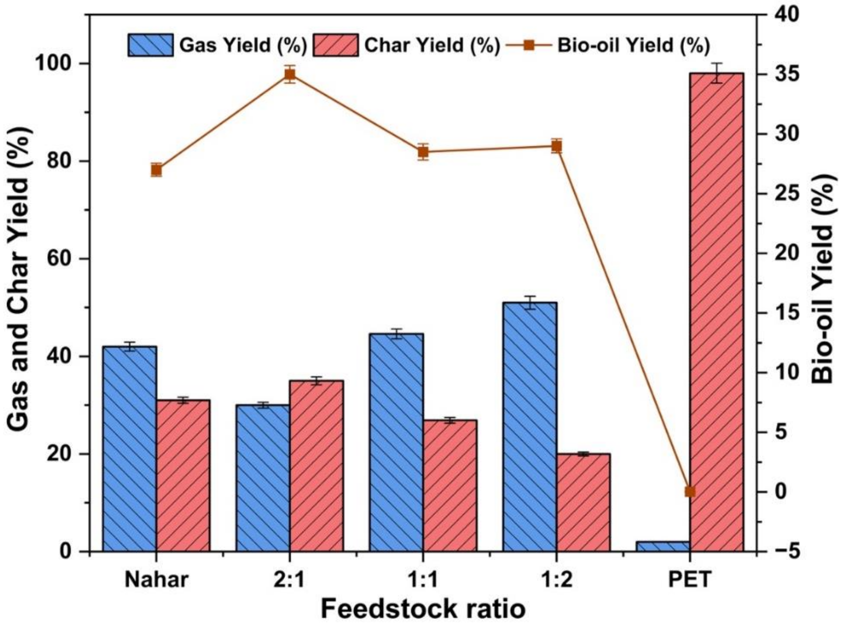

Figure 20. Effect of feedstock ratio of co-pyrolysis of oilseed and PET plastic in fixed-bed pyrolysis

4.3.3 Characterization of Bio-oil

4.3.3.1 Physico-chemical characterization of bio-oil

The elemental CHNS/O composition of the pyrolytic-oils produced at temperature of 600 °C is shown in Table 27. The bio-oil obtained at the optimal condition was characterized in detail to decipher the elemental composition, calorific value, and functional groups through FTIR spectroscopy and NMR spectroscopy. The pyrolytic liquid derived from nahar seed, generally referred to as the bio-oil, is reported to possess HHV in the range of 15-30 MJ kg^{-1}. The elemental composition of bio oil C (68.32%), H (10.57%), N (4.42%), S (0.01%), and O (16.77%) with an emipirical formula, $CH_{1.85}N_{0.05}S_{0.00005}O_{0.184}$, has HHV of 32.78 MJ kg^{-1}. Elemental analysis of bio-oil derived from *Silybum marianum* L. seeds revealed that the carbon content (76%) and nitrogen content (2.32%) were higher and lower than that in the present study. Additionally, the H/C and O/C values are 1.85 and 0.184 which is in accordance with the literature [215]. The proportions of oxygen, hydrogen, and carbon in bio-oil differ greatly from those in the original biomass. Because of the significant potential for NOx emissions, burning bio-oils with organic nitrogen compounds present can be challenging. Many oxygenated functional groups such as hydroxyl, carboxyl, and carbonyl are present in the bio-oils. Oxygen is the cause of several of the undesirable characteristics of bio-oils, including their low heating value, thermal and storage instability [216]. Meanwhile, the oxygen content varied in 6.12-12% range for co-pyrolysis oil, which is clearly due to the addition of plastic to biomass. This also tends to reduce the oil's nitrogen content to less than 0.5% at all feedstock ratios, which further implies that plastic reduces the nitrogen content of the oil. When compared to the O/C of the thermal pyrolysis, the co-pyrolytic oil contains less O/C ratio. This indicates that the addition of plastic reduces the oxygen content. The Higher Heating Value of the co-pyrolysis oil (41.32 MJ kg^{-1} for 2:1 ratio) was greater than that of thermal pyrolysis oil, indicating that the addition of plastic enhances the fuel characteristics of the oil. Therefore, bio-oils should be mildly deoxygenated catalytically to enhance their heating values and stability. The co-pyrolysis oil is better than petroleum crude oil in terms of sulfur-based pollution owing to negligible sulfur content in it [217].

Table 27. Physico-chemical characterization of bio-oil obtained from thermal and co-pyrolysis of *Mesua ferrea* L. oilseed and PET plastic

Analysis	**Nahar**	**1:1**	**2:1**	**1:2**
Color	Black	Dark Brown	Dark Brown	Dark Brown
Odour	Smoky	Smoky	Smoky	Smoky
C (%)	68.32	72.8	78.12	79.13
H (%)	10.57	11.34	11.11	9.07
O* (%)	16.77	14.34	10.33	11.21
N (%)	4.42	1.52	0.42	0.68
S (%)	0.01	--	0.02	0.01
HHV (MJ kg^{-1})	32.78	37.21	39.28	40.78
H/C (mol/mol)	1.85	1.87	1.71	1.38
O/C (mol/mol)	0.18	0.14	0.11	0.10

* Indicates by difference

The bio-oil produced at 600 °C was also analyzed for its functional groups using FTIR spectroscopy and presented in Fig. 21. The functional groups of the classes containing -OH bond in aqueous phase and acidic compounds were assigned to a broader range of 3600-3400 cm^{-1}. The peaks at 3000- 2700 cm^{-1} indicates C-H bonds of alkane compounds, whereas the stretch at 1700 cm^{-1} is assigned to ketone and aldehyde groups. C=O and C-C bond stretching vibrations were observed at 1300 and 1650 cm^{-1}, respectively From the above observations, it is understood that the bio-oil contains different types of saturated, unsaturated, and oxygen-containing compounds. This is in accordance with the literature [218].

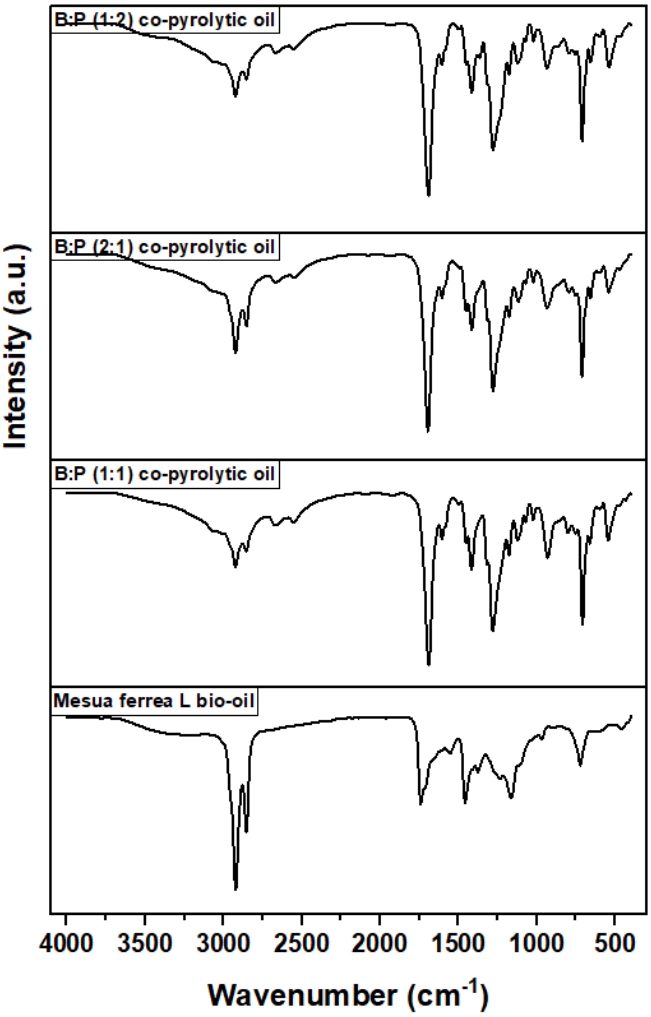

Figure 21. Functional group analysis of bio-oil derived at different feedstock ratios

^{1}H-NMR spectra of bio-oil obtained from *Mesua ferrea* L. oilseed and PET plastic pyrolysis are presented is Fig. 22. The proton NMR, characterizes the H atoms bound to a particular functional group by causing a spin state. The NMR data analysis was carried out using MestReNova software. The 2.52 ppm peak represents the DMSO-d6 peak in the ^{1}H NMR spectra. The functional groups are assigned to different chemical shifts [219]. The ^{1}H NMR analysis is vital in determining the aromatics, paraffins, olefins, and H/C of the oil. A considerable accumulation of peaks in the 1-2.5 ppm region, indicative of the presence of aliphatic compounds, and a single peak at 6-8 ppm, indicative of a lesser amount of aromatic compounds in thermal pyrolytic oil are evident. Whereas, the co-pyrolytic oils contained a significant amount of aromatics. A study on apricot pyrolysis revealed a similar but more significant number of peaks in the aliphatic region than in aromatic compounds (Reference required). From the results, it can be concluded that the paraffin (30.96 vol%) is higher in bio-oil obtained from a 2:1 feedstock ratio, whereas aromatics (55 vol%) are predominant in bio-oil produced from a 1:2 feedstock ratio and olefins (55 vol%) in case of biomass. The addition of plastic enhances the aromatic nature of the bio-oil. Moreover, the H/C ratio calculated from the NMR data is similar to that obtained from the elemental composition for all cases.

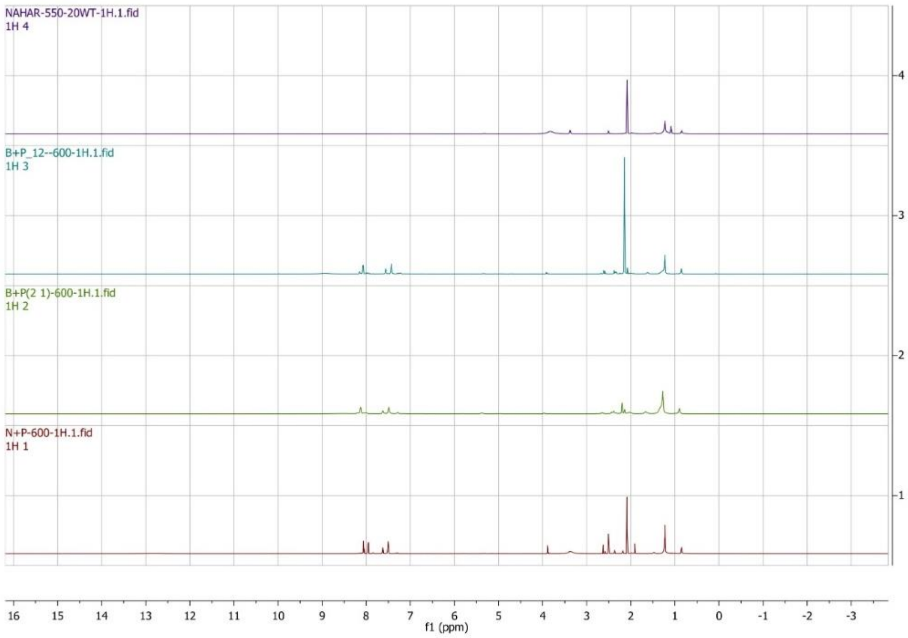

Figure 22. ^{1}H NMR analysis of bio-oil produced at different feedstock ratios

4.3.4 Insights into Reaction Mechanism

4.3.4.1 Biomass Pyrolysis

GC/MS was used to differentiate various classes of organic compounds in the pyrolytic-oil and the analysis is presented in Fig. 23. A detailed list of compounds is given Table 28-31. It is important to note that the structure of these compounds changes drastically depending on the process parameters. Biomass pyrolysis results in major products such as esters, amides, nitriles, hydrocarbons, aromatics, alcohols, acids, and others (ketones, aldehyde). The significant compounds of the bio-oil obtained from the GC/MS analysis of the bio-oil were pentadecane ($C_{15}H_{32}$) (2.3%), hexadecane ($C_{16}H_{34}$) (1.0%), 8-heptadecene ($C_{17}H_{34}$) (5.2%), heptadecane ($C_{17}H_{36}$) (3.2%), hexadecanenitrile ($C_{16}H_{31}N$) (2.7%), hexadecanoic acid methyl ester ($C_{17}H_{34}O$) (3.6%), 9-octadecenenitrile ($C_{18}H_{33}N$) (6.9%), methyl 9-cis,11-trans-octadecadienoate ($C_{19}H_{34}O$) (2.7%), heptadecanenitrile ($C_{17}H_{33}N$) (5.4%), methyl stearate ($C_{19}H_{38}O$) (3.5%), hexadecanamide ($C_{16}H_{33}NO$) (1.1%), 13-docosenamide ($C_{22}H_{43}NO$) (1.5%), nonadecanenitrile ($C_{19}H_{37}N$) (2.0%), 9-octadecenoic acid methyl ester ($C_{19}H_{36}O$)

(10.4%). Moreover, the alkanes contained in in smaller fractions indicate the partial conversion of unsaturated fatty acids[220]. However, more advanced upgrading procedures, such as cracking of pyrolytic vapours in the presence of catalyst or co-pyrolysis must be used as a substitute for diesel fuel.

Table 28. GC/MS analysis of Bio-oil obtained from thermal pyrolysis of *Mesua ferrea* L. oilseed, 600 °C, 2 h

Compounds	Peak area (%)
Decane	0.16
Carbetamide	0.29
Decane	0.40
2-Decenal, (E)-	0.45
Undecane	0.50
2-Hexadecene, 2,6,10,14-tetramethyl-	0.36
1-Undecene	0.12
Benzene, pentyl-	0.14
Benzene, pentyl-	0.11
Triadimenol	0.21
Dodecane	0.27
Dodecane	0.45
Isoprocarb	0.03
Isoprocarb	0.12
Allethrin	0.05
2H-1,2,3,4-Tetrazole-2-acetamide, N-(2-ethylphenyl)-5-(4-pyridinyl)-	0.15
1-Tridecene	0.17
1-Tridecene	0.28
Nonane, 3-methyl-5-propyl-	0.13
Undecane, 4,7-dimethyl-	0.27
5H-1-Pyrindine	0.13
Allethrin	0.32
Tolylfluanid	0.13
3-Hexadecene, (Z)-	0.71
Tetradecane	0.79
Cyclopentane, undecyl-	0.15
Cyclopentene, 1-octyl-	0.10
Dimepiperate	0.01
Bicyclo[3.1.0]hexan-3-ol, 4-methylene-1-(1-methylethyl)-, (1.alpha.,3.alpha.,5.alpha.)-	0.15
Cinmethylin	0.11
Dimepiperate	0.11
3-Hexadecene, (Z)-	0.23

1-Pentadecene	0.57
Pentadecane	2.34
Cetene	0.13
Cinmethylin	0.11
Pyrethrin II	0.13
Cyclohexene, 3-(2-methylpropyl)-	0.11
n-Nonylcyclohexane	0.25
Cinmethylin	0.12
Cyclohexene, 1-nonyl-	0.48
3-Hexadecene, (Z)-	0.62
8-Heptadecene	0.59
E-14-Hexadecenal	0.85
Hexadecane	1.02
Cetene	0.16
Cyclohexene, 1-decyl-	0.11
Cyclohexane, (3-cyclopentylpropyl)-	0.15
10-Heneicosene (c,t)	0.30
E-7-Tetradecenol	0.29
8-Heptadecene	2.93
8-Heptadecene	2.68
5-Cyclohexyl-1-pentene	0.15
1-Heptadecene	0.67
Heptadecane	3.40
1-Heptadecene	0.19
Benzene, (1-methyldecyl)-	0.19
Benzene, (1-methyldecyl)-	0.17
E-14-Hexadecenal	0.14
Cinmethylin	0.28
Undec-10-ynoic acid, tetradecyl ester	0.14
7-Hexadecenal, (Z)-	0.13
Benzene, 1,1'-[oxybis(methylene)]bis[4-ethyl-	0.15
6,9-Heptadecadiene	0.20
Cyclohexane, undecyl-	0.20
cis-7-Tetradecen-1-ol	0.25
Oxirane, tetradecyl-	0.35
cis-1-Chloro-9-octadecene	0.43
(3-Methylphenyl) methanol, 2-methylpropyl ether	0.25
1-Nonadecene	0.35
Heneicosane	0.70
E-15-Heptadecenal	0.14
9-Octadecanone	0.33
cis-9-Hexadecenal	0.26
(R)-(-)-14-Methyl-8-hexadecyn-1-ol	0.14
1-Nonadecene	0.24
Heneicosane	0.72
Hexadecanenitrile	2.93

Hexadecanoic acid, methyl ester	3.88
1-Nonadecene	0.19
Heneicosane	0.48
2-Pentadecanone, 6,10,14-trimethyl-	0.17
Palmitic Acid, TMS derivative	0.45
Palmitic Acid, TMS derivative	0.76
Jasmolin II	0.08
Cinerin II	0.11
Jasmolin II	0.11
Octadecanoic acid, 2-propenyl ester	0.77
Oxirane, hexadecyl-	0.84
9-Octadecenenitrile, (Z)-	4.16
9-Octadecenenitrile, (Z)-	3.19
Methyl 9-cis,11-trans-octadecadienoate	2.88
Tetradecanamide	1.04
Heptadecanenitrile	5.83
Buprofezin	0.24
Methyl stearate	3.79
Pyrethrin II	0.11
Nopyl acetate	0.25
Ethoxyquin	0.15
o-Dodecylphenol	0.45
Cinmethylin	0.12
DMP	0.14
9,12-Octadecadien-1-ol, (Z,Z)-	0.30
E-2-Tetradecen-1-ol	0.21
Cinmethylin	0.18
9-Octadecenoic acid, 1,2,3-propanetriyl ester, (E,E,E)-	1.06
Heneicosane	0.33
3-Eicosanone	0.20
Arachidamide, N-methyl-	0.63
Aldicarb	0.14
Fluacrypyrim	0.12
Heptadecanenitrile	1.19
2-Dodecen-1-yl(-)succinic anhydride	0.90
Octadecanoic acid, 2-propenyl ester	0.67
Oxiraneoctanoic acid, 3-octyl-, methyl ester, cis-	0.29
Prohydrojasmon-1	0.40
2-Methylhexacosane	0.87
9-Octadecanone	0.52
Hexadecanamide	1.20
2(3H)-Furanone, 5-dodecyldihydro-	0.10
Methyl 18-methylnonadecanoate	0.57
i-Propyl 11,12-methylene-octadecanoate	0.18
13-Docosenamide, (Z)-	1.63
13-Docosenamide, (Z)-	0.78

Triclopyl 2-butoxyethyl	0.11
Nonadecanenitrile	2.16
N-Methyldodecanamide	0.48
Propanamide, 3-cyclopentyl-N-methyl-	0.31
Heptadecanenitrile	0.14
Arachidamide, N-methyl-	0.67
9-Octadecenamide, N,N-dimethyl-	0.31
DMP	0.24
trans-9-Octadecenoic acid, pentyl ester	0.33
Arachidamide, N-ethyl-	0.31
Hexadecanoic acid, octadecyl ester	0.18
Octadecanoic acid, pentyl ester	0.17
Eicosane	0.28
2-Pentatriacontanone	0.39
9-Octadecenoic acid, methyl ester, (E)-	11.14
Methyl 20-methyl-heneicosanoate	0.40
Eicosen-1-ol, cis-9-	0.15
13-Docosen-1-ol, (Z)-	0.29
Succinic acid, dec-4-enyl propyl ester	0.16
Tricosyl acetate	0.16
Tridemorph	0.14
10-Methyl-dodecanoic acid, pyrrolidide	0.12
Nonacosane	0.19
Hexadecanamide	0.21
Uniconazole-P	0.12
Heptadecanenitrile	0.15
Arachidamide, N-methyl-	0.15
Decyl oleate	0.13
Triadimenol	0.16
Vamidothion	0.13
Octadecanoic acid, heptyl ester	0.16
DMP	0.18
Fenbuconazole	0.23
Eicosane	0.27
Arachidamide, N-3-methylbutyl-	0.17
Nonadecanenitrile	0.58
trans-9-Octadecenoic acid, pentyl ester	0.19
Prohydrojasmon-2	0.11
Pyrrolidine, 1-(1-oxo-9-octadecenyl)-, (Z)-	0.15
9-Heptadecanone	0.11
Octadecanamide	0.29
Arachidamide, N-methyl-	0.15
Cinmethylin	0.11
Jasmolin II	0.12

The oilseeds usually contain high amounts of fatty acids, which is confirmed by the analytical fast pyrolysis of the seed. The pyrolytic-oil also contains a major proportion of nitriles and amides (29.1%) in addition to hydrocarbons (28.7%) and esters (29.9%). This is due to pyrolytic vapor's secondary cracking and functionalization to form different classes of compounds. It is evident from the literature that the nitrogen-containing compounds are formed with an increase in temperature. Hence, the parameters such as feedstock composition and operating temperature play a major role in determining the quality of the bio-oil. A study on the pyrolysis of fish fats at different temperatures found that the bio-oil was mainly composed of nitrogen groups, alkanes, alkenes, and aromatic compounds [221]. The origin of these compounds is due to the pyrolysis of the fats present in the raw material. A research on the thermal pyrolysis of fats at 300 °C led to the formation of fatty acids, wherein, increase in temperature facilitated the production of short-chain hydrocarbons [220].

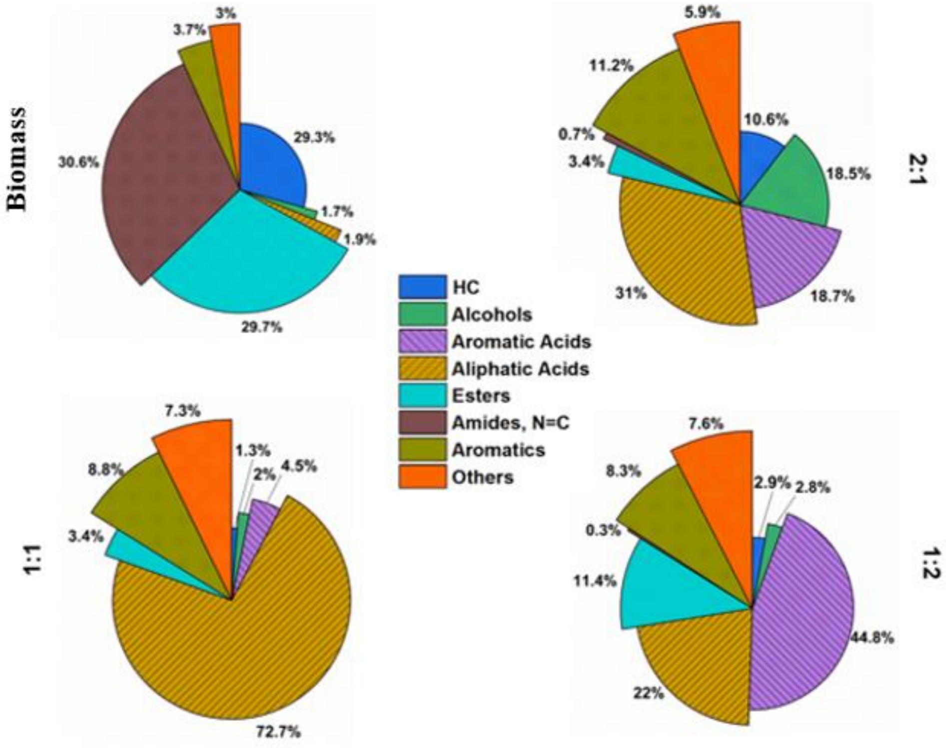

Figure 23. Classification of compounds from GC/MS analysis of bio-oil derived at 600 °C

In this study, some compounds such as n-hexadecanoic acid (28-34%) observed in the analytical fast pyrolysis is converted to hexadecanaamide (2.7%), hexadecanitrile (1.1%), hexadecane (1.0%), hecadecanoic acid methyl ester (3.6%), which were observed in GC/MS of bio-oil. Similarly, octadecanoic acid (31-39%) is converted to 9-octadecenenitrile (3.9%), 9-octadecenoic acid, 1,2,3-propanetriyl ester (1.0%), 9-octadecenoic acid, methyl ester (10.4%), methyl stearate (3.5%), methyl 9-cis,11-trans-octadecadienoate (2.7%). A detailed description of different types of compounds is given in Table 27. The reaction between amino acids and fatty acids present in oilseed is the probable reason for the production of fatty acid amides of the oil. Moreover, the amide-containing groups, generally unstable in an inert atmosphere at elevated temperatures, undergo dehydration reaction to form nitriles [222]. Fig. 24 presents the plausible conversion pathways of octadecanoic acid to different compounds, which is typical in nahar seed pyrolysis.

Table 29. GC/MS analysis of Bio-oil obtained from co-pyrolysis of *Mesua ferrea* L. oilseed and PET plastic for B:P-1:1 feedstock ratio 600 °C, 2 h

Compounds	Peak area (%)
Ethanone, 1-Phenyl-	3.53
Benzoic Acid, Methyl Ester	1.21
1,2-Propanedione, 1-Phenyl-	1.48
Benzoic Acid, 4-Methyl-	2.14
1,1'-Biphenyl	2.64
1-Tetradecanol	0.9
2,2-Diphenyl-N-(3,3,5-Trimethylcyclohexyl)Acetamide #	0.66
Phenol, 2,4-Bis(1,1-Dimethylethyl)-	0.57
4-Acetylbenzoic Acid	2.89
1,4-Benzenedicarboxylic Acid, Methyl Ester	1.74
1-Hexadecanol	0.97
4-Acetylbenzoic Acid	1.71
Tetradecanoic Acid	10.36
1-Nonadecene	0.56
2-Nonadecanone	0.69
N-Hexadecanoic Acid	25.25
1-Nonadecene	0.6
Z,Z-6,28-Heptatriactontadien-2-One	0.48
2-Nonadecanone	0.55

Oleic Acid	11.26
Oleic Acid	5.68
1,2-Ethanediol, Dibenzoate	0.92
Octadecanoic Acid	13.74
Bis(2-Ethylhexyl) Phthalate	1.94
Phenol, 2,4-Bis(1,1-Dimethylethyl)-, Phosphite (3:1)	7.53

Table 30. GC/MS analysis of Bio-oil obtained from co-pyrolysis of *Mesua ferrea* L. oilseed and PET plastic for B:P-2:1 feedstock ratio 600 °C, 2 h

Compounds	Peak area (%)
Methane, Dichloro-	0.13
Ethylbenzene	0.2
2-Phenethyl-.Beta.-Phenylpropionate	0.22
Benzaldehyde	0.66
Phenol	0.23
Benzonitrile	0.73
1-Decene	0.21
Benzene, [(2-Propenyloxy)Methyl]-	0.25
Acetophenone	2.24
Benzene, (2-Methyl-1-Propenyl)-	0.23
Phenol, 4-Methyl-	0.28
1-Undecene	0.34
Methyl Benzoate	1.35
Undecane	0.14
3-(Benzoylsulfanyl)-2-Methylpropanoic Acid	0.69
2a,4a,6a,6b-Tetrahydrocyclopenta[Cd]Pentalene	0.2
Benzene, Pentyl-	0.37
2,2-Dimethyl-1,3-Diphenyl-3-Buten-1-One	0.44
1-Dodecanol	17.34
Benzoic Acid	13.68
1-(4-Methylphenyl)-3-Buten-1-One #	0.15
Bicyclo[6.4.0]Dodeca-9,11-Diene	0.24
Benzene, (1,3-Dimethylbutyl)-	0.17
Nonanoic Acid	0.18
Benzoic Acid, 4-Methyl-	2.68
1-Tridecene	0.44
Naphthalene, 1-Methyl-	0.36
Naphthalene, 1-Methyl-	0.18
Benzene, Heptyl-	0.23
Decanoic Acid	1.37
Benzoic Acid, Ethyl-	1.17
1,1'-Biphenyl	2
1-Tetradecene	0.68
Tetradecane	0.41

Diphenylmethane	0.2
Benzene, Octyl-	0.15
Benzoic Acid, 4-Acetyl-, Methyl Ester	0.4
1-Pentadecene	0.72
Hexadecane	2.01
1,4-Dimethyladamantane #	0.55
1-Hexadecanol	0.8
Hexadecane, 2,6,10,14-Tetramethyl-	0.31
3-Heptadecene, (Z)-	0.74
3-Heptadecene, (Z)-	0.83
1-Heptadecene	0.23
Heptadecane	1.57
Benzene, (1-Methyldecyl)-	0.21
(3-Methylphenyl) Methanol, 2-Methylbutyl Ether	0.19
9,10-Ethanoanthracene, 9,10-Dihydro-11,12-Diacetyl-	0.25
Carbonic Acid, Octadecyl Prop-1-En-2-Yl Ester	0.57
Hexadecanoic Acid, Methyl Ester	0.29
N-Hexadecanoic Acid	6.74
Z,Z-6,28-Heptatriactontadien-2-One	0.63
Z,Z-6,28-Heptatriactontadien-2-One	0.31
9-Octadecenoic Acid (Z)-, Methyl Ester	0.42
2-Pentadecanone, 6,10,14-Trimethyl-	0.63
Methyl Stearate	0.2
Oleic Acid	7.73
Oleic Acid	5.69
Octadecanoic Acid	8.38
1,1':4',1"-Terphenyl	0.15
Hahnfett	0.2
1,4,7-Trioxaspiro[4.5]Decane	0.27
7,9-Di-Tert-Butyl-1-Oxaspiro(4,5)Deca-6,9-Diene-2,8-Dione	0.31
Oleoyl Chloride	0.14
9-Octadecenoic Acid (Z)-, 2,3-Dihydroxypropyl Ester	0.4
1,4-Dioxaspiro[4.5]Decan-8-Ol	0.2
Bis(2-Ethylhexyl) Phthalate	0.62
1,4-Epoxynaphthalene-1(2H)-Methanol, 4,5,7-Tris(1,1-Dimethylethyl)-3,4-Dihydro-	5.89
Benzenepropanoic Acid, 3,5-Bis(1,1-Dimethylethyl)-4-Hydroxy-, Octadecyl Ester	0.3
Acetophenone	0.33
Phenacyl 11-Octadecenoate	0.25

Table 31. GC/MS analysis of Bio-oil obtained from co-pyrolysis of *Mesua ferrea* L. oilseed and PET plastic for B:P-1:2 feedstock ratio, 600 °C, 2 h

Compounds	Peak area (%)
Methane, Dichloro-	0.05
Benzene, Methyl-	0.06
Butanoic Acid, 3-Methyl-	0.09
Ethylbenzene	0.13
Styrene	0.21
Benzene, Propyl-	0.05
Benzaldehyde	0.81
Phenyl .Alpha.-D-Sedoheptuloside	0.18
Benzonitrile	0.28
1-Decene	0.16
Benzene, 1-Ethenyl-2-Methyl-	0.08
Benzene, 2-Propenyl-	0.05
1H-Indene, 1-Chloro-2,3-Dihydro-	0.1
Benzenepropanal	0.11
Ethanone, 1-Phenyl-	2.25
6-Heptenoic Acid	0.34
Heptanoic Acid	0.39
Benzaldehyde, 2-Methyl-	0.16
1-Undecene	0.33
Methyl Benzoate	0.64
1-Undecene	0.05
Ethanedione, Diphenyl-	1.15
1h-Indene, 2-Methyl-	0.11
Benzene, Pentyl-	0.18
4-Chlorophenyl Benzoate	0.15
1,4-Benzodioxin, 2,3-Dihydro-	0.25
O-Toluic Acid, 2-Chlorophenyl Ester	4.68
1-Dodecanol	1.71
Benzoic Acid	33.98
1-(4-Methylphenyl)-3-Buten-1-One #	0.2
4a,5,6,7,8,9,10,10a-Octahydrobenzo[A]Cyclooctene	0.13
Nonanoic Acid	0.21
Benzoic Acid, 4-Methyl-	5.02
Naphthalene, 1-Methyl-	0.26
4-Bromophenyl 3,4-Dimethylbenzoate #	0.19
Bicyclo[3.1.0]Hexan-3-Ol, 4-Methylene-1-(1-Methylethyl)-, [1S-(1.Alpha.,3.Beta.,5.Alpha.)]-	0.32
N-Decanoic Acid	0.47
1,1'-Biphenyl	4.8
1-Tetradecene	0.6
4-Vinylbenzoic Acid	0.54
Diphenylmethane	0.25

Ethanone, 1,1'-(1,4-Phenylene)Bis-	0.25
Undecylenic Acid	0.33
Cyclohexene, 1-Octyl-	0.26
Benzoic Acid, 4-Acetyl-, Methyl Ester	0.34
1,1'-Biphenyl, 4-Methyl-	0.55
1,1'-Biphenyl, 3-Methyl-	0.78
Propiophenone, 2,2',4',6'-Tetramethyl-	0.27
4-Acetylbenzoic Acid	3.44
1,4-Benzenedicarboxylic Acid, Methyl Ester	2.37
1-Hexadecanol	0.74
4-Ethylbiphenyl	0.15
4-Acetylbenzoic Acid	1.17
3-Heptadecene, (Z)-	0.16
1-Nonadecene	0.1
Heptadecane	0.29
9h-Fluoren-9-One	0.15
Cis-10-Heptadecenoic Acid	0.06
<No Name>	0.19
Ethanone, 1-[1,1'-Biphenyl]-4-Yl-	0.17
2-Pentadecanone	0.45
Biphenyl-4-Carboxylic Acid	0.11
N-Hexadecanoic Acid	5.82
2-Phenylnaphthalene	0.12
Z,Z-6,28-Heptatriactontadien-2-One	0.5
Z,Z-6,28-Heptatriactontadien-2-One	0.26
2-Nonadecanone	0.65
Oleic Acid	8.55
Octadecanoic Acid	5.59
2-Norpinene-2-Ethanol, 6,6-Dimethyl-, Acetate	0.57
M-Terphenyl	0.47
1,4,7-Trioxaspiro[4.5]Decane	0.33
2-(3-Methyl-Undec-3-Enyl)-[1,3]Dioxolane	0.42
1,4-Dioxaspiro[4.5]Decan-8-Ol	0.27
Bis(2-Ethylhexyl) Phthalate	2.4

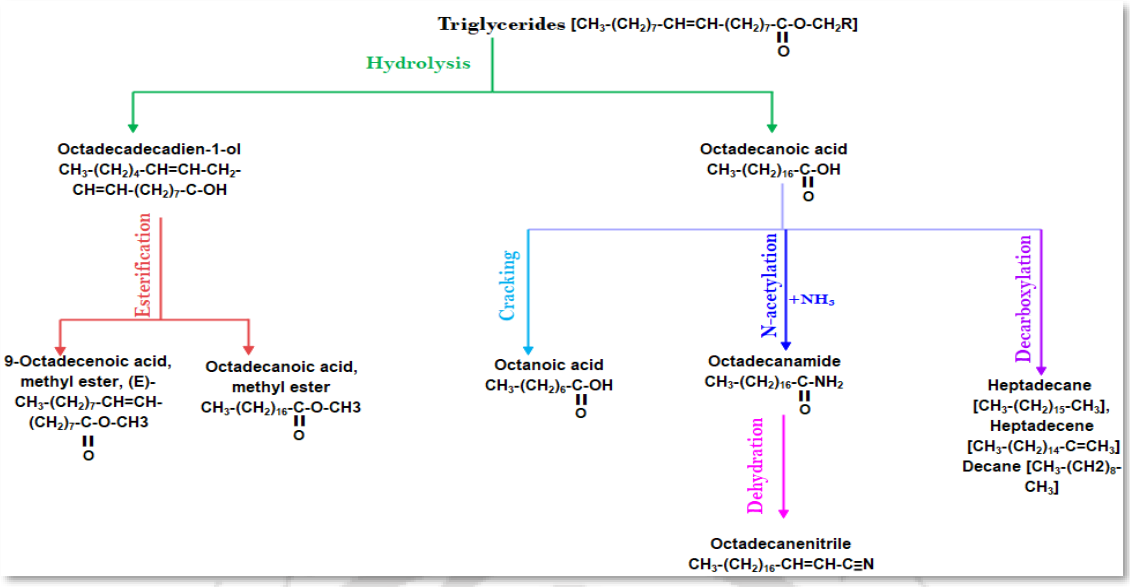

Figure 24. Reaction pathway of *Mesua ferrea* L. oilseed pyrolysis

4.3.4.2 Interactions during co-pyrolysis process

The effect of co-pyrolysis on the chemical composition of bio-oil can be seen in Fig. 23. Thermal pyrolytic oil from biomass generates 29.3% hydrocarbons, 29.7% esters, 30.6% amides, and nitrogen-containing compounds, 3.7% aromatics, whereas adding plastics enhanced the aromatic content in the co-pyrolytic oil 2:1 (11.2%) >1:1 (8.8%) >1:2 (8.4%). In particular, the yield of aromatic acids and esters increased with increased in PET ratio, while decreasing the amount of hydrocarbons and alcohols. A positive synergistic effect promoted the hydrocarbon (10.6%) yield up to 60% biomass, which reduced the acid content (aliphatic acid: 31%; aromatic acids: 18.7%). This indicates that the primary reaction was the decarboxylation of carboxylic acid to form aliphatic hydrocarbon. To further streamline, the PET decomposition is usually prompted by β-scission at the carboxylic functional group, where the ester bond is broken to form benzene carboxylic acid and vinyl benzoate [223]. Increasing temperature (up to 600 °C) would further decompose the vinyl benzoate to form aromatics in the liquid phase. The benzene carboxylic acid group would further dissociate to form carboxylic acid and olefin compounds [224]. From the thermal pyrolytic oil, it was observed that the oil contained a significant amount of nitrogen-containing and amide groups (30.6%). This got significantly reduced to <0.5% when the biomass was co-pyrolyzed with plastic indicating the possible denitrogenation of the oxygenated compounds. Fig. 25 represents the comparison of GC/MS peak area (%) of major compounds such as benzoic acid, n-hexadecanoic acid, oleic acid, stearic acid at different feedstock ratios. This indicates that, at feedstock ratios of 1:1 and 2:1 (B:P), the presence of aliphatic fatty acids is significant whereas aromatic acids content increased with increase in PET proportion in the feedstock ratio.

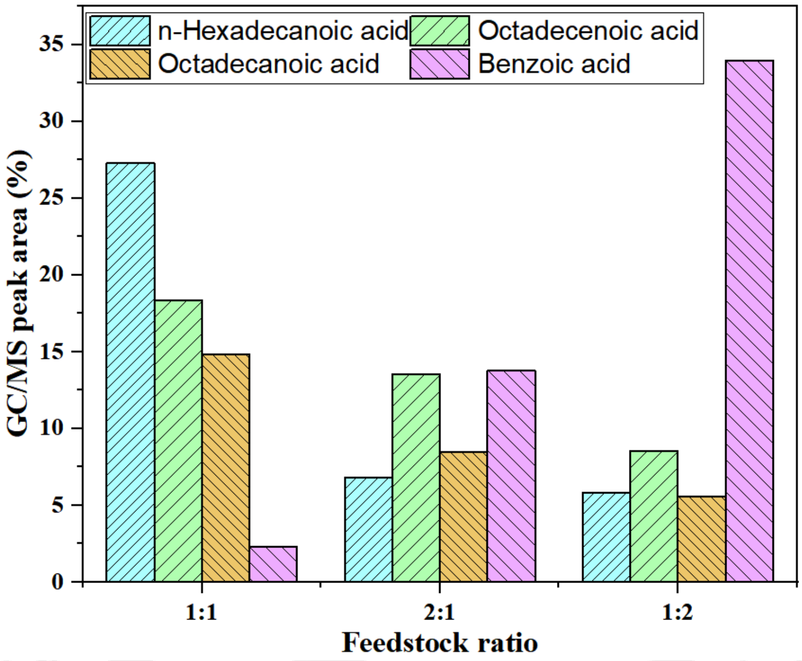

Figure 25. Quantitative comparison of acids produced at different feedstock ratio at optimal conditions

Fig. 26 represents the reaction mechanism of co-pyrolysis of oilseed and PET plastic. The key reaction pathways followed in the co-pyrolysis of *Mesua ferrea* L. oilseed and PET plastic are the decarboxylation of acidic groups and the dehydration of oxygenated compounds. These reactions occur due to the formation of reactive free radicals. In contrast to the decomposition of PET plastic, the triglycerides in oilseed decompose at lower temperatures, producing oxygenated compounds such as long-chain fatty acids and hydroxyl radicals. These compounds initiate the decomposition of PET plastic by hydrogen abstraction, further generating aliphatic hydrocarbons with activated hydrogen species that interact with the free radicals produced from oilseed decomposition to form aliphatic long-chain alcohols [225]. Additionally, the hydroxyl radicals favour the secondary reactions of volatiles produced from PET plastic degradation. The hydrogen released through the midchain β-scission reaction of PET facilitated the breakdown of triglycerides and carboxylic acid through decarboxylation and decarbonylation processes, eliminating oxygen as CO_2 and CO, respectively. This increases the H/C of the oil, thereby increasing the HHV and stability of the bio-oil [224].

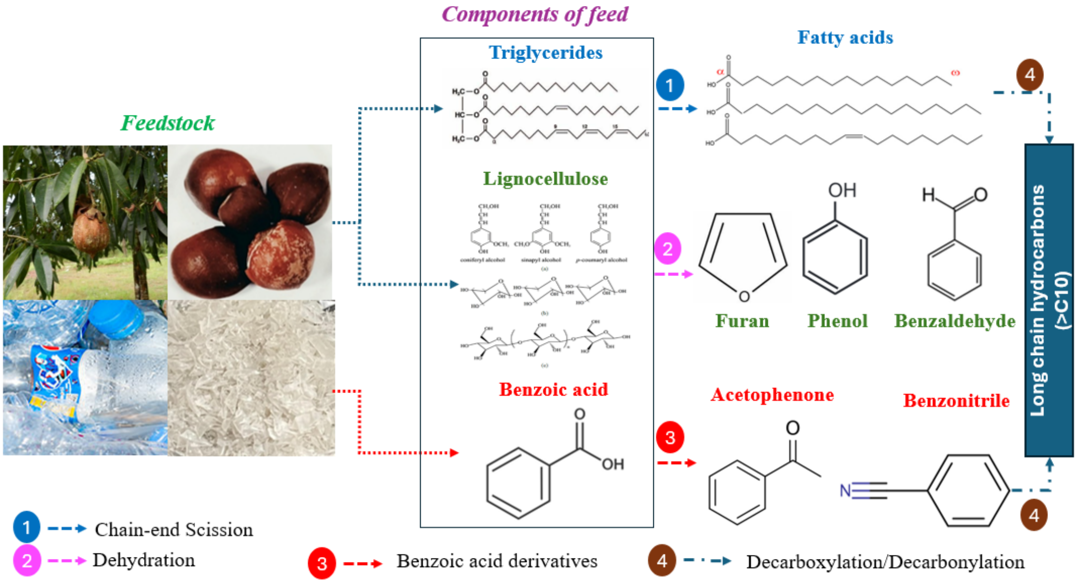

Figure 26. Typical reaction steps involved in co-pyrolysis of oilseed and PET plastic

4.4 Conclusion

This research explored the combined impacts on oil yield and quality when *Mesua ferrea* L. and PET plastic were co-pyrolyzed in varying ratios (1:1, 2:1, 1:2 w/w) at 550 to 650 °C. The maximum oil yield (35 wt.%) was observed at 600 °C for 2:1 feedstock ratio. The HHV of the oil 39.28 MJ kg^{-1}. The hydrocarbon content of the co-pyrolytic oil of 2:1 feedstock ratio was higher (10%) as compared to other feedstock ratios (1:1- 1.3% and 1:2- 2.9%). The presence of plastic hindered the degradation of oilseed, particularly at lower temperatures such as 550 °C, leading to higher yield of solid biochar and hindering the production of low molecular weight compounds. Plastic interactions with aromatic compounds interfered with the breakdown of oxygen molecules of the acidic functional groups of the oilseed. When the two feedstocks were mixed, synergy among the different intermediates facilitated the cracking of each polymer, resulting in the combined effect of more significant aromatic compounds (≥3 rings). As observed in the present study, these synergistic effects hold the potential for effective utilization and optimization of such feedstocks in pyrolytic-oil production processes, enabling their transformation into various value-added products.

Chapter 5.

Low cost-catalyst development using red-mud for catalytic hydrodeoxygenation of model compound

5.1 Introduction

Recently, much research is focused on the oxygen group removal of ROOH and R-O-R, which are significant compounds of bio-oil derived from non-edible oilseed [142]. These compounds are usually converted to high-grade biofuels through catalytic hydrodeoxygenation (HDO) reactions, offering a pathway for oxygen removal without carbon loss i.e., without decarboxylation or decarbonylation reactions [226]. In this perspective, noble metals such as Pd, Pt are the most effective and durable catalysts, but their high cost and limited availability inhibit widespread practical application. Therefore, there is an urgent need to develop affordable and readily available catalysts that exhibit high activity for this purpose [147].

Catalysts play a vital role in hydrodeoxygenation of fatty acids. Traditional catalysts supported with sulfided or noble metals are extensively studied in the hydrogenation/hydrodeoxygenation (HYD)/HDO process. Conventional catalysts such as metal sulfides (CoMoS and NiMoS) are proven to yield high conversion; however, due to the continuous addition of sulfur to the catalyst, the products suffer contamination [126]. The phosphides, carbides, and nitrides exhibit activity similar to sulfur and have gained attention in deoxygenation reactions. The major challenge of using these catalysts is that they are easily prone to deactivation by dehydration reactions [227]. Moreover, noble metals such as Ru, Pt, and Pd are also expensive. Conversely, transition metals like Ni, Co, and Mo were demonstrated to be very effective in producing hydrocarbons [228].

Among the non-noble metals, Ni is considered a feasible catalyst due to the ability of hydrogenation to produce deoxygenated reactions at low temperatures. According to the literature, both the dispersion of Ni particles and the nature of the support material affect the catalytic activity of the catalyst. A recent study on the hydrodeoxygenation of stearic acid in the presence of Ni-doped over hierarchical ZSM-5 showed a conversion of 100% to produce C8-C17 hydrocarbons [148]. However, a significant drawback of using mono-metallic Ni is the accumulation of Ni particles on the surface of the support due to excess surface energy. This challenge is usually addressed either using a high surface area support or doping with two or more metals over the support. In this respect, adding Co to Ni-based catalysts has gained much attention due to its stability and reduction in coke formation [149]. A study on the synergistic effect of Ni and Co over carbon support demonstrated a positive interaction of both metals when compared to the mono-metallic HDO of guaiacol, leading to C-O cleavage [229].

The support material plays a critical role in the HDO process. The traditional support materials, such as zeolites and metal oxides, have poor stability and lower tolerance to water, and are cost-ineffective. Therefore, developing a practical, cheap, and readily available catalyst support is crucial. This study employs red mud, a waste produced during bauxite ore processing activity. This is composed of various oxides such as Fe_2O_3, Al_2O_3, and SiO_2. Red mud is an alkaline material and dumping it in landfills creates many problems, like groundwater contamination. The presence of various metal oxides indicates its possibility of being used as catalysts[230]. Additionally, the presence of alkaline earth metals such as CaO and Na_2O can effectively reduce the formation of coke. The hydrogenolysis cleavage and formation of hydrogen are also favourable in red mud-supported catalysts due to the presence of the basic sites [230].

Additionally, recent research has explored the HDO of palmitic acid using Ni/RM and Ni-MoOx/RM catalysts. With 7 wt% Ni loading on RM at 260 °C, the reduced Ni/RM catalyst achieved 100% conversion of palmitic acid with a strong selectivity for pentadecane formation, indicating a decarboxylation/decarbonylation reaction pathway [152]. When MoOx was added at 7 wt% loading to Ni/RM and the reaction was conducted at 250 °C, the maximum yields were 40% hexadecane and 20% pentadecane [151]. While studies have explored catalytic HDO of palmitic acid using reduced red mud catalysts, there is limited literature focusing on the role of Ni and Co oxides (in pre-reduced or calcined form) in promoting the hydrodeoxygenation pathway to produce hexadecane at lower temperatures, around 240 °C.

In this work, Ni and Ni-Co oxide catalysts supported on RM were synthesized using the wetness co-impregnation technique and calcined at 550 °C. The catalytic activity tests carried on palmitic acid which is a major component of fatty acid in waste cooking oil used to produce diesel/sustainable aviation fuel. Meanwhile, operating parameters such as reaction temperature (210 – 270 °C), reaction time (3 – 5 h), initial hydrogen pressure (3 – 5 MPa) and recyclability of the best suitable catalyst were also performed to propose a plausible reaction mechanism.

5.2 Materials and Methods

The HDO experiments were carried out using a 100 mL high pressure stirred batch reactor. In a typical experiment, the reactor was charged with 30 mL of 5 wt.% palmitic acid in n-decane (solvent), and 10 wt.% of the calcined catalyst. In the case of HDO with physically mixed catalysts, each of the 10 wt.% of X/RM (M: Ni, Ni-Co) was charged into the reactor. The reactor was closed tightly, and in order to remove the trapped air, it was purged several times using H_2. Finally, the reactor was pressurized with H_2 to 30-50 bar at room temperature. The reactor was then heated to the final temperature while continuously stirring the reaction mixture at 450 rpm. After holding the reaction mixture at the set temperature for definite period of time (3-5 h), the reactor was opened after cooling it to 35 °C. The reaction products were separated from the catalyst by filtration, and analyzed using GC/MS. More details on the product characterization methods are available in Section 2.2.3.2. A schematic of experimental procedure is provided in Fig. 27.

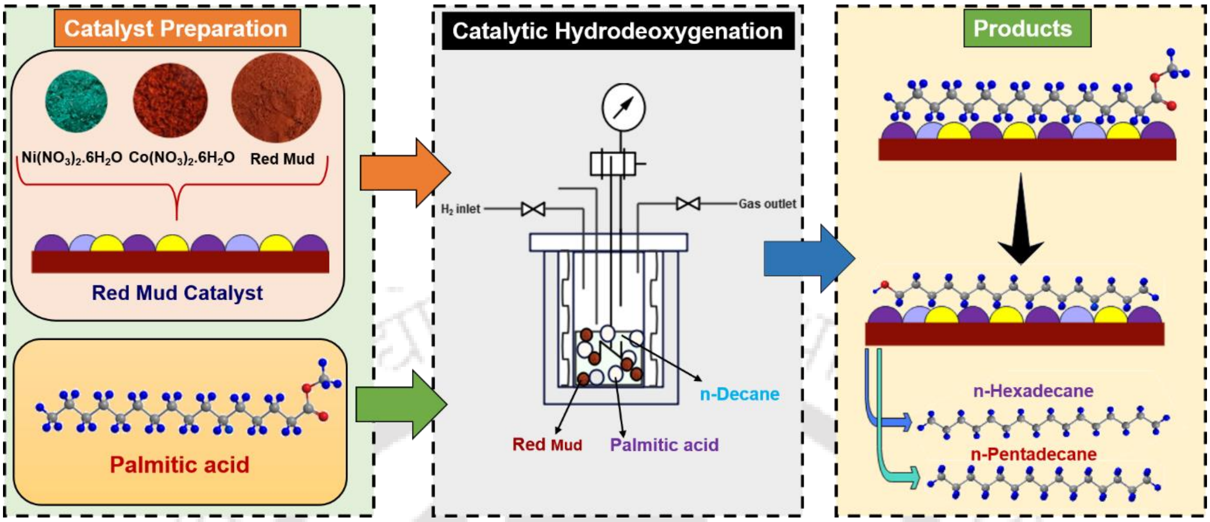

Figure 27. Schematic representation of catalytic hydrodeoxygenation of palmitic acid

5.3 Results and Discussion

5.3.1 Catalyst Characterization

The chemical composition of the crystalline oxides in the calcined RM samples as analysed using XRD and presented in Fig. 28. From the XRD analysis; it can be observed that the RM contains various metal oxides such as aluminium oxide (Al_2O_3), hematite (Fe_2O_3, 2θ: 54.16), Quartz (SiO_2), titanium oxide (TiO_2), and Hercynite ($FeAl_2O_4$) [231]. The diffraction peak at 2θ of 37.1° confirmed the SiO_2 (1 1 0), 24.2° is due to the TiO_2 (rutile) phase (1 0 1), and at 2θ of 41° corresponds to $Ca_2Al_2SiO_7$. A peak of sodalite ($Na_8Al_6(SiO_4)_6Cl_2$) was observed at 2θ 14.06° corresponding plane at (1 1 0) [140]. The XRD pattern had a combination of amorphous and crystalline peaks. The presence of characteristic elements such as Fe (42-47 wt%), Si (14-15 wt%), Al (21-22 wt%), Ti (5-6 wt%), Ca (3-5 wt%), and Na (3-4 wt%) are also confirmed from ICP-AES elemental analysis. Importantly, the XRD pattern of the RM support was retained in Ni/RM and Ni-Co/RM catalysts. The presence of NiO was detected at 2θ 35° (1 1 1) and 41° (2 0 0), and Co_3O_4 and Co were observed at 2θ 36° and 45° corresponding to (3 1

1) and (1 1 1) respectively and these proved the successful impregnation active metals on the support [232]. Additionally, the peak of $NiFe_2O_4$ was observed due to a possible interaction between the Ni and Fe compounds. From the ionic radius of Fe (92 pm), Ni (83 pm), and Co (79 pm), it can be inferred that Ni, and Co could have penetrated into Fe lattice [233]. According to Debye-Scherrer equation, the average crystallite size of the mono-metallic catalyst was calculated to be 18 nm and 15 nm for bimetallic catalyst. This indicates that the increase of metals on the surface of the support decreases the crystallite size. The addition of Co into the lattice Ni can also be confirmed from the lattice distortion parameters. It can be calculated using $(2\beta)^2\cos^2\theta = 4/\pi 2(\lambda/D_{hkl})^2 + 32 <\varepsilon^2_{hkl}> \sin 2\theta$, where D_{hkl} is the average thickness of the lattice face, λ is the wavelength of X-ray, θ is the diffraction angle, and β is the corrected full-width at half-maximum of the diffraction peak; $<\varepsilon^2_{hkl}>^{1/2}$ is the lattice distortion. From the above, the lattice distortion values of Ni-Co/RM (0.19×10^{-2}) is found to be greater than Ni/RM (0.15×10^{-2}), indicating the incorporation of Co in the NiO lattice. From, the BET surface area analysis, it was noticed that the average pore size of Ni/RM (22 nm) and Ni-Co/RM (20 nm) agreed with the results obtained from the crystallite size obtained from the XRD analysis [231].

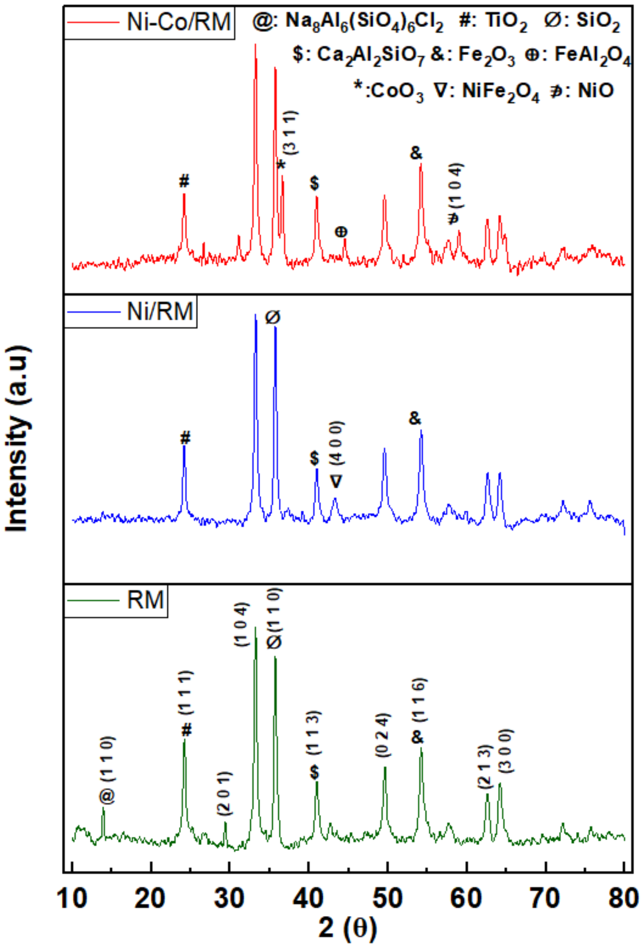

Figure 28. XRD pattern of fresh red mud supported catalysts

Catalyst surface morphology and topology were studied using SEM. Fig. 29 shows the agglomeration of support particles with random configuration. It was also confirmed that RM particles are of irregular size and shape with few particles having elongated with rough surfaces. It was observed that some tiny particles are stuck over other moderately sized particles along with agglomerations and cluster formation. Hence from the SEM of RM, it can be concluded that the particles were polydisperse with uneven surface and functionalities. Such a surface provides active catalyst sites for adsorption and reaction of oxygen [137]. The morphology changes in the RM support are evident due to the immobilization of Ni, Co active metals. However, it was confirmed that the physical structure and texture of RM remain unchanged after impregnation. The SEM and TEM images reveal the dispersion of Ni nanoparticles of an average particle size of ~100 nm. Additionally, a higher accumulation of particles compared to the RM was observed indicating a similar rough surface. Moreover, Ni loading may block the pores of RM, resulting in a decrease in surface area as indicated in Table 1. When Co metal was immobilized on the support along with Ni, there was a decrease in the average particle size (~90 nm). For Ni-Co (Fig. 29 (c)), some tiny curvy metal particles are found to be coated over RM particles [234]. FETEM-EDX analyses of all catalysts are shown in Fig. 30. The presence of elements namely Si, Na, Fe, Ti, and Al can be seen in the RM. Furthermore, Ni (in case of Ni/RM: 9.13 wt% and Ni-Co/RM: 4.31 wt%) and Co (4.01 wt%) are found in RM supported catalysts, which is consistent with the ICP-AES results. Uniform dispersion of Ni and Co is shown in mapping results. SAED pattern of all the catalysts confirm the polydisperse nature. The d-spacing obtained from SAED patterns are in well agreement with the XRD patterns.

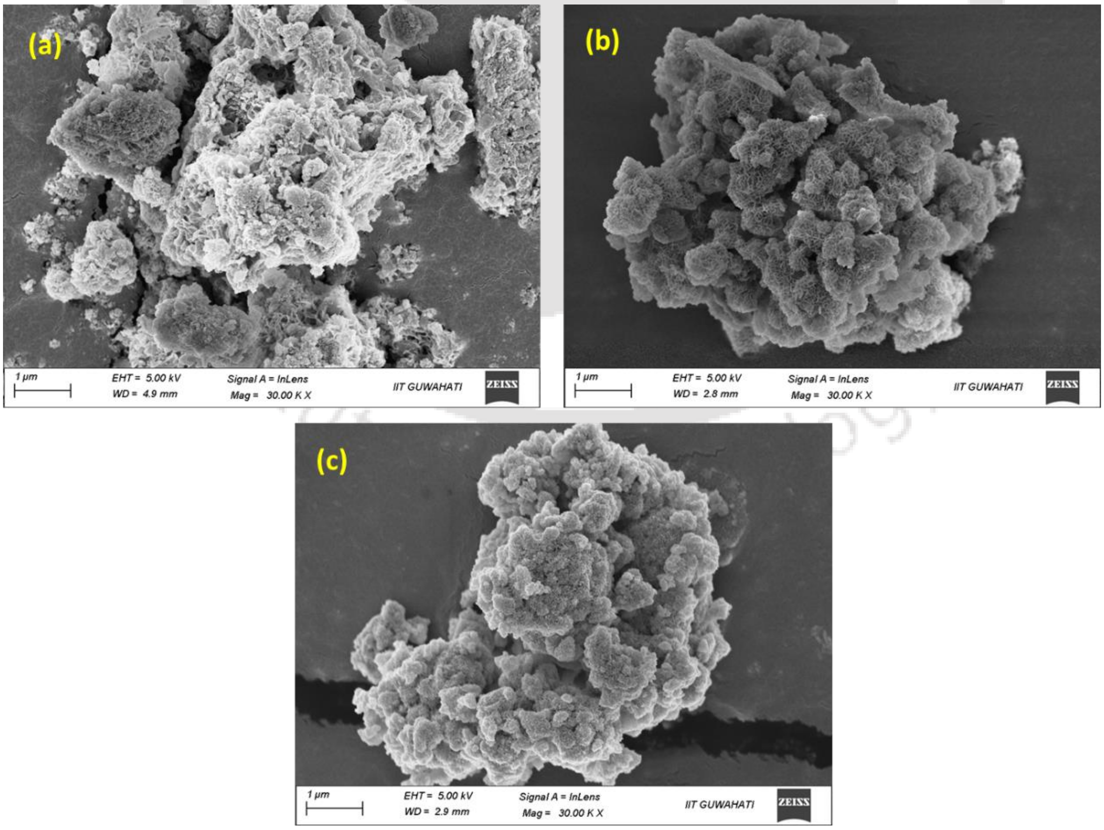

Figure 29. FESEM image of fresh (a) RM (b) Ni/RM (c) Ni-Co/RM

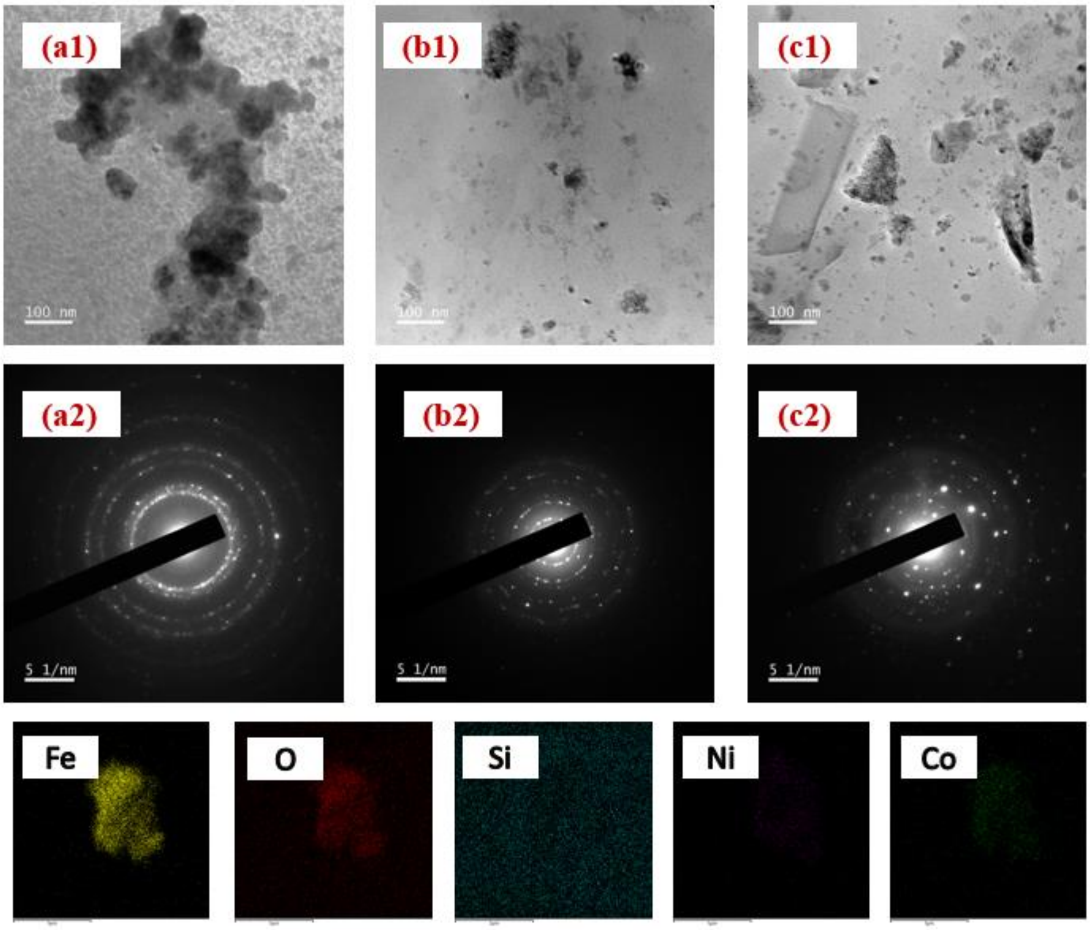

Figure 30. FETEM image of fresh (a1) RM (b1) Ni/RM (c1) Ni-Co/RM; SAED pattern of (a2) RM (b2) Ni/RM (c2) Ni-Co/RM; Elemental mapping of (c2) Ni-Co/RM

The N_2 adsorption−desorption measurements were used to calculate the BET surface area and textural properties of the RM support and the Ni/RM, Ni-Co/RM catalyst. These pores generally facilitate a better the mass transfer between reactant and intermediate molecules [235]. The porous characteristics of the catalysts are displayed in Table 32. It is evident that BSA of Ni/RM is lesser than Ni-Co/RM.

Table 32. N_2 - sorption analysis for different red mud supported catalysts

Catalysts	BSA (m^2/g)	A_{ps} (nm)	T_{pv} (cc/g)
RM	38	11	0.1
Ni/RM	25	22	0.1
Ni-Co/RM	29	20	0.2

*RM: Red mud (support), Ni: Nickel, Co: Cobalt, BSA: BET surface area, A_{ps}: Average pore size, T_{pv}: Total pore volume

As presented in Table 32, the parameters such as pore volume, pore diameter, and BET surface area of all the samples are significantly lesser than that of the support. The high specific surface area of the RM support is advantageous for immobilizing and distributing active metals on its surface. This contributes to enhancing the activity of the catalysts while resisting the deactivating process [236].

The electronic state of the various elements and their composition were determined by the XPS analysis. Fig 31(a) shows the survey spectra of all the catalysts indicating the existence of elements mainly Na, Al, Si, Fe, O, Ni and Co. The results from survey spectra of XPS are in accordance with EDS and ICP-AES analysis. Moreover, the elements present in the support were also seen in the catalyst indicating that the properties were not affected by the wet impregnation of active metal. Fig. 31(b) describes the presence of Fe 2p in three distinct peaks which are found at Fe 2p3/2 (710.9 eV), Fe 2p1/2 (724.5 eV) and a satellite peak (718.9 eV) confirming the presence of Fe_2O_3 [237]. The amounts of Fe were calculated to be 9.3 at%, 4.9 at%, and 5.0 at% in RM, Ni/RM and Ni-Co/RM, respectively. The presence of Ni 2p is confirmed from Fig. 31(d), with different peaks at Ni 2p1/2 (873.8 eV) with a satellite peak (879.1 eV) and Ni 2p3/2 (856.2 eV) with its satellite peak (861.2 eV). This shows the presence of Ni-O in both Ni/RM and Ni-Co/RM catalysts [238]. Additionally, Ni 2p peaks were present in both the catalysts at 852.2 eV and 869.4 eV [238]. The concentration of Ni 2p3/2 in Ni/RM was in the range 7-8% in Ni/RM and Ni-Co/RM indicating a higher concentration at the surface. This indicates that the metal dispersion on the support could be slightly non-uniform. Furthermore, the presence of Co 2p spectrum was confirmed in the Ni-Co catalyst as shown in Fig. 4(e). The peak corresponding to two spin orbit doublets of cobalt oxides at 780.8 and 795.9 eV are assigned to Co^{+3} $2p_{3/2}$ and Co^{+3} $2p_{1/2}$ [239] ,respectively. The difference of 15 eV in binding energy between Co $2p_{3/2}$ and Co $2p_{1/2}$ indicates that the Co_3O_4 is in cubic phase[240].

Further, the Co-O bond is also confirmed from the XPS spectra at 530.0 eV with atomic composition of 3.74%.

Fig 31(c) represents the oxygen species associated to O_α and O_β. The peak (O_β) at 531.1 eV is represented by lattice oxygen of the metal oxides (Fe-O, Ni-O, Co-O), electrophilic oxygen, and oxygen vacancy. The peak (O_α) at 530.9 eV represents the oxygen in the crystal lattice[18]. As per the atomic concentration report, the oxygen content was 67.1 at%, 61.14 at%, and 67.1 at% in RM, Ni/RM and Ni-Co/RM respectively. The decrease oxygen content in Ni/RM shows that it forms Ni-O. Among the three types of oxygen, O_β (531.1 eV) is assigned with O^{2-} ions near the oxygen defects with metal oxides. This peak generally indicates the presence of lattice defects, also known as oxygen vacancies. The ratio of $O_\beta/O_\alpha+O_\beta$ is used to determine the density of lattice defects. From the area under the curve, the ratio of $O_\beta/O_\alpha+O_\beta$ of the Ni-Co/RM (0.694) is higher than Ni/RM (0.614) [241]. This indicates that the oxygen vacancies at the surface are higher than those in a mono-metallic catalyst. It is well-documented in the literature that incorporating smaller metal ions causes adjacent oxygen atoms to shift toward the dopants. These shifts create distortions in the oxygen lattice potentially increasing the lattice strain, which can be alleviated by forming an oxygen vacancy near the dopant. XRD studies demonstrated that Co ion doping in a bimetallic catalyst resulted in greater lattice distortion and a significant increase in oxygen vacancies compared to that of a mono-metallic catalyst [242].

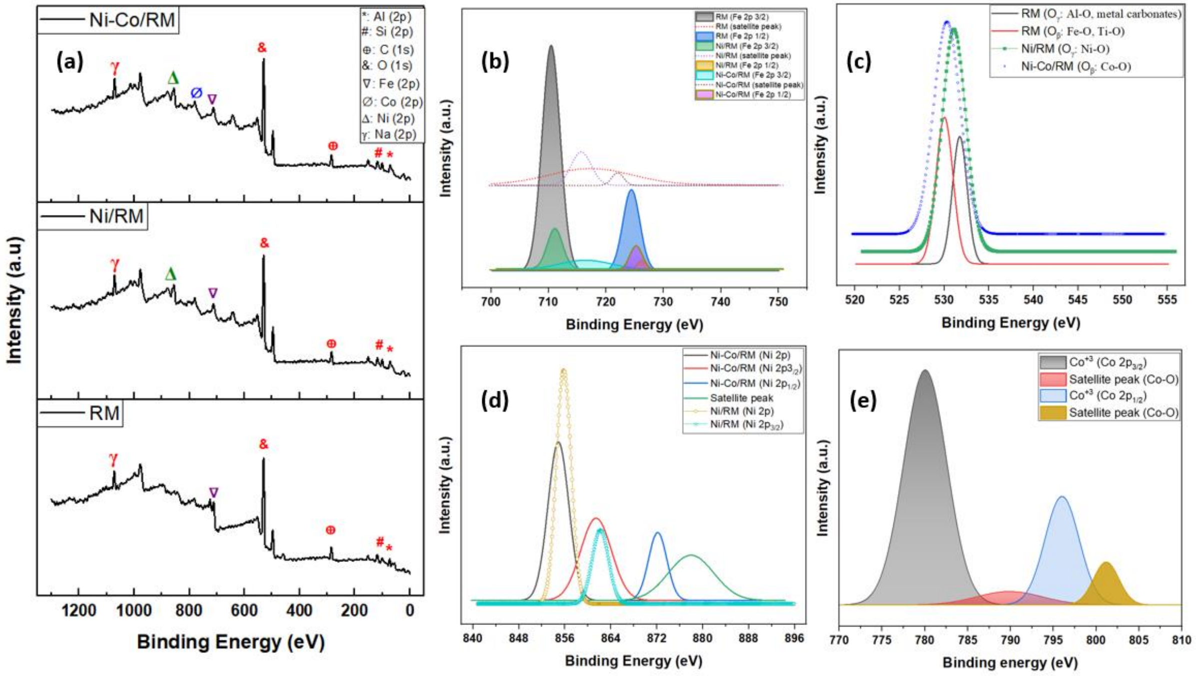

Figure 31. (a) XPS Survey spectra of all catalysts; XPS spectra of (b) Fe 2p (c) O 1s (d) Ni 2p (e) Co 2p

5.3.2. Catalytic Hydrodeoxygenation of palmitic acid

Long-chain fatty acids represent a significant fraction of bio-oil derived from biomass such as oilseeds and microalgae[182,243]. Hence, palmitic acid was used as a model compound in this study. Initially, the effect of support (RM), mono-metallic (Ni/RM), and bi-metallic catalysts (Ni-Co/RM) was investigated, and the result indicated that Ni-Co/RM is better suited catalyst with respect to conversion of palmitic acid to alkanes with high selectivity to hexadecane.

The conversion of palmitic acid is 100% with all catalysts as shown in Fig. 32. The calcined RM facilitates the decomposition of hydroxides and carbonates into oxide. Adding metals to catalyst support increases the catalytic activity concerning the scission of chemical bonds. The catalytic activity of RM support indicated 100% conversion with high selectivity towards pentadecane, indicating decarboxylation as a primary pathway. The addition of Ni metal to RM decreased the selectivity toward pentadecane (8.37%) while increasing of the selectivity of hexadecanol (59.6%) and hexadecane (22.2%). A recent study suggests that the scission of H-OH bond of intermediate alcohol is the rate-controlling step in conversion of palmitic acid to linear chain alkanes[241]. Compared to mono-metallic catalysts, the bi-metallic catalyst exhibited superior activity in terms of yield and selectivity of alkanes. Adding Co enhances the selectivity of hexadecane (64.5%) while significantly decreasing the formation of pentadecane (0.8%). According to the literature, the oxygen vacancies play a vital role in the adsorption of acid and alcohol molecules in the active sites by weakening the C-O bond. This adsorption usually facilitates the dehydration reaction[244]. In light of the above findings, Ni-Co/RM was chosen as a well-suited catalyst for optimization of reaction conditions.

As shown in Fig 32 (a), adding Ni over red mud favours a decarboxylation (DCX) route by increasing the selectivity towards pentadecane (C15). The scission of C-C bond over Ni sites can be attributed to the DCX pathway. Adding Co to Ni/RM increases the oxygen vacancies, leading to higher selectivity towards hexadecanol, which further undergoes dehydration and hydrogenation to produce hexadecane (C16). This is the preferred route, favouring the hydrodeoxygenation (HDO) route by preserving the carbon chain length. The oxygen vacancies play a critical role in the HDO pathway as an adsorbent for fatty alcohols, facilitating conversion to long-chain alkanes[245]. Hence, the carboxylic group (-COO) is activated to be transformed into intermediates namely hexadecanol and hexadecanal, while the DCX reaction occurring on the Ni active sites is effectively controlled. The presence of weak acid sites can also efficiently catalyse the conversion of hexadecanol into the corresponding alkanes by dehydration reactions[150].

As described in the XPS analysis, the electronic properties of Ni enhance the C-C and C-H bond cleavage. Additionally, the NiO-supported catalysts significantly reduce the activation energy of hydrogen dissociation as the oxygen vacancies can trap hydrogen[246]. A study on the deoxygenation concerning the DCX pathway of triolein indicated that the NiO-supported Zeolite Y (84.28%) had better selectivity towards the production of hydrocarbons (C13-C18) compared to CoO, which had higher selectivity towards heavy hydrocarbons (3.80%)[247]. Also, studies on the hydrodeoxygenation of palm oil indicated that Co/Al_2O_3 exhibited superior performance concerning conversion and yield (HDO pathway) when compared to Ni, Pd, and Pt [248].

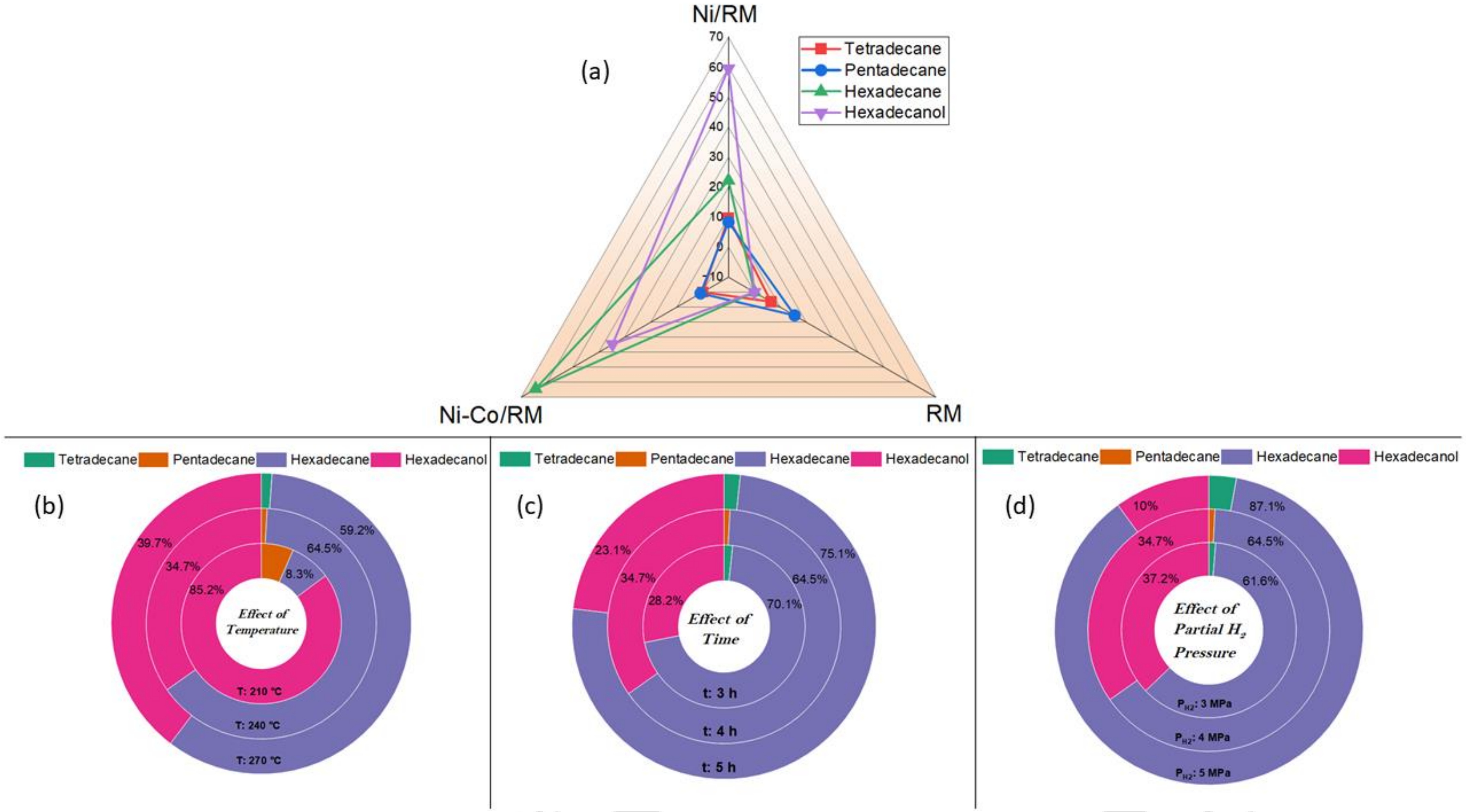

Figure 32. Effect of different operating conditions on catalytic hydrodeoxygenation of products (a) types of catalyst (b), (c), (d) effect of temperature (°C), time (h), initial partial pressure (MPa) when Ni-Co/RM is used

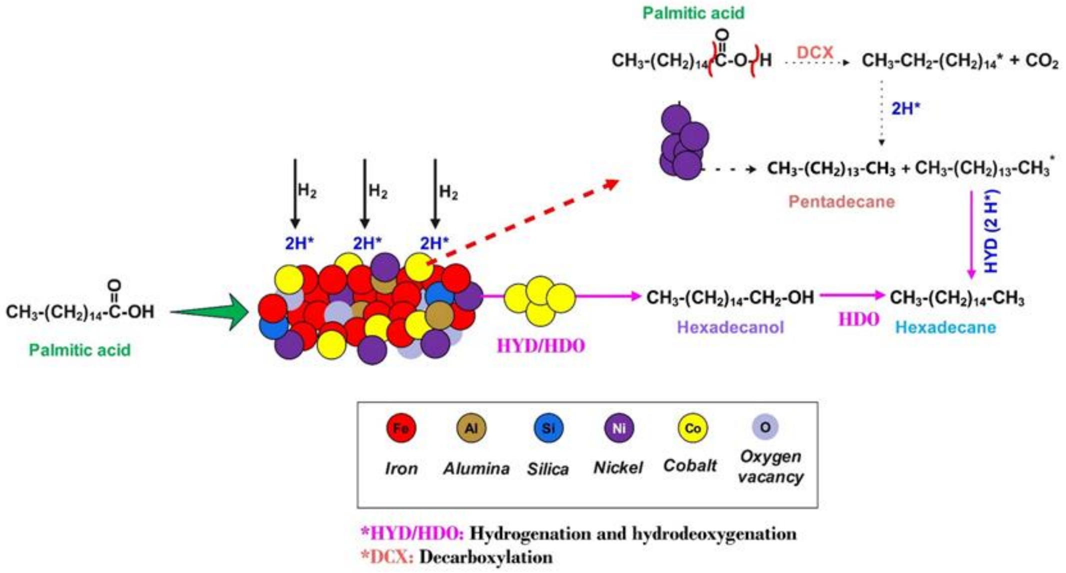

Figure 33. Reaction mechanism describing the conversion of palmitic acid

Temperature plays a vital role in the hydrodeoxygenation reactions. As shown in Fig. 32 (b), the temperature was varied from 210-270 °C with a gradient of 30 °C. At 210 °C, the primary product was methyl palmitate, followed by hexadecanol (selectivity: 85%). At a lower temperature of 210 °C, the formation of pentadecane and hexadecane was observed to be low (6.53% and 8.32%, respectively). Moreover, there was traces of tetradecanal, indicating that the reaction pathway followed is predominantly decarbonylation to give fatty aldehydes. As the temperature was increased to 240 °C, the conversion was still 100%, but the selectivity to hexadecanol decreased (34.73%), while hexadecane (64.45%) increased with traces of pentadecane (0.81%) was in traces. Further increase in the temperature, increased the yield of short-chain alkenes and alkanes while increasing the selectivity of hexadecanol (39.66%). A study reported 100% conversion with 99% selectivity to hydrocarbons at 300 °C over 7% Ni/RM [151]. Another study indicated that the addition of 7% of Mo over Ni/RM decreases the conversion while increasing the deoxygenated products at 250 °C [152]. The HDO of palmitic acid involves 3 major pathways, viz., decarbonylation (DCN), decarboxylation (DCX) and hydrodeoxygenation (HDO). Typically, in DCN and DCX, loss of carbon atom occurs in the form of carbon monoxide (CO) and carbon dioxide (CO_2), respectively. As a result, the overall chain length of alkanes decreases, forming compounds such as pentadecane (C15). In contrast, the HDO pathway removes the oxygen without affecting the carbon chain length. At higher temperatures, the reaction pathway shifts from DCN/DCX to HDO as indicated by the higher ratio of hexadecane/pentadecane [249].

Compared to RM, Ni/RM shows higher HDO activity with regard to selectivity towards hydrocarbons. Residence time is considered an important reaction parameter in HDO. As observed from Fig. 32 (b), at a reaction time of 3 h, the selectivity to tetradecane was 1.7%, and hexadecane was 70.1%. An increase in reaction time to 4 h decreases the selectivity to hexadecanol (34.73%), while increasing the selectivity to hexadecane (64.45%). The highest hexadecane (75.1%) was obtained at 5 h, indicating that the hydrodeoxygenation pathway is the dominant reaction. At 5 h, the production of hexadecanol was reduced to 23%, while palmitic acid conversion was still maintained at 100%. This indicates that increased reaction time increases the selectivity to heavier hydrocarbons (C16) while reducing that of the oxygenates. A study on the HDO of palmitic acid over Ni/TS-1 catalyst indicated that a reaction time of 8 h is required for the complete conversion of palmitic acid with selectivity of hexadecane as high as 8.4%. In this study, the primary product formed was pentadecane, indicating that decarbonylation is a significant pathway [153].

The hydrogen (H_2) partial pressure is crucial for the hydrogenation reaction. As shown in Fig. 32 (d), the H_2 partial pressure significantly impacts the conversion of long chain fatty acid. At a lower H_2 pressure of 3 MPa, alkanes, fatty alcohols, and fatty aldehydes were detected, indicating that the deoxygenation efficiency of catalyst is insufficient at low hydrogen pressures. Additionally, hexadecanol remains the primary product with a selectivity of 37.15%

at 3 MPa. At 4 MPa, fatty aldehyde disappeared. The selectivities to fatty alcohol at 4 MPa and 5 MPa were 34.75% and 10.0%, respectively. These findings show that higher H_2 pressure enhances the selectivity of hexadecanol and hexadecane. The partial pressure of H_2 influences the adsorption of it on surface of catalyst. Consequently, increasing H_2 pressure increases the formation of hexadecane, aligning with previous studies[151]. The hexadecane content rises with higher H_2 pressure i.e., 87.5% at 5 MPa, making alkanes the main product. Hexadecanal was not detected at 4-5 MPa. The above-mentioned results suggest that the primary reaction pathway is HDO. Fig. 33 indicates the plausible reaction mechanism for conversion of palmitic acid to linear-chain hydrocarbons.

5.3.3 Recyclability of Catalyst

The catalyst obtained at optimal conditions was recovered using filtration and dried at 105 °C for 12 h before performing the recyclability test and it is described in Fig. 34. These reactions were performed at 240 °C, 5 MPa H_2 for 4 h. The selectivity to hexadecanol remains stable at around 12.9%, with higher selectivity towards hexadecane (73%) upto 3 cycles. In the 3rd run, the conversion and selectivity to alkanes were 92% and 69%, respectively. However, reduction catalyst activity was observed at the 4th and 5th runs. In the 5th cycle, the conversion decreases to 77% at 240 °C. The fatty alcohol, i.e., hexadecanol, is the primary compound 4th and 5th recycle with selectivity of 28% and 43%, respectively. The reduction in conversion and alkane selectivity is possibly resulted from the deactivation of the catalyst via coking. The FTIR patterns of fresh and spent catalyst indicate that the presence of coke along with the peaks of actual metals in the catalyst. In particular, the presence of H-O-H of cancrinite (1649 cm^{-1}), C-O of carbonate (1402 cm^{-1}), Si-O-Al (973 cm^{-1}), Fe-O of hematite (534 cm^{-1}), Co-O of spinel Co_3O_4 (663 cm^{-1}) is observed in both fresh and spent catalysts [250]. The functional groups associated to coke formation such as C=O of carboxylic acid and C-O in alcohols is evident in the spent catalyst [251]. These findings indicate the formation of coke in the spent catalyst which are provided in Fig. 35.

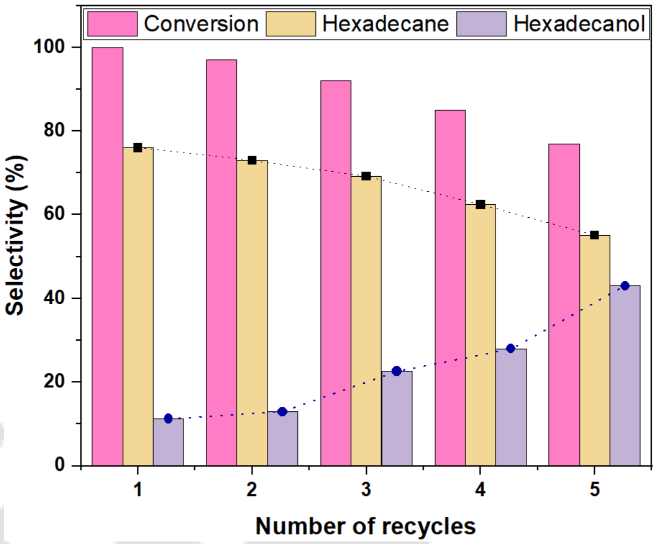

Figure 34. Effect of catalyst recycle with respect to conversion of palmitic acid and product selectivity

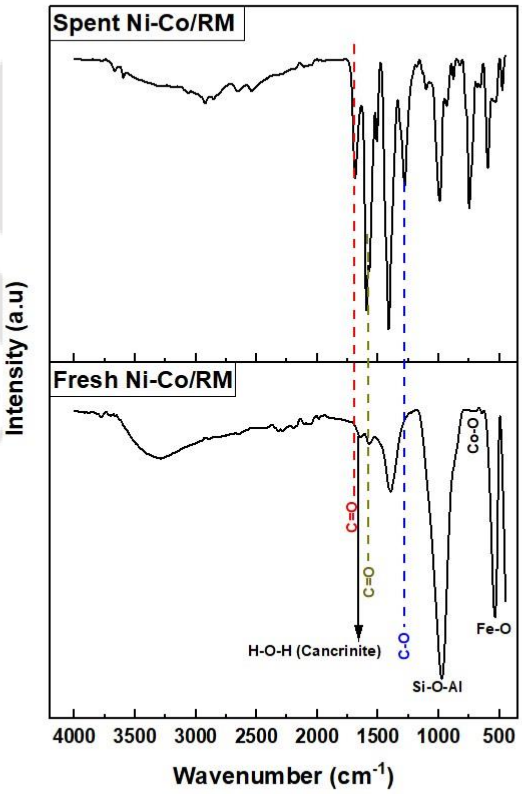

Figure 35. FTIR of fresh and spent Ni-Co/RM catalyst

5.4 Conclusion

In this study, Ni/red-mud and Ni-Co/red-mud catalysts were prepared and their activity for hydrodeoxygenation of palmitic acid was systematically studied. Optimizing the process parameters for Ni-Co/RM catalysts led to selective production of alkanes and fatty alcohols. XRD analysis indicated that Ni and Co metals were successfully incorporated into the calcined red mud. XPS analysis revealed the formation of increased Ni-O and Co-O species and lattice defects on the catalyst. These defects were crucial for the enhanced catalytic activity of the Ni-Co/RM, which also exhibited a synergistic effect between the active centres, resulting in high efficiency for hexadecane production. At 240 °C, palmitic acid was completely converted by all catalysts, with Ni-Co/RM showing the highest selectivity towards hexadecane at 77.3%. Furthermore, Ni-Co/RM demonstrated stable catalytic activity even after three recycles. This study suggests that oxide-based red mud can be a favourable catalyst for HDO of fatty acids to produce sustainable aviation fuels/value-added chemicals.

Chapter 6.

Catalytic hydrodeoxygenation of the produced co-pyrolytic oil in the presence of the red-mud catalysts and characterization of catalytically hydrodexoygenated oil using different techniques

6.1 Background

The pyrolytic liquid derived from biomass/plastic, known as bio-oil, contains more than 400 types of oxygenated compounds with functional groups, including linear fatty acids, ketones, aromatic acids, and ethers [252]. The elemental analysis of bio-oil indicates that carbon and oxygen are present at 20-50% and 30-40%, respectively. While hydrogen is 10-20% and sulfur and nitrogen are minimal (1-5%). Due to the highly oxygenated nature of the bio-oil, the composition is different from crude oil. Additionally, the bio-oil has an acidic pH and chemical compounds that cause reactions during storage, enhancing the instability of the bio-oil. Compared to crude oil (42 MJ kg^{-1}), the higher heating values of the bio-fuels are very low (15-35 MJ kg^{-1}), which makes them incompatible with being used as an alternate fuel [253]. Hence, to overcome these challenges, it is necessary to reduce the oxygen content of the bio-oil. Given this, catalytic cracking, hydrogenation, or hydrodeoxygenation transforms these oxygenated compounds into hydrocarbons (aliphatic and aromatic). Processes such as catalytic cracking and hydrogenation pose significant challenges, such as excessive coking and poor conversions, prompting more research in catalytic hydrodeoxygenation [254]. During the HDO process, oxygenated compounds are removed by high hydrogen partial pressures (>10 MPa) and a catalyst. This process ensures the conversion of low-quality bio-oil into high-grade biofuels, usually used in motor fuels or the refinery for blending [255].

The reaction mechanism involved in the HDO process usually depends on the structure of the organic compounds. For example, the unsaturated molecules (C=C) undergo hydrogenation, whereas the saturated molecules (C=O) exhibit hydrogen cracking and deoxygenation reactions. Therefore, the oxygenated compounds present in the heavy phase of bio-oil are classified into saturated (convert to alkenes due to hydrogenation) and unsaturated molecules (convert to saturated oxygen compounds due to deoxygenation) [256].

Several parameters, such as reaction temperature, catalyst loading, and hydrogen partial pressure, are crucial in determining the quality of the upgraded bio-oil. The reaction temperature is a vital factor in hydrodeoxygenation among the different parameters. The boiling points of many organic compounds are different; hence, the thermal decomposition of these compounds occurs over a wide range of temperatures [257]. For example, the compounds with functional groups of -CHO (aldehydes) and C=O (ketone) decompose in hydrogen at a temperature between 150 °C and 200 °C. For ether and aliphatic compounds, the thermal degradation temperature is usually considered to be less than 250 °C. Meanwhile, the fatty acids can easily convert to hydrocarbons at a temperature of 250-300 °C [258].

Heterogeneous catalysts play a vital role in the hydrodeoxygenation processes. Much research is focused on developing heterogeneous catalysts due to various challenges. Some of these challenges include easy coke pruning and deactivation [259]. Usually metal oxides are employed in the hydrodeoxygenation of bio-oil as they exhibit high selectivity towards reducing the oxygen content. A study on catalytic hydrodeoxygenation of bio-oil in the presence of Al_2O_3 indicated that the oxygen content was reduced from 42% to 24% [260]. Additionally, it is established in the literature that calcium oxide (CaO) is used to reduce the acid content [261]. Metal oxides like ferric oxide (Fe_2O_3) have less activity in the conversion of ketones and alcohols, whereas Silica (SiO_2) demonstrated better stability in terms of coking [262,263]. Hence, the incorporation of suitable catalysts enhances selectivity toward specific compounds. Furthermore, the cost of the catalysts is also considered an important parameter as it contributes to the overall cost of the process. Selecting an effective catalyst for both activity and economic viability is necessary. In this regard, red mud is a suitable support material for the catalyst [259].

Red mud contains complex pore structures alongside catalytically active metals such as Fe, Ca, Ti, Al, etc [264]. Red mud-supported catalysts have already demonstrated higher selectivity towards facilitating an increase in the number of carbons in the chain. Chemical compounds such as furan and phenols follow the reaction mechanism suggested by Mars-Van Krevelen [265]. A study on the pyrolysis of lignin in the presence of RM revealed that lignin is selectively converted to alkylphenols [266]. Another study suggested that the acidic compounds of the oil can be decreased in the presence of RM. These acids are usually transformed into ketones, but metal oxides such as Fe_2O_3 and CaO inhibit the acid-to-ketones reaction [267].

Bio-oil hydrotreatment is usually accelerated in the presence of noble metals such as Pd, Ru, and Pt supported on alumina, biochar, or other waste materials [268]. Although the advantages of using such metals are typically high, the main challenge is their increased production cost, which limits industrial use [269]. In this regard, transition metals (Ni and Co) have gained widespread interest in the HDO of bio-oil. Nevertheless, the bio-oil's acidity significantly impacts these catalysts' performance. These catalysts are easily deactivated due to the coking and leaching of metals [270]. A study on the HDO of bio-oil in the presence of Ni/RM indicated that at higher loading of Ni (40 wt.%), the upgraded oil yield was 69%. Also, the catalytic activity of Ni/RM was comparable to that of the commercial catalyst (Ni/SiO_2-Al_2O_3) [271].

In this work, Ni and Ni-Co oxide catalysts supported on RM were synthesized using the wetness co-impregnation technique and calcined at 550 °C. The catalytic activity tests was carried out on raw pyrolytic oil produced from co-pyrolysis of *Mesua ferrea* L. oilseed and PET plastic (B:P-2:1). Meanwhile, operating parameters such as type of catalyst (RM, Ni/RM, Ni-Co/RM) reaction temperature (180 – 300 °C), reaction time (2 – 6 h), catalyst loading (10 - 20 wt.%) and recyclability of the best suitable catalyst were also performed to propose a plausible reaction mechanism.

6.2 Materials and Methods

The HDO experiments were conducted in a 100 mL high-pressure stirred batch reactor (make & model). The reactor was loaded with 25 g of bio-oil in a typical run. Initially, the effect of temperature (180-300 ºC) on RM support (alone) was tested. The temperature at which maximum hydrocarbons are produced is used to optimize other parameters. In our study, T:300 ºC produced the maximum aliphatic and aromatic hydrocarbons. Hence, the selection of catalyst was done at this temperature. HDO experiments involves physical mixing catalysts with raw co-pyrolytic oil. The reactor was sealed and purged multiple times with H_2 to eliminate trapped air. It was then pressurized with H_2 to 4 MPa at room temperature. The reactor was heated to the desired temperature while stirring the reaction mixture continuously at 315 rpm. After maintaining the reaction mixture at the target temperature for a specified duration (2-6 h), the reactor was cooled to 35 °C and opened. The reaction products were separated from the catalyst by filtration and analyzed using GC/MS (make & model). The catalyst recyclability test was performed with the catalyst that yielded higher hydrocarbon yield. The spent catalyst was directly fed to the reactor in the same bio-oil to catalyst loading ratio and then the recovered catalyst was further regenerated to analyse the catalyst properties. Further details on product characterization methods are provided in Section 2.2.5.1, and a schematic of the experimental procedure is shown in Fig. 36.

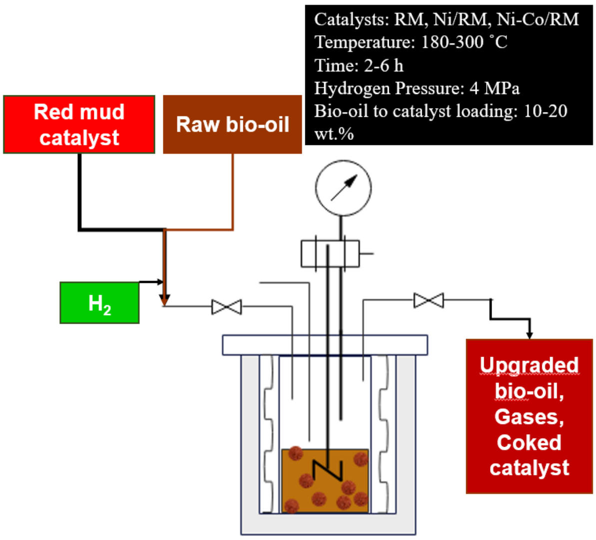

Figure 36. Experimental methodology for catalytic hydrodeoxygenation of bio-oil

6.3 Results and Discussions

The results of fresh catalyst such as RM, Ni/RM and Ni-Co/RM are discussed in detail in section 5.3.1 of Chapter 05.

6.3.1 Effect of temperature on catalytic HDO of raw bio-oil

As red mud contains different metal oxides and can be used as a catalyst, the effect of reaction temperature on the HDO of raw bio-oil was tested. The as-produced raw co-pyrolytic oil (including the aqueous phase) was subjected to HDO in 10 wt.% red mud at 180-300 °C and 4 MPa of initial hydrogen pressure in a Parr reactor. The pressure during the reaction increased to 7.5-8 MPa as the temperature reached 180-300 °C. At the end of the 2 h reaction time, the upgraded oil, coke, and gas were collected, and the effect of temperature on the product distribution is presented in Fig 37 (a). It was observed that the yield of upgraded bio-oil was increased with a decrease in the yield of coke/carbon deposition. The upgraded bio-oil was thick and dark in color. The coke deposition was noted to be less (2.95 wt.%) at higher temperatures (300 °C). This is due to the alkaline nature of the red mud support. Hence, this temperature was chosen for further optimization conditions. The composition of raw bio-oil significantly differed in the temperature range of 180-300 °C. As shown in Fig. 37 (b), the amount of fatty acids decreased from 35.82% to 22.41% as the temperature increased from 180-300 °C. Aromatic acid amounts also decreased drastically from 21.9% to 14.68%. The conversion of fatty acids to linear chain aliphatic hydrocarbons was also observed at higher temperatures (T: 300 °C). An increase in temperature facilitated the formation of more hydrocarbons (39%). The red mud contains many metal oxides of both acidic and basic nature. Generally, the basicity of the catalyst enhances the C-O bond scission via a decarboxylation reaction and reduces coke formation. Meanwhile, the acidic sites facilitate the C-C bond cleavage during deoxygenation reactions. The catalytic effect of RM metal oxides resulted in CO, CO_2, and CH_4 release via decarboxylation (DCX), decarbonylation (DCN), and dehydration reactions [272]. The presence of alkaline metal oxides such as Fe_2O_3, Alumina, CaO, and others usually increases the breakdown of acidic compounds in bio-oil [273].

For example, the decomposition of heavy organic compounds into small-molecule gases often occurs in the presence of Fe_2O_3. The ferric oxide usually promotes the demethylation, demethoxylation, and cleavage of long-chain hydrocarbons. This also increases the production of gases like H_2 and CH_4. Due to the weak acidic nature of the calcium oxide in the red mud, the ketonization of compounds increases [274]. Furthermore, metal oxides, such as alumina, promote forming acids and aldehydes, whereas TiO_2 helps remove methoxy groups. There are also studies showing the effect of CaO and MgO on the deoxygenation of vegetable oil via DCX/DCN reaction. The catalysts containing Cao and MgO have a substantial amount of basicity, due to which the CO_2 is adsorbed on the surface of the catalyst, thereby reducing the coking of the catalyst [275]. Although the catalytic conversion of carboxylic acids (such as fatty acids/aromatic acids) undergoes various reactions, one of the significant routes is ketonization followed by aldol condensation/hydrogenation [273]. Low acidic and aldehyde content is preferable for a bio-oil to maintain stability in terms of physicochemical properties.

Additionally, an enhanced alcohol content of the bio-oil reduces the effect of aging and improves the fluidity of the bio-oil [276]. As the highest amount of hydrocarbons (39%) are produced at T: 300 °C, this temperature is considered for further optimization studies.

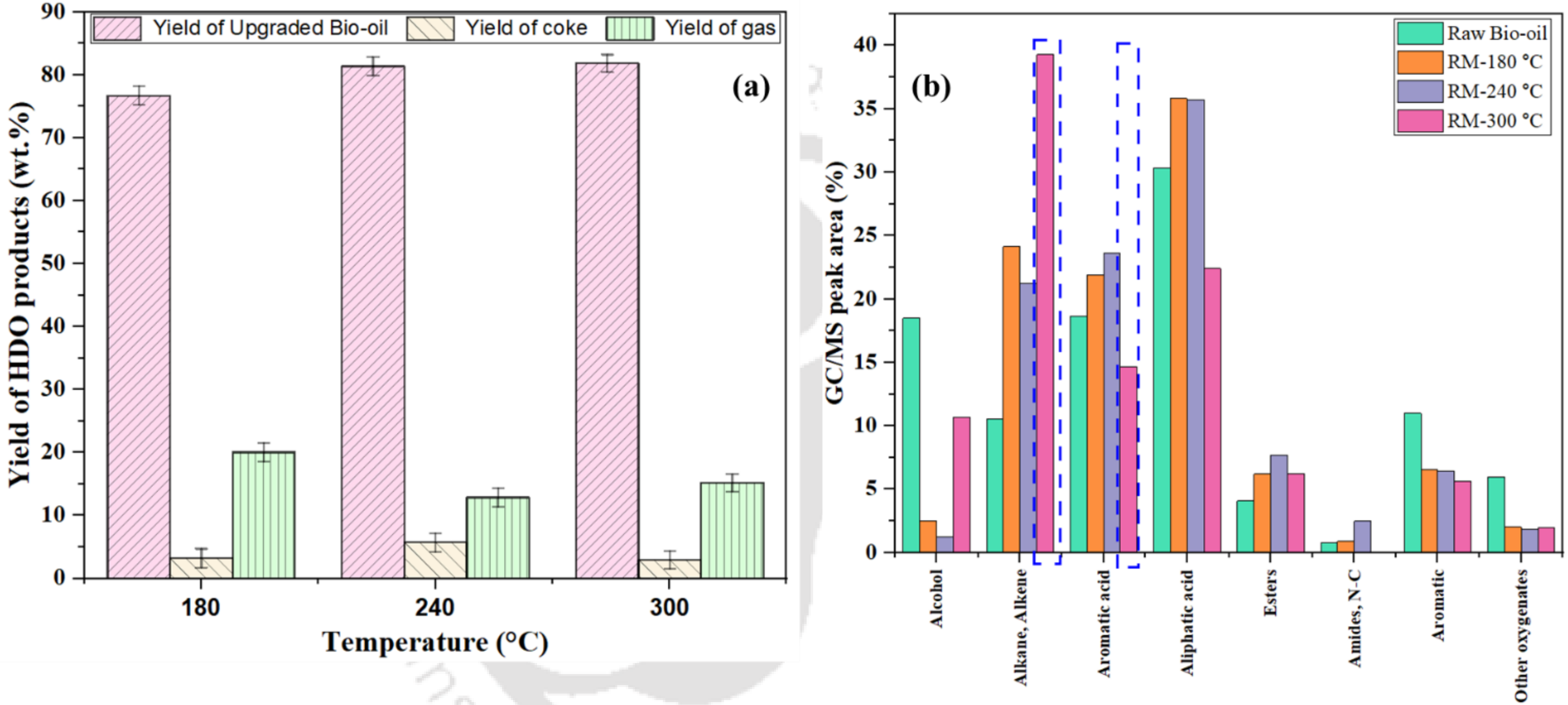

Figure 37. Effect of temperature on HDO of co-pyrolytic oil in the presence of red mud support (a) HDO product distribution (b) Chemical composition of upgraded bio-oil.

6.3.2 Effect of different types of catalyst and reaction time

The as-produced raw co-pyrolytic oil (including the aqueous phase) was subjected to HDO in 10 wt.% RM, Ni/RM, Ni-Co/RM at 300 °C and 4 MPa. The pressure during the reaction increased to 7.5 MPa for RM and Ni/RM. In contrast, it increased to 8 MPa in the presence of Ni-Co/RM as the temperature reached 300 °C. At the end of the 2 h reaction time, the upgraded oil, coke, and gas were collected, and the effect of catalyst type on the product distribution is presented in Fig 38 (a). It was observed that the yield of upgraded bio-oil was decreased with an increase in the yield of coke/carbon deposition with respect to the yield obtained from the red mud catalyst. The coke deposition was lower (6.04 wt.%) in Ni-Co/RM compared to Ni/RM (9.46 wt.%). It was suggested in the literature, that the Nickel loaded catalyst provide excellent coke resistance and further addition of Co to Ni catalyst further reduces the coke deposition. The obtained results are well in agreement with the literature [277]. The raw bio-oil produced from the co-pyrolysis of *Mesua ferrea* L. oilseed and PET plastic contains primary acids, i.e., linear chain fatty acids (hexadecanoic acid, oleic acid, stearic acid), and aromatic acid (benzoic acid). The products from the deoxygenation of linear chain fatty acids usually include compounds with carbon numbers of C15-17, depending on the length of the feed chain. Additionally, CO_2, CO, and H_2O are associated with converting linear chain fatty acids [278]. Decarboxylation/decarbonylation is the usual pathway to transform linear fatty acids into hydrocarbons. The advantage of the hydrodeoxygenation pathway is that the length of the carbon chain is unaffected compared to decarboxylation, where the carbon atoms of the compounds are lost to the atmosphere in terms of CO/CO_2. For example, the decarboxylation/decarbonylation of palmitic acid (C16) leads to n-pentadecane/n-pentadecene (C15) [279].

As shown in Fig. 38 (b), the addition of Ni to RM enhanced the hydrogenation-esterification reaction. In this present study, the formation of octadecanoic acid, 4-hydroxy methyl ester (16%), was observed due to the conversion of octadecanoic acid in the raw co-pyrolytic oil. Usually, the Ni-based catalysts are known to adsorb hydrogen due to the hydrogen-spill over process. The generated H_2 radicals on the Ni-supported catalysts favor the promotion of hydrogenolysis of fatty acids. However, the production lighter gases increase due to the scission of C-C or C-H bonds of hydrocarbons in the presence of NiO catalysts [280]. Additionally, it should also be noted that at lower temperatures (<350 ℃), the bio-oil containing higher amount of fatty acids and fatty alcohols are usually converted to long-chain fatty esters with the fatty acid chain remaining intact. The hydrodeoxygenation of long-chain fatty acids to produce long-chain fatty esters is associated to the properties of the support materials employed in the studies [281]. Since, red-mud is considered to be a basic/alkaline material, the formation of such esters is possible. A study on hydrodeoxygenation of a mixture of fatty acids showed that octadecyl stearate (56 mol%) was the major product in the presence of 10% Ni supported on SiO_2 [282].

Compared to the mono-metallic catalyst, the bimetallic catalysts can transfer electrons efficiently, enhancing bio-oil hydro conversion due to better reducibility. Additionally, metals such as Pt, Pd, Co, and Ni usually provide hydrogenating sites for hydrogenolysis/hydrogenation reactions to occur at the surface of the catalyst. When doped on mildly acidic support or added as a secondary metal, these metals promote the C-O bond scission [281]. In the present study, adding Co (5 wt.%) to Ni/RM increased the hydrocarbon content to 73.9%. The major products include Heptadecane (32%), Heptadecene (4.27%), Pentadecane (14.63%), Pentadecene, and Tetradecane. Cobalt-supported catalysts are generally active in the oxide form (Co_3O_4), leading to a higher degree of hydrogenolysis [281]. A study carried out on the selective hydrodeoxygenation of lignin bio-oil in the presence of Ni-

Co/Al_2O_3-MgO at 300 °C for 5 h with a hydrogen partial pressure of 20 bar indicated that the highest yield of cyclohexanol was 65.6 wt.% [283]. From the above analysis, it was found that Ni-Co/RM used at 300 °C, 2 h, 10 wt.% catalyst loading produced higher hydrocarbon yield (73.28%), hence, this catalyst at these conditions is chosen for optimizing the time and catalyst loading studies.

The as-produced raw co-pyrolytic oil (including the aqueous phase) was subjected to HDO in 10 wt.% Ni-Co/RM at 300 ºC and 4 MPa. The pressure during the reaction increased to 8 MPa as the temperature reached 300 ºC. At the end of the 2-6 h reaction time, the upgraded oil, coke, and gas were collected, and the effect of reaction time on the product distribution is presented in Fig 39 (a and b) It was observed that the yield of upgraded bio-oil decreased significantly with a rapid increase in the yield of coke/carbon deposition. The coke deposition was lower (6.04 wt.%) at 2 h compared to 11.05 wt.% at 6 h. A study on the evolution of cooking on bio-oil in the pyrolysis process revealed that coke is not formed instantly but needs an induction period. In this time, the light components polymerize into heavy compounds which dissolve and accumulate in the bio-oil. As these reach a dissolution limit, they precipitate and polymerize to form coke. Hence, prolonged catalyst exposure to longer residence times increases the coke deposition [284]. As the reaction time increased (from 2 to 6 h), the hydrocarbon yields significantly decreased, whereas there was a slight increase in alcohol. Additionally, at a reaction time of 6 h, it was observed that the aliphatic fatty acids increased and converted to esters and linear-chain hydrocarbons, increasing the ester content (39.63%) of the upgraded bio-oil. Also, other oxygenated compounds, such as ketone and aldehyde, increased compared to the upgraded oil produced at 2 h. The selectivity of n-Pentadecane decreased drastically from 13.3% (at 2 h) to 1.47% (at 6 h). Further, the selectivity of octadecenoic acid methyl ester was not found at 2 h but was observed at 4 and 6 h with an increase in selectivity towards it. The reaction between alcohols and aliphatic acids forms esters at longer reaction times. A study operating with similar operating conditions as the present study on the hydrotreatment of bio-oil used Pd/$NbOPO_4$ as a catalyst, indicating that the ester content drastically increased up to 23.7% at T=280 °C and t=8 h. The study also revealed that compared to crude bio-oil, the upgraded bio-oil contained more esters [285].

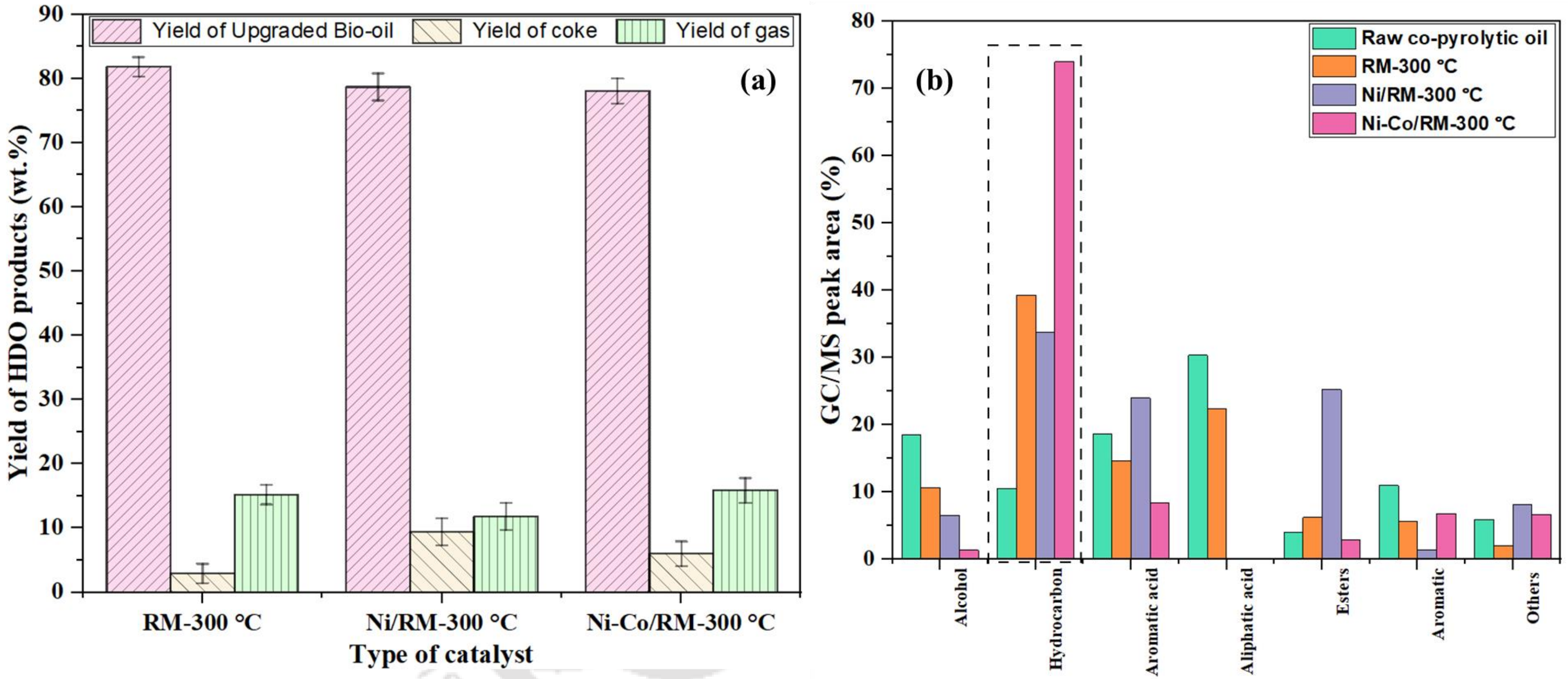

Figure 38. Effect of catalyst type on the HDO of co-pyrolytic oil at 300 ºC (a) HDO product distribution (b) Chemical composition of upgraded bio-oil.

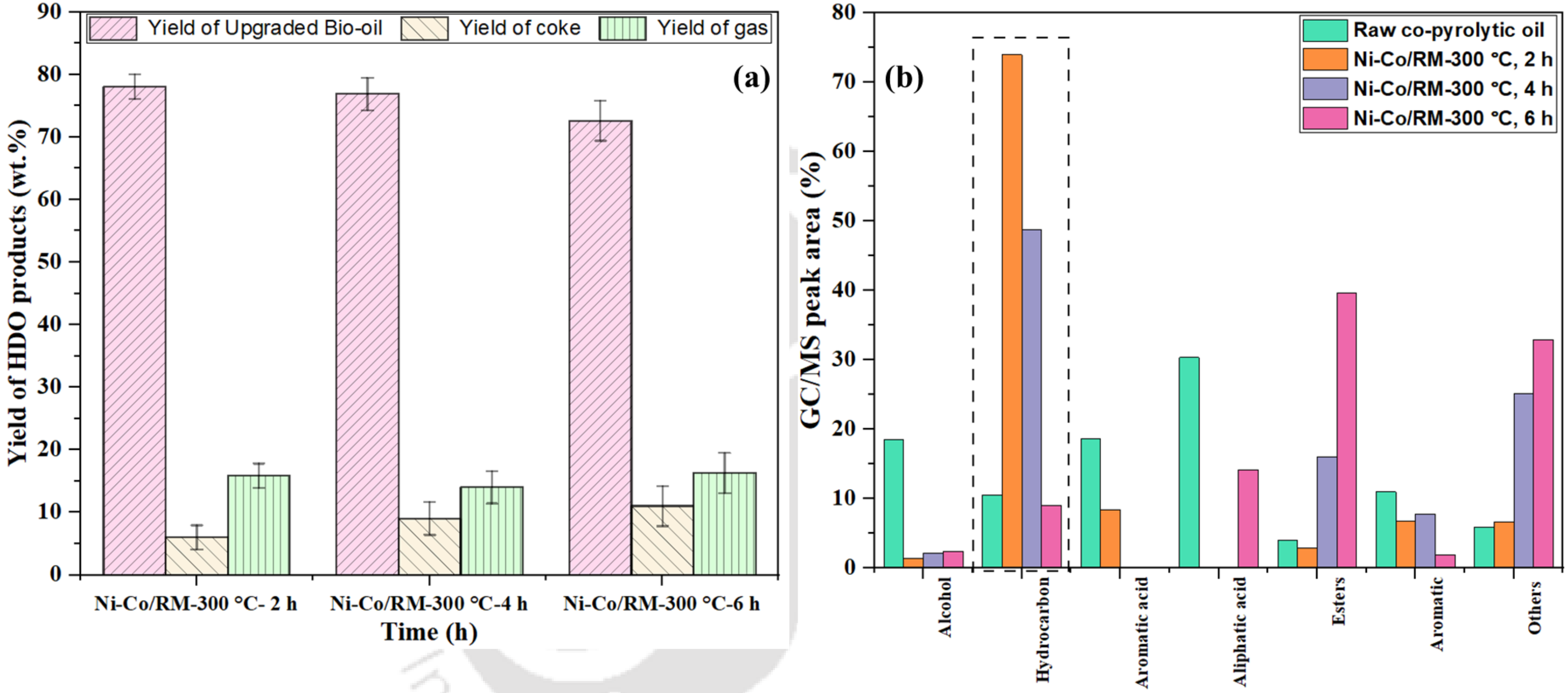

Figure 39. Effect of reaction time on the HDO of bio-oil in the presence of Ni-Co/RM at T=300 ºC (a) HDO product distribution (b) Chemical composition of upgraded bio-oil.

6.3.3 Reusability of catalyst

Catalytic reusability is one of the industry's most critical parameters for scale-up. The as-produced raw co-pyrolytic oil (including the aqueous phase) was subjected to HDO in 10 wt.% Ni-Co/RM at 300 °C and 4 MPa. The catalyst obtained from this experiment was reused directly in the subsequent runs. The catalyst was recycled up to 3 times. The pressure during the reaction increased to 7.5 MPa as the temperature reached 300 °C. At the end of the 2 h reaction time, the upgraded oil, coke, and gas were collected, and the effect of reusability of catalyst on the product distribution is presented in Fig 40 (a and b). It was observed that the yield of upgraded bio-oil decreased significantly with a rapid increase in the yield of coke/carbon deposition. The coke deposition was lower (6.04 wt.%) when fresh catalyst was used. Compared to 11.34 wt.% at the third recycle. As described in fig 5 (b), the chemical composition of the upgraded bio-oil had a pronounced effect of esterification of the fatty acids present in the crude bio-oil. The primary esters observed in the upgraded bio-oil were 9-octadecenoic acid (Z)-, ethyl ester (32%), hexadecanoic acid, methyl ester (3%). The hydrocarbons such as heptadecane and heptadecene were also found in 7.05% and 7.15%, which is less when compared to heptadecane (29.29%) obtained from 1st run. This remarkable decrease in the hydrocarbon yield indicates the deactivation of the catalyst caused by the coke. Generally, the coke deposition blocks the pores, reducing the surface area and available active sites for catalytic processes. However, the literature suggests that alkaline earth metals are prone to less coke formation [286]. Additionally, the presence of iron oxides increases the life span of the catalyst by converting the coke to carbon dioxide as per the Boudouard reaction [287]. Nevertheless, metals such as Ni and Co make coke formation inevitable [286].

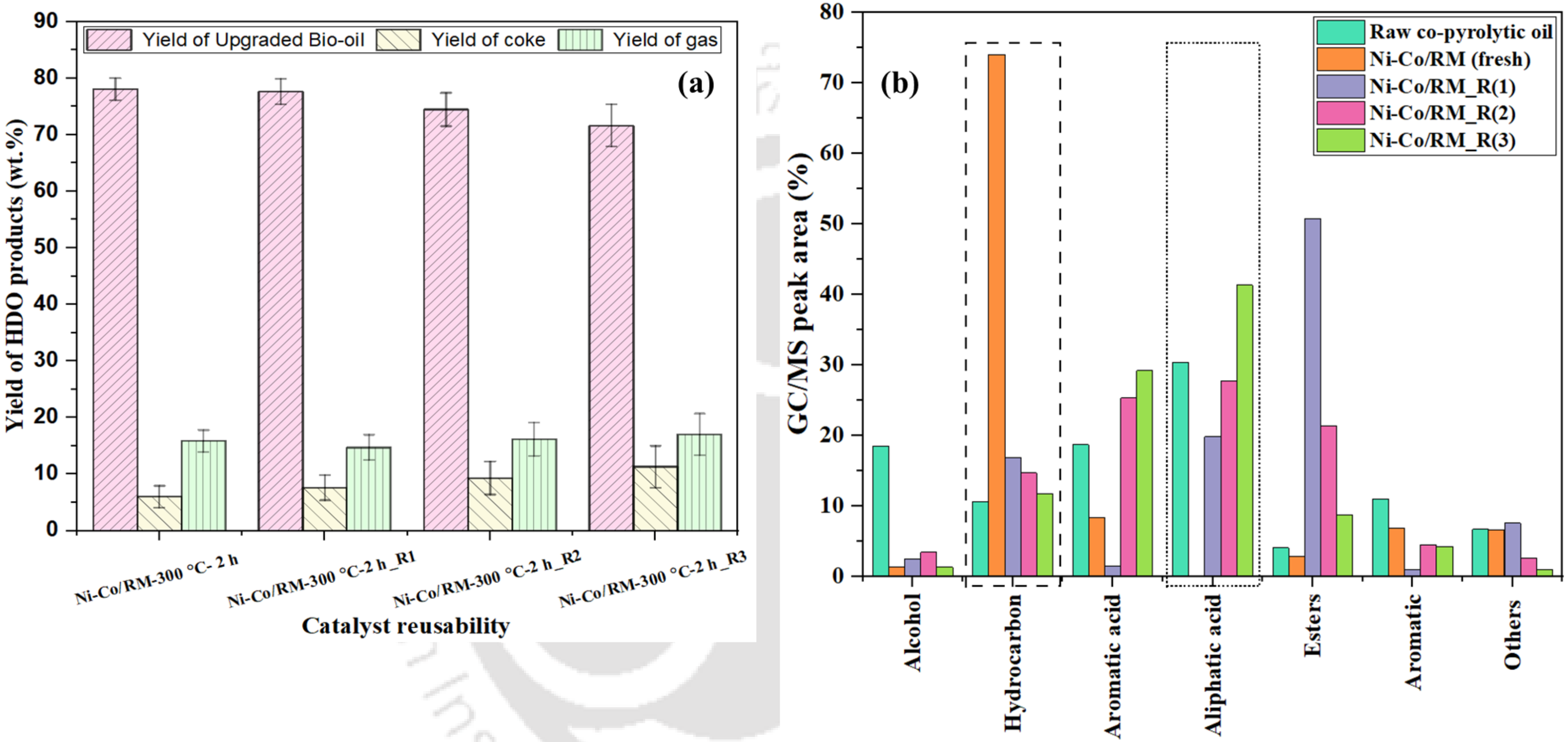

Figure 40. Effect of catalyst reusability on the HDO of bio-oil in the presence of Ni-Co/RM at T=300 ºC (a) HDO product distribution (b) Chemical composition of upgraded bio-oil.

6.3.4 Physicochemical characterization of Upgraded bio-oil

The elemental composition of the raw bio-oil and upgraded bio-oil are provided in Table 33. Compared to raw co-pyrolytic oil, the carbon content of the upgraded bio-oil increased from 67.32% to 76.23%. Meanwhile, the hydrogen content of bio-oil has also increased from 8.9% to 9.4%. The effect of deoxygenation was also observed in the bio-oil produced in the presence of Ni-Co/RM at T=300 ºC, t=2 h, and catalyst loading of 10 wt.%. The oxygen content reduced from 23.39% to 13.90%. The Van Krevelen diagram revealed that the O/C ratio of the hydrotreated bio-oil significantly decreased (from 0.28 to 0.13) due to the active sites of Ni-Co on red mud that promoted the effect of hydrogenation and deoxygenation. Additionally, the calorific value of upgraded bio-oil was found to be 42.25 MJ kg^{-1}.

Table 33. Physicochemical characterization of raw and upgraded bio-oil

Bio-oil	C	H	N	S	O	O/C	H/C	HHV (MJ kg^{-1})	Degree of deoxygenation (DOD)
Raw Bio-oil	67.32	8.90	0.44	0	23.33	0.26	1.58	39.28	0
RM, 300 °C, 2 h	71.79	11.95	0.33	0	15.93	0.17	1.99	40.48	35.99
Ni/RM, 300 °C, 2 h	73.15	9.16	0.33	0	17.35	0.18	1.50	41.32	31.57
Ni-Co/RM, 300 °C, 2 h	76.23	9.45	0.41	0	13.90	0.13	1.48	42.25	47.40
Ni-Co/RM, 300 °C, 4 h	73.61	10.17	0.34	0	15.88	0.16	1.65	41.04	37.78
Ni-Co/RM, 300 °C, 6 h	72.93	10.20	0.35	0	16.51	0.17	1.67	39.81	34.67
Ni-Co/RM, 300 °C, 2 h, R (3)	70.12	12.00	0.33	0	17.54	0.18	2.05	37.92	27.82

The high oxygen content in bio-oil leads to poor calorific values, high acidity, and viscosity; hence, deoxygenation is essential to decrease the bio-oil's oxygen level. The degree of deoxygenation defines the extent to which the oxygen is reduced. The DOD was calculated based on the atomic O/C ratio. From the Van Kervelen Diagram (Fig. 41), the crude or raw co-pyrolytic bio-oil contained an O/C ratio of 0.26, which after HDO in the presence of Ni-Co/RM decreased to 0.13. Compared to RM and Ni/RM, the O/C ratio of the bi-metallic catalyst was less, as evident from the hydrocarbon yield observed in the GC/MS results. Additionally, the O/C (0.13) of bio-oil obtained from fresh Ni-Co/RM was less than the O/C (0.18) of upgraded bio-oil obtained from spent Ni-Co/RM, indicating the deactivation of catalysts after reuse. The degree of deoxygenation (DOD) of bio-oil varied between 35.6% to 47.4% in the presence of all the catalysts. Bimetallic catalyst (Ni-Co/RM) showed the highest DOD (47.4%), which suggests that high pore volume (0.15 cc g^{-1}) and considerable pore size (20 nm) reacted with oxygenated compounds. Furthermore, a decrease in the H/C ratio (1.48) of the upgraded oil was also observed, indicating the possibility of dehydration and deoxygenation. Similar observations were made in a study using Ni/Al-SBA-15 for catalytic hydrodeoxygenation of bio-oil obtained *Liriodendron tulipifera* biomass. The study reported a decrease in H/C of heavy oil (1.4) and DOD of 54.9% [288].

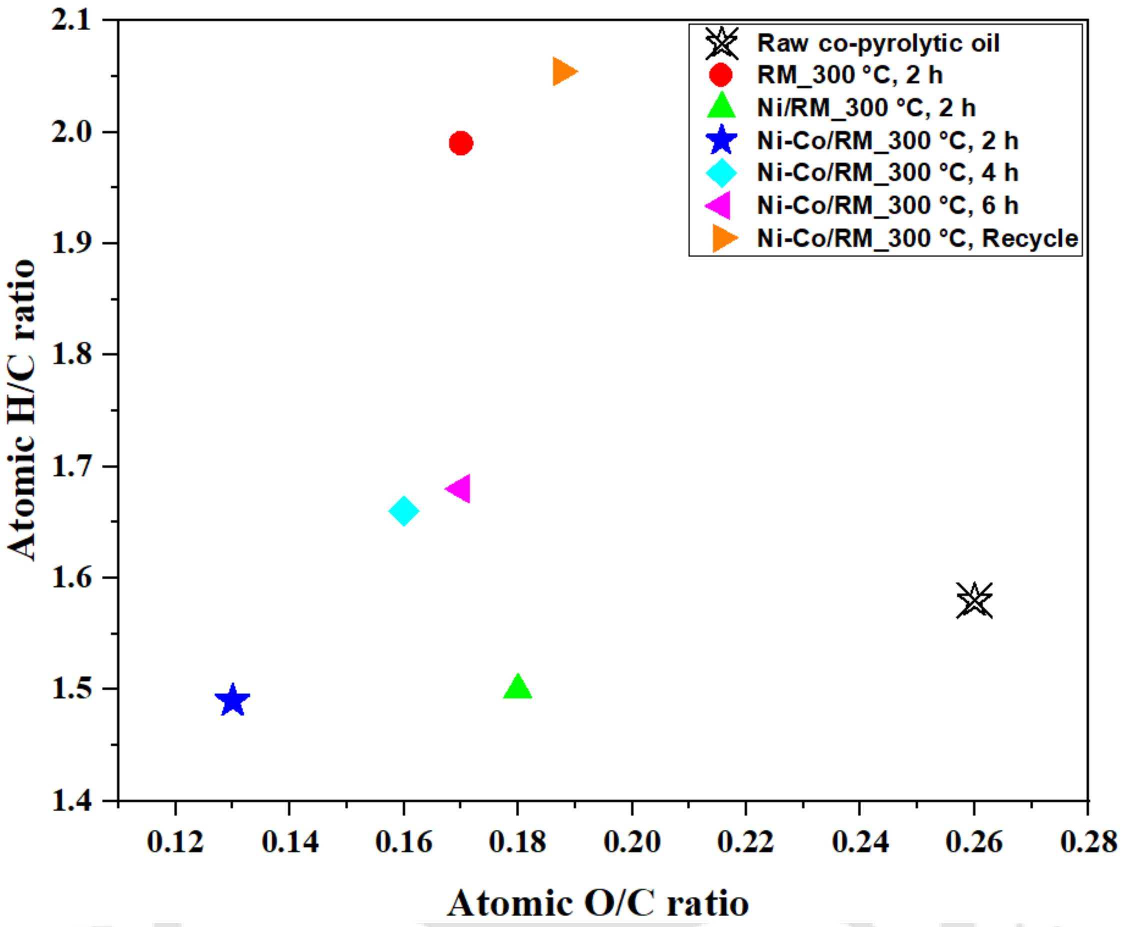

Figure 41. Van Krevelen diagram of raw and upgraded of bio-oil

6.3.4.1 Functional group analysis in bio-oil

The FITR analysis to determine the functional groups of the raw co-pyrolytic oil and upgraded bio-oil obtained in the presence of different functional groups is provided in Fig. 42. The functional group analysis revealed that the crude and upgraded bio-oil had similar functional groups. However, the intensities of the peaks varied at different conditions. Significant peaks were found at 2923, 1702, 1420, 1285, 932, and 707 cm^{-1} corresponding to C-H (methyl), C=O (acid, ketone), C-H (alkanes), C-O (ethers, esters), C=C (alkenes), and C-H (aromatic) respectively. Compared to raw co-pyrolytic oil, the peak intensity of carboxylic acids was reduced in the upgraded bio-oil. At the same time, there is a substantial increase in the intensities of C-H and C=C groups. The absence of O-H peaks at 3400 cm^{-1} indicates the deoxygenation of acids to hydrocarbons. From the above results, it is clear that the crude oil underwent deoxygenation reactions to produce upgraded bio-oil. A similar work reported the elimination of oxygenated compounds from crude pyrolytic oils [289].

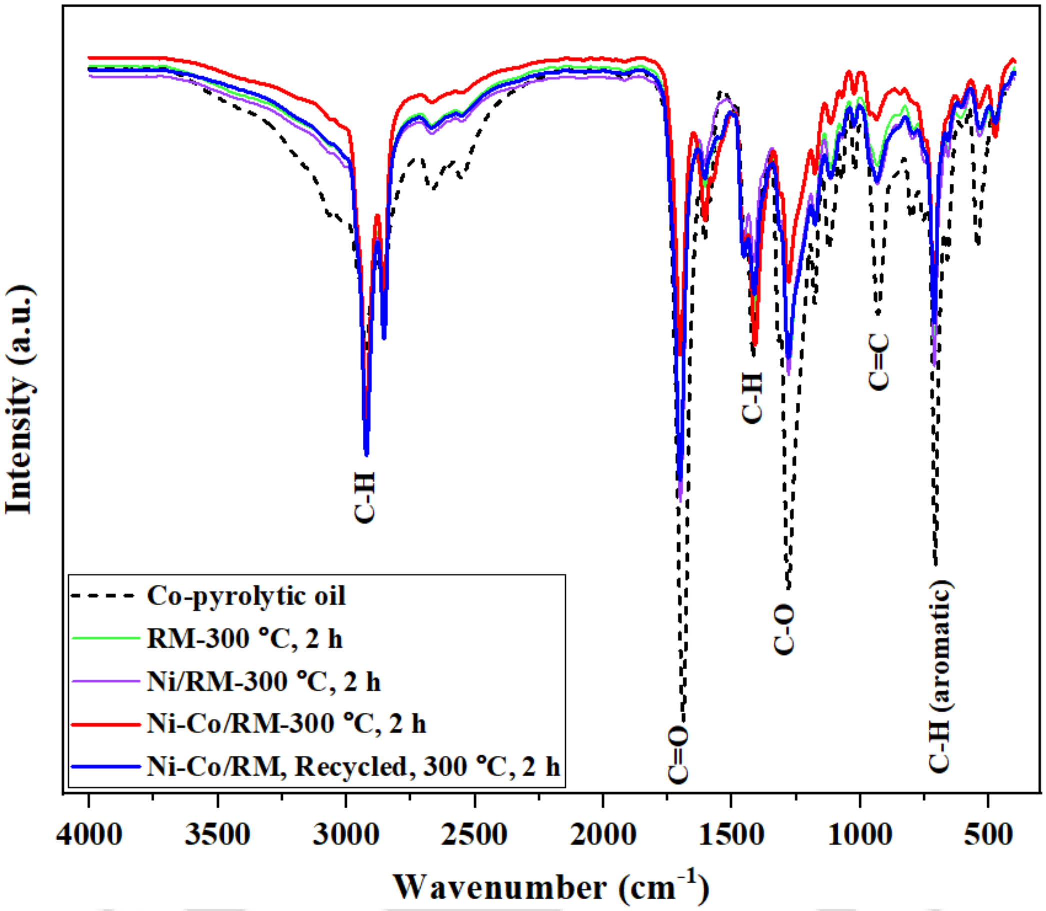

Figure 42. FTIR of raw and upgraded bio-oil.

6.3.5 Characterization of Spent catalyst

The XRD peaks of fresh, spent (R3), and regenerated Ni-Co/RM catalysts are shown in Fig 43. The results show that Co_3O_4 peaks at 2ϴ=36.8 in the coked catalyst have disappeared, and new peaks at 40.7 and 45.3 have formed, indicating the reduction of Co_3O_4 to the metallic Co (hcp) phase [290]. Additionally, the reduction of the hematite phase of Fe_2O_3 has occurred to form the magnetite phase of Fe_2O_3. It was also observed that Fe_2NiO_4 (trevorite) peaks formed after HDO reaction, which could also contribute to the deactivation of active Ni sites. Due to the above reasons, the catalyst was partially deactivated [271]. Prior to recycling the catalyst, it was regenerated in a muffle furnace at 550 °C for 4 h to remove the deposited carbonaceous compounds (coke). The XRD pattern of the regenerated catalyst (Fig. 3c) displayed prominent NiO diffraction peaks at 2Θ values of 43.9°, 50.8°, and 75°, attributed to the oxidation of nickel into NiO during heat treatment in air alongside the oxidation of metallic Co to Co_3O_4. Additionally, the presence of hematite (Fe_2O_3) diffraction peaks in the regenerated catalyst was attributed to the oxidation of magnetite [271].

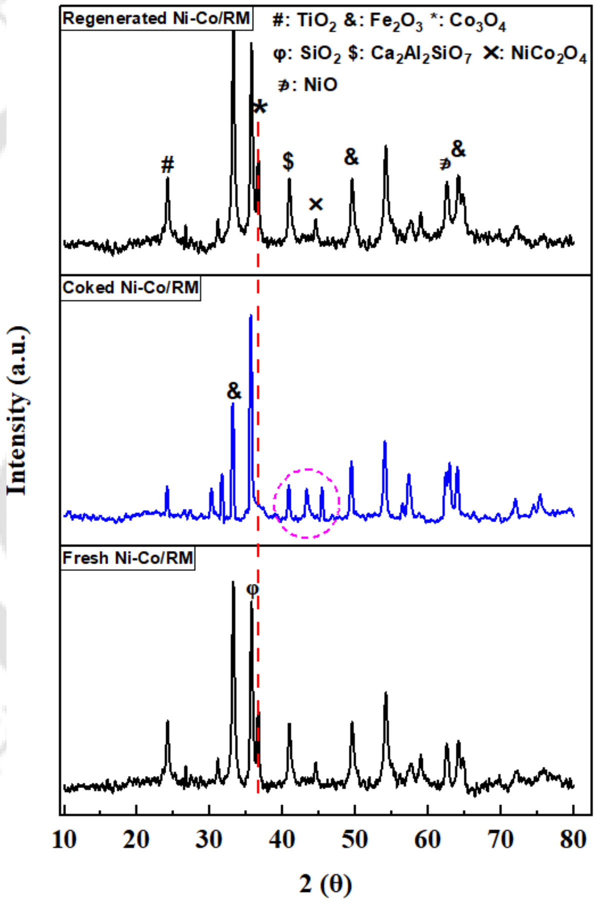

Figure 43. XRD of fresh, spent (R3) and regenerated catalyst of Ni-Co/RM

The surface morphology determined by FESEM of the fresh, spent (R3), and regenerated catalyst is shown in Fig. 44. The SEM images of the fresh catalyst show unique flower-like structures present on the irregularly shaped particles of RM in which the particles look like dense granules. These particles are usually formed due to the interaction of Ni and CO with the red mud support. Such flower-like structures exhibit distinctive textural properties and high catalytic activity in reactions such as CO oxidation [291]. From Fig 44 (b), it can be seen that the catalyst was coated with coke, and particles were agglomerated. This shows the catalyst's partial deactivation, indicating a limitation of hydrogen transfer [271]. Regeneration of the catalyst restored the properties, and the flower-like structures reappeared.

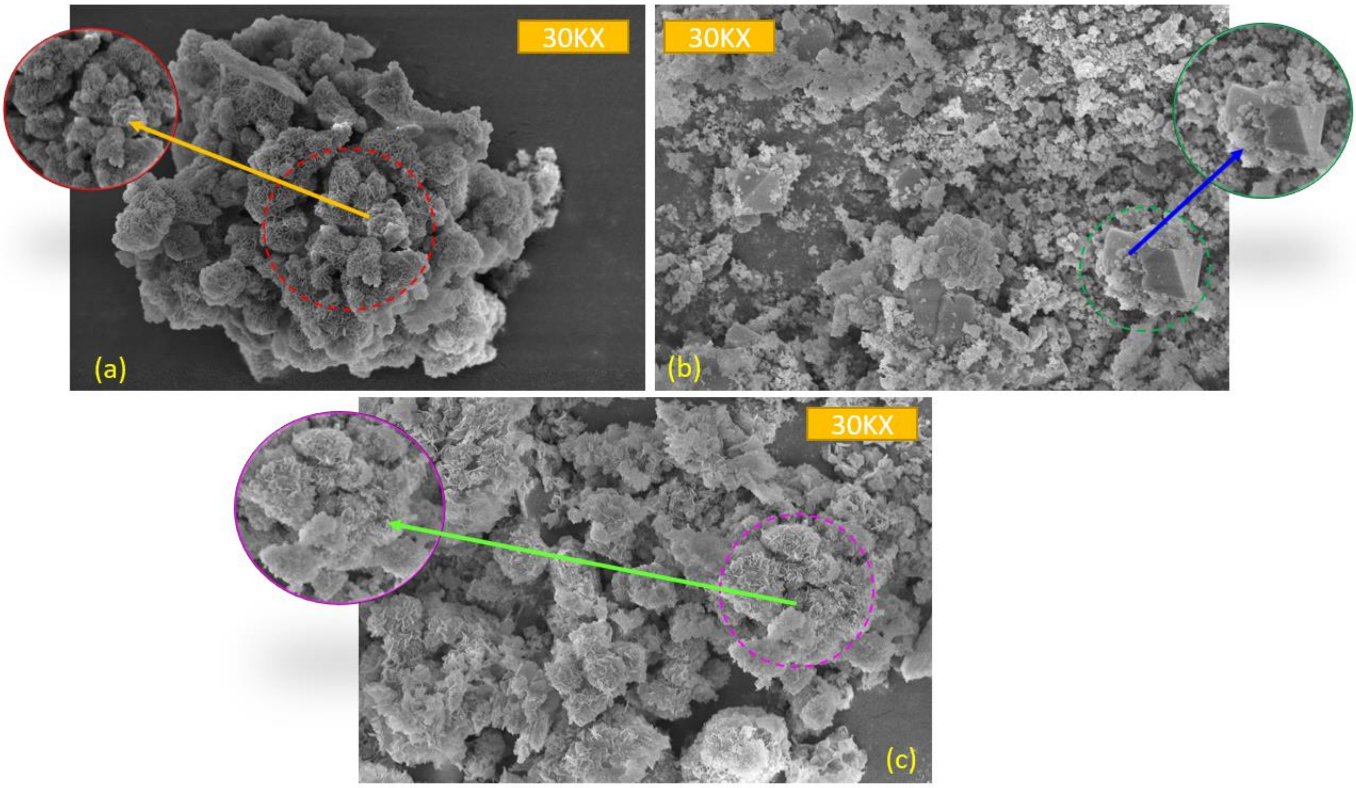

Figure 44. FESEM morphology of Ni-Co/RM (a) fresh (b) spent (R3) (c) regenerated

Table 34. N_2 adsorption-desorption characteristics of fresh, spent and regenerated Ni-Co/RM

Catalyst	BET surface area (m^2/g)	Average pore size (nm)	Total pore volume (cc/g)
Ni-Co/RM	34.99	20.07	0.15
Ni-Co/RM- coked	20.04	5.61	0.12

The oxygenated compounds in the bio-oil usually get adsorbed on the active sites of the catalysts and converted into low-molecular-weight compounds that are small and condensed into coke residues. As provided in Table 34, the BET surface area of the coked catalyst was reduced significantly, indicating the clogging of pores. As described, there were notable changes in the morphology (such as agglomeration seen in SEM images) and pore size distribution. The BET surface area of the fresh Ni-Co/RM catalyst was found to be 34.99 m^2 g^{-1}, whereas the surface area of the spent catalyst was observed to be 20.04 m^2 g^{-1}. This indicates that the pores were clogged by tar components from bio-oil. It was also observed that the total pore volume decreased due to coking. Since the catalyst had both micro and mesopores, it is known from earlier studies that the kinetic diameter of oxygenated molecules present in bio-oil is mainly in the mesopores range, influencing the catalytic cracking efficiency of tar compounds. The BET surface area of the Ni-Co/RM was comparable to that of the fresh catalyst, indicating that the carbon was burnt off efficiently.

The functional group analysis of fresh and spent catalysts is provided in Fig 45. It can be seen from the spent catalyst analysis that benzoic acid is adsorbed on the surface of the catalyst. It is confirmed by the peaks at 1754, 1681, 1448 cm^{-1} which are assigned to $\nu(COOH)$, $\nu(CC) + \delta(CH)$ ring of the benzoic acid [292].

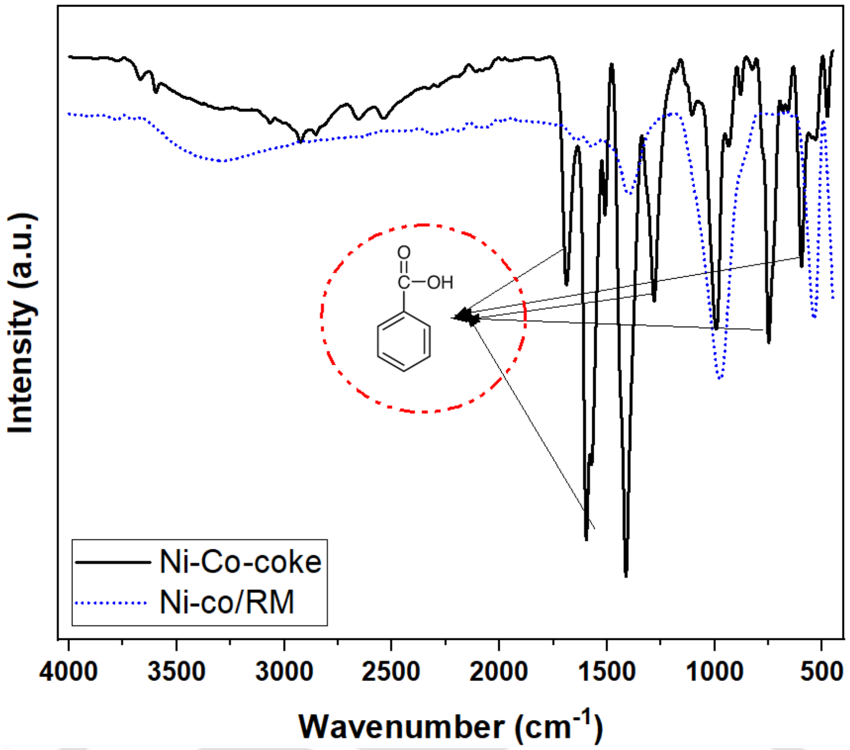

Figure 45. FTIR analysis of fresh and spent Ni-Co/RM catalyst (R3)

The elemental composition and surface electronic states of fresh and spent Ni-Co/RM were analyzed using XPS analysis and are represented in Fig 46 (a,b). The fresh catalyst had 710.7 and 724.3 eV peaks, attributed to the Fe $2p_{3/2}$ and Fe $2p_{1/2}$, respectively. These peaks are usually assigned to the combination of Fe^{+3} and Fe^{+2} states. Furthermore, the binding energy (BE) between these samples is noted to be 13.6 eV, which indicates that Fe-O is in Fe_2O_3 form. However, the spent catalyst has peaks at 711.03 and 724.3, indicating that the Fe-O is in magnetite form, i.e., Fe_3O_4. The O (1s) of both the fresh and spent catalyst are observed at 530.3 eV. This suggests that oxygen is present in the crystal lattice as Fe-O bonds [293]. Additionally, there was a decrease in the intensity of the O 1s peaks of the spent catalyst compared to the fresh catalyst, indicating a decrease in the atomic concentration in the spent catalyst (45.45%) [294].

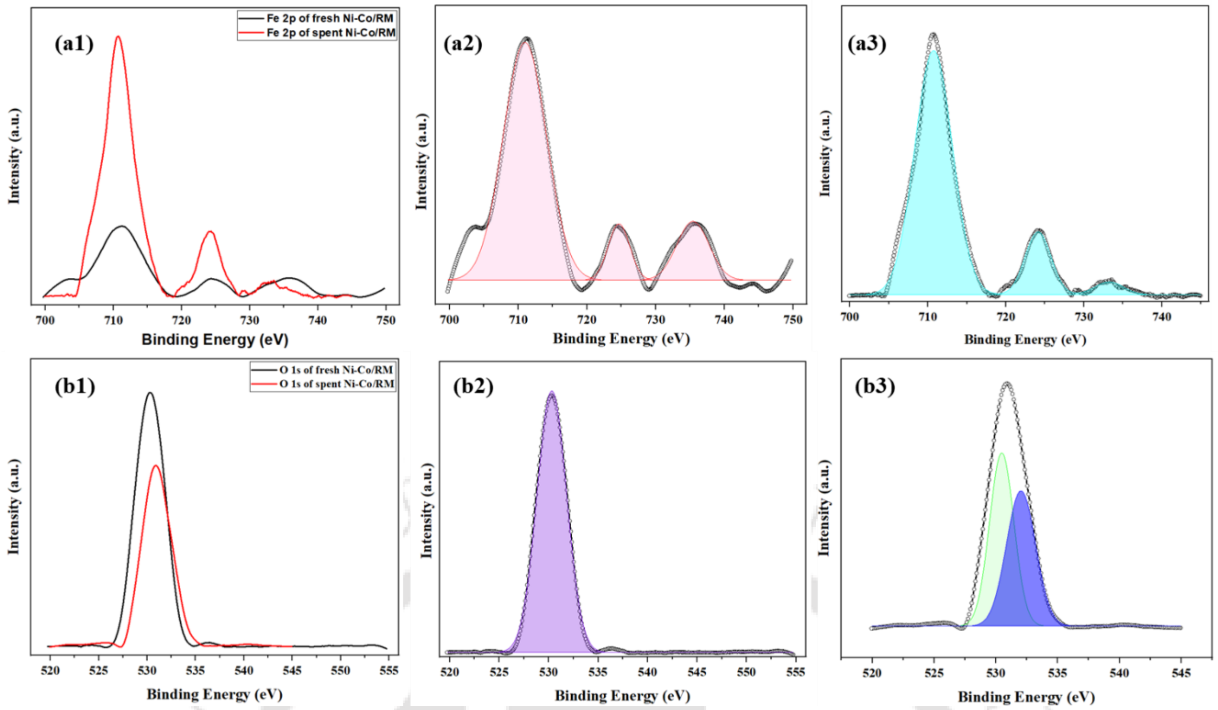

Figure 46. (a1). Comparison of Fe 2p of fresh and spent Ni-Co/RM; (a2) Fe 2p of Fresh Ni-CO/RM; (a3) Fe 2p of spent Ni-Co/RM; (b1) O 1s of fresh and spent Ni-Co/RM catalyst; (b2) O 1s of fresh Ni-Co/RM catalyst; (b3) O 1s of spent Ni-Co/RM catalyst

The XPS spectrum of Co 2p in Co3O4 is presented in Fig 47 (c,d). Two significant peaks corresponding to Co $2p_{3/2}$ and Co $2p_{1/2}$ at 779.6 and 795.30, with a difference of 15 eV in the fresh catalyst. Further, one satellite peak at 803.2 eV was also observed, indicating the characteristic cobalt oxide peak. The deconvolution peak at 779.5 confirms the presence of Co^{+3} in Co_3O_4. Co^{+3} on the surface is reported to alter the performance of catalytic reactions. Compared to the fresh Ni-Co/RM, the peaks of the spent catalyst are slights shifted towards higher binding energy, meaning a possible interaction with NiO forming an alloy of $NiCoO_2$. The peak corresponds to 783 eV with an electronic state of Co^{+2}. The XPS peak fitting of Ni 2p is shown in Fig. 47 (d1-3) and represents two prominent peaks at 854.6 and 872.3, conforming to the presence of Ni $2p_{3/2}$ and Ni $2p_{1/2}$, respectively. The binding energy difference of 17.4 eV is related to Ni^{+3}. Moreover, satellite peaks at 861.42 and 879.9 are associated with Ni-O. The same trend as O 1s was followed in Ni 2p, where the intensity of characteristic peaks decreased and slightly shifted to lower binding energies (1.88 eV) with an overall decrease in the atomic concentration from 7.03 to 0.69% [295].

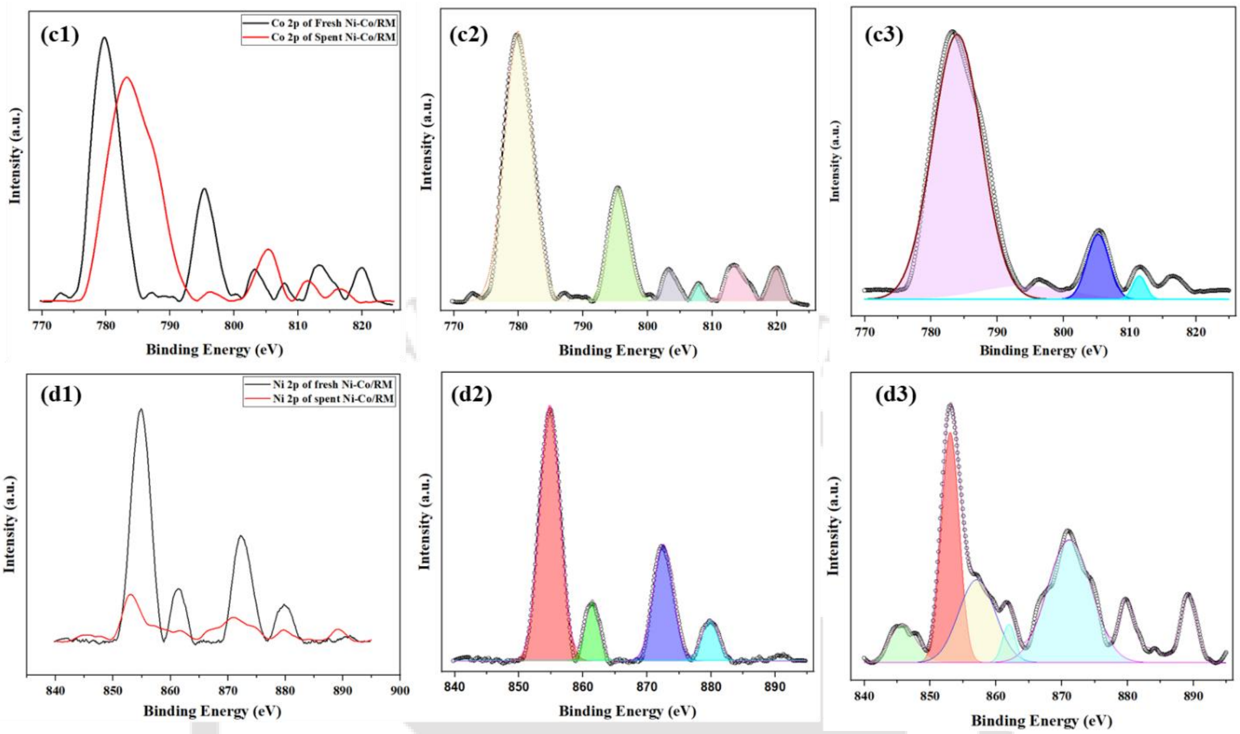

Figure 47. (c1). Comparison of Co 2p of fresh and spent Ni-Co/RM; (c2) Co 2p of fresh Ni-CO/RM; (c3) Co 2p of spent Ni-Co/RM; (d1) Ni 2p of fresh and spent Ni-Co/RM; (d2) Ni 2p of fresh Ni-Co/RM; (d3) Ni 2p of spent Ni-Co/RM.

The carbon formation due to the coking of the catalysts was further analyzed by XPS and presented in Fig 48 (e). The C 1s peaks of the fresh catalyst were found at 284.5 eV, corresponding to the metal-carbide bond. The deconvoluted peaks of C 1s found at 284.5 in fresh and spent catalysts are assigned to the graphite sp^2 carbon (C-C) bond on the carbon nanofibers/tube structures. There are also peaks seen at 288.7 eV in the spent catalyst, which are associated with the sp^3 hybridized atoms. Fig 48 (e) represents the oxygen O1 s of the spent catalyst. The deconvoluted peaks at 532.04 eV correspond to the -C-O-C- bond, indicating the presence of oxygenated molecules.

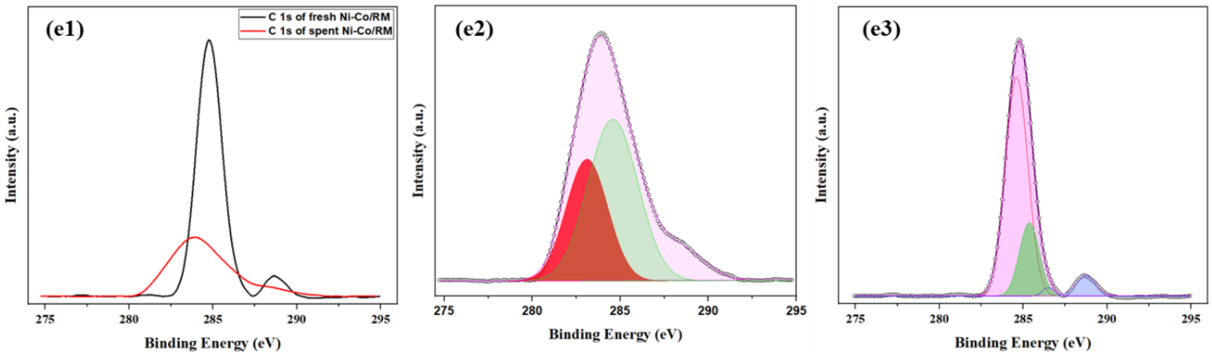

Figure 48. (e1). Comparison of C 1s of fresh and spent Ni-Co/RM; (e2) C 1s of fresh Ni-CO/RM; (e3) C 1s of spent Ni-Co/RM

6.4 Conclusion

Red mud, an industry waste from aluminium manufacturing process was used as a support material in the preparation of monometallic (Ni) and bimetallic (Ni-Co) catalyst for hydrodeoxygenation of raw co-pyrolysis oil. The bimetallic catalyst provided better selectivity regarding hydrocarbon yield (73.9%). There was a substantial decrease in both aliphatic and aromatic acids. The reaction conditions at T=300 ºC, t=2 h, and bio-oil to catalyst loading= 10 wt.% were found to be optimum to achieve high conversion and selectivity towards hydrocarbons. The activity of the Ni-Co/RM catalyst was decreased due to the partial deactivation of the catalyst. This is due to the formation of the trevorite phase and deposition of coke substances. Coke deposition was also observed using different analytical techniques such as XRD, XPS, and FESEM. The adsorption of benzoic acid was also confirmed from the FTIR analysis of the spent catalyst. After regeneration of the spent catalyst, the activity of Ni-Co/RM was restored. This study demonstrated that red mud can be a favourable Ni-Co catalyst support for the HDO process.

CHAPTER 7.

Conclusions and Future Perspective

This section summarizes the conclusions derived from the research conducted in this thesis and provides recommendations for future studies building on the foundation established in this work. In this research work, research gaps present in the catalytic upgradation of bio-oil produced from co-pyrolysis are addressed. Identifying valuable feedstocks for producing value-added products is crucial in thermochemical conversion processes. Notably, this involves different parameters such as kinetics estimation, pyrolysate vapor composition, and synergistic effect of biomass and plastic feedstocks. This study investigated different biomass feedstocks such as wheat straw, oilseed, and deoiled cake. Among the different types of biomasses tested, Mesua ferrea L. *oilseed was found to have suitable physicochemical characteristics to produce pyrolytic products. PET plastic has a pronounced effect on volatile matter in the plastic feedstocks. Although the literature states that adding plastic feedstocks increases the H/C of the produced pyrolytic oil, PET is an oxygen-rich plastic. The effect of such plastic feedstocks on the bio-oil composition is of much interest to thermochemical conversion processes. Additionally, among the different kinetic models fitted for thermal and co-pyrolysis of feedstocks, DAEM provided lower activation energy. Hence, this oilseed and PET plastic combination was tested for analytical and applied pyrolysis. In the analytical pyrolysis, Py-GC/MS was used to understand the pyrolysate composition of the feedstocks. Further comparison of analytical and applied pyrolysis was conducted to observe the synergistic effect of co-feedstocks. The Bio-oil obtained from thermal and co-pyrolysis contained high oxygen content. Therefore, to reduce the oxygen content of the sample, it was upgraded by a catalytic hydrodeoxygenation process in the presence of a low-cost red mud catalyst.*

7.1 Conclusion

- Different regional biomass feedstocks were analyzed to identify potential feedstocks: Wheat straw, Ground deoiled cake, and *Mesua ferrea* L. oilseed. The physicochemical characterization and thermal analysis of the *Mesua ferrea* L. oilseed, groundnut de-oiled cake, wheat straw and PET plastic confirms the bioenergy potential of feedstocks to produce biofuel.
- In the oilseed ie., *Mesua ferrea* L., a minimal weight loss (1-1.66 wt.%) for all heating rates was observed in this zone. Meanwhile, the groundnut deoiled cake (GDC) and wheat straw (WS) were noted to be 2.5-4 wt.% and 1.2-2.4 wt.%, respectively. In the second stage, thermal decomposition of hemicellulose (200 °C - 350 °C) and cellulose (230 °C - 500 °C) occurred.
- From the DTG graph, it was evident that biomass degradation occurred in three stages corresponding to degradation of hemicellulose (200 °C - 350 °C), cellulose (350 °C - 550 °C), and lignin (>550 °C). A negative sloped peak with shoulders at different temperatures indicated degradation of these compounds via depolymerization reaction.
- In contrast, plastic has shown a higher initial stability and the three zones occurred in the temperature ranges of 30–375 °C; 375–600 °C; 600–900 °C. The plastic degradation occured due to additive fillers, diethylene glycol, and terephthalate monomers.
- The DTG shift for the co-pyrolysis mixture (GDC: PET) was found to be 420 °C, 435 °C, and 440 °C. A similar trend was observed for *Mesua ferrea* L.: PET (409.08–433.51 °C) and wheat straw: PET (437.67–465.64 °C).
- The useful functional groups present in the material were confirmed by the FTIR analysis. The peak at 2859 cm^{-1} was mainly attributed to the C–H bond in the methylene group present in aliphatic compounds.

- The activation energy and the pre-exponential factor, also known as the kinetic variables, were estimated using five model-free iso-conversional methods: DFM, KAS, OFW, STR, and DAEM. Among all of the methods, the DAEM method provided the lowest activation energy (for the oilseed, E= 127.9 kJ mol^{-1}; PET, E = 201.5 kJ mol^{-1}; and co-pyrolysis, E = 156. 2 kJ mol^{-1}).
- The co-pyrolysis of non-edible oil seed (*Mesua ferrea* L.) and PET plastic at different feedstock ratios was performed in analytical and applied pyrolysis. The primary aim is to study the composition of the condensable pyrolytic vapour (which is usually the oil fraction) by analytical curie-point pyrolyzer with a gas chromatograph/mass spectrometer (Py-GC/MS). Further, the effects of temperature on pyrolysis of oil seed, and the mixtures of oil seed with PET (Biomass: PET (B:P) of 1:1, 2:1, and 1:2 w/w) on the yield and quality of the pyrolytic-oil were studied, and the optimal temperature was evaluated.
- The aliphatic acids include octanoic acid ($C_8H_{16}O_2$) (2.4%); nonanoic acid ($C_9H_{18}O_2$) (1.0%); n-hexadecanoic acid ($C_{16}H_{32}O_2$) (28.3%); 9-octadecenoic acid ($C_{18}H_{34}O_2$) (33.4%); octadecanoic acid ($C_{18}H_{36}O_2$) (25.0%) were found to be major aliphatic acids in analytical pyrolysis of *Mesua ferrea* L. oilseed. The PET waste in this study showed the presence of aromatic acids, aromatics and ester in higher ratio. Some of those include, benzoic acid (43%), 4-acetyl benzoic acid (16%), benzene (4.88%) and 1,2-ethanediol, dibenzoate (13%). The pyrolysate composition of co-feed (1:1, 2:1, 1:2 w/w) revealed that the vapor contains a mixture of aliphatic acids and aromatic acids. The major compounds observed in the vapor was n-hexadecanoic acid of 15% for 1:1 w/w; 9-octadecenoic acid of 51% for 2:1 w/w; benzoic acid of 18% for 1:2 w/w.
- This research explored the combined impacts on oil yield and quality when *Mesua ferrea* L. and PET plastic were co-pyrolyzed in varying ratios (1:1, 2:1, 1:2 w/w) at 550

°C to 650 °C. The maximum oil yield (35 wt.%) was observed at 600 °C for 2:1 feedstock ratio. The HHV of the oil 39.28 MJ kg^{-1}. The hydrocarbon content of the co-pyrolytic oil of 2:1 feedstock ratio was higher (10%) as compared to other feedstock ratios (1:1- 1.3% and 1:2- 2.9%).

- At 600 °C, the yield of bio-oil increased to a maximum of 27 wt.% for biomass and 28.5 wt.% for 1:1 co-feed. A further increment in temperature reduced the oil yield (biomass 24.5 wt.%, co-feed (1:1) 26 wt.%). Further increasing the pyrolysis temperature to 600 °C and 650 °C led to an increase in yield of non-condensable gases. The gas yield increased from 31 wt.% to 42 wt.% as the temperature rose from 550 °C to 650 °C.
- The pyrolytic liquid derived from nahar seed, generally referred to as the bio-oil, is reported to possess HHV in the range of 15-30 MJ kg^{-1}. The elemental composition of bio oil C (68.32%), H (10.57%), N (4.42%), S (0.01%), and O (16.77%) with an emipirical formula, $CH_{1.85}N_{0.05}S_{0.00005}O_{0.184}$, has HHV of 32.78 MJ kg^{-1}.
- The oilseeds usually contain high amounts of fatty acids, which is confirmed by the analytical fast pyrolysis of the seed. The pyrolytic-oil also contains a major proportion of nitriles and amides (29.1%) in addition to hydrocarbons (28.7%) and esters (29.9%). Some of the siginificant products were n-hexadecanoic acid (28-34%) observed in the analytical fast pyrolysis is converted to hexadecanaamide (2.7%), hexadecanitrile (1.1%), hexadecane (1.0%), hecadecanoic acid methyl ester (3.6%), which were observed in GC/MS of bio-oil. Similarly, octadecanoic acid (31-39%) is converted to 9-octadecenenitrile (3.9%), 9-octadecenoic acid, 1,2,3-propanetriyl ester (1.0%), 9-octadecenoic acid, methyl ester (10.4%), methyl stearate (3.5%), methyl 9-cis,11-trans-octadecadienoate (2.7%).

- Higher amount of plastic in the feedstock ratio of 1:1, 1:2, had a negative synergistic effect when compared to 2:1. From the individual pyrolysis and pyrolysis of co-feed with 1:1 biomass: plastic ratio, the operating parameters such as temperature (600 °C), residence time (2 h) were fixed. The bio-oil yield was maximum (35 wt.%) at 2:1 (B: P).
- The oxygen content varied in the 6.12-12% range for co-pyrolysis oil, which is clearly due to the addition of plastic to biomass. This also tends to reduce the oil's nitrogen content to less than 0.5% at all feedstock ratios implies that plastic reduced the nitrogen content of the oil.
- Addition of plastics enhanced the aromatic content in the co-pyrolytic oil 2:1 (11.2%) >1:1 (8.8%) >1:2 (8.4%). In particular, the yield of aromatic acids and esters increased with increased in PET ratio, while decreasing the amount of hydrocarbons and alcohols. A positive synergistic effect promoted the hydrocarbon (10.6%) yield up to 60% biomass, which reduced the acid content (aliphatic acid: 31%; aromatic acids: 18.7%).
- The key reaction pathways followed in the co-pyrolysis of *Mesua ferrea* L. oilseed and PET plastic are the decarboxylation of acidic groups and the dehydration of oxygenated compounds. These reactions occur due to the formation of reactive free radicals.
- Red mud is an alkaline material and dumping it in landfills creates many problems, like groundwater contamination. The presence of various metal oxides indicates its possibility of being used as catalysts.
- Ni and Ni-Co oxide catalysts supported on RM were synthesized using the wetness co-impregnation technique and calcined at 550 °C. The catalytic activity tests carried on palmitic acid which is a major component of fatty acid in waste cooking oil used to produce diesel/sustainable aviation fuel. Meanwhile, operating parameters such as

reaction temperature (210 – 270 °C), reaction time (3 – 5 h), initial hydrogen pressure (3 – 5 MPa) and recyclability of the best suitable catalyst were also performed to propose a plausible reaction mechanism.

- From the XRD analysis; it can be observed that the RM contains various metal oxides such as aluminium oxide (Al_2O_3), hematite (Fe_2O_3, 2θ: 54.16), Quartz (SiO_2), titanium oxide (TiO_2), and Hercynite ($FeAl_2O_4$). The presence of NiO was detected at 2θ 35° (1 1 1) and 41° (2 0 0), and Co_3O_4 and Co were observed at 2θ 36° and 45° corresponding to (3 1 1) and (1 1 1) respectively these prove the successful impregnation active metals on the support.
- The SEM and TEM images revealed the dispersion of Ni nanoparticles of an average particle size of ~100 nm. Additionally, a higher accumulation of particles compared to the RM was observed indicating a similar rough surface. Moreover, Ni loading may block the pores of RM, resulting in a decrease in surface area as indicated in Table 1. When Co metal was immobilized on the support along with Ni, there was a decrease in the average particle size (~90 nm).
- The N_2 adsorption−desorption measurements were used to calculate the BET surface area and textural properties of the RM support and the Ni/RM, Ni-Co/RM catalyst. It is evident that BSA of Ni/RM (25 $m^2\ g^{-1}$) was lesser than Ni-Co/RM (29 $m^2\ g^{-1}$).
- XPS analysis revealed the formation of increased Ni-O and Co-O species and lattice defects on the catalyst. These defects were crucial for the enhanced catalytic activity of the Ni-Co/RM, which also exhibited a synergistic effect between the active centres, resulting in high efficiency for hexadecane production.
- At 240 °C, palmitic acid was completely converted by all catalysts, with Ni-Co/RM showing the highest selectivity towards hexadecane at 77.3%. Furthermore, Ni-Co/RM demonstrated stable catalytic activity even after three recycles.

- The catalytic activity tests were also carried on raw pyrolytic oil produced from co-pyrolysis of *Mesua ferrea* L. oilseed and PET plastic (B:P-2:1). Meanwhile, operating parameters such as type of catalyst (RM, Ni/RM, Ni-Co/RM), reaction temperature (180 – 300 °C), reaction time (2 – 6 h), catalyst loading (10 -20 wt.%) and recyclability of the best suitable catalyst were also performed to propose a plausible reaction mechanism.
- The bimetallic catalyst (Ni-Co/RM) provided better selectivity regarding hydrocarbon yield (73.9%). There was a substantial decrease in both aliphatic and aromatic acids. The reaction conditions at T = 300 °C, t = 2 h, and bio-oil to catalyst loading = 10 wt.% were found to be optimum to achieve high conversion and selectivity towards hydrocarbons.
- The activity of the Ni-Co/RM catalyst was decreased due to the partial deactivation of the catalyst. This is due to the formation of the trevorite phase and deposition of coke substances. Coke deposition was also observed using different analytical techniques such as XRD, XPS, and FESEM.
- After regeneration of the spent catalyst, the activity of Ni-Co/RM was restored. This study demonstrated that red mud can be a favourable Ni-Co catalyst support for the HDO process.

7.2 SWOT analysis and social impact for production of biofuel

Many countries worldwide acknowledge the benefits of biofuel production and are vigorously advancing their bioenergy initiatives. In 2019, global biofuel production approximated 1,800 thousand barrels of oil equivalent per day, a substantial increase compared to the 187 thousand barrels per day produced in 2001. This evolution has been predominantly driven by policies encouraging biofuel use and production, fuelled by its potential to improve energy security and reduce greenhouse gas emissions in key sectors. A SWOT analysis identifies the main factors influencing the future development of global biofuel production by thermochemical conversion processes such as pyrolysis, catalytic upgradation, and others.

Some technical recommendations from the SWOT analysis provided in Fig. 49 include:

1. Workshops/seminars and training of workers and skilled labour to enhance the production of biofuels.
2. Development of advanced technologies for the production of biofuels. Industrial robustness in employing these advanced technologies with the existing infrastructure.
3. Focus on producing second- and third-generation biomass feedstocks and using plastic materials to avoid fuel vs food problems.

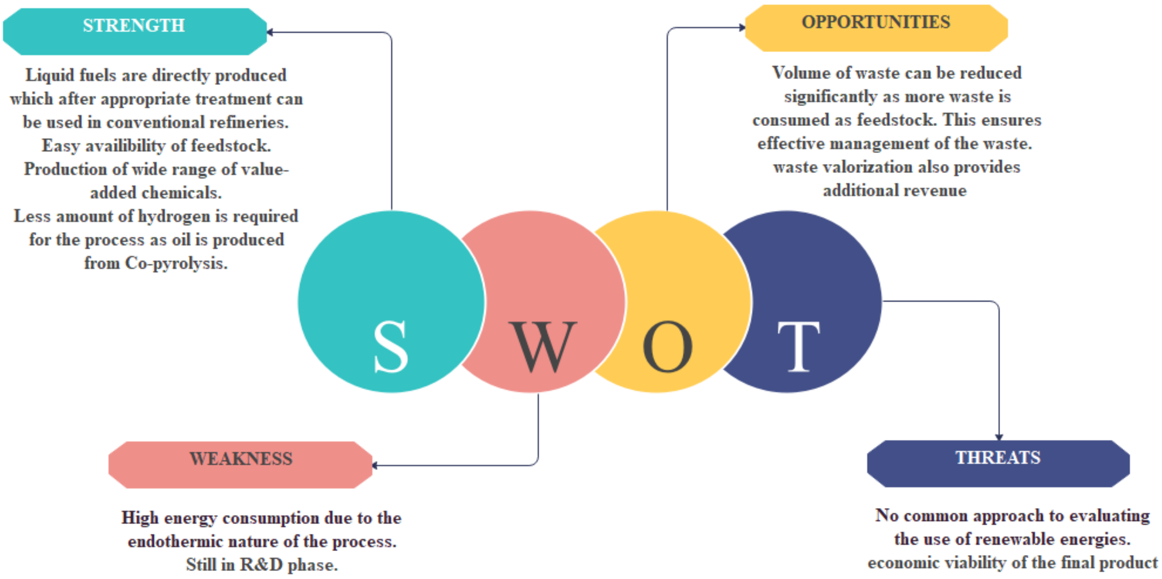

Figure 49. SWOT analysis of production of liquid biofuels from thermochemical conversion processes.

The social impact of research is closely aligned with the United Nations' Sustainable Development Goals (SDGs), as it directly tackles societal challenges and fosters positive change across various domains. The work presented in this thesis contributes to multiple SDGs, such as SDG 7 (Clean and affordable energy), SDG 12 (Responsible production and consumption), SDG 8 (Decent work and economic growth), and SDG 11 (Sustainable cities and communities).

7.3 Future Perspective

- Advanced mechanistic studies using in situ spectroscopy and computational modeling to understand deoxygenation pathways and optimize reaction conditions.
- Development of continuous-flow reactors to enhance process efficiency and scalability for industrial applications.
- Optimization of co-product recovery processes to maximize value from by-products, such as aromatics or chemicals derived from PET depolymerization.
- Investigation of bio-oil fractionation methods to selectively target desirable fractions for HDO upgrading.
- Exploration of doped and defect-engineered metal-oxide supports for improved catalyst dispersion and durability under reaction conditions.
- Comprehensive life cycle assessment (LCA) and carbon footprint analysis to ensure environmental sustainability of the integrated process.

References

[1] Dida G. Biotechnology towards energy crops. CABI Agriculture and Bioscience 2024;5. https://doi.org/10.1186/s43170-024-00245-y.

[2] Abramson M, Shoseyov O, Shani Z. Plant cell wall reconstruction toward improved lignocellulosic production and processability. Plant Science 2010;178:61–72. https://doi.org/10.1016/j.plantsci.2009.11.003.

[3] Komandur J, Mohanty K. Chapter 2 - Fast pyrolysis of biomass and hydrodeoxygenation of bio-oil for the sustainable production of hydrocarbon biofuels. In: Maity SK, Gayen K, Bhowmick TK, editors. Hydrocarbon Biorefinery, Elsevier; 2022, p. 47–76. https://doi.org/https://doi.org/10.1016/B978-0-12-823306-1.00003-0.

[4] Gielen D, Boshell F, Saygin D, Bazilian MD, Wagner N, Gorini R. The role of renewable energy in the global energy transformation. Energy Strategy Reviews 2019;24:38–50. https://doi.org/10.1016/j.esr.2019.01.006.

[5] Council), Pirttimaa L. 00% RENEWABLE ENERGY SCENARIOS SUPPORTING AMBITIOUS POLICY TARGETS Oliphant (ISES) [now representing WWEA]; and IRENA colleagues Ilina. 2024.

[6] Indian stats n.d.

[7] National Policy on Biofuels. n.d.

[8] THIS REPORT CONTAINS ASSESSMENTS OF COMMODITY AND TRADE ISSUES MADE BY USDA STAFF AND NOT NECESSARILY STATEMENTS OF OFFICIAL U.S. GOVERNMENT POLICY. 2023.

[9] Mujtaba M, Fernandes Fraceto L, Fazeli M, Mukherjee S, Savassa SM, Araujo de Medeiros G, et al. Lignocellulosic biomass from agricultural waste to the circular economy: a review with focus on biofuels, biocomposites and bioplastics. J Clean Prod 2023;402. https://doi.org/10.1016/j.jclepro.2023.136815.

[10] Renewable Energy Agency I. REmap: Renewable Energy Prospects for India. 2017.

[11] Nawaz A, Razzak SA. Co-pyrolysis of biomass and different plastic waste to reduce hazardous waste and subsequent production of energy products: A review on advancement, synergies, and future prospects. Renew Energy 2024;224. https://doi.org/10.1016/j.renene.2024.120103.

[12] Poornima S, Manikandan S, Prakash R, Deena SR, Subbaiya R, Karmegam N, et al. Biofuel and biochemical production through biomass transformation using advanced thermochemical and biochemical processes – A review. Fuel 2024;372. https://doi.org/10.1016/j.fuel.2024.132204.

[13] Kumar M, Olajire Oyedun A, Kumar A. A review on the current status of various hydrothermal technologies on biomass feedstock. Renewable and Sustainable Energy Reviews 2018;81:1742–70. https://doi.org/10.1016/j.rser.2017.05.270.

[14] Nawaz A, Kumar P. Impact of temperature severity on hydrothermal carbonization: Fuel properties, kinetic and thermodynamic parameters. Fuel 2023;336. https://doi.org/10.1016/j.fuel.2022.127166.

[15] Nawaz A, Kumar P. A novel pseudo-multicomponent isoconversional approach for the estimation of kinetic and thermodynamic parameters of potato stalk thermal degradation. Bioresour Technol 2023;376. https://doi.org/10.1016/j.biortech.2023.128846.

[16] Mishra A, Nanda S, Ranjan Parida M, Jena PK, Dwibedi SK, Manjari Samantaray S, et al. A comparative study on pyrolysis kinetics and thermodynamic parameters of little millet and sunflower stems biomass using thermogravimetric analysis. Bioresour Technol 2023;367. https://doi.org/10.1016/j.biortech.2022.128231.

[17] Singh RK, Pandey D, Patil T, Sawarkar AN. Pyrolysis of banana leaves biomass: Physico-chemical characterization, thermal decomposition behavior, kinetic and thermodynamic analyses. Bioresour Technol 2020;310. https://doi.org/10.1016/j.biortech.2020.123464.

[18] Mohan I, Panda AK, Mandal S, Kumar S. Co-pyrolysis of Azadirachta indica non-edible seed and waste LDPE: Analysis of kinetic models using thermogravimetric analyser and

prediction modeling with Artificial Neural Network (ANN). Fuel 2023;350. https://doi.org/10.1016/j.fuel.2023.128765.

[19] Mishra RK, Mohanty K. Kinetic analysis and pyrolysis behaviour of waste biomass towards its bioenergy potential. Bioresour Technol 2020;311. https://doi.org/10.1016/j.biortech.2020.123480.

[20] Wang G, Fan B, Chen H, Li Y. Understanding the pyrolysis behavior of agriculture, forest and aquatic biomass: Products distribution and characterization. Journal of the Energy Institute 2020;93:1892–900. https://doi.org/10.1016/j.joei.2020.04.004.

[21] Carregosa ISC, Carregosa J de C, Silva WR, Santos TM, Wisniewski A. Thermochemical conversion of aquatic weed biomass in a rotary kiln reactor for production of bio-based derivatives. J Anal Appl Pyrolysis 2023;173. https://doi.org/10.1016/j.jaap.2023.106048.

[22] Singh B, Singh S, Kumar P. In-depth analyses of kinetics, thermodynamics and solid reaction mechanism for pyrolysis of hazardous petroleum sludge based on isoconversional models for its energy potential. Process Safety and Environmental Protection 2021;146:85–94. https://doi.org/10.1016/j.psep.2020.08.038.

[23] Özsin G, Pütün AE. Insights into pyrolysis and co-pyrolysis of biomass and polystyrene: Thermochemical behaviors, kinetics and evolved gas analysis. Energy Convers Manag 2017;149:675–85. https://doi.org/10.1016/j.enconman.2017.07.059.

[24] Ahmad MS, Mehmood MA, Liu CG, Tawab A, Bai FW, Sakdaronnarong C, et al. Bioenergy potential of Wolffia arrhiza appraised through pyrolysis, kinetics, thermodynamics parameters and TG-FTIR-MS study of the evolved gases. Bioresour Technol 2018;253:297–303. https://doi.org/10.1016/j.biortech.2018.01.033.

[25] Zhou CH, Xia X, Lin CX, Tong DS, Beltramini J. Catalytic conversion of lignocellulosic biomass to fine chemicals and fuels. Chem Soc Rev 2011;40:5588–617. https://doi.org/10.1039/c1cs15124j.

[26] Agbor VB, Cicek N, Sparling R, Berlin A, Levin DB. Biomass pretreatment: Fundamentals toward application. Biotechnol Adv 2011;29:675–85. https://doi.org/10.1016/j.biotechadv.2011.05.005.

[27] Rubin EM. Genomics of cellulosic biofuels. Nature 2008;454:841–5. https://doi.org/10.1038/nature07190.

[28] Isikgor FH, Becer CR. Lignocellulosic biomass: a sustainable platform for the production of bio-based chemicals and polymers. Polym Chem 2015;6:4497–559. https://doi.org/10.1039/c5py00263j.

[29] Uzoejinwa BB, He X, Wang S, El-Fatah Abomohra A, Hu Y, Wang Q. Co-pyrolysis of biomass and waste plastics as a thermochemical conversion technology for high-grade biofuel production: Recent progress and future directions elsewhere worldwide. Energy Convers Manag 2018;163:468–92. https://doi.org/10.1016/j.enconman.2018.02.004.

[30] Osman AI, Mehta N, Elgarahy AM, Al-Hinai A, Al-Muhtaseb AH, Rooney DW. Conversion of biomass to biofuels and life cycle assessment: a review. Environ Chem Lett 2021;19:4075–118. https://doi.org/10.1007/s10311-021-01273-0.

[31] Lee SH, Eom MS, Yoo KS, Kim NC, Jeon JK, Park YK, et al. The yields and composition of bio-oil produced from Quercus Acutissima in a bubbling fluidized bed pyrolyzer. J Anal Appl Pyrolysis 2008;83:110–4. https://doi.org/10.1016/j.jaap.2008.06.006.

[32] plastic pyrolysis n.d.

[33] Csiro. A Roadmap for India’s Circular Economy for Plastics | Summary. n.d.

[34] plastic pyrolysis 3 n.d.

[35] Horák J, Kuboňová L, Bajer S, Dej M, Hopan F, Krpec K, et al. Composition of ashes from the combustion of solid fuels and municipal waste in households. J Environ Manage 2019;248. https://doi.org/10.1016/j.jenvman.2019.109269.

[36] Berthold EES, Deng W, Zhou J, Bertrand AME, Xu J, Jiang L, et al. Impact of plastic type on synergistic effects during co-pyrolysis of rice husk and plastics. Energy 2023;281. https://doi.org/10.1016/j.energy.2023.128270.

[37] Suriapparao D V., Kumar DA, Vinu R. Microwave co-pyrolysis of PET bottle waste and rice husk: effect of plastic waste loading on product formation. Sustainable Energy Technologies and Assessments 2022;49. https://doi.org/10.1016/j.seta.2021.101781.

[38] Ling CCY, Li SFY. Synergistic interactions between sewage sludge, polypropylene, and high-density polyethylene during co-pyrolysis: An investigation based on iso-conversional model-free methods and master plot analysis. J Hazard Mater 2023;455. https://doi.org/10.1016/j.jhazmat.2023.131600.

[39] Sekyere DT, Zhang J, Chen Y, Huang Y, Wang M, Wang J, et al. Production of light olefins and aromatics via catalytic co-pyrolysis of biomass and plastic. Fuel 2023;333. https://doi.org/10.1016/j.fuel.2022.126339.

[40] Zhang X, Li X, Li R, Wu Y. Hydrothermal Carbonization and Liquefaction of Sludge for Harmless and Resource Purposes: A Review. Energy and Fuels 2020;34:13268–90. https://doi.org/10.1021/acs.energyfuels.0c02467.

[41] Basar IA, Liu H, Carrere H, Trably E, Eskicioglu C. A review on key design and operational parameters to optimize and develop hydrothermal liquefaction of biomass for biorefinery applications. Green Chemistry 2021;23:1404–46. https://doi.org/10.1039/d0gc04092d.

[42] Khempila J, Kongto P, Meena P. Comparative study of solid biofuels derived from sugarcane leaves with two different thermochemical conversion methods: wet and dry torrefaction. Bioenergy Res 2022;15:1265–80. https://doi.org/10.1007/s12155-021-10348-3.

[43] Vashishtha M, Patidar K. Property enhancement of mustard stalk biomass by Torrefaction: Characterization and optimization of process parameters using response surface methodology. Mater Sci Energy Technol 2021;4:432–41. https://doi.org/10.1016/j.mset.2021.08.002.

[44] Zhang S, Chen T, Xiong Y, Dong Q. Effects of wet torrefaction on the physicochemical properties and pyrolysis product properties of rice husk. Energy Convers Manag 2017;141:403–9. https://doi.org/10.1016/j.enconman.2016.10.002.

[45] Chen D, Chen F, Cen K, Cao X, Zhang J, Zhou J. Upgrading rice husk via oxidative torrefaction: Characterization of solid, liquid, gaseous products and a comparison with non-oxidative torrefaction. Fuel 2020;275. https://doi.org/10.1016/j.fuel.2020.117936.

[46] Chan YH, Yusup S, Quitain AT, Tan RR, Sasaki M, Lam HL, et al. Effect of process parameters on hydrothermal liquefaction of oil palm biomass for bio-oil production and its life cycle assessment. Energy Convers Manag 2015;104:180–8. https://doi.org/10.1016/j.enconman.2015.03.075.

[47] Singh R, Chaudhary K, Biswas B, Balagurumurthy B, Bhaskar T. Hydrothermal liquefaction of rice straw: Effect of reaction environment. Journal of Supercritical Fluids 2015;104:70–5. https://doi.org/10.1016/j.supflu.2015.05.027.

[48] Ding YJ, Zhao CX, Liu ZC. Catalytic hydrothermal liquefaction of rice straw for production of monomers phenol over metal supported mesoporous catalyst. Bioresour Technol 2019;294. https://doi.org/10.1016/j.biortech.2019.122097.

[49] González-Arias J, Sánchez ME, Martínez EJ, Covalski C, Alonso-Simón A, González R, et al. Hydrothermal carbonization of olive tree pruning as a sustainableway for improving biomass energy potential: Effect of reaction parameters on fuel properties. Processes 2020;8. https://doi.org/10.3390/PR8101201.

[50] Codignole Luz F, Volpe M, Fiori L, Manni A, Cordiner S, Mulone V, et al. Spent coffee enhanced biomethane potential via an integrated hydrothermal carbonization-anaerobic digestion process. Bioresour Technol 2018;256:102–9. https://doi.org/10.1016/j.biortech.2018.02.021.

[51] Mohan I, Panda AK, Volli V, Kumar S. An insight on upgrading of biomass pyrolysis products and utilization: Current status and future prospect of biomass in India. Biomass Convers Biorefin 2024;14:6185–203. https://doi.org/10.1007/s13399-022-02833-2.

[52] Ore OT, Adebiyi FM. A review on current trends and prospects in the pyrolysis of heavy oils. Journal of Petroleum Exploration and Production 2021;11:1521–30. https://doi.org/10.1007/s13202-021-01099-0.

[53] Raza M, Inayat A, Ahmed A, Jamil F, Ghenai C, Naqvi SR, et al. Progress of the pyrolyzer reactors and advanced technologies for biomass pyrolysis processing. Sustainability (Switzerland) 2021;13. https://doi.org/10.3390/su131911061.

[54] Wang Y, He T, Liu K, Wu J, Fang Y. From biomass to advanced bio-fuel by catalytic pyrolysis/hydro-processing: Hydrodeoxygenation of bio-oil derived from biomass

catalytic pyrolysis. Bioresour Technol 2012;108:280–4. https://doi.org/10.1016/j.biortech.2011.12.132.

[55] Dewangan A, Pradhan D, Singh RK. Co-pyrolysis of sugarcane bagasse and low-density polyethylene: Influence of plastic on pyrolysis product yield. Fuel 2016;185:508–16. https://doi.org/10.1016/j.fuel.2016.08.011.

[56] Suriapparao D V., Tejasvi R. A review on role of process parameters on pyrolysis of biomass and plastics: Present scope and future opportunities in conventional and microwave-assisted pyrolysis technologies. Process Safety and Environmental Protection 2022;162:435–62. https://doi.org/10.1016/j.psep.2022.04.024.

[57] Rahman MH, Bhoi PR, Menezes PL. Pyrolysis of waste plastics into fuels and chemicals: A review. Renewable and Sustainable Energy Reviews 2023;188. https://doi.org/10.1016/j.rser.2023.113799.

[58] Kannan P, Al Shoaibi A, Srinivasakannan C. Temperature effects on the yield of gaseous olefins from waste polyethylene via flash pyrolysis. Energy and Fuels 2014;28:3363–6. https://doi.org/10.1021/ef500516n.

[59] Bok JP, Choi YS, Choi SK, Jeong YW. Fast pyrolysis of Douglas fir by using tilted-slide reactor andcharacteristics of biocrude-oil fractions. Renew Energy 2014;65:7–13. https://doi.org/10.1016/j.renene.2013.06.035.

[60] Guedes RE, Luna AS, Torres AR. Operating parameters for bio-oil production in biomass pyrolysis: A review. J Anal Appl Pyrolysis 2018;129:134–49. https://doi.org/10.1016/j.jaap.2017.11.019.

[61] Bridgwater A V. Review of fast pyrolysis of biomass and product upgrading. Biomass Bioenergy 2012;38:68–94. https://doi.org/10.1016/j.biombioe.2011.01.048.

[62] Cai J, Xu D, Dong Z, Yu X, Yang Y, Banks SW, et al. Processing thermogravimetric analysis data for isoconversional kinetic analysis of lignocellulosic biomass pyrolysis: Case study of corn stalk. Renewable and Sustainable Energy Reviews 2018;82:2705–15. https://doi.org/10.1016/j.rser.2017.09.113.

[63] Sahoo A, Gautam R, Kumar S, Mohanty K. Energy optimization from a binary mixture of non-edible oilseeds pyrolysis: Kinetic triplets analysis using Thermogravimetric Analyser and prediction modeling by Artificial Neural Network. J Environ Manage 2021;297. https://doi.org/10.1016/j.jenvman.2021.113253.

[64] Mortezaeikia V, Tavakoli O, Khodaparasti MS. A review on kinetic study approach for pyrolysis of plastic wastes using thermogravimetric analysis. J Anal Appl Pyrolysis 2021;160. https://doi.org/10.1016/j.jaap.2021.105340.

[65] Friedman HL. Kinetics of thermal degradation of char-forming plastics from thermogravimetry. Application to a phenolic plastic. Journal of Polymer Science Part C: Polymer Symposia 2007;6:183–95. https://doi.org/10.1002/polc.5070060121.

[66] Murray P. Kinetics of Clay Dehydration. Clay Miner 1955;2:255–64. https://doi.org/10.1180/claymin.1955.002.13.07.

[67] Doyle CD. Estimating isothermal life from thermogravimetric data. J Appl Polym Sci 1962;6:639–42. https://doi.org/10.1002/app.1962.070062406.

[68] Starink MJ. The determination of activation energy from linear heating rate experiments: A comparison of the accuracy of isoconversion methods. Thermochim Acta 2003;404:163–76. https://doi.org/10.1016/S0040-6031(03)00144-8.

[69] Soria-Verdugo A, Goos E, García-Hernando N. Effect of the number of TGA curves employed on the biomass pyrolysis kinetics results obtained using the Distributed Activation Energy Model. Fuel Processing Technology 2015;134:360–71. https://doi.org/10.1016/j.fuproc.2015.02.018.

[70] MY G, H B, L EM, A M, A A, K E harfi, et al. Utilization of Starink Approach and Avrami Theory to Evaluate the Kinetic Parameters of the Pyrolysis of Olive Mill Solid Waste and Olive Mill Wastewater. Journal of Advanced Chemical Engineering 2017;07:1–8. https://doi.org/10.4172/2090-4568.1000155.

[71] Vo TA, Tran QK, Ly HV, Kwon B, Hwang HT, Kim J, et al. Co-pyrolysis of lignocellulosic biomass and plastics: A comprehensive study on pyrolysis kinetics and characteristics. J Anal Appl Pyrolysis 2022;163. https://doi.org/10.1016/j.jaap.2022.105464.

[72] Alam M, Bhavanam A, Jana A, Viroja J kumar S, Peela NR. Co-pyrolysis of bamboo sawdust and plastic: Synergistic effects and kinetics. Renew Energy 2020;149:1133–45. https://doi.org/10.1016/j.renene.2019.10.103.

[73] Chen R, Zhang S, Yang X, Li G, Zhou H, Li Q, et al. Thermal behaviour and kinetic study of co-pyrolysis of microalgae with different plastics. Waste Management 2021;126:331–9. https://doi.org/10.1016/j.wasman.2021.03.001.

[74] Xie T, Zhao L, Yao Z, Kang K, Jia J, Hu T, et al. Co-pyrolysis of biomass and polyethylene: Insights into characteristics, kinetic and evolution paths of the reaction process. Science of the Total Environment 2023;897. https://doi.org/10.1016/j.scitotenv.2023.165443.

[75] Shagali AA, Hu S, Li H, Chi H, Qing H, Xu J, et al. Thermal behavior, synergistic effect and thermodynamic parameter evaluations of biomass/plastics co–pyrolysis in a concentrating photothermal TGA. Fuel 2023;331. https://doi.org/10.1016/j.fuel.2022.125724.

[76] Mohan I, Panda AK, Mandal S, Kumar S. Co-pyrolysis of Azadirachta indica non-edible seed and waste LDPE: Analysis of kinetic models using thermogravimetric analyser and prediction modeling with Artificial Neural Network (ANN). Fuel 2023;350. https://doi.org/10.1016/j.fuel.2023.128765.

[77] Mariyam S, Zuhara S, Parthasarathy P, McKay G. A Review on Catalytic Fast Co-Pyrolysis Using Analytical Py-GC/MS. Molecules 2023;28. https://doi.org/10.3390/molecules28052313.

[78] Chen WH, Ho KY, Aniza R, Sharma AK, Saravanakumar A, Hoang AT. A review of noncatalytic and catalytic pyrolysis and co-pyrolysis products from lignocellulosic and algal biomass using Py-GC/MS. Journal of Industrial and Engineering Chemistry 2024;134:51–64. https://doi.org/10.1016/j.jiec.2024.01.020.

[79] Fabbri D, Rombolà AG, Vassura I, Torri C, Franzellitti S, Capolupo M, et al. Off-line analytical pyrolysis GC–MS to study the accumulation of polystyrene microparticles in exposed mussels. J Anal Appl Pyrolysis 2020;149. https://doi.org/10.1016/j.jaap.2020.104836.

[80] Prashanth F, Narayana Sarma R, Jain A, Segar S, Choudhari H, Vinu R. Biomass fast pyrolysis kinetics using curie-point pyrolysis: Comparison with pyroprobe and thermogravimetric analysis. Journal of the Energy Institute 2024;115. https://doi.org/10.1016/j.joei.2024.101699.

[81] Sobeih KL, Baron M, Gonzalez-Rodriguez J. Recent trends and developments in pyrolysis-gas chromatography. J Chromatogr A 2008;1186:51–66. https://doi.org/10.1016/j.chroma.2007.10.017.

[82] Poulin J, Kearney M, Veall MA. Direct Inlet Py-GC-MS analysis of cultural heritage materials. J Anal Appl Pyrolysis 2022;164. https://doi.org/10.1016/j.jaap.2022.105506.

[83] Picó Y, Barceló D. Pyrolysis gas chromatography-mass spectrometry in environmental analysis: Focus on organic matter and microplastics. TrAC - Trends in Analytical Chemistry 2020;130. https://doi.org/10.1016/j.trac.2020.115964.

[84] Chen P, Hu C, Gu J, Lin X, Yang C, Leu SY, et al. Pyrolysis characteristics of tea oil camellia (Camellia oleifera Abel.) shells and their chemically pre-treated residues: Kinetics, mechanisms, product evaluation and joint optimization. J Anal Appl Pyrolysis 2022;164. https://doi.org/10.1016/j.jaap.2022.105526.

[85] Hodgson EM, Nowakowski DJ, Shield I, Riche A, Bridgwater A V., Clifton-Brown JC, et al. Variation in Miscanthus chemical composition and implications for conversion by pyrolysis and thermo-chemical bio-refining for fuels and chemicals. Bioresour Technol 2011;102:3411–8. https://doi.org/10.1016/j.biortech.2010.10.017.

[86] Idris IA, Nisamaneenate J, Atong D, Sricharoenchaikul V. A comprehensive study of facemasks pyrolysis using Py-GC/MS, kinetic analysis and ANN modeling. Arabian Journal of Chemistry 2024;17. https://doi.org/10.1016/j.arabjc.2024.105605.

[87] Jia D, Liang J, Liu J, Chen D, Evrendilek F, Wen T, et al. Insights into pyrolysis of ginger via TG-FTIR and Py-GC/MS analyses: Thermochemical behaviors, kinetics, evolved gas, and products. J Anal Appl Pyrolysis 2024;179. https://doi.org/10.1016/j.jaap.2024.106442.

[88] Kumar Mishra R. Pyrolysis of low-value waste switchgrass: Physicochemical characterization, kinetic investigation, and online characterization of hot pyrolysis vapours. Bioresour Technol 2022;347. https://doi.org/10.1016/j.biortech.2022.126720.

[89] Volli V, Gollakota ARK, Shu CM. Comparative studies on thermochemical behavior and kinetics of lignocellulosic biomass residues using TG-FTIR and Py-GC/MS. Science of the Total Environment 2021;792. https://doi.org/10.1016/j.scitotenv.2021.148392.

[90] Gu X, Ma X, Li L, Liu C, Cheng K, Li Z. Pyrolysis of poplar wood sawdust by TG-FTIR and Py-GC/MS. J Anal Appl Pyrolysis 2013;102:16–23. https://doi.org/10.1016/j.jaap.2013.04.009.

[91] Kumagai S, Takahashi Y, Kameda T, Saito Y, Yoshioka T. Quantification of cellulose pyrolyzates via a tube reactor and a pyrolyzer-gas chromatograph/flame ionization detector-based system. ACS Omega 2021;6:12022–6. https://doi.org/10.1021/acsomega.1c00622.

[92] Priyadarshi S, Vinu R. Catalytic Fast Pyrolysis of JP-10 and 3-Carene Using Analytical Py-GC/MS for the Production of Low Molecular Weight Hydrocarbons. Energy and Fuels 2022;36:12144–59. https://doi.org/10.1021/acs.energyfuels.2c01436.

[93] Pal SK, Garcés-Sánchez G, Kranert M, Vinu R. Characterization and evaluation of resource recovery potential of beach plastic wastes using analytical Py-GC/MS. J Anal Appl Pyrolysis 2023;172. https://doi.org/10.1016/j.jaap.2023.105996.

[94] Chaihad N, Kurnia I, Yoshida A, Watanabe C, Tei K, Reubroycharoen P, et al. Catalytic pyrolysis of wasted fishing net over calcined scallop shells: Analytical Py-GC/MS study. J Anal Appl Pyrolysis 2020;146. https://doi.org/10.1016/j.jaap.2019.104750.

[95] Wang M, Tian J, Roberts DG, Chang L, Xie K. Interactions between corncob and lignite during temperature-programmed co-pyrolysis. Fuel 2015;142:102–8. https://doi.org/10.1016/j.fuel.2014.11.003.

[96] Gouws SM, Carrier M, Bunt JR, Neomagus HWJP. Co-pyrolysis of coal and raw/torrefied biomass: A review on chemistry, kinetics and implementation. Renewable and Sustainable Energy Reviews 2021;135. https://doi.org/10.1016/j.rser.2020.110189.

[97] Mariyam S, Alherbawi M, Rashid N, Al-Ansari T, McKay G. Bio-Oil Production from Multi-Waste Biomass Co-Pyrolysis Using Analytical Py–GC/MS. Energies (Basel) 2022;15. https://doi.org/10.3390/en15197409.

[98] Li X, Luo S, Zuo Z, Zhang W, Ren D. The Pyrolysis Behaviors of Blended Pellets of Pine Wood and Urea-Formaldehyde Resin. Energies (Basel) 2023;16. https://doi.org/10.3390/en16042049.

[99] Nardella F, Bellavia S, Mattonai M, Ribechini E. Co-pyrolysis of biomass and plastic: Synergistic effects and estimation of elemental composition of pyrolysis oil by analytical pyrolysis–gas chromatography/mass spectrometry. Bioresour Technol 2022;354. https://doi.org/10.1016/j.biortech.2022.127170.

[100] Johansson AC, Sandström L, Öhrman OGW, Jilvero H. Co-pyrolysis of woody biomass and plastic waste in both analytical and pilot scale. J Anal Appl Pyrolysis 2018;134:102–13. https://doi.org/10.1016/j.jaap.2018.05.015.

[101] Sophonrat N, Sandström L, Johansson AC, Yang W. Co-pyrolysis of Mixed Plastics and Cellulose: An Interaction Study by Py-GC×GC/MS. Energy and Fuels 2017;31:11078–90. https://doi.org/10.1021/acs.energyfuels.7b01887.

[102] Sun J-P, Sui S-J, Zhang Z-J, Tan S, Wang Q-W. Pyrolysis of WPCs. vol. 8. 2013.

[103] Kumar A, Komandur J, Chaudhary V, Mohanty K. Catalytic Co-Pyrolysis of Mesua ferrea L. De-Oiled Cake and Garlic Husk in the Presence of Red-Mud-Based Catalysts. Catalysts 2023;13. https://doi.org/10.3390/catal13111401.

[104] Komandur J, Kumar A, Para P, Mohanty K. Kinetic Parameters Estimation of Thermal and Co-Pyrolysis of Groundnut De-oiled Cake and Polyethylene Terephthalate (PET) Waste. Energies (Basel) 2022;15. https://doi.org/10.3390/en15207502.

[105] Sahoo A, Kumar S, Mohanty K. Kinetic and thermodynamic analysis of Putranjiva roxburghii (putranjiva) and Cassia fistula (amaltas) non-edible oilseeds using thermogravimetric analyzer. Renew Energy 2021;165:261–77. https://doi.org/10.1016/j.renene.2020.11.011.

[106] Jha S, Pattnaik F, Nanda S, Zapata O, Acharya B, Dalai AK. Investigations of thermal effects during pyrolysis of agro-forestry biomass and physicochemical characterization of biofuel products. Biocatal Agric Biotechnol 2024:103379. https://doi.org/10.1016/j.bcab.2024.103379.

[107] Mukhambet Y, Shah D, Tatkeyeva G, Sarbassov Y. Slow pyrolysis of flax straw biomass produced in Kazakhstan: Characterization of enhanced tar and high-quality biochar. Fuel 2022;324. https://doi.org/10.1016/j.fuel.2022.124676.

[108] Singh A, Nanda S, Guayaquil-Sosa JF, Berruti F. Pyrolysis of Miscanthus and characterization of value-added bio-oil and biochar products. Canadian Journal of Chemical Engineering 2021;99:S55–68. https://doi.org/10.1002/cjce.23978.

[109] Patra BR, Nanda S, Dalai AK, Meda V. Slow pyrolysis of agro-food wastes and physicochemical characterization of biofuel products. Chemosphere 2021;285. https://doi.org/10.1016/j.chemosphere.2021.131431.

[110] Pradhan D, Bendu H, Singh RK, Murugan S. Mahua seed pyrolysis oil blends as an alternative fuel for light-duty diesel engines. Energy 2017;118:600–12. https://doi.org/10.1016/j.energy.2016.10.091.

[111] Ghorbannezhad P, Park S, Onwudili JA. Co-pyrolysis of biomass and plastic waste over zeolite- and sodium-based catalysts for enhanced yields of hydrocarbon products. Waste Management 2020;102:909–18. https://doi.org/10.1016/j.wasman.2019.12.006.

[112] Oyedun AO, Tee CZ, Hanson S, Hui CW. Thermogravimetric analysis of the pyrolysis characteristics and kinetics of plastics and biomass blends. Fuel Processing Technology 2014;128:471–81. https://doi.org/10.1016/j.fuproc.2014.08.010.

[113] Johansson AC, Sandström L, Öhrman OGW, Jilvero H. Co-pyrolysis of woody biomass and plastic waste in both analytical and pilot scale. J Anal Appl Pyrolysis 2018;134:102–13. https://doi.org/10.1016/j.jaap.2018.05.015.

[114] Chen L, Wang S, Meng H, Wu Z, Zhao J. Study on Gas Products Distributions during Fast Co-pyrolysis of Paulownia Wood and PET at High Temperature. Energy Procedia, vol. 105, Elsevier Ltd; 2017, p. 391–7. https://doi.org/10.1016/j.egypro.2017.03.331.

[115] Ephraim A, Pham Minh D, Lebonnois D, Peregrina C, Sharrock P, Nzihou A. Co-pyrolysis of wood and plastics: Influence of plastic type and content on product yield, gas composition and quality. Fuel 2018;231:110–7. https://doi.org/10.1016/j.fuel.2018.04.140.

[116] Akancha, Kumari N, Singh RK. Co-pyrolysis of waste polypropylene and rice bran wax– production of biofuel and its characterization. Journal of the Energy Institute 2019;92:933–46. https://doi.org/10.1016/j.joei.2018.07.011.

[117] Reshad AS, Tiwari P, Goud V V. Thermal and co-pyrolysis of rubber seed cake with waste polystyrene for bio-oil production. J Anal Appl Pyrolysis 2019;139:333–43. https://doi.org/10.1016/j.jaap.2019.03.010.

[118] Inayat A, Rocha-Meneses L, Ghenai C, Abdallah M, Shanableh A, Al-Ali K, et al. Co-pyrolysis for bio-oil production via fixed bed reactor using date seeds and plastic waste as biomass. Case Studies in Thermal Engineering 2022;31. https://doi.org/10.1016/j.csite.2022.101841.

[119] Shafaghat H, Rezaei PS, Ashri Wan Daud WM. Effective parameters on selective catalytic hydrodeoxygenation of phenolic compounds of pyrolysis bio-oil to high-value hydrocarbons. RSC Adv 2015;5:103999–4042. https://doi.org/10.1039/c5ra22137d.

[120] Bridgwater A V. Review of fast pyrolysis of biomass and product upgrading. Biomass Bioenergy 2012;38:68–94. https://doi.org/10.1016/j.biombioe.2011.01.048.

[121] Bridgwater T. Challenges and opportunities in fast pyrolysis of biomass: Part II. Johnson Matthey Technology Review 2018;62:150–60. https://doi.org/10.1595/205651318X696738.

[122] Gollakota ARK, Reddy M, Subramanyam MD, Kishore N. A review on the upgradation techniques of pyrolysis oil. Renewable and Sustainable Energy Reviews 2016;58:1543–68. https://doi.org/10.1016/j.rser.2015.12.180.

[123] Kim S, Kwon EE, Kim YT, Jung S, Kim HJ, Huber GW, et al. Recent advances in hydrodeoxygenation of biomass-derived oxygenates over heterogeneous catalysts. Green Chemistry 2019;21:3715–43. https://doi.org/10.1039/c9gc01210a.

[124] Oyedun AO, Patel M, Kumar M, Kumar A. The Upgrading of Bio-Oil via Hydrodeoxygenation. Chemical Catalysts for Biomass Upgrading 2020:35–60. https://doi.org/10.1002/9783527814794.ch2.

[125] Kim S, Kwon EE, Kim YT, Jung S, Kim HJ, Huber GW, et al. Recent advances in hydrodeoxygenation of biomass-derived oxygenates over heterogeneous catalysts. Green Chemistry 2019;21:3715–43. https://doi.org/10.1039/c9gc01210a.

[126] Dabros TMH, Stummann MZ, Høj M, Jensen PA, Grunwaldt JD, Gabrielsen J, et al. Transportation fuels from biomass fast pyrolysis, catalytic hydrodeoxygenation, and catalytic fast hydropyrolysis. Prog Energy Combust Sci 2018;68:268–309. https://doi.org/10.1016/j.pecs.2018.05.002.

[127] Prasomsri T, Nimmanwudipong T, Román-Leshkov Y. Effective hydrodeoxygenation of biomass-derived oxygenates into unsaturated hydrocarbons by MoO3 using low H2 pressures. Energy Environ Sci 2013;6:1732–8. https://doi.org/10.1039/c3ee24360e.

[128] Mortensen PM, Gardini D, Damsgaard CD, Grunwaldt JD, Jensen PA, Wagner JB, et al. Deactivation of Ni-MoS2 by bio-oil impurities during hydrodeoxygenation of phenol and octanol. Appl Catal A Gen 2016;523:159–70. https://doi.org/10.1016/j.apcata.2016.06.002.

[129] Berenguer A, Sankaranarayanan TM, Gómez G, Moreno I, Coronado JM, Pizarro P, et al. Evaluation of transition metal phosphides supported on ordered mesoporous materials as catalysts for phenol hydrodeoxygenation. Green Chemistry 2016;18:1938–51. https://doi.org/10.1039/c5gc02188j.

[130] Mortensen PM, Grunwaldt JD, Jensen PA, Knudsen KG, Jensen AD. A review of catalytic upgrading of bio-oil to engine fuels. Appl Catal A Gen 2011;407:1–19. https://doi.org/10.1016/j.apcata.2011.08.046.

[131] Centeno A, Laurent E, Delmon B. Influence of the support of CoMo Sulfide Catalysts and of the Addition of Potassium and Platinum on the Catalytic Performances for the hydrodeoxygenation of guaicol. E. Delmon.pdf. J Catal 1995:288–98.

[132] Jin S, Xiao Z, Li C, Chen X, Wang L, Xing J, et al. Catalytic hydrodeoxygenation of anisole as lignin model compound over supported nickel catalysts. Catal Today 2014;234:125–32. https://doi.org/10.1016/j.cattod.2014.02.014.

[133] Ahmadi S, Reyhanitash E, Yuan Z, Rohani S, Xu C (Charles). Upgrading of fast pyrolysis oil via catalytic hydrodeoxygenation: Effects of type of solvents. Renew Energy 2017;114:376–82. https://doi.org/10.1016/j.renene.2017.07.041.

[134] Kim TS, Oh S, Kim JY, Choi IG, Choi JW. Study on the hydrodeoxygenative upgrading of crude bio-oil produced from woody biomass by fast pyrolysis. Energy 2014;68:437–43. https://doi.org/10.1016/j.energy.2014.03.004.

[135] Routray K, Barnett KJ, Huber GW. Hydrodeoxygenation of Pyrolysis Oils. Energy Technology 2017;5:80–93. https://doi.org/10.1002/ente.201600084.

[136] Dabros TMH, Andersen ML, Lindahl SB, Hansen TW, Høj M, Gabrielsen J, et al. Hydrodeoxygenation (HDO) of Aliphatic Oxygenates. Catalysts 2019;9.

[137] Yang X, Zhang J, Zheng J, Liu Z, Liu J, Li S, et al. In-situ and ex-situ catalytic pyrolysis of cellulose to produce furans over red mud-supported transition metal catalysts. J Anal Appl Pyrolysis 2023;169. https://doi.org/10.1016/j.jaap.2022.105830.

[138] Sushil S, Batra VS. Catalytic applications of red mud, an aluminium industry waste: A review. Appl Catal B 2008;81:64–77. https://doi.org/10.1016/j.apcatb.2007.12.002.

[139] Yathavan BK, Agblevor FA. Catalytic pyrolysis of pinyon-juniper using red mud and HZSM-5. Energy and Fuels 2013;27:6858–65. https://doi.org/10.1021/ef401853a.

[140] Jahromi H, Agblevor FA. Hydrodeoxygenation of pinyon-juniper catalytic pyrolysis oil using red mud-supported nickel catalysts. Appl Catal B 2018;236:1–12. https://doi.org/10.1016/j.apcatb.2018.05.008.

[141] Klopries B, Hodek W, Bandermann F. Catalytic hydroliquefaction of biomass with red mud and COO-MOO, catalysts. n.d.

[142] Ruangudomsakul M, Osakoo N, Wittayakun J, Keawkumay C, Butburee T, Youngjan S, et al. Hydrodeoxygenation of palm oil to green diesel products on mixed-phase nickel phosphides. Molecular Catalysis 2022;523. https://doi.org/10.1016/j.mcat.2021.111422.

[143] Yan P, Mensah J, Adesina A, Kennedy E, Stockenhuber M. Highly-dispersed Ni on BEA catalyst prepared by ion-exchange-deposition-precipitation for improved hydrodeoxygenation activity. Appl Catal B 2020;267. https://doi.org/10.1016/j.apcatb.2020.118690.

[144] Ding S, Parlett CMA, Fan X. Recent developments in multifunctional catalysts for fatty acid hydrodeoxygenation as a route towards biofuels. Molecular Catalysis 2022;523. https://doi.org/10.1016/j.mcat.2021.111492.

[145] Besse X, Schuurman Y, Guilhaume N. Hydrothermal conversion of linoleic acid and ethanol for biofuel production. Appl Catal A Gen 2016;524:139–48. https://doi.org/10.1016/j.apcata.2016.06.030.

[146] Ameen M, Azizan MT, Yusup S, Ramli A, Yasir M. Catalytic hydrodeoxygenation of triglycerides: An approach to clean diesel fuel production. Renewable and Sustainable Energy Reviews 2017;80:1072–88. https://doi.org/10.1016/j.rser.2017.05.268.

[147] Zhang M, Xiang L, Fan G, Yang L, Li F. Unveiling the role of surface basic sites on ruthenium-based nanocatalysts for enhanced hydrodeoxygenation of guaiacol. Molecular Catalysis 2022;533. https://doi.org/10.1016/j.mcat.2022.112794.

[148] Wang W, Guo L, He X, Deng L, Qiao C, Tian Y. Uniform Ni species encapsulated in nanocrystalline ZSM–5 with enhanced catalytic performance for upgrading of fatty acids. Fuel 2023;346. https://doi.org/10.1016/j.fuel.2023.128411.

[149] Philippov AA, Nasokhov DE, Prosvirin IP, Martyanov ON. Bimetallic Ni-Co catalyst for improving selectivity in transfer hydrogenation of phenolic compounds. Molecular Catalysis 2024;561. https://doi.org/10.1016/j.mcat.2024.114200.

[150] Duan J, Wu Y, Zheng J, Li X, Lin X, Wang D, et al. Enhancing catalytic performance of red mud for palmitic acid hydrodeoxygenation by acid pretreatment-induced structural modification. Fuel Processing Technology 2023;248. https://doi.org/10.1016/j.fuproc.2023.107839.

[151] Chen J, Wang D, Luo F, Yang X, Li X, Li S, et al. Selective production of alkanes and fatty alcohol via hydrodeoxygenation of palmitic acid over red mud-supported nickel catalysts. Fuel 2022;314. https://doi.org/10.1016/j.fuel.2021.122780.

[152] Wang Q, Li X, Duan J, Chen J, Ye Y, Wang D, et al. Rationally control the path of hydrodeoxygenation of palmitic acid over Ni/red-mud catalysts by surface decoration of oxophilic MoOx species. Fuel 2022;329. https://doi.org/10.1016/j.fuel.2022.125447.

[153] Chen J, Zhu Y, Li W, Luo F, Li S, Li X, et al. Production of diesel-like hydrocarbons via hydrodeoxygenation of palmitic acid over Ni/TS-1 catalyst. Biomass Bioenergy 2021;149. https://doi.org/10.1016/j.biombioe.2021.106081.

[154] Lee CW, Lin PY, Chen BH, Kukushkin RG, Yakovlev VA. Hydrodeoxygenation of palmitic acid over zeolite-supported nickel catalysts. Catal Today 2021;379:124–31. https://doi.org/10.1016/j.cattod.2020.05.013.

[155] Liang J, Chen T, Liu J, Zhang Q, Peng WC, Li Y, et al. Chemoselective hydrodeoxygenation of palmitic acid to diesel-like hydrocarbons over Ni/MoO2@Mo2CTx catalyst with extraordinary synergic effect. Chemical Engineering Journal 2020;391. https://doi.org/10.1016/j.cej.2019.123472.

[156] Ahmadi S, Reyhanitash E, Yuan Z, Rohani S, Xu C (Charles). Upgrading of fast pyrolysis oil via catalytic hydrodeoxygenation: Effects of type of solvents. Renew Energy 2017;114:376–82. https://doi.org/10.1016/j.renene.2017.07.041.

[157] Wang H, Elliott DC, French RJ, Deutch S, Iisa K. Biomass conversion to produce hydrocarbon liquid fuel via hot-vapor filtered fast pyrolysis and catalytic hydrotreating. Journal of Visualized Experiments 2016;2016:1–13. https://doi.org/10.3791/54088.

[158] Mohan D, Pittman CU, Steele PH. Pyrolysis of wood/biomass for bio-oil: A critical review. Energy and Fuels 2006;20:848–89. https://doi.org/10.1021/ef0502397.

[159] Gea S, Hutapea YA, Piliang AFR, Pulungan AN, Rahayu R, Layla J, et al. A Comprehensive Review of Experimental Parameters in Bio-oil Upgrading from Pyrolysis of Biomass to Biofuel Through Catalytic Hydrodeoxygenation. Bioenergy Res 2023;16:325–47. https://doi.org/10.1007/s12155-022-10438-w.

[160] Shu R, Li R, Lin B, Luo B, Tian Z. High dispersed Ru/SiO2-ZrO2 catalyst prepared by polyol reduction method and its catalytic applications in the hydrodeoxygenation of phenolic compounds and pyrolysis lignin-oil. Fuel 2020;265. https://doi.org/10.1016/j.fuel.2019.116962.

[161] Hu L, Wei XY, Zong ZM. Ru/Hβ catalyst prepared by the deposition-precipitation method for enhancing hydrodeoxygenation ability of guaiacol and lignin-derived bio-oil to produce hydrocarbons. Journal of the Energy Institute 2021;97:48–57. https://doi.org/10.1016/j.joei.2021.04.001.

[162] Li Z, Yi W, Li Z, Bai X, Fu P, Tian C, et al. Hydrodeoxygenation of bio-oil and model compounds for production of chemical materials at atmospheric pressure over nickel-based zeolite catalysts. Energy Sources, Part A: Recovery, Utilization and Environmental Effects 2020. https://doi.org/10.1080/15567036.2020.1765901.

[163] Remón J, Casales M, Gracia J, Callén MS, Pinilla JL, Suelves I. Sustainable production of liquid biofuels and value-added platform chemicals by hydrodeoxygenation of lignocellulosic bio-oil over a carbon–neutral Mo2C/CNF catalyst. Chemical Engineering Journal 2021;405. https://doi.org/10.1016/j.cej.2020.126705.

[164] Cheng S, Wei L, Julson J, Muthukumarappan K, Kharel PR. Upgrading pyrolysis bio-oil to biofuel over bifunctional Co-Zn/HZSM-5 catalyst in supercritical methanol. Energy Convers Manag 2017;147:19–28. https://doi.org/10.1016/j.enconman.2017.05.044.

[165] Sluiter A, Hames B, Ruiz R, Scarlata C, Sluiter J, Templeton D, et al. Determination of Structural Carbohydrates and Lignin in Biomass: Laboratory Analytical Procedure (LAP) (Revised July 2011). 2008.

[166] Obernberger I, Thek G. Physical characterisation and chemical composition of densified biomass fuels with regard to their combustion behaviour. Biomass Bioenergy 2004;27:653–69. https://doi.org/10.1016/j.biombioe.2003.07.006.

[167] Priyadarshi S, Vinu R. Catalytic Fast Pyrolysis of JP-10 and 3-Carene Using Analytical Py-GC/MS for the Production of Low Molecular Weight Hydrocarbons. Energy and Fuels 2022;36:12144–59. https://doi.org/10.1021/acs.energyfuels.2c01436.

[168] Cai W, Liu R. Performance of a commercial-scale biomass fast pyrolysis plant for bio-oil production. Fuel 2016;182:677–86. https://doi.org/10.1016/j.fuel.2016.06.030.

[169] Williams CL, Westover TL, Emerson RM, Tumuluru JS, Li C. Sources of Biomass Feedstock Variability and the Potential Impact on Biofuels Production. Bioenergy Res 2016;9:1–14. https://doi.org/10.1007/s12155-015-9694-y.

[170] Agrawalla A, Kumar S, Singh RK. Pyrolysis of groundnut de-oiled cake and characterization of the liquid product. Bioresour Technol 2011;102:10711–6. https://doi.org/10.1016/j.biortech.2011.08.113.

[171] Volli V, Singh RK. Pyrolysis kinetics of de-oiled cakes by thermogravimetric analysis. Journal of Renewable and Sustainable Energy 2013;5. https://doi.org/10.1063/1.4811794.

[172] Mahapatra SS, Karak N. Synthesis and characterization of polyesteramide resins from Nahar seed oil for surface coating applications. Prog Org Coat 2004;51:103–8. https://doi.org/10.1016/j.porgcoat.2004.07.003.

[173] Devi A, Singh A, Kothari R. Fungi based valorization of wheat straw and rice straw for cellulase and xylanase production. Sustainable Chemistry for the Environment 2024;5. https://doi.org/10.1016/j.scenv.2024.100077.

[174] Osman AI, Farrell C, Al-Muhtaseb AH, Al-Fatesh AS, Harrison J, Rooney DW. Pyrolysis kinetic modelling of abundant plastic waste (PET) and in-situ emission monitoring. Environ Sci Eur 2020;32. https://doi.org/10.1186/s12302-020-00390-x.

[175] He Q, Ding L, Gong Y, Li W, Wei J, Yu G. Effect of torrefaction on pinewood pyrolysis kinetics and thermal behavior using thermogravimetric analysis. Bioresour Technol 2019;280:104–11. https://doi.org/10.1016/j.biortech.2019.01.138.

[176] Chutia RS, Kataki R, Bhaskar T. Thermogravimetric and decomposition kinetic studies of Mesua ferrea L. deoiled cake. Bioresour Technol 2013;139:66–72. https://doi.org/10.1016/j.biortech.2013.03.191.

[177] Chen Y, Wang Z, Chen G, Wang Q, Sun T, Zhang M, et al. Synergistic effects and products yield analyses based on co-pyrolysis of poplar tree and rape stalks with polyethylene terephthalate and polypropylene. Journal of the Energy Institute 2024;112. https://doi.org/10.1016/j.joei.2023.101461.

[178] Sait HH, Hussain A, Salema AA, Ani FN. Pyrolysis and combustion kinetics of date palm biomass using thermogravimetric analysis. Bioresour Technol 2012;118:382–9. https://doi.org/10.1016/j.biortech.2012.04.081.

[179] Rammohan D, Kishore N, Uppaluri RVS. Reaction kinetics and thermodynamic analysis of non-isothermal co-pyrolysis of Delonix regia and tube waste. Bioresour Technol Rep 2022;18. https://doi.org/10.1016/j.biteb.2022.101032.

[180] Praveen Kumar K, Srinivas S. Catalytic Co-pyrolysis of Biomass and Plastics (Polypropylene and Polystyrene) Using Spent FCC Catalyst. Energy and Fuels 2020;34:460–73. https://doi.org/10.1021/acs.energyfuels.9b03135.

[181] Burra KG, Gupta AK. Kinetics of synergistic effects in co-pyrolysis of biomass with plastic wastes. Appl Energy 2018;220:408–18. https://doi.org/10.1016/j.apenergy.2018.03.117.

[182] Komandur J, Vinu R, Mohanty K. Pyrolysis kinetics and pyrolysate composition analysis of Mesua ferrea L: A non-edible oilseed towards the production of sustainable renewable fuel. Bioresour Technol 2022;351. https://doi.org/10.1016/j.biortech.2022.126987.

[183] Dos Santos Pereira AP, Da Silva MHP, Lima ÉP, Dos Santos Paula A, Tommasini FJ. Processing and characterization of PET composites reinforced with geopolymer concrete waste. Materials Research 2017;20:411–20. https://doi.org/10.1590/1980-5373-MR-2017-0734.

[184] Gonnella G, Ischia G, Fambri L, Fiori L. Thermal Analysis and Kinetic Modeling of Pyrolysis and Oxidation of Hydrochars. Energies (Basel) 2022;15. https://doi.org/10.3390/en15030950.

[185] El-Sayed SA, Khass TM, Mostafa ME. Thermal degradation behaviour and chemical kinetic characteristics of biomass pyrolysis using TG/DTG/DTA techniques. Biomass Convers Biorefin 2024;14:17779–803. https://doi.org/10.1007/s13399-023-03926-2.

[186] Mishra RK, Sahoo A, Mohanty K. Pyrolysis kinetics and synergistic effect in co-pyrolysis of Samanea saman seeds and polyethylene terephthalate using

thermogravimetric analyser. Bioresour Technol 2019;289:121608. https://doi.org/10.1016/j.biortech.2019.121608.

[187] Cai H, Liu J, Xie W, Kuo J, Buyukada M, Evrendilek F. Pyrolytic kinetics, reaction mechanisms and products of waste tea via TG-FTIR and Py-GC/MS. Energy Convers Manag 2019;184:436–47. https://doi.org/10.1016/j.enconman.2019.01.031.

[188] Kumar Mishra R. Pyrolysis of low-value waste switchgrass: Physicochemical characterization, kinetic investigation, and online characterization of hot pyrolysis vapours. Bioresour Technol 2022;347. https://doi.org/10.1016/j.biortech.2022.126720.

[189] Mishra RK, Lu Q, Mohanty K. Thermal behaviour, kinetics and fast pyrolysis of Cynodon dactylon grass using Py-GC/MS and Py-FTIR analyser. J Anal Appl Pyrolysis 2020;150:104887. https://doi.org/10.1016/j.jaap.2020.104887.

[190] Várhegyi G, Wang L, Skreiberg Ø. Non-isothermal kinetics: best-fitting empirical models instead of model-free methods. J Therm Anal Calorim 2019. https://doi.org/10.1007/s10973-019-09162-z.

[191] Cai H, Liu J, Xie W, Kuo J, Buyukada M, Evrendilek F. Pyrolytic kinetics, reaction mechanisms and products of waste tea via TG-FTIR and Py-GC/MS. Energy Convers Manag 2019;184:436–47. https://doi.org/10.1016/j.enconman.2019.01.031.

[192] Mohan I, Sahoo A, Mandal S, Kumar S. Kinetic modeling and thermogravimetric investigation of Phoenix dactylifera and Phyllanthus emblica non-edible oil seeds: artificial neural network (ANN) prediction modeling. Biomass Convers Biorefin 2024;14:20635–54. https://doi.org/10.1007/s13399-023-04094-z.

[193] Muktham R, Ball AS, Bhargava SK, Bankupalli S. Study of thermal behavior of deoiled karanja seed cake biomass: Thermogravimetric analysis and pyrolysis kinetics. Energy Sci Eng 2016;4:86–95. https://doi.org/10.1002/ese3.109.

[194] Fu Q. The Pyrolysis of Inorganic Fire Retardant Polyolefin Cable Materials. Procedia Eng, vol. 135, Elsevier Ltd; 2016, p. 293–8. https://doi.org/10.1016/j.proeng.2016.01.127.

[195] Pihl O, Khaskhachikh V, Kravetskaja J, Niidu A, Siirde A. Co-Pyrolysis of Estonian Oil Shale with Polymer Wastes. ACS Omega 2021;6:31658–66. https://doi.org/10.1021/acsomega.1c04188.

[196] Farobie O, Amrullah A, Syaftika N, Bayu A, Hartulistiyoso E, Fatriasari W, et al. Valorization of Rejected Macroalgae Kappaphycopsis cottonii for Bio-Oil and Bio-Char Production via Slow Pyrolysis. ACS Omega 2024;9:16665–75. https://doi.org/10.1021/acsomega.4c00678.

[197] Wang S, Mandfloen P, Jönsson P, Yang W. Synergistic effects in the copyrolysis of municipal sewage sludge digestate and salix: Reaction mechanism, product characterization and char stability. Appl Energy 2021;289. https://doi.org/10.1016/j.apenergy.2021.116687.

[198] Ren Q, Zhao C. Evolution of fuel-N in gas phase during biomass pyrolysis. Renewable and Sustainable Energy Reviews 2015;50:408–18. https://doi.org/10.1016/j.rser.2015.05.043.

[199] Liu N, Huang H, Huang X, Li R, Feng J, Wu Y. Co-pyrolysis Behavior of Coal and Biomass: Synergistic Effect and Kinetic Analysis. ACS Omega 2024;9:31803–13. https://doi.org/10.1021/acsomega.4c03053.

[200] Krishna JVJ, Prashanth PF, Vinu R. Distributed Activation Energy Modeling and Py-GC/MS Studies on Pyrolysis of Different Printed Circuit Boards for Resource Recovery. ACS Omega 2022;7:31713–25. https://doi.org/10.1021/acsomega.2c02003.

[201] Kojić I, Bechtel A, Aleksić N, Životić D, Trifunović S, Gajica G, et al. Study of the synergetic effect of co-pyrolysis of lignite and high-density polyethylene aiming to improve utilization of low-rank coal. Polymers (Basel) 2021;13:1–25. https://doi.org/10.3390/polym13050759.

[202] Chen W, Shi S, Zhang J, Chen M, Zhou X. Co-pyrolysis of waste newspaper with high-density polyethylene: Synergistic effect and oil characterization. Energy Convers Manag 2016;112:41–8. https://doi.org/10.1016/j.enconman.2016.01.005.

[203] Chattopadhyay J, Pathak TS, Srivastava R, Singh AC. Catalytic co-pyrolysis of paper biomass and plastic mixtures (HDPE (high density polyethylene), PP (polypropylene)

and PET (polyethylene terephthalate)) and product analysis. Energy 2016;103:513–21. https://doi.org/10.1016/j.energy.2016.03.015.

[204] M AK, A.P S, J S, C SD, P S, Hatamleh AA, et al. Pyrolysis behaviour and synergistic effect in co-pyrolysis of wheat straw and polyethylene terephthalate: A study on product distribution and oil characterization. Heliyon 2024;10. https://doi.org/10.1016/j.heliyon.2024.e37255.

[205] Anandaram H, Srivastava BK, Vijayakumar B, Madhu P, Depoures MV, Patil PP, et al. Co-pyrolysis Characteristics and Synergistic Interaction of Waste Polyethylene Terephthalate and Woody Biomass towards Bio-Oil Production. J Chem 2022;2022. https://doi.org/10.1155/2022/3699076.

[206] Fukushima M, Yamamoto M, Komai T, Yamamoto K. Studies of structural alterations of humic acids from conifer bark residue during composting by pyrolysis-gas chromatography/mass spectrometry using tetramethylammonium hydroxide (TMAH-py-GC/MS). J Anal Appl Pyrolysis 2009;86:200–6. https://doi.org/10.1016/j.jaap.2009.06.005.

[207] Gallois N, Templier J, Derenne S. Pyrolysis-gas chromatography-mass spectrometry of the 20 protein amino acids in the presence of TMAH. J Anal Appl Pyrolysis 2007;80:216–30. https://doi.org/10.1016/j.jaap.2007.02.010.

[208] Iwai H, Fukushima M, Yamamoto M, Komai T, Kawabe Y. Characterization of seawater extractable organic matter from bark compost by TMAH-py-GC/MS. J Anal Appl Pyrolysis 2013;99:9–15. https://doi.org/10.1016/j.jaap.2012.11.012.

[209] Kaal J, Goñi-Urtiaga A, Wenig P, Veliu M, Moreno-Jiménez E, Plaza C, et al. Simultaneous molecular fingerprinting of natural organic matter and synthetic polymers (PE, PET, PP, PS and PVC) using analytical pyrolysis. J Anal Appl Pyrolysis 2023;175. https://doi.org/10.1016/j.jaap.2023.106159.

[210] Bashir M, Hassan NU, Ibrahim M, Ali HM, Tahir MH, Naseem K, et al. Synergistic Interaction during Copyrolysis of Soybean Straw and Tire Waste: Improving Emissions and Product Quality. ACS Omega 2024. https://doi.org/10.1021/acsomega.4c02366.

[211] Garg R, Anand N, Kumar D. Pyrolysis of babool seeds (Acacia nilotica) in a fixed bed reactor and bio-oil characterization. Renew Energy 2016;96:167–71. https://doi.org/10.1016/j.renene.2016.04.059.

[212] Mohan I, Arya A, Singh R, Kumar S. Materials Today : Proceedings Pyrolysis of Phoenix Dactylifera and Phyllanthus Emblica seeds to produce biofuel. Mater Today Proc 2023;72:713–8. https://doi.org/10.1016/j.matpr.2022.08.490.

[213] Berthold EES, Deng W, Zhou J, Bertrand AME, Xu J, Jiang L, et al. Impact of plastic type on synergistic effects during co-pyrolysis of rice husk and plastics. Energy 2023;281. https://doi.org/10.1016/j.energy.2023.128270.

[214] Hu Q, Zhang H, Mao Q, Zhu J, Zhang S, Yang H, et al. The effect of co-pyrolysis of bamboo waste and polypropylene on biomass deoxygenation and carbonization processes. Energy 2024;291. https://doi.org/10.1016/j.energy.2024.130339.

[215] Al-Layla NMT, Saleh LA, Fadhil AB. Liquid bio-fuels and carbon adsorbents production via pyrolysis of non-edible feedstock. J Anal Appl Pyrolysis 2021;156. https://doi.org/10.1016/j.jaap.2021.105088.

[216] Wu F, Ben H, Yang Y, Jia H, Wang R, Han G. Effects of different conditions on co-pyrolysis behavior of corn stover and polypropylene. Polymers (Basel) 2020;12. https://doi.org/10.3390/POLYM12040973.

[217] Marais C, Bunt JR, Leokaoke NT, Coetzer RLJ, Neomagus HWJP. Slow Pyrolysis Products Derived from Extrudates Produced from Discard Coal Fines and Recycled Plastics as Binders. ACS Omega 2024;9:6627–41. https://doi.org/10.1021/acsomega.3c07626.

[218] Al-Layla NMT, Saleh LA, Fadhil AB. Liquid bio-fuels and carbon adsorbents production via pyrolysis of non-edible feedstock. J Anal Appl Pyrolysis 2021;156. https://doi.org/10.1016/j.jaap.2021.105088.

[219] Das P, Tiwari P. Valorization of packaging plastic waste by slow pyrolysis. Resour Conserv Recycl 2018;128:69–77. https://doi.org/10.1016/j.resconrec.2017.09.025.

[220] Maher KD, Kirkwood KM, Gray MR, Bressler DC. Pyrolytic decarboxylation and cracking of stearic acid. Ind Eng Chem Res 2008;47:5328–36. https://doi.org/10.1021/ie0714551.

[221] Kraiem T, Hassen-Trabelsi A Ben, Naoui S, Belayouni H, Jeguirim M. Characterization of the liquid products obtained from Tunisian waste fish fats using the pyrolysis process. Fuel Processing Technology 2015;138:404–12. https://doi.org/10.1016/j.fuproc.2015.05.007.

[222] Zhang Y, Ma Z, Yan J. Effect of water, fat, and protein in raw pork from swine carcasses on the pyrolytic gaseous and liquid product distribution. Fuel Processing Technology 2018;171:45–53. https://doi.org/10.1016/j.fuproc.2017.10.020.

[223] Dhahak A, Hild G, Rouaud M, Mauviel G, Burkle-Vitzthum V. Slow pyrolysis of polyethylene terephthalate: Online monitoring of gas production and quantitative analysis of waxy products. J Anal Appl Pyrolysis 2019;142. https://doi.org/10.1016/j.jaap.2019.104664.

[224] Özsin G, Pütün AE. A comparative study on co-pyrolysis of lignocellulosic biomass with polyethylene terephthalate, polystyrene, and polyvinyl chloride: Synergistic effects and product characteristics. J Clean Prod 2018;205:1127–38. https://doi.org/10.1016/j.jclepro.2018.09.134.

[225] Hassan H, Hameed BH, Lim JK. Co-pyrolysis of sugarcane bagasse and waste high-density polyethylene: Synergistic effect and product distributions. Energy 2020;191. https://doi.org/10.1016/j.energy.2019.116545.

[226] Tan KB, Qiu Y, Li Y, Chen B, Xia L, Cai D, et al. Enhanced catalytic deoxygenation of stearic acid into biofuels over supported FeNi catalysts. Molecular Catalysis 2024;565. https://doi.org/10.1016/j.mcat.2024.114361.

[227] Ding S, Parlett CMA, Fan X. Recent developments in multifunctional catalysts for fatty acid hydrodeoxygenation as a route towards biofuels. Molecular Catalysis 2022;523. https://doi.org/10.1016/j.mcat.2021.111492.

[228] Raikwar D, Majumdar S, Shee D. Synergistic effect of Ni-Co alloying on hydrodeoxygenation of guaiacol over Ni-Co/Al2O3 catalysts. Molecular Catalysis 2021;499. https://doi.org/10.1016/j.mcat.2020.111290.

[229] Blanco E, Dongil AB, Escalona N. Synergy between ni and co nanoparticles supported on carbon in guaiacol conversion. Nanomaterials 2020;10:1–18. https://doi.org/10.3390/nano10112199.

[230] Das B, Mohanty K. A review on advances in sustainable energy production through various catalytic processes by using catalysts derived from waste red mud. Renew Energy 2019;143:1791–811. https://doi.org/10.1016/j.renene.2019.05.114.

[231] Wang Q, Chen J, Li X, Yang X, Wu Y, Li S, et al. Calcination temperature induced structural change of red mud and its enhanced catalytic performance for hydrocarbon-based biofuels production. Fuel Processing Technology 2022;233. https://doi.org/10.1016/j.fuproc.2022.107316.

[232] Ali B, Tasirin SM, Aminayi P, Yaakob Z, Ali NT, Noori W. Non-supported nickel-based coral sponge-like porous magnetic alloys for catalytic production of syngas and carbon bio-nanofilaments via a biogas decomposition approach. Nanomaterials 2018;8. https://doi.org/10.3390/NANO8121053.

[233] Raju P, Jesuraj JP, Muthukumaran S. Influence of Ni2+ ions on the structural, morphological, photoluminescence, photo-catalytic and anti-bacterial studies of Cd0.9Zn0.1S nanostructures. Journal of Materials Science: Materials in Electronics 2021;32:14310–27. https://doi.org/10.1007/s10854-021-05994-4.

[234] Hamid S, Bae S, Lee W. Novel bimetallic catalyst supported by red mud for enhanced nitrate reduction. Chemical Engineering Journal 2018;348:877–87. https://doi.org/10.1016/j.cej.2018.05.016.

[235] Liang J, Zhang Q, Zhao H, Zhao S, Wu Y, Fan X. Hydrodeoxygenation of Palmitic Acid with Novel Two-Dimensional Ti3C2T xMXene-Supported Ni Catalyst. Ind Eng Chem Res 2022. https://doi.org/10.1021/acs.iecr.2c02090.

[236] Ding X, Li T, Wang J, Wu L, Zheng L, Wang Y. Catalytic co-liquefaction of microalgae + corn straw over K3PO4+γ-Al2O3 supported Fe and Ni mono- / bimetallic in-situ

composite catalysts for the production of liquid biofuel. Chemical Engineering Journal 2023;471. https://doi.org/10.1016/j.cej.2023.144668.

[237] Wang D, Li Y, Jin L, Hao K, Wei B, Yao D, et al. Integrated process for partial oxidation of heavy oil and in-situ reduction of red mud. Appl Catal B 2019;258. https://doi.org/10.1016/j.apcatb.2019.117944.

[238] Witsuthammakul A, Sooknoi T. Selective hydrodeoxygenation of bio-oil derived products: Ketones to olefins. Catal Sci Technol 2015;5:3639–48. https://doi.org/10.1039/c5cy00367a.

[239] Zheng W, Bi W, Gao X, Zhang Z, Yuan W, Li L. A nickel and cobalt bimetal organic framework with high capacity as an anode material for lithium-ion batteries. Sustain Energy Fuels 2020;4:5757–64. https://doi.org/10.1039/d0se00983k.

[240] Nashim A, Pany S, Parida K. Effect of synthesis methods on the activity of NiO/Co3O4 as an electrode material for supercapacitor: in the light of X-ray diffraction study. RSC Adv 2024;14:233–44. https://doi.org/10.1039/d3ra05200a.

[241] Ding R, Wu Y, Chen Y, Chen H, Wang J, Shi Y, et al. Catalytic hydrodeoxygenation of palmitic acid over a bifunctional Co-doped MoO2/CNTs catalyst: An insight into the promoting effect of cobalt. Catal Sci Technol 2016;6:2065–76. https://doi.org/10.1039/c5cy01575h.

[242] Mallesham B, Sudarsanam P, Raju G, Reddy BM. Design of highly efficient Mo and W-promoted SnO2 solid acids for heterogeneous catalysis: Acetalization of bio-glycerol. Green Chemistry 2013;15:478–89. https://doi.org/10.1039/c2gc36152c.

[243] Gautam R, Vinu R. Non-catalytic fast pyrolysis and catalytic fast pyrolysis of Nannochloropsis oculata using Co-Mo/γ-Al2O3 catalyst for valuable chemicals. Algal Res 2018;34:12–24. https://doi.org/10.1016/j.algal.2018.06.024.

[244] Prasomsri T, Shetty M, Murugappan K, Román-Leshkov Y. Insights into the catalytic activity and surface modification of MoO 3 during the hydrodeoxygenation of lignin-derived model compounds into aromatic hydrocarbons under low hydrogen pressures. Energy Environ Sci 2014;7:2660–9. https://doi.org/10.1039/c4ee00890a.

[245] Lam JE, Mohamed AR, Kay Lup AN, Koh MK. Palm fatty acid distillate derived biofuels via deoxygenation: Properties, catalysts and processes. Fuel Processing Technology 2022;236. https://doi.org/10.1016/j.fuproc.2022.107394.

[246] Hongloi N, Prapainainar P, Seubsai A, Sudsakorn K, Prapainainar C. Nickel catalyst with different supports for green diesel production. Energy 2019;182:306–20. https://doi.org/10.1016/j.energy.2019.06.020.

[247] Choo MY, Oi LE, Ling TC, Ng EP, Lin YC, Centi G, et al. Deoxygenation of triolein to green diesel in the H2-free condition: Effect of transition metal oxide supported on zeolite Y. J Anal Appl Pyrolysis 2020;147. https://doi.org/10.1016/j.jaap.2020.104797.

[248] Srifa A, Viriya-Empikul N, Assabumrungrat S, Faungnawakij K. Catalytic behaviors of Ni/γ-Al2O3 and Co/γ-Al2O3 during the hydrodeoxygenation of palm oil. Catal Sci Technol 2015;5:3693–705. https://doi.org/10.1039/c5cy00425j.

[249] Liu X, Yang M, Deng Z, Dasgupta A, Guo Y. Hydrothermal hydrodeoxygenation of palmitic acid over Pt/C catalyst: Mechanism and kinetic modeling. Chemical Engineering Journal 2021;407. https://doi.org/10.1016/j.cej.2020.126332.

[250] Mucsi G, Halyag N, Kurusta T, Kristály F. Control of Carbon Dioxide Sequestration by Mechanical Activation of Red Mud. Waste Biomass Valorization 2021;12:6481–95. https://doi.org/10.1007/s12649-021-01466-2.

[251] Wahyudi A, Kurniawan W, Hinode H. Study on Deactivation and Regeneration of Modified Red Mud Catalyst Used in Biodiesel Production. Green and Sustainable Chemistry 2017;07:247–58. https://doi.org/10.4236/gsc.2017.74019.

[252] Chen C, Qu S, Guo M, Lu J, Yi W, Liu R, et al. Waste limescale derived recyclable catalyst and soybean dregs oil for biodiesel production: Analysis and optimization. Process Safety and Environmental Protection 2021;149:465–75. https://doi.org/10.1016/j.psep.2020.11.022.

[253] Saidi M, Zhandnezhad A. Valorization of neem seeds biomass to biofuel via non-catalytic and catalytic pyrolysis process: Investigation of catalytic activity of Co–Mo/Al2O3 and Ni–Mo/Al2O3 for biofuel production. J Environ Manage 2023;326. https://doi.org/10.1016/j.jenvman.2022.116761.

[254] Saidi M, Safaripour M. Aqueous phase hydrodeoxygenation of anisole as a pyrolysis lignin-derived bio-oil by ether-functionalized ionic polymer-stabilized Ni-Mo nanocatalyst. Sustainable Energy Technologies and Assessments 2022;49. https://doi.org/10.1016/j.seta.2021.101770.

[255] Han Y, Gholizadeh M, Tran CC, Kaliaguine S, Li CZ, Olarte M, et al. Hydrotreatment of pyrolysis bio-oil: A review. Fuel Processing Technology 2019;195. https://doi.org/10.1016/j.fuproc.2019.106140.

[256] Zhang B, Gao M, Geng J, Cheng Y, Wang X, Wu C, et al. Catalytic performance and deactivation mechanism of a one-step sulfonated carbon-based solid-acid catalyst in an esterification reaction. Renew Energy 2021;164:824–32. https://doi.org/10.1016/j.renene.2020.09.076.

[257] Bhoi PR, Ouedraogo AS, Soloiu V, Quirino R. Recent advances on catalysts for improving hydrocarbon compounds in bio-oil of biomass catalytic pyrolysis. Renewable and Sustainable Energy Reviews 2020;121. https://doi.org/10.1016/j.rser.2019.109676.

[258] Bagnato G, Sanna A, Paone E, Catizzone E. Recent catalytic advances in hydrotreatment processes of pyrolysis bio-oil. Catalysts 2021;11:1–19. https://doi.org/10.3390/catal11020157.

[259] Saidi M, Inaloo EB, Liu H, Zhao H. Olive pomace waste conversion to bio-fuel by application of integrated configuration of pyrolysis/hydrodeoxygenation process. Process Safety and Environmental Protection 2024;192:1271–81. https://doi.org/10.1016/j.psep.2024.10.123.

[260] Stefanidis SD, Kalogiannis KG, Iliopoulou EF, Lappas AA, Pilavachi PA. In-situ upgrading of biomass pyrolysis vapors: Catalyst screening on a fixed bed reactor. Bioresour Technol 2011;102:8261–7. https://doi.org/10.1016/j.biortech.2011.06.032.

[261] Lin Y, Zhang C, Zhang M, Zhang J. Deoxygenation of bio-oil during pyrolysis of biomass in the presence of CaO in a fluidized-bed reactor. Energy and Fuels 2010;24:5686–95. https://doi.org/10.1021/ef1009605.

[262] Zhang CT, Zhang L, Li Q, Wang Y, Liu Q, Wei T, et al. Catalytic pyrolysis of poplar wood over transition metal oxides: Correlation of catalytic behaviors with

physiochemical properties of the oxides. Biomass Bioenergy 2019;124:125–41. https://doi.org/10.1016/j.biombioe.2019.03.017.

[263] Mochizuki T, Atong D, Chen SY, Toba M, Yoshimura Y. Effect of SiO2 pore size on catalytic fast pyrolysis of Jatropha residues by using pyrolyzer-GC/MS. Catal Commun 2013;36:1–4. https://doi.org/10.1016/j.catcom.2013.02.018.

[264] Yang Y, Xiao P, Wen M, Liu T, Yang J, Dai S, et al. A review on the modified red mud for biomass catalytic pyrolysis: Preparation, mechanisms and perspectives. J Anal Appl Pyrolysis 2024;178. https://doi.org/10.1016/j.jaap.2024.106430.

[265] Shao S, Xiang X, Li X, Zhang H, Xiao R, Cai Y. Synergy in the Selective Production of Ketone Platform Compounds from Biomass Pyrolysis Vapors over CeO2 Catalysts. Ind Eng Chem Res 2020;59:6460–9. https://doi.org/10.1021/acs.iecr.9b06454.

[266] Wang S, Li Z, Bai X, Yi W, Fu P. Catalytic pyrolysis of lignin with red mud derived hierarchical porous catalyst for alkyl-phenols and hydrocarbons production. J Anal Appl Pyrolysis 2018;136:8–17. https://doi.org/10.1016/j.jaap.2018.10.024.

[267] Wang L, Si B, Han X, Yi W, Li Z, Zhang A. Study on the effect of red mud and its component oxides on the composition of bio-oil derived from corn stover catalytic pyrolysis. Ind Crops Prod 2022;184. https://doi.org/10.1016/j.indcrop.2022.114973.

[268] Yang Y, Xu X, He H, Huo D, Li X, Dai L, et al. The catalytic hydrodeoxygenation of bio-oil for upgradation from lignocellulosic biomass. Int J Biol Macromol 2023;242. https://doi.org/10.1016/j.ijbiomac.2023.124773.

[269] Farokhi G, Saidi M. Catalytic activity of bimetallic spinel magnetic catalysts (NiZnFe2O4, CoZnFe2O4 and CuZnFe2O4) in biodiesel production process from neem oil: Process evaluation and optimization. Chemical Engineering and Processing - Process Intensification 2022;181. https://doi.org/10.1016/j.cep.2022.109170.

[270] Muangsuwan C, Kriprasertkul W, Ratchahat S, Liu CG, Posoknistakul P, Laosiripojana N, et al. Upgrading of Light Bio-oil from Solvothermolysis Liquefaction of an Oil Palm Empty Fruit Bunch in Glycerol by Catalytic Hydrodeoxygenation Using NiMo/Al2O3or CoMo/Al2O3Catalysts. ACS Omega 2021;6:2999–3016. https://doi.org/10.1021/acsomega.0c05387.

[271] Jahromi H, Agblevor FA. Hydrodeoxygenation of pinyon-juniper catalytic pyrolysis oil using red mud-supported nickel catalysts. Appl Catal B 2018;236:1–12. https://doi.org/10.1016/j.apcatb.2018.05.008.

[272] Kumar R, Enjamuri N, Shah S, Al-Fatesh AS, Bravo-Suárez JJ, Chowdhury B. Ketonization of oxygenated hydrocarbons on metal oxide based catalysts. Catal Today 2018;302:16–49. https://doi.org/10.1016/j.cattod.2017.09.044.

[273] Yang Y, Xiao P, Wen M, Liu T, Yang J, Dai S, et al. A review on the modified red mud for biomass catalytic pyrolysis: Preparation, mechanisms and perspectives. J Anal Appl Pyrolysis 2024;178. https://doi.org/10.1016/j.jaap.2024.106430.

[274] Chen X, Che Q, Li S, Liu Z, Yang H, Chen Y, et al. Recent developments in lignocellulosic biomass catalytic fast pyrolysis: Strategies for the optimization of bio-oil quality and yield. Fuel Processing Technology 2019;196. https://doi.org/10.1016/j.fuproc.2019.106180.

[275] Asikin-Mijan N, Lee H V., Juan JC, Noorsaadah AR, Abdulkareem-Alsultan G, Arumugam M, et al. Waste clamshell-derived CaO supported Co and W catalysts for renewable fuels production via cracking-deoxygenation of triolein. J Anal Appl Pyrolysis 2016;120:110–20. https://doi.org/10.1016/j.jaap.2016.04.015.

[276] Cai J, Rahman MM, Zhang S, Sarker M, Zhang X, Zhang Y, et al. Review on Aging of Bio-Oil from Biomass Pyrolysis and Strategy to Slowing Aging. Energy and Fuels 2021;35:11665–92. https://doi.org/10.1021/acs.energyfuels.1c01214.

[277] Yang E, Nam E, Jo Y, An K. Coke resistant NiCo/CeO2 catalysts for dry reforming of methane derived from core@shell Ni@Co nanoparticles. Appl Catal B 2023;339. https://doi.org/10.1016/j.apcatb.2023.123152.

[278] Robota HJ, Alger JC, Shafer L. Converting algal triglycerides to diesel and HEFA jet fuel fractions. Energy and Fuels 2013;27:985–96. https://doi.org/10.1021/ef301977b.

[279] Lee CW, Lin PY, Chen BH, Kukushkin RG, Yakovlev VA. Hydrodeoxygenation of palmitic acid over zeolite-supported nickel catalysts. Catal Today 2021;379:124–31. https://doi.org/10.1016/j.cattod.2020.05.013.

[280] Hongloi N, Prapainainar P, Seubsai A, Sudsakorn K, Prapainainar C. Nickel catalyst with different supports for green diesel production. Energy 2019;182:306–20. https://doi.org/10.1016/j.energy.2019.06.020.

[281] Žula M, Grilc M, Likozar B. Hydrocracking, hydrogenation and hydro-deoxygenation of fatty acids, esters and glycerides: Mechanisms, kinetics and transport phenomena. Chemical Engineering Journal 2022;444. https://doi.org/10.1016/j.cej.2022.136564.

[282] Xing S, Liu Y, Liu X, Li M, Fu J, Liu P, et al. Solvent-free hydrodeoxygenation of bio-lipids into renewable alkanes over NiW bimetallic catalyst under mild conditions. Appl Catal B 2020;269. https://doi.org/10.1016/j.apcatb.2020.118718.

[283] He C, Ruan T, Ouyang X, Ma Y, Qian Y, Qiu X. Selective hydrodeoxygenation of monophenolics from lignin bio-oil for preparing cyclohexanol and its derivatives over Ni-Co/Al2O3-MgO catalyst. Ind Crops Prod 2023;202. https://doi.org/10.1016/j.indcrop.2023.117045.

[284] Ma L, Deng W, Hu X, Xu K, Xu J, Jiang L, et al. Identifying the coking of bio-oil in pyrolysis: An in-situ EPR investigation. Fuel Processing Technology 2024;253. https://doi.org/10.1016/j.fuproc.2023.108012.

[285] Li J, Lv X, Wang Y, Li Q, Hu C. Hydrotreatment Upgrading of Bio-oil from Torrefaction of Pubescens in Alcohol over Pd/NbOPO4. ACS Omega 2018;3:4836–46. https://doi.org/10.1021/acsomega.8b00180.

[286] Wang Q, Chen J, Li X, Yang X, Wu Y, Li S, et al. Calcination temperature induced structural change of red mud and its enhanced catalytic performance for hydrocarbon-based biofuels production. Fuel Processing Technology 2022;233. https://doi.org/10.1016/j.fuproc.2022.107316.

[287] Adzahar NA, Asikin-Mijan N, Saiman MI, Alsultan GA, Mastuli MS, Shamsuddin MR, et al. Chemoselective decarboxylation of ceiba oil to diesel-range alkanes over a red mud based catalyst under H2-free conditions. RSC Adv 2022;12:16903–17. https://doi.org/10.1039/d2ra00853j.

[288] Oh S, Choi HS, Choi IG, Choi JW. Evaluation of hydrodeoxygenation reactivity of pyrolysis bio-oil with various Ni-based catalysts for improvement of fuel properties. RSC Adv 2017;7:15116–26. https://doi.org/10.1039/c7ra01166k.

[289] Muangsuwan C, Kriprasertkul W, Ratchahat S, Liu CG, Posoknistakul P, Laosiripojana N, et al. Upgrading of Light Bio-oil from Solvothermolysis Liquefaction of an Oil Palm Empty Fruit Bunch in Glycerol by Catalytic Hydrodeoxygenation Using NiMo/Al2O3or CoMo/Al2O3Catalysts. ACS Omega 2021;6:2999–3016. https://doi.org/10.1021/acsomega.0c05387.

[290] Bulavchenko OA, Cherepanova S V., Tsybulya S V. In situ XRD investigation of Co 3O 4 reduction. Zeitschrift fur Kristallographie, Supplement, 2009, p. 329–34. https://doi.org/10.1524/zksu.2009.0048.

[291] Yi Y, Zhang P, Qin Z, Yu C, Li W, Qin Q, et al. Low temperature CO oxidation catalysed by flower-like Ni-Co-O: How physicochemical properties influence catalytic performance. RSC Adv 2018;8:7110–22. https://doi.org/10.1039/c7ra12635b.

[292] Jia Z, Wang X, Thevenet F, Rousseau A. Dynamic probing of plasma-catalytic surface processes: Oxidation of toluene on CeO2. Plasma Processes and Polymers 2017;14. https://doi.org/10.1002/ppap.201600114.

[293] Li Q, Wei G, Yang Y, Li Z, Zhang L, Huang Q. Mechanochemical synthesis of Fe2O3/Zn-Al layered double hydroxide based on red mud. J Hazard Mater 2020;394. https://doi.org/10.1016/j.jhazmat.2020.122566.

[294] Jin Q, Ma L, Zhou W, Shen Y, Fernandez-Delgado O, Li XJ. Smart paper transformer: New insight for enhanced catalytic efficiency and reusability of noble metal nanocatalysts. Chem Sci 2020;11:2915–25. https://doi.org/10.1039/c9sc05287a.

[295] Ashok A, Kumar A, Ponraj J, Mansour SA, Tarlochan F. Effect of Ni incorporation in cobalt oxide lattice on carbon formation during ethanol decomposition reaction. Appl Catal B 2019;254:300–11. https://doi.org/10.1016/j.apcatb.2019.05.013.

List of Publications

➢ *From Thesis*

- **Komandur, J**., Vinu, R., & Mohanty, K. (2022). Pyrolysis kinetics and pyrolysate composition analysis of Mesua ferrea L: A non-edible oilseed towards the production of sustainable renewable fuel. Bioresource Technology, 351. https://doi.org/10.1016/j.biortech.2022.126987.
- **Komandur, J**., Kumar, A., Para, P., & Mohanty, K. (2022). Kinetic Parameters Estimation of Thermal and Co-Pyrolysis of Groundnut De-oiled Cake and Polyethylene Terephthalate (PET) Waste. Energies, 15(20). https://doi.org/10.3390/en15207502.
- **Komandur, J.,** Vinu, R., & Mohanty, K. (2025). Analytical and Applied Copyrolysis of Mesua ferrea L. and Polyethyelene Terephthalate Plastic for Hydrocarbon-Rich Bio-oil. ACS Omega, 10(1), 529–540. https://doi.org/10.1021/acsomega.4c07019
- **Janaki Komandur**, Anindita Das, Kaustubha Mohanty, Chapter 6 – Thermochemical conversion of woody biomass to energy and high-value products, Sustainable Biorefining of Woody Biomass to Biofuels and Biochemicals, Woodhead Publishing, 2024, Pages 125-162, ISBN 9780323911870, https://doi.org/10.1016/B978-0-323-91187-0.00006-0.
- **Janaki Komandur**, Kaustubha Mohanty, Chapter 2 - Fast pyrolysis of biomass and hydrodeoxygenation of bio-oil for the sustainable production of hydrocarbon biofuels, Hydrocarbon Biorefinery, Elsevier, 2022, Pages 47-76, ISBN 9780128233061, https://doi.org/10.1016/B978-0-12-823306-1.00003-0.

➢ *Other Publications*

- Kumar, A., **Komandur, J**., Chaudhary, V., & Mohanty, K. (2023). Catalytic Co-Pyrolysis of Mesua ferrea L. De-Oiled Cake and Garlic Husk in the Presence of Red-Mud-Based Catalysts. Catalysts, 13(11). https://doi.org/10.3390/catal13111401.

- Agarwalla, A., **Komandur, J**., & Mohanty, K. (2023). Current trends in the pretreatment of microalgal biomass for efficient and enhanced bioenergy production. In Bioresource Technology (Vol. 369). Elsevier Ltd. https://doi.org/10.1016/j.biortech.2022.128330.

List of Conferences Attended

- **AIChE 2024 Annual Meeting, San Diego, California**
- **PyroAsia Symposium 2024, India**
- 4th International Conference for Bioresource Technology for Bioenergy, Bioproducts & Environmental Sustainability. **(BIORESTEC 2023), Lake Garda, Italy**
- **PyroAsia Symposium 2023, Kuala Lumpur, Malaysia**
- Sustainable waste management for circular economy Sustainable waste management for circular economy. A winter school by Indo-German Centre for sustainability **(IGCS-2022)**.
- International Conference on Biotechnology, Sustainable Bioresources and Bioeconomy. **(BSBB 2022), India.**